University of Zurich[UZH]

Soil dynamics related to the escarpment retreat of a quartz sandstone in a sedimentary tableland: Data analysis of Pu-Isotopes and soil properties from a catena at Urwisko Batorowskie in the Stołowe Mountains in Poland

GEO 511 Master's Thesis

Author
Simon Amrein
10-865-046

Supervised by
Prof. Dr. Markus Egli

Faculty representative
Prof. Dr. Markus Egli

30.04.2024
Department of Geography, University of Zurich

University of Zurich[UZH]

Department of Geography

Soil dynamics related to the escarpment retreat of a quartz sandstone in a sedimentary tableland

Data analysis of Pu-Isotopes and soil properties from a catena at Urwisko Batorowskie in the Stołowe Mountains in Poland

GEO 511 Master's Thesis

Author

Simon R. Amrein

10-865-046

Supervisor / Faculty representative

Prof. Dr. Markus Egli

30th of April 2024

Department of Geography, University of Zurich

IMPRESSUM

Title	Soil dynamics related to the escarpment retreat of a quartz sandstone in a sedimentary tableland: Data analysis of Pu-Isotopes and soil properties from a catena at Urwisko Batorowskie in the Stołowe Mountains in Poland
Institution	Department of Geography, University of Zurich
Author	Simon R. Amrein
Contact	simon.amrein@uzh.ch
Supervisor	Prof. Dr. Markus Egli
Citation	Amrein, S. R. (2024): Soil dynamics related to the escarpment retreat of a quartz sandstone in a sedimentary tableland: Data analysis of Pu-Isotopes and soil properties from a catena at Urwisko Batorowskie in the Stołowe Mountains in Poland. Department of Geography, University of Zurich.
Version	Version 1: 30 April 2024
Copyright	© 2024

ABSTRACT

This thesis examines the soil dynamics associated with the retreat of quartz sandstone escarpments in the sedimentary tableland of the Stołowe Mountains, Poland. Using fallout radionuclide $^{239+240}$Pu as a tracer, this study assesses soil erosion and deposition rates along a catena at the plateau of Urwisko Batorowskie. Erosion and deposition rates are calculated using a combination of erosion modeling methods (IM, PDM, and MODERN).

Furthermore, the study incorporates an analysis of physical and chemical soil properties, including bulk density, grain size distribution, pH, amorphous iron and aluminum concentrations, organic matter content and total elemental content, to offer a comprehensive understanding of soil characteristics in relation to erosion processes. The additional application of luminescence dating enhances the understanding of soil formation and weathering processes, contributing to a broader perspective on landscape evolution in sandstone environments.

A soilscape with several different pedons from Podzols via Stagnosols to Gleysols and possibly polygenetic soils was discovered. Soil erosion and deposition, vary significantly along the slope, with estimated erosion rates of 0.6–6.9 t ha^{-1} yr^{-1} and deposition rates of 0.23–7.72 t ha^{-1} yr^{-1}. The physical and chemical soil properties which were assessed to determine their relation to erosion and deposition, suggest a dynamic interaction between biological and geomorphological processes.

Keywords: Sedimentary tableland; sandstone caprock; escarpment retreat; fallout radionuclides; $^{239+240}$Pu activity and inventory; erosion and deposition; soil redistribution; Infrared and optical stimulated luminescence; weathering indices; soil properties; Podzol; Stołowe Mountains; Urwisko Batorowskie; Sudetes.

CONTENT

1 INTRODUCTION 1
1.1 Outline of previous research 1
1.2 Objectives of this study 8

2 STUDY AREA 11
2.1 Topography and relief 12
2.2 Geology 13
2.3 Geomorphology and landforms 17
2.4 Climate 20
2.5 Soils 20
2.6 Vegetation 21

3 MATERIAL AND METHODS 23
3.1 Sampling sites 23
3.2 Soil profiles 23
3.3 Sampling 23
3.4 Physical soil properties 26
3.5 Chemical soil properties 28
3.6 Weathering indices 29
3.7 Infrared and Optical Stimulated Luminescence 31
3.8 Pu-Activity 31
3.9 Modelling erosion and deposition rates with MODERN 35
3.10 Statistics 37

4 RESULTS 38
4.1 Soil profiles 38
4.2 Soil properties 40
4.3 Weathering indices 55
4.4 Luminescence 60
4.5 $^{239+240}$Pu 63
4.6 Soil erosion and accumulation rates 68
4.7 Correlations 75

5 DISCUSSION 78

5.1 Distribution of soil properties 78
5.2 Lithological Discontinuities 80
5.3 Weathering states 83
5.4 Podzolization processes along the slope 84
5.5 Trace elements and anthropogenic pollution 86
5.6 Relative deposition ages 87
5.7 Soil redistribution 88
5.8 Escarpment retreat and evolution of slope 91

6 CONCLUSION 93

7 OUTLOOK 94

8 REFERENCES 95

ACKNOWLEDGEMENTS 118

GLOSSARY 119

FIGURES 121

TABLES 126

EQUATIONS 127

PHOTOS 128

APPENDIX 129

1 INTRODUCTION

The Stołowe Mountains are a stepped tableland in the Central Sudetes in southwest Poland and belong to the middle altitude mountains. The Sudetes show in general an extremely wide variety of landforms (Migoń 2011). However the Stołowe Mountains stand out with its impressive tableland morphology (Kasprzak & Migoń 2015c) which is characterized by various impressive landforms such as plateaus, mesas, steep cliffs, rock labyrinths and ruin-like reliefs (Migoń & Jancewicz 2024).

The Sudetes had an increasing population since the 14th century, which shaped the landscape progressively with forest clearance and quarrying (Latocha & Migoń 2006). The anthropogenic influence lead to deforestation and forest dieback due to air pollution (Latocha & Migoń 2006). But since the second half of the 19th century the population declines due to emigration caused by the harsh environmental conditions and the search for jobs in industrialized regions (Latocha & Migoń 2006). Since then renaturalization has been observed (Latocha & Migoń 2006). The Stołowe Mountains represent a considerable geoheritage and touristic value due to its bewildering geomorphological sites (Migoń & Parzóch 2021; Wojewoda 2011). Nowadays, the biggest threat to the integrity of these geosites is mainly tourism (Duszyński & Migoń 2022a). To protect specifically its diverse geoheritage the Stołowe Mountains National Park was established in 1993 (Duszyński 2024). Hence, today there are limitations for anthropogenic influence through nature and landscape protection (Migoń & Latocha 2013).

1.1 OUTLINE OF PREVIOUS RESEARCH

Due to their geomorphic diversity, numerous and manifold research on the formation and development of the Sudetes in general and the Stołowe Mountains in particular have been conducted.

The Sudetes had been influenced by many successive cold periods during the Pleistocene (Traczyk & Migoń 2003) and the landforms often have a periglacial influence, which would include rock glaciers, blockfields, scree slopes, loess covers, solifluction mantles, cryoplanation and patterned ground (Traczyk & Migoń 2003). Glacial and periglacial landforms were found for example in the Karkonosze Mountains (Migoń *et al.* 2013) as well as signs of solifluction and permafrost creep (Traczyk & Migoń 2003). But no uniform periglacial slope profile has been created (Migoń 2011).

Although the last glacial period was of relatively minor importance, periglacial cover deposits are usually of the last glacial age (Traczyk & Migoń 2003).

With remote sensing using LiDAR to generate digital elevation models (DEM) Migoń *et al.* (2013) were able to identify and reinterpret various landforms such as glacial, periglacial, and fluvial features in densely forested and mountainous terrains, which were previously partially unrecognized. Further detection of morphological features and calculation of slope elevation and relief was done by Kasprzak & Migoń (2015a) and the structure of the caprock and escarpment (Migoń & Kasprzak 2016). Jancewicz *et al.* (2019) found connectivity patterns in contrasting tableland and ridge-and-valley landscapes, while Burliga *et al.* (2023) looked at the extent and structure of mire ecosystems in the area. Despite the high spatial resolution of remote sensing forest cover obscures terrain features (Jancewicz & Porębna 2022) which makes field verification necessary (Jancewicz *et al.* 2019). With the use of electrical resistivity tomography (ERT) the surface relief and the subsurface sedimentary layer was studied at different cross-section around the Sudetes (Burliga *et al.* 2023; Duszyński *et al.* 2016, 2017; Migoń *et al.* 2017b; Pawlik & Kasprzak 2015). These revealed a multipart structure and, in some cases, an inclination of the lithological layers.

The relief is formed by complex interactions of lithology, climate, and geomorphic processes. Traczyk and Migoń (2003) describe the range of periglacial landforms like tors, cryoplanation terraces, and patterned grounds influenced by the lithological diversity and Pleistocene climatic conditions. They suggest that the geomorphic evolution of the Sudetes is a cumulative effect of multiple cold periods, rather than the result of the last glacial period alone, indicating a complex history of periglacial geomorphology shaped by lithology, inherited relief, and glacial history (Traczyk & Migoń 2003). Pawlik and Kasprzak (2015) and Valtera and Schaetzl (2017) described the development and extent of soil surface in natural forests is typically unevenly broken with pit and mound relief. pit-and-mound microrelief in forested environments which influences the ecosystems capacity to retain and redistribute water. In managed forests a gradual loss of microrelief is seen (Valtera & Schaetzl 2017). Intense rainfall events often exceed the retention threshold of forested watersheds and the microrelief is important to mediate potential runoff (Valtera & Schaetzl 2017). Jancewicz et al. (2019) saw that surface runoff are often not connected to the main drainage channels but infiltrates into porous lithology.

A variety of slope forms is found in the Sudetes. These include stepped, gravitational rectilinear, convex-concave, talus and pediment-like slopes, which are largely inherited from Prepleistocene (Traczyk & Migoń 2003). The majority of slopes in the Stołowe Mountains is in strength equilibrium, which means that their development is primarily controlled by rock mass characteristic (Synowiec 1999). But some initial stages of deep-seated gravitational slope deformation was found by (Migoń et al. 2017b). These deformations are driven by lithostatic stress in favorable lithological and structural settings and can even occur in non-glaciated regions due to the inherent geological weaknesses in facilitating slope instability (Migoń et al. 2017b).

The caprock is made of quartz-containing sandstone (Wojewoda 1997; Wojewoda *et al.* 2011). The cliff line recedes through a combination of processes (Duszyński & Migoń 2015) without following a single pathway of escarpment evolution (Migoń & Kasprzak 2016). One significant mechanism contributing to the retreat is sapping (Kasprzak & Migoń 2015a), which involves the subsurface selective disintegration of the rock mass (see Figure 1) (Duszyński *et al.* 2015, 2018, 2019; Duszyński & Migoń 2015; Filippi *et al.* 2021; Migoń & Parzóch 2021; Parzóch & Migoń 2015). Groundwater emergence, silica dissolution, and the underground removal of dissolved solids also contribute to the escarpment retreat through downslope succession (Dumanowski 1961; Duszyński *et al.* 2019; Migoń *et al.* 2013; Migoń & Kasprzak 2011; Pulinowa 1989). These processes not only lower the slope surface but also result in the denudation of the underlying incompetent rock layers (Duszyński & Migoń 2015; Migoń & Parzóch 2021) which include less competent sediments such as mudstones and claystones (Duszyński *et al.* 2017). Both the caprock and the underlying layers show signs of instability (Migoń & Kasprzak 2016). Instable areas are prone to large-scale caprock failures, toppling of tors (Michniewicz *et al.* 2020) and shallow landslips below the caprock (Migoń & Kasprzak 2016). Although such events significantly influencing the morphology of the escarpment, they occur rarely and are highly localized (Migoń & Kasprzak 2016). The continuous slow retreat of the sandstone rock faces occurs through the detachment of individual joint-bound blocks (Migoń & Kasprzak 2016) and the sub-caprock slope lowering and retreat is leaving separated sandstone boulders (Duszyński et al. 2015).

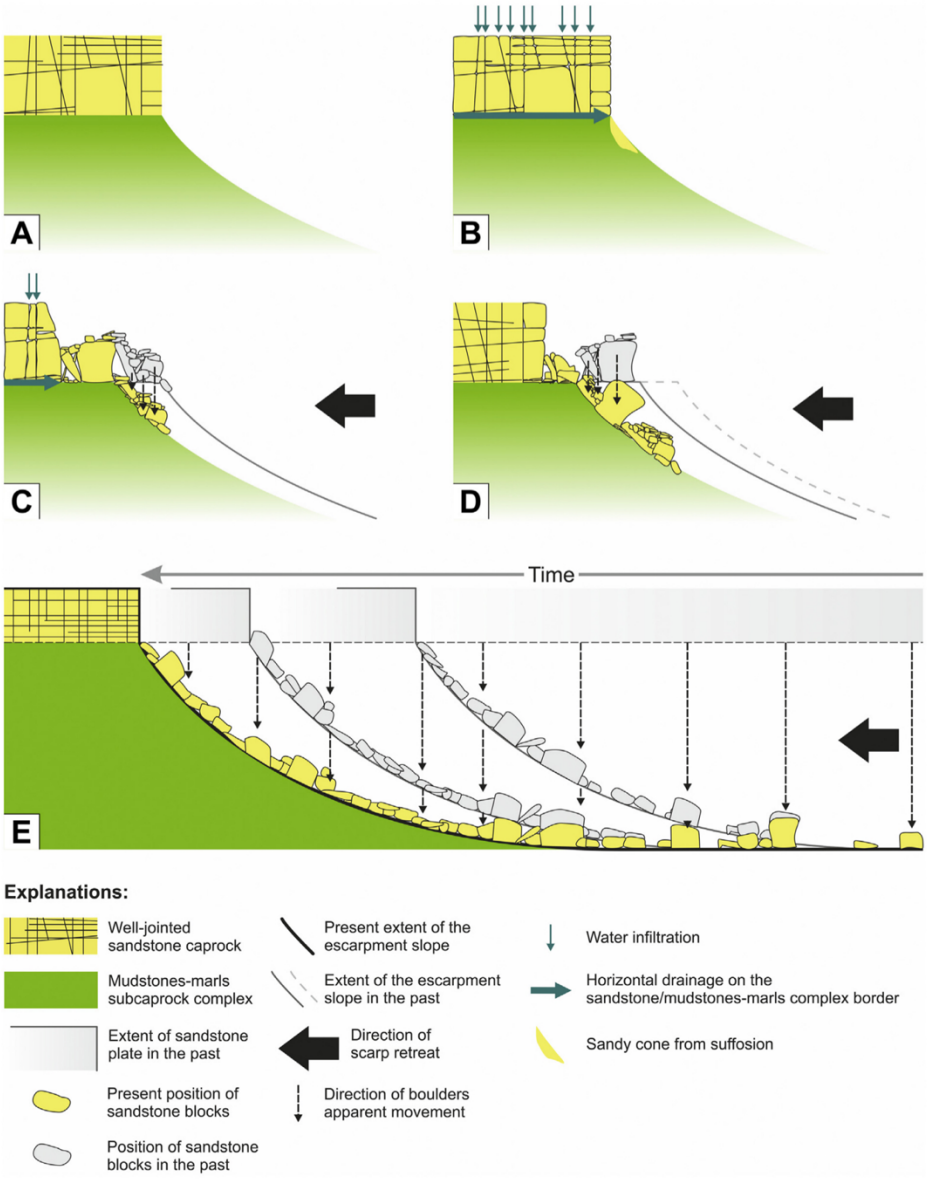

Figure 1: Conceptual model of in situ disintegration according to (Duszyński & Migoń 2015) (modified after Duszyński et al. (2019)).

Duszyński & Migoń (2015) were mapping the extent of the boulders which are spread up to 1 km away from caprock (Duszyński *et al.* 2017). They confirmed that the boulders are allochthonous derived from quartz sandstone beds of the upper plateau and are remains from the sandstone layer which was stratigraphically 50 m above the present-day altitudinal position of these boulders (Migoń & Parzóch 2021). Duszyński & Migoń (2015) also found a systematic decrease in rock strength with increasing distance from the sandstone cliff.

Although landslides are able to transport allochthonous boulders further and accumulate boulders in clusters and linear belts (Duszyński *et al.* 2017), remnant boulders occupy a position increasingly

further away from escarpment rims but experience little movement (Duszyński & Migoń 2015). Simulations of rockfall run-out zones (Duszyński et al. 2015) and mass movement models (Parzóch & Migoń 2015) could not explain the current distribution, as the actual extent of boulders is much larger than the simulations. So rockfall and mass movement scenarios are doubted (Duszyński *et al.* 2015; Parzóch & Migoń 2015). The boulders are theorized to be the remnants of in situ degraded caprock (Migoń & Parzóch 2021) and long eroded sandstone mesas (Parzóch & Migoń 2015) and are settling with denudation of the escarpment (see Figure 1) (Migoń & Parzóch 2021). So the boulder aprons are diachronic and record long-term retreat of escarpments (Duszyński & Migoń 2015).

The physical and chemical weathering processes play a significant role in shaping the landscapes in the Stołowe Mountains. Quartz, present in the occurring sandstone, is poorly soluble and hardly affected by chemical weathering (Wray & Sauro 2017). But solutional weathering through arenization (chemical decay), intergranular dissolution of quartz, mechanical erosion and sapping (Migoń 2021) increases the porosity and decreases rock strength (Wray & Sauro 2017). The restricted surface runoff and drainage diversion underground due to porous and jointed sandstone may lead to higher weathering in the sandstone caprock (Jancewicz *et al.* 2019). Subsurface processes play an important part in the evolution of the sandstone (Migoń 2021). Duszyński et al. (2016) have demonstrated that underground erosion and mechanical removal of sand from sandstone caprocks, facilitated by fracture networks, play a crucial role in the morphogenetic development of the Stołowe Mountains. Sand grains are detached, fluvially transported and removed from the rock capstone (Migoń & Duszyński 2017). This process results in gradual subsidence and the formation of ruiniform landscapes, where sand is actively transported from beneath the rock faces to the lateral surface, significantly impacting the geomorphological evolution of tablelands. Additionally, Pawlik et al. (2023) explore how trees influence weathering and soil production. Their study emphasizes the biogeophysical interactions, particularly the role of tree roots as they develop along most accessible surfaces, in weathering processes, cause rock cliff retreat and scree formation which enhance soil formation and alter the hydrological and mechanical properties of the subsurface environment. This highlights the complexity of weathering processes, which include both abiotic factors such as underground erosion and biotic factors such as vegetation, in shaping the geomorphological character of sandstone landscapes (Duszyński *et al.* 2016, 2021; Pawlik *et al.* 2023).

In plane areas peatlands and mires are common and often anthropogenically influenced (Glina *et al.* 2017a). Bogacz et al. (2018) found that drainage has altered soil properties, increasing siltation

and acidity, which indicates lasting effects of historical land use on peatland structure and chemistry and also leads to changes in organic matter (Zawieja & Glina 2017) and vegetation composition (Glina *et al.* 2019). Additionally, Glina et al. (2017b) showed how peatlands act as repositories for trace elements like lead, influenced by historical air pollution and groundwater flows.

The Sudetes are also largely covered by forests which are either managed (Reczyńska & Świerkosz 2012) or natural ecosystems (Boratyńska *et al.* 2021). Although the protective function of trees against erosion is widely accepted (Pawlik *et al.* 2013), trees are not only a factor to reduce erosion probability, but can also contribute to erosion, downslope or even upslope mass transport (Gallaway *et al.* 2009; Šamonil *et al.* 2018) due to tree uprooting (Pawlik 2013).

Tree uprooting is a process of toppling trees and the roots tearing up a lens of soil, which is mostly caused by wind throw (Armson & Fessenden 1973; Clinton & Baker 2000; Lyford & MacLean 1966; Peterson & Pickett 1990). Tree uprooting plays a critical role in modifying the physical properties of regolith and soils and in sediment transport which leads to uneven distribution across hillslope (Pawlik & Kasprzak 2015; Strzyżowski *et al.* 2018; Valtera & Schaetzl 2017). In temperate mountain forests, wind throw is widely spread and tree uprooting is an important process (Šamonil *et al.* 2017, 2018). It is one of the most frequent disturbances in mountain forest ecosystems (Schaetzl *et al.* 1989) and can dominate slope processes through direct and indirect impact (Phillips *et al.* 2017). It leaves a unique microtopography with pits and mounds (Šamonil *et al.* 2009) or small scale stepped topography formed through gravel armors (Pawlik *et al.* 2016). Tree uprooting may also lead to structural changes in cover deposits so that they lose their inherited periglacial signatures (Pawlik *et al.* 2013).

Studies in the Tatra Mountains reported that 3.9 % of the surface area was affected by a single windthrow event with locally up to 14.5 % (Strzyżowski *et al.* 2016). From remnants of other windthrow events root plates covered 1.3–5.4 % of the area and a total area of 34–94 % was affected (Strzyżowski 2021). In temperate mountain forests, roots can reach an area of up to 40 m^2 (Šamonil *et al.* 2014) and volumes of up to 60 m^3 (Phillips *et al.* 2017). The root plate dimensions increase with increasing DBH and with coarse fragment content (Strzyżowski *et al.* 2018). The root depth increases with tree fall angle, decreasing slope inclination and decreasing coarse fragment content (Strzyżowski *et al.* 2018) and the average depth of uprooting pits decreases on steep slopes (Strzyżowski *et al.* 2016). Root plate degradation after tree uprooting occasionally leaves coarse

fragments of regolith and bedrock (Pawlik 2014), large boulders and cladding of angular clasts on the surface, which are not necessarily residuals of washed Solifluction from the Pleistocene (Pawlik *et al.* 2013). The combination of such coarse rock fragment and roots can inhibit erosion by armoring the surface (Phillips *et al.* 2017). In the Sudetes tree uprooting is only locally proofed (Pawlik 2014).

Human interventions can change slope processes in forests (Phillips *et al.* 2017). Although managed forests are more prone to wind damage (Pawlik *et al.* 2016), tree uprooting dynamics are often blocked in managed forests (Phillips *et al.* 2017). Tree uprooting is governed by topography, regolith properties and forest stand structure (Pawlik *et al.* 2016) and uprooting dynamics can be much more effective on steeper slopes (Pawlik 2014). But the type of forest is more important than local bedrock geology, regolith characteristics and slope inclination (Pawlik *et al.* 2017).

The landscape evolution is also influenced by different natural surface processes driven by geomorphic events. Migoń (2017) emphasizes that extreme meteorological events like heavy rain and strong winds occasionally trigger significant geomorphic changes, such as landslides, debris flows, and tree uprooting, reshaping forested slopes. These events are rare but profound, highlighting the dynamic nature of these mountain ranges despite their apparent stability under current forested conditions. Other factors like lithology and slope steepness seemed to play a subordinate role. Furthermore, Pawlik and Šamonil (2018) categorize forest ecosystems as probably the most active environment of biogenic creep, mainly due to tree uprooting, root channel infilling, tree mounding and other biomechanical effects. Within forest ecosystems, sediment transport and erosion is highly influenced by tree roots and the physical structure of the forest floor (Pawlik *et al.* 2013). Soil creep driven by both biotic (like tree roots) and also abiotic factors (like rainfall), was identified as another regional key factor in hillslope dynamics (Pawlik & Šamonil 2018). Soil creep continuously modifies the soil and regolith layers beneath the forest canopy. Indicators for soil creep on mudstone-derived regolith are tree bending and abrupt changes in tree ring width (Pawlik *et al.* 2013).

Mass movements like landslides also have geomorphic significance in the Sudetes. Some of them were identified with remote sensing data (Kasprzak & Migoń 2015b; Migoń *et al.* 2013). Migoń et al. (2017b) found a slope instability with incipient deep-seated gravitational slope deformation not related to deglaciation. Kacprzak and Migoń (2013) found evidence of multiple generations of landslides, with soil formation in the top layer indicating relatively recent Holocene activity. Duszyński et al. (2017) highlight the critical role of landslides in the transport of clastic material across steep

slopes, particularly emphasizing their role in shaping the landscape through the redistribution of debris. Their findings suggest that landslides are significant geomorphic agents and drivers to denudation, particularly in response to intense rainfall events (Migoń 2017), contributing to the evolution of the mountainous landscape.

Another driver of denudation, erosion, was also studied with different methods and at different sites in the Sudetes. Soil erosion in particular is depending on organic matter content, water content, structure, permeability, slope gradient, soil cover, particle size distribution and skeletal fraction (Lal & Elliot 1994). Due to the increased slopes, mountainous areas are often more likely to be affected by erosion (Singer & Blackard 1982; Zingg 1940). The locally different uplift of the Sudetes changed the low-lying landscape to a higher relief with increasing erosion and led to different relief generations (Migoń 2011). Szymanowski et al. (2019) stated that erosion depends only partially on altitude and geology. Some areas that experienced more uplift exhibited stronger erosional signals and dissection, other areas showed more endogenic interaction like through precipitation (Szymanowski *et al.* 2019). Pawlik et al. (2013) described how the biological components, particularly tree roots, significantly affect soil stability and erosion. Comparably, Latocha et al. (2016) investigated the effects of land abandonment and climate change, showing how these factors accelerate erosion in previously cultivated lands, altering landscape connectivity and sediment flow. To combat soil erosion terraces were built on arable land which lead to stepped longitudinal slope profiles where soil erosion wasn't eliminated but the fluvial sediment trapped (Latocha & Migoń 2006). Such terraces were not found in the study area. The recent abandonment of agricultural practices and reforestation led to a stabilization of slopes, reducing sediment transport and restoring more natural geomorphic processes (Latocha & Migoń 2006). Kowalska et al. (2023) have applied meteoric ^{10}Be analysis to trace soil redistribution rates, demonstrating the influence of climatic factors and land management on erosion processes.

1.2 OBJECTIVES OF THIS STUDY

In order to make a further contribution to the research of this landscape, the soil dynamics, including erosion and deposition rates, in the hillslopes surrounding the escarpment shall be investigated. The aim of this master thesis is to look at the soils in the quartz sandstone and the underlying incompetent layers along a catena and to further break down the history of the landscape. For this, the

following research questions were formulated: (a) How does the composition and the properties of the soils change with distance to the sandstone caprock escarpment? (b) What is the weathering state of the soil material? (c) What is the relative deposition age of the soil horizons? (d) What is the history of erosion and deposition along a downslope catena through the escarpment cliff?

Therefore, data on soil properties and soil redistribution was collected and soil samples were taken from a catena of soil profiles along the slope of Urwisko Batorowskie. This includes physical and chemical soil properties, including bulk density, grain size distribution, pH, organic matter and total elemental content and amorphous iron and aluminum concentrations.

To assess soil development and weathering depth, different weathering indices can be applied (Derakhshan-Babaei *et al.* 2020; Fiantis *et al.* 2010; Price & Velbel 2003) In this study, the Chemical Index of Alteration (CIA) (Nesbitt & Young 1982), the Chemical Index of Weathering (CIW) (Harnois 1988), the Weathering Index of Parker (WIP) (Parker 1970), the [(CA+K)/TI]-index (Dorn 1983) and the [(NA+K)/TI]-index (Egli *et al.* 2020; Egli & Fitze 2000; Stiles *et al.* 2003) were used. Additionally, infrared (IRSL) and optical stimulated luminescence (OSL) was used for the relative dating of sediments (Rhodes 2011). Luminescence dating is based on the ability of certain minerals, to store and accumulate energy from ionizing environmental radiation when buried in the form of trapped charges, which it loses again when exposed to sunlight or other spectral sources (Aitken 1998; Munyikwa *et al.* 2021). With illumination within infrared and optical spectrum, the energy accumulation rate can be measured and based on this rate, the relative age of deposition can be dated (Rhodes 2011).

To estimate soil erosion rates fallout radionuclides (FRN) are suitable as proxies (Lal *et al.* 2013; Meusburger *et al.* 2016; Wallbrink & Murray 1993). They have already been widely used to trace mid-term soil redistribution rates in natural and agricultural areas worldwide (Alewell *et al.* 2014; He & Walling 1997). FRN are a product of above-ground nuclear weapons testing and nuclear reactor accidents, and were emitted to the upper atmosphere particularly during the 1950s–1960s with peaks in 1963–1964 (Matisoff & Whiting 2012). Therefore, FRN inventories provide information only over the last 60 years (Alewell *et al.* 2014; Lal & Elliot 1994). Due to their insoluble characteristics (Meusburger *et al.* 2016), lateral redistribution of FRN in soils is therefore associated with erosion, rather than leaching, translocation or biological processes (Ketterer *et al.* 2012). The FRN inventories of sampling sites with expected erosion or accumulation are compared with inventories of an

undisturbed reference site of assumably negligible soil erosion or deposition (He & Walling 1996). The FRN inventory in the reference sites is lost by radioactive decay, while sites with accumulation gain in FRN inventory with deposition, and sites with erosion lose FRN inventory by both decay and erosion (Lal *et al.* 2013).

Based on the previous research, the aims of the study and the research questions, the following hypothesis are formulated: (i) The sand and SiO_2 content decrease with distance from the remaining sandstone caprock, (ii) deeper weathering and soil formation can be found in the flatter slope positions, (iii) there is a continuous increase in depositional age with soil horizon depth, and (iv) the erosion rates are higher on the steep escarpment and continuously decrease with decreasing slope inclination.

2 STUDY AREA

This study is looking at sites at the cliffside of Urwisko Batorowskie in the tableland of the Stołowe Mountains in Poland (see Photo 2). The Stołowe Mountains, or Góry Stołowe in polish, are a sedimentary rock tableland and part of the Central Sudetes mountain range at the border between Poland and the Czech Republic. The cliffside of Urwisko Batorowskie is located on the south-western side of the Batorówa massif which belongs to the Narożnik plateau.

The Stołowe Mountains were established as a national park (Park Narodowy Gór Stołowych) in 1993 (Duszyński 2024). The park covers an area of 63.39 square kilometers and the coordinates of its center are 50°28'00.1"N 16°19'59.9"E (WGS84).

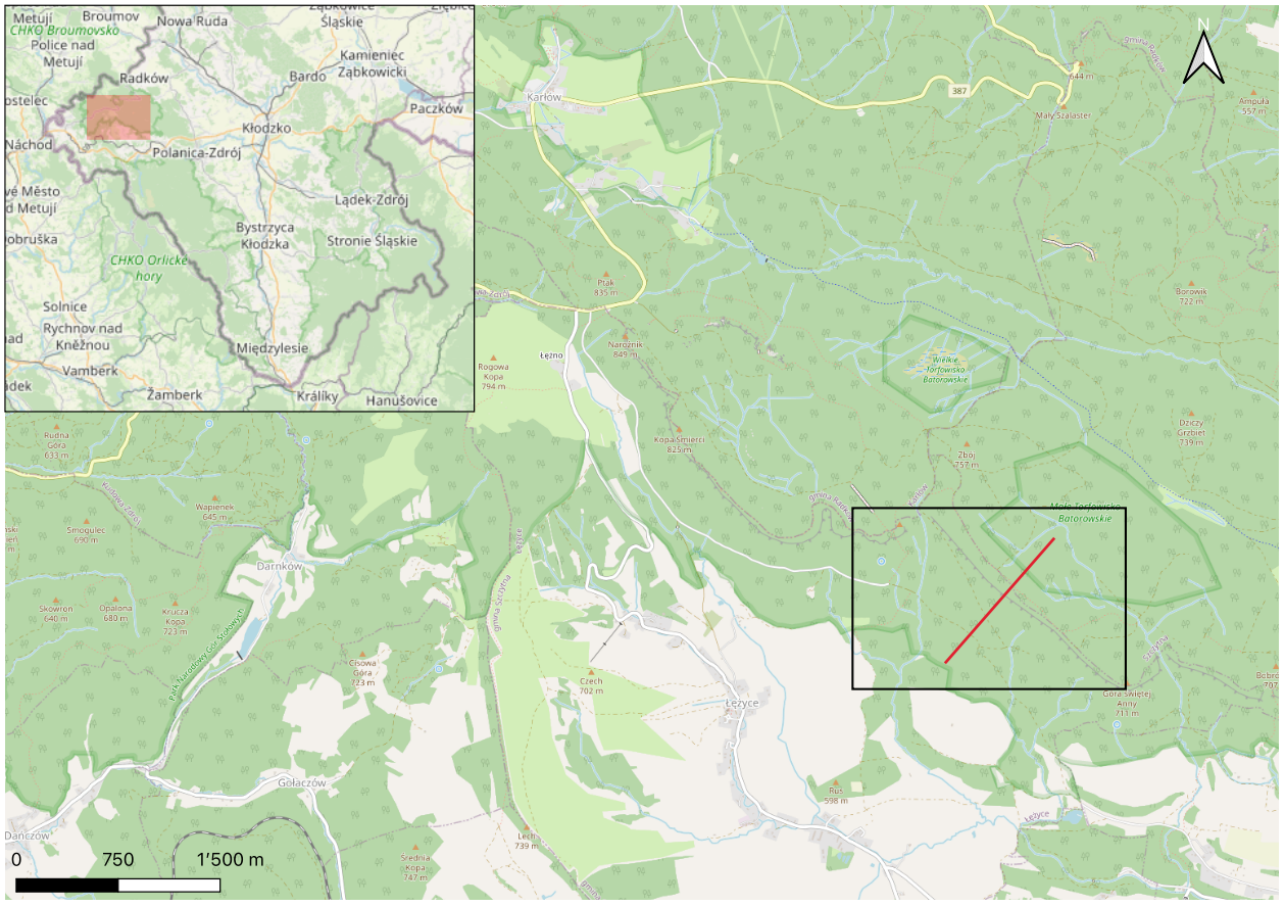

Figure 2: Location of the study area and the topographic cross-section (red line) in the Stołowe Góry National Park ("Topographic map" 2023).

2.1 TOPOGRAPHY AND RELIEF

The altitude varies between 391 reaches up to the summit of Szczeliniec Wielki at 922 m above sea level (see Photo 1), with an average altitude of 681 m a.s.l. (Waroszewski *et al.* 2015a; Wojewoda *et al.* 2011). More than 52 % of the area lies on flat or nearly flat highlands on mudstone and sandstone bedrock with a slope of no more than 10°, a further 26 % of the area has a slope of between 10°–20°, and only 22% of the total area is on steep slopes (Kasprzak & Migoń 2015a; Migoń *et al.* 2011).

Photo 1: The sandstone top of Szczeliniec Wielki in the Stołowe Mountains.

The altitude of the study site at Urwisko Batorowskie ranges from 601 m a.s.l. to 733 m a.s.l. and the coordinates of its center are 50°26'31.5"N 16°23'07.2"E (WGS84). The lowest point is on an even meadow from where the concave escarpment rises to the flat caprock. A forest road with a width of approximately 5 m crosses the study area twice, once at an altitude of 606 m a.s.l. and again at 634 m a.s.l. The slope inclination along the catena ranges from 2° to 78° (see Table 1).

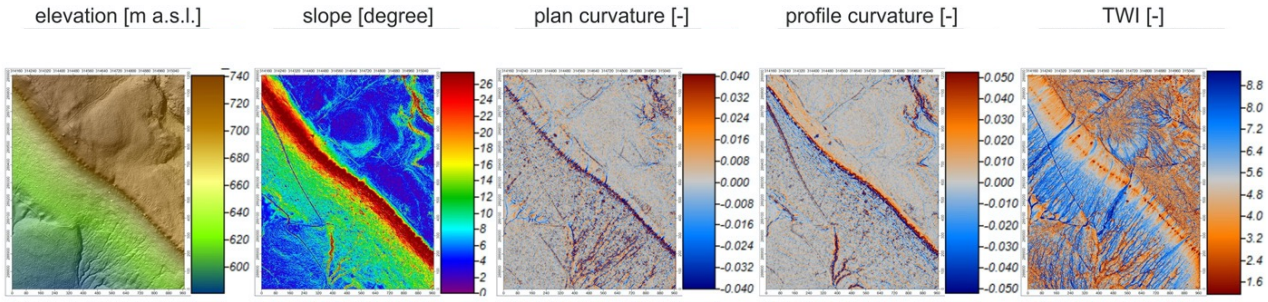

Figure 3: Relief models and geomorphometric parametrization of land surface of the study areas based on 1 × 1 m DEM built from LiDAR data (modified after Kasprzak & Migoń (2015a)).

2.2 GEOLOGY

The Sudetes belong to the north-eastern edge of the Bohemian Massif which was formed during the Variscan orogeny (Mazur 2024). The Stołowe Mountains are situated within the Sudetes in a large intramontane depression known as the Intra-Sudetic Synclinorium (Duszyński 2024). The mountain ranges basement is built of Proterozoic and early Paleozoic crystalline rocks overlain by younger Carboniferous to Cretaceous sedimentary rocks (Migoń & Kasprzak 2016). The plateau of the Stołowe Mountains consists of a more than 300 meters thick sequence of sandstones and fine-grained sediments from the Upper Cretaceous period (Wojewoda 1997; Wojewoda *et al.* 2011). The quartz and arkose sandstone form beds of several meters thickness. The fine-grained rocks are of shallow marine origin and include silicious marls, claystones, mudstones, siltstones, spongiolites, gaizes and calcareous sandstones (Rotnicka 2007; Wojewoda 1997).

The Stołowe Mountains are intersected by numerous faults, primarily extending from the northwest to the southeast (Čech & Gawlikowska 1999). The area has undergone significant post-Cretaceous tectonic changes, including inversion and uplift, leading to the formation and subsequent erosion of faulted escarpments (Migoń & Kasprzak 2016).

Topmost, the caprock consists of quartz sandstones from the Conacium age. Beneath lays the sequence from the Turonian age with an upper fine-grained heterolithic complex, followed by arkosic sandstone beds and a lower fine-grained heterolithic complex. This sequence is underlain by Cenomanian glauconitic sandstones and basal conglomerates. The bedrock of the Cretaceous sequence consists of Permian sedimentary rocks in the north and Carboniferous granites and older

metamorphic rocks in the south (Migoń & Kasprzak 2016). At Urwisko Batarowskie only the quartz sandstones and fine-grained heterolithic of the uppermost 140 m are present in the relief and partially outcropped on the surface (see Figure 7). The Cretaceous sandstones and finer-grained sediments are highly jointed in an orthogonal pattern and are spaced from less than 1 m to more than 10 m (Duszyński & Migoń 2015). The joints strike in 35° and 120–130° (Jerzykiewicz 1968b; Pulinowa 1989). The groundwater flows mainly towards the plateau rims, and it is assumed that this mainly occurs via the system of interconnected joints (Kowalski 1980).

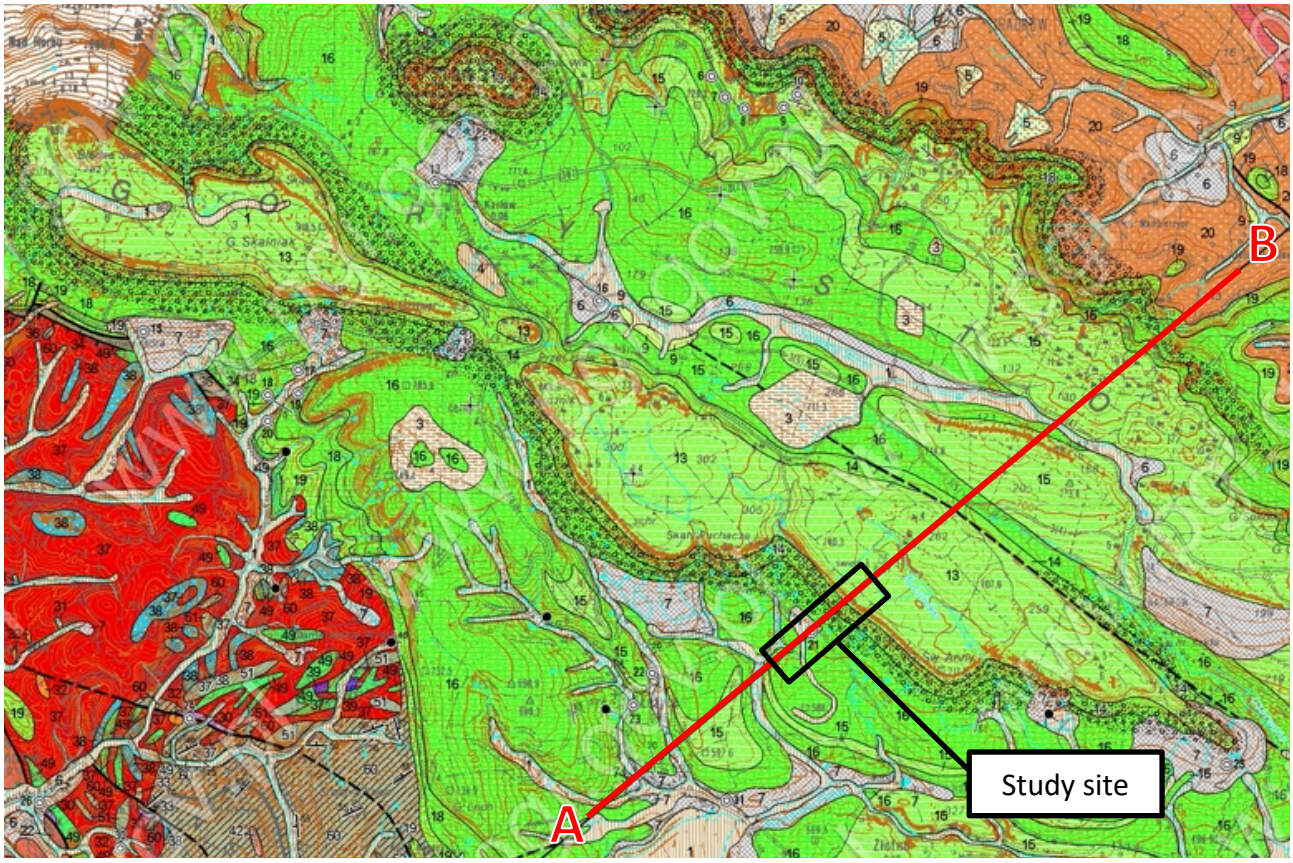

Figure 4: Extract of the detailed geological map of Poland 1:50'000 and cross-section line A–B (modified after (Cymerman 2019))

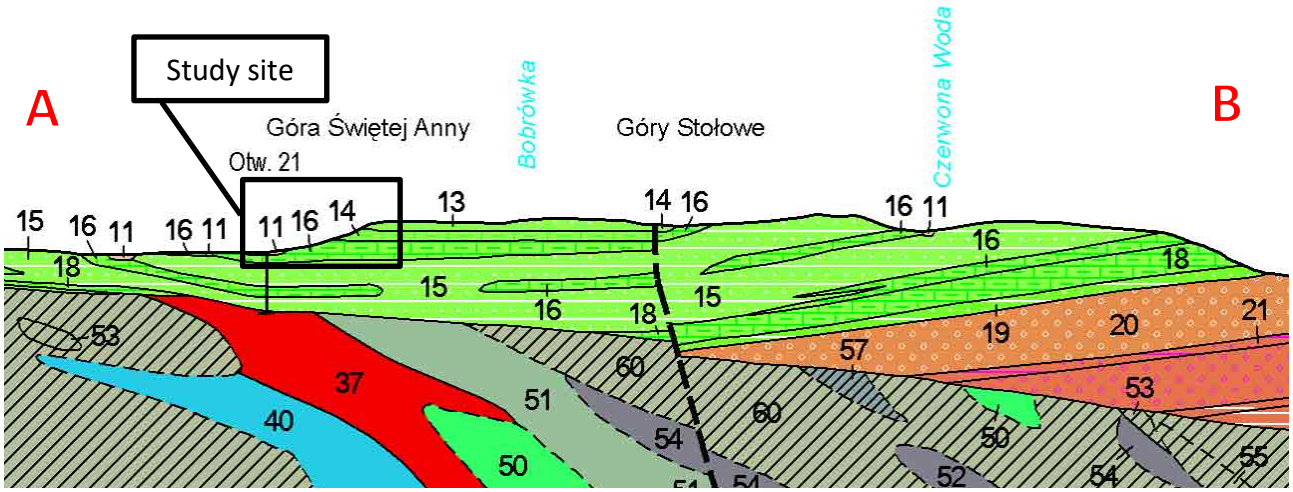

Figure 5: Geological cross-section A–B (modified after (Cymerman 2019))

11	Q	Quaternary formations not separated
12	$Pt_3–Cr_3$	Subquaternary basement formations not separated
13	$_{poQ}Cr_{t3}$	Quartz sandstone, ashlar
14	$_{ma}Cr_{t3}$	Clay marls and calcareous claystones of the *Inoceramus schloenbachii* level
15	$_{pc}Cr_{t1}$	Equal-grained, ashlar sandstones of the *Inoceramus Lamarcki* level
16	$_{ma}Cr_{t1}$	Sandy-silica marls of the *Inoceramus Lamarcki* level
17	$_{wp}Cr_{t1}$	Sandy limestones of the *Inoceramus Lamarcki* level
18	$_{mek}Cr_{t1}$	Silica marls and marly mudstones of the *Inoceramus labiatus* level
19	$_{pc}Cr_{c3}$	Quartz-feldspathic sandstones with glauconite, locally mudstones and conglomerates
20	$_{zc}PZ$	Conglomerates and conglomeratic sandstones
21	$_{pc}P_{cs3}$	Sandstones and sandy-calcareous shales - the Radków formation
37	$_{\gamma}C_1$	Granites and granodiorites
40	$_{\gamma\delta}C_1$	Granodiorites, granites and tonalites
50	$_{ak}Pt_3–Cm_3$	Amphibolites, amphibole schists and granitoids
51	$_{A}Pt_3–Cm_3$	Amphibole schists and mica schists with granitoid veins
52	$_{do}Pt_3–Cm_3$	Crystalline dolomites (dolomite marbles)
53	$_{\#}Pt_3–Cm_3$	Mica-carbonate shales
54	$_{dok}Pt_3–Cm_3$	Crystalline dolomites (dolomite marbles) and mica-carbonate schists
55	$_{\#my}Pt_3–Cm_3$	Mica-carbonate shales and mylonites
56	$_{\#gf}Pt_3–Cm_3$	Graft slates and mica slates
57	$_{kw}Pt_3–Cm_3$	Graphite quartzites and graphite schists
58	$_{\#Z}Pt_3–Cm_3$	Chlorite-zoisite schists
59	$_{\#G}Pt_3–Cm_3$	Mica schists with garnets
60	$_{\#}Pt_3–Cm_3$	Mica slates

Figure 6: Extract of the legend of the detailed geological map of Poland 1:50'000 (modified after (Cymerman 2019))

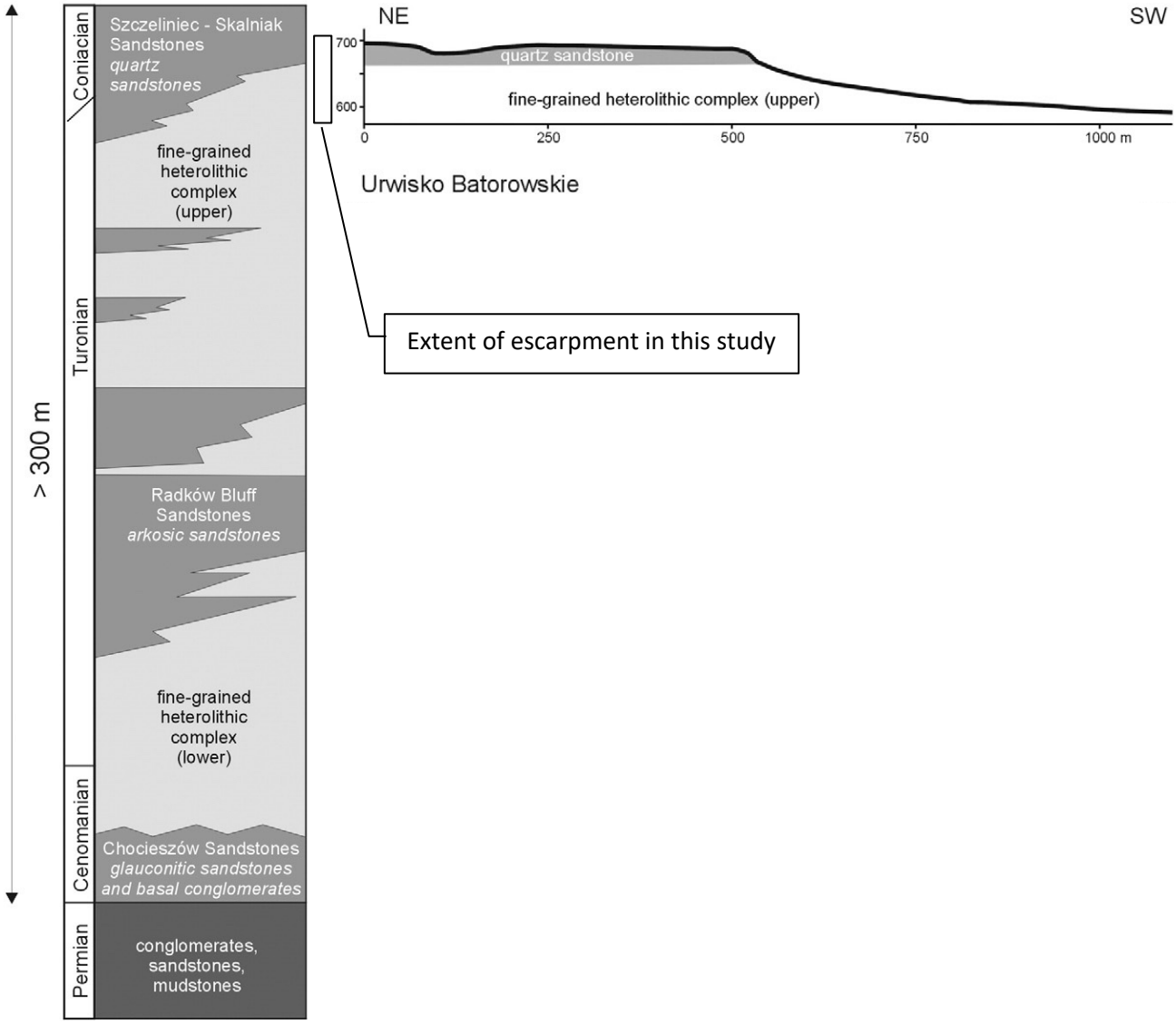

Figure 7: Stratigraphy of the Stołowe Mountains tableland (left) and geological boundaries on cross-sections of Urwisko Batorowskie (right) with its position in respect to the stratigraphic column (modified after Wojewoda et al. (2011) and Migoń & Kasprzak (2016)).

The sediment layers are almost horizontal, but locally can be inclined up to 6° (Migoń & Duszyński 2017). At Urwisko Batarowskie, the layers dip towards north-east. The cross-bedding within the layers dips south-west and exhibiting inclinations up to 30° (Jerzykiewicz 1968a). The probably sandstone-derived slope cover material reaches a thickness of 5 m in the upper slope, 2–3 m in the midslope and < 2 m in the lower slope (see Figure 8) (Duszyński *et al.* 2016).

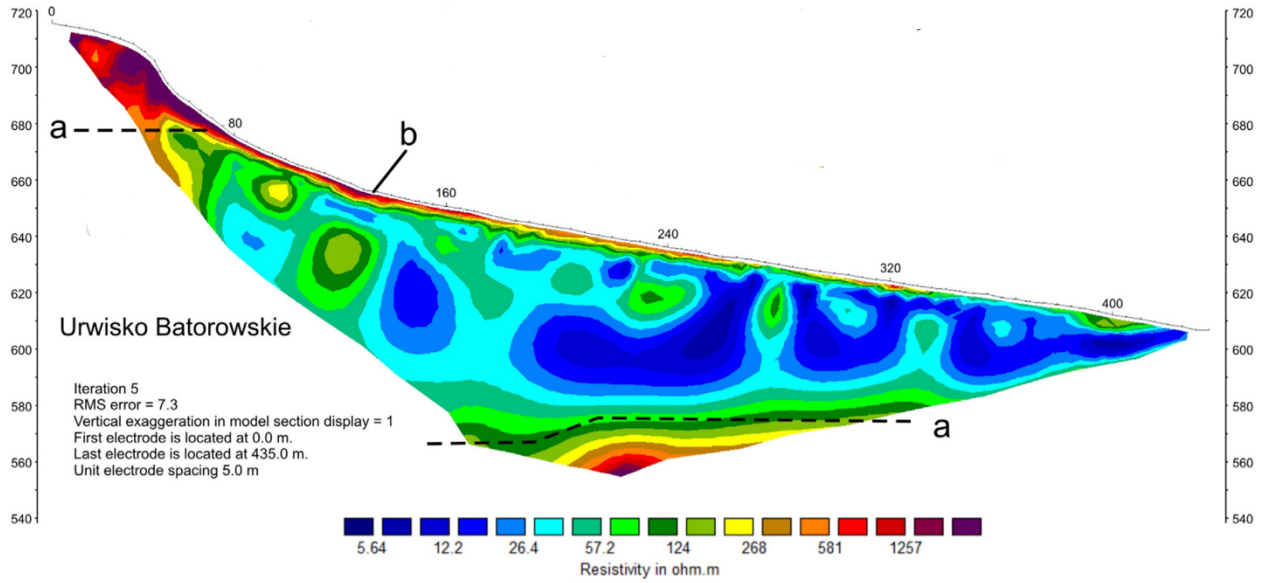

Fig. 7. Results of ERT surveys. A – Szczeliniec Wielki, B – Białe Ściany, C – Urwisko Batorowskie (for location see Fig. 1). a – clear lithological boundaries, b – high resistivity slope cover.

Figure 8: Electrical resistivity tomography (ERT) at Urwisko Batarowskie (modified after Duszyński et al. (2016))

2.3 GEOMORPHOLOGY AND LANDFORMS

The present-day extent of the tableland is considered as a remnant of a once much more extensive sedimentary terrain (Pulinowa, 1989; Wojewoda, 1997). Most of the summit areas are covered with regolith, with sandstone outcrops only occurring in some areas like Szczeliniec Wielki and Szczeliniec Mały (Duszyński 2024).

The joints of the sandstone and the finer-grained sediments have a considerable impact on the development and distribution of small-scale landforms. In particular, defining the extent and dimensions of sandstone tors and erosional incisions (Pulinowa 1989). The joint lines serve as preferential contact points for weathering forming clefts (Migoń *et al.* 2017a) and further promote the upward propagation of cavities, evacuation of sandy detritus, and collapsing of sandstone blocks and tors (Duszyński & Migoń 2017). In contrast to highly porous sandstones, the fine-grained rocks are characterized by low permeability (Duszyński 2024). The damp conditions on impermeable bedrock seemed to enhances the decay at the base of the rocks (Migoń *et al.* 2017a). Fault zones, on the other hand, appear to have only an indirect geomorphological effect by focusing drainage lines and preferential erosion upwards (Kasprzak & Migoń 2015a). Due to the lack of Pleistocene glaciation,

no features of the contemporary relief can be explained by glacial influence (Duszyński *et al.* 2016; Jahn 1977). Although there are morphological signatures that indicate periglacial processes, the morphology is essentially due to the lithological characteristics of the cap deposits (Duszyński *et al.* 2016; Pulinowa 1989; Traczyk & Migoń 2003).

The alternating resistant sandstones and weaker fine-grained rock complexes result in a terraced landscape featuring diverse landforms at various elevations (Duszyński 2024). This leads to the development of various landforms such as plateaus, mesas, escarpments, rock cities, ruiniform reliefs, tors, gorges, gates, pedestal rocks, canyons and solitary boulders (Duszyński & Migoń 2018; Migoń 2008; Migoń *et al.* 2017a; Pulinowa 1989; Walczak 1963).

The uppermost plateau encloses the flat-topped residual hills Szczeliniec Wielki and Szczeliniec Mały rising above the surrounding area. These elevated positions of Cretaceous rocks reaching up to 922 m a.s.l. with plateaus and mesas that are enclosed by the escarpments of the cliff-forming sandstones. The escarpment of the upper quartz sandstone forms cliffs with vertical rock walls of 10–40 m (Duszyński 2024), the lower sandstone forms the longest sections of steep slopes. The cliffs are intersected by ravines caused by fluvial incisions (Migoń & Kasprzak 2016). There are only few canyons in the Stołowe Mountains. These reach a depth of 30–40 m and a length of several 100 m (Duszyński 2024).

Due to the orthogonal connection of the rock layers, the formation of characteristic geomorphological features, including corridors and niches are favored, as can be seen in the rock labyrinth of Błędne Skały (Duszyński 2024). These formations are bordered by escarpments that reach inclinations of up to 50° (Pawlik *et al.* 2013). The escarpments form concave longitudinal slope profiles that merge into an extensive main plateau (see Figure 3), which consists mainly of fine-grained rock and gradually decreases in height from west to southeast (Duszyński *et al.* 2018). The gradual slopes are interrupted by longitudinal profile rises and terraces, possibly originating from landslides and form sinuous slope (Duszyński *et al.* 2017; Kasprzak & Migoń 2015a; Pawlik *et al.* 2013).

Other geomorphological formations such as tors, multi-story pedestal rocks, towers, pinnacles, sandstone walls are the most resistant remnants of the sandstone caprock (Duszyński & Migoń 2022a; Migoń *et al.* 2017a). Typical pedestal rocks with bipartite morphology, also called mushroom rocks due to wider cap compared to stem, occur farther away from the escarpment rim, where the degree of dissection is lower (Duszyński 2024). Some tors also show thinner caps on a wider stem

(Migoń 2021) due to the geological formation which e.g. comprises of conglomeratic sandstone (tempestite) (Duszyński 2024).

Solitary sandstone boulders of the upper Turonian quartz sandstone are scattered around the plateaus (Parzóch & Migoń 2015). Some boulders were also deposited in recesses, clefts and joints (Dumanowski, B. 1961; Duszyński *et al.* 2016). Boulders with sizes of 15–20 m can be encountered up to 400 m away from the present cliff line at Szczeliniec Wielki and up to 1 km at Biała Skała (Duszyński & Migoń 2015). These boulders are remnants of the former sandstone caprock outliers that are no longer existant (Migoń & Parzóch 2021). Their tabular shape is originating from the sandstone layering.

Photo 2: Escarpment of Urwisko Batorowskie at the study site with sandstone boulders and single-aged planted stands of Norway spruce.

2.4 CLIMATE

The Stołowe Mountains, situated in a humid temperate climate region, display a localized climate pattern with both temperature and precipitation depending heavily on altitude gradient (Migoń & Kasprzak 2016; Waroszewski *et al.* 2015b).

At the eastern border of the area, at an altitude of 500 m a.s.l., the mean annual air temperature is 6.5 °C (Waroszewski *et al.* 2015b, a). Whereas in the central and western parts, at an altitude of 750 to 919 m a.s.l., the mean annual air temperature is 4 °C (Waroszewski *et al.* 2015b, a). The warmest month is July with temperatures of 13.5 to 15 °C and the coldest months are January and February with temperatures of 3 to 4.5 ° (Błaś & Ojrzyńska 2024; Waroszewski *et al.* 2015b, a).

The mean annual precipitation increases with altitude from 750 to 920 mm, approximately evenly distributed throughout the year (Dubicki & Głowicki 2008) with the maximum in July. Depending on the altitude, between mid-November and the end of April the number of days with snowfall is 54–161 days and a snow cover may be present for an average of 70–95 days, also (Pawlak *et al.* 2008). The longest duration of snow cover is typical for open fissures in sandstone plateaus and for the north-facing foot slopes of sandstone cliffs. Before the beginning of the Holocene, the region had a cold climate with permafrost (Jahn 1977), but the altitude of the Stołowe Mountains was too low to create the conditions for the development of local glaciation (Kasprzak & Migoń 2015a).

The prevailing wind direction is SW and W which accounts for 50 % of total (Dubicki & Głowicki 2008). The wind velocity generally does not exceed 4–5 m s^{-1} (Waroszewski *et al.* 2015b). However, the velocity of westward winds can be influenced by nearby mountain ranges and lead to rare events of more than 20 m s^{-1} (Dubicki & Głowicki 2008). On the plateau, fen winds occur more regularly and are responsible for extensive windthrow (Brázdil 1998; Jewula 1974; Sobik & Błaś 2010; Waroszewski *et al.* 2015b), which is the process of trees or large vegetation being damaged or up-rooted by the force of the wind (Armson & Fessenden 1973; Norton 1989).

2.5 SOILS

Soil formation is among other factors (Jenny 1941) strongly characterized by parent material and topography. Locally the parent material is either bedrock or allochthonous cover deposits (Kabala *et al.* 2011).

The most widespread soil types are Folic, Albic and Histic podzols, which dominate on sandstones (Duszyński *et al.* 2016; Waroszewski *et al.* 2015b, a). Depending on slope morphology, regolith texture and drainage conditions, podzols come in several varieties. However, all have a texture of sand and sandy loam, low pH of 3.3–4.0 and low base saturation of generally < 20 % throughout the entire profile (Waroszewski *et al.* 2015b, a).

On slopes on Cretaceous mudstones Dystric (Kabała & Szerszeń 2002; Pawlik *et al.* 2017), Endoleptic or Haplic Cambisols (Pawlik *et al.* 2013; Waroszewski *et al.* 2015a) are found. They have a texture of silt loam, which changes to loam with increasing depth. They also have a low pH of 3.5–4.2 and a low base saturation of 20–50 % throughout the soil profile (Waroszewski *et al.* 2015b, a).

On mudstones in the central part of the plateau, Eutric Cambisols are common on steep slopes (Waroszewski *et al.* 2015b). In contrast, on flat and less well drained terrain Stagnic Luvisols, Luvic and Histic Stagnosols, Histic Planosols, Albeluvisols and Alisols are encountered (Duszyński *et al.* 2016; Waroszewski *et al.* 2015b). These soils generally have the texture of loam and silt loam, a low pH at the surface, which rises to 6.4-7 at a depth of 50 cm, and a base saturation between 40 and 90 % (Waroszewski *et al.* 2015b, a).

On steep slopes in shallow sites, Haplic Arenosols and Folic Regosols can be found (Waroszewski *et al.* 2015a). On sandstone outcrops, shallow and extremely stony soils like Leptosols cover less than 5% of the area. (Waroszewski *et al.* 2015b). In 1–3 % of the area Gleysols, Histosols and Fluvisols are encountered in wet areas and surrounding springs and streams (Waroszewski *et al.* 2015b).

2.6 VEGETATION

Within these ecological conditions montane forests would be expected with a natural forest composition dominated by *Fagus sylvatica* (European beech) and *Abies alba* (European silver fir) (Jędryszczak & Miscicki 2001) accompanied by *Pinus mugo Turra* (Mountain dwarf pine) at higher elevation (Jahn 1989). These tree species occur with the plant association *Calamagrostio villosae–Piceetum* and *Pinetum mughi sudeticum* respectively. Sometimes *Fagus sylvatica* is also accompanied by *Acer pseudoplatanus* (sycamore) forming the plant association *Dentario enneaphylli-Fagetum* (Pawlik *et al.* 2013). But with the current use in forestry a mono-species coniferous forest is found at the slopes where most of the tree layer (more than 70 % of the area) is formed by single-aged planted stands of *Picea abies* (Norway spruce) (Migoń & Kasprzak 2016) which was introduced

in 18th and 19th century. The tree line is at 1'200–1'250 m a.s.l. (Treml *et al.* 2006) and is therefore not reached in the Stołowe Mountains.

In wet habitats on the plateau in the peatland of Wielkie Torfowisko Batorowskie (pl. great peat bog) (Marek 1998), the vegetation forms a rooted turf cover, that includes ferns like *Athyrium alpestris* (Jahn 1989), shrubs such as *Vaccinium myrtillus* and grass species like *Brachypodium sylvaticum* and *Hierochloë australis* (Waroszewski *et al.* 2015a). On the escarpment very little undergrowth is present but the surface is covered by litter of tree leaves. In shaded spots at the foot slope the undergrowth can there be very compact and thick (Migoń & Kasprzak 2016) with mosses like *Hylocomium splendens*, *Leucobryum glaucum*, *Pleurozium schreberi* and *Polytrichum commune* dominating the forest floor (Waroszewski *et al.* 2015a).

Photo 3: Plateau of Urwisko Batorowskie at the study site with peatland vegetation of Wielkie Torfowisko Batorowskie.

3 MATERIAL AND METHODS

3.1 SAMPLING SITES

Ten sampling sites were selected along the southern slope of Urwisko Batorowskie (see Figure 9, Figure 10 and Figure 11). The sites were chosen as a toposequence aligned along the fall line with the topmost site on the sandstone plateau at 733 m a.s.l. and the lowermost site at the toe slope at 601 m a.s.l. Accordingly the sampling sites are spread over a vertical distance of 132 m and a horizontal distance of 584 m. At each site four soil pits were dug and sampled in 2022. Eight sites were used for main analysis (P1–P8) and two assumably undisturbed sites serve as reference (R1 and R2). For each sampling site coordinates, altitude, slope aspect, slope inclination, position along the relief and general vegetation were collected (see Table 1).

3.2 SOIL PROFILES

One soil profile at each sampling site (P1–P8) was described according to the Food and Agriculture Organization of the United Nations (FAO 2006) and classified using the World Reference Base for soil resources (IUSS Working Group WRB 2022).

3.3 SAMPLING

At each sampling site (P1–P8) four soil pits were excavated. While the main soil profile pit served for collecting the disturbed and deeper samples (deeper than 20 cm below the surface) the other three soil pits served for additional soil sample collection.

From each soil profile a disturbed sample of 200 g was taken of each soil horizon. This led to a total of 41 disturbed soil samples. Additionally, two undisturbed volumetric samples were taken per horizon with a 100 ml steel cylinder. So, a total of 80 undisturbed soil samples were collected.

For Pu-Isotope analysis, each of the soil pits was sampled in four depth intervals: 0–5 cm, 5–10 cm, 10–15 cm and 15–20 cm, so four replicates per plot and depth were taken. At the reference sites R1 four soil pits and at the refence site R2 two soil pits were sampled accordingly. A total of 160 samples for Pu-Isotope analysis were collected.

Table 1: Coordinates of the sites soil profile (P1–P8) and the reference sampling sites (R1 and R2).

Site	Coordinates		Altitude	Slope aspect	Slope exposition	Slope inclination
	Latitude	Longitude	(m a.s.l.)	(°)		(°)
P1	50° 26' 38.290" N	16° 23' 15.300" E	733	160	SSO	2
P2	50° 26' 34.806" N	16° 23' 13.396" E	723	210	SSW	9
P3	50° 26' 33.752" N	16° 23' 10.968" E	697	225	SW	78
P4	50° 26' 32.856" N	16° 23' 10.320" E	691	215	SW	26
P5	50° 26' 32.388" N	16° 23' 09.096" E	680	205	SSW	19
P6	50° 26' 29.954" N	16° 23' 07.184" E	660	215	SW	10
P7	50° 26' 27.665" N	16° 23' 02.821" E	633	210	SSW	4
P8	50° 26' 24.472" N	16° 22' 58.742" E	610	185	S	14
R1	50° 26' 23.341" N	16° 22' 57.097" E	601	220	SW	3
R2	50° 26' 25.325" N	16° 22' 52.554" E	602	195	SSW	2

Figure 9: Orthophoto ("Ortofotomapa" 2023) with sampling sites P1–P8 (red points) and cross-section (red line) at the southwestern slope of Urwisko Batarowskie.

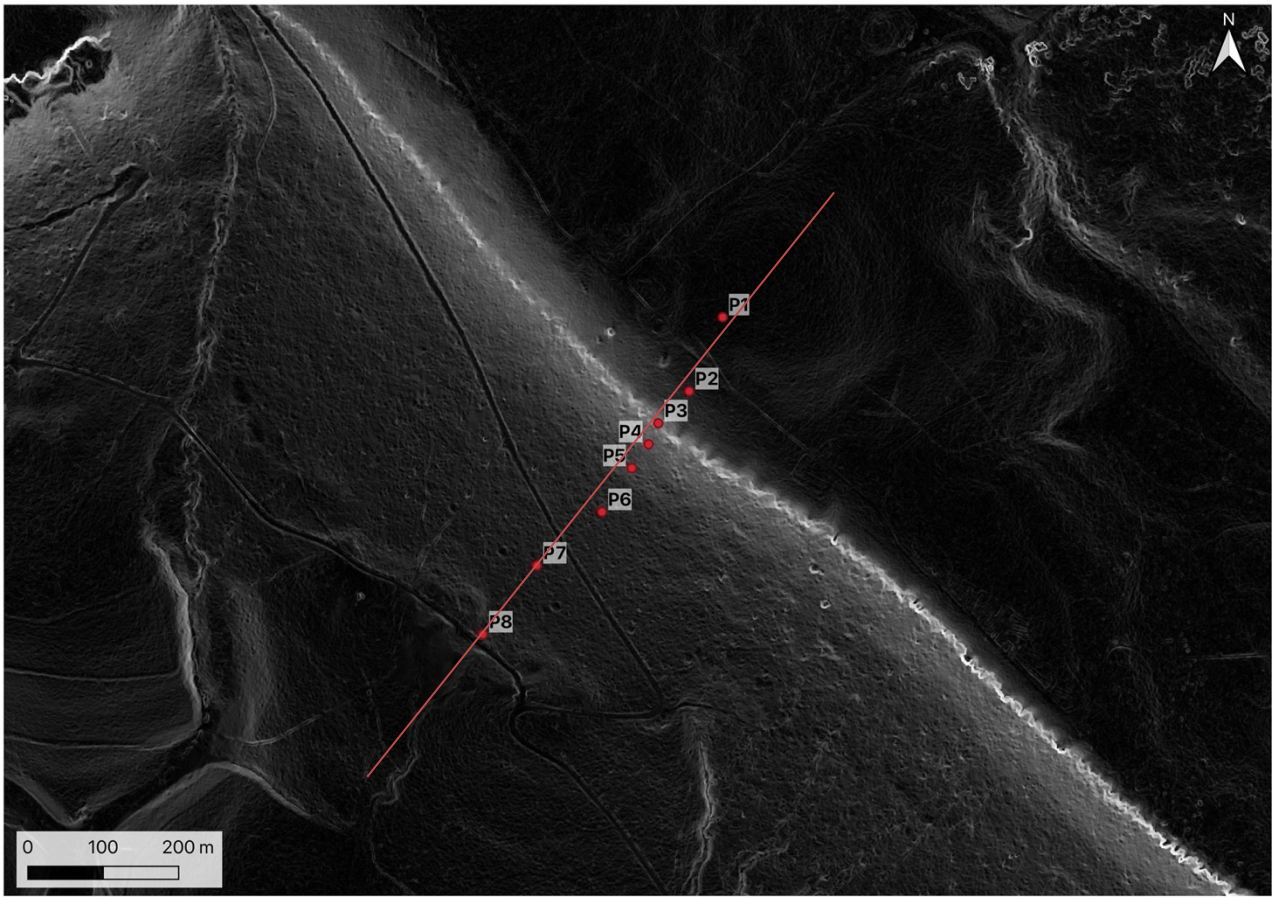

Figure 10: Relief from Digital elevation model (DEM) ("Digital Terrain Model" 2023) with sampling sites P1–P8 (red points) and cross-section (red line) at the southwestern slope of Urwisko Batarowskie.

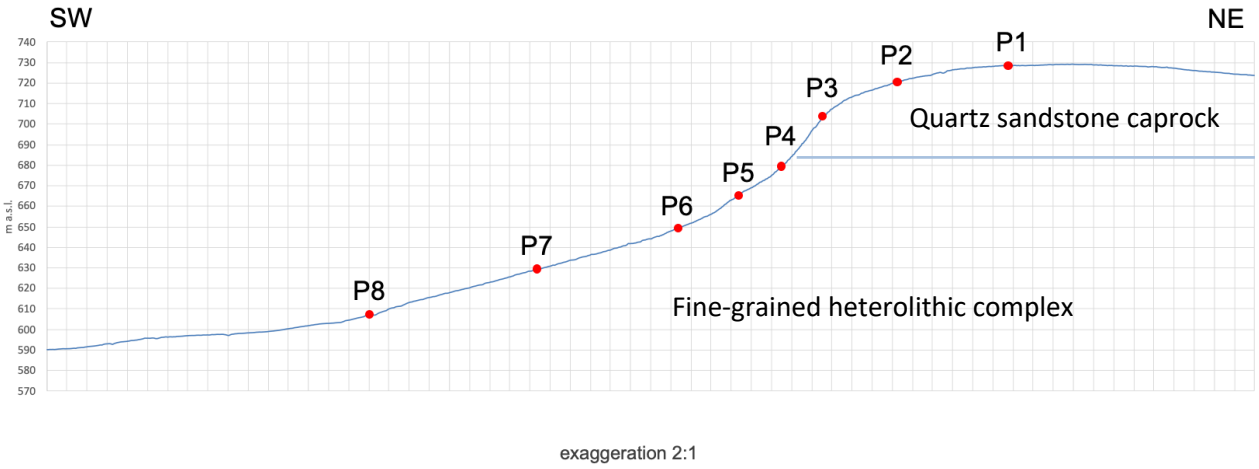

Figure 11: Longitudinal slope profile of the topography and relative position of the sampling sites P1–P8 at the south-western slope of Urwisko Batarowskie (height exaggeration 2:1).

Covering from direct and indirect sunlight immission with a tarpaulin, undisturbed samples were collected with 100 ml steel cylinders in 3–4 different depths at each soil profile to measure their luminescence (using a portable OSL-reader). This led to 31 samples which were stored fresh in the fridge. All other samples (281 samples) were dried for a minimum of 48 hours at 70 °C.

3.4 PHYSICAL SOIL PROPERTIES

3.4.1 BULK DENSITY

The dried volumetric samples were weighed. The bulk density was calculated by dividing the mass of each sample through the volume of 100 cm^3 (see Equation 1).

Equation 1: Bulk density

$$\rho_a = \frac{M}{V}$$

ρ_a = *bulk density (g cm^{-3})*

M = *sample mass (g)*

V = *sample volume (cm^3)*

3.4.2 FRACTION OF ROCK FRAGMENTS (SOIL SKELETON)

The fine earth (≤ 2 mm) and rock fragment fraction (> 2 mm) of the dried volumetric samples were separated with a 2 mm sieve and each fraction weighed. The soil skeleton fraction (C_{skel}) in given as mass-% (see Equation 2).

Equation 2: Skeletal fraction

$$C_{skel} = \frac{M_{skel}}{M_{tot}}$$

C_{skel} = *skeletal fraction (mass-%)*

M_{skel} = *mass of the fraction > 2 mm (g)*

M_{tot} = *total sample mass (g)*

3.4.3 GRAIN SIZE DISTRIBUTION

The grain size distribution relates to the fraction ≤ 2 mm of the disturbed samples. First grain sizes were separated with sieves of the mesh sizes 2000 µm, 1000 µm, 500 µm, 250 µm, 125 µm, 63 µm,

45 µm and 32 µm. The fraction ≤ 32 µm is mixed with up to 300 ml of a 3 % solution of hydrogen peroxide (H_2O_2) and heated at 90 °C to disperse the aggregate and destroy organic substance.

From the < 32 µm soil sample fraction, an aliquot 20 or 40 ml with a corresponding amount of 3–5 g of soil was transferred into a beaker. A 1 % solution of sodium hexametaphosphate $(NaPO_3)_6$ was added in a ratio of 1:1 to the aliquot as dispersing agent. The sample was homogenized with the ultrasonic Bandelin Sonoplus HD 2070 for 5 minutes at 70 % and 5 cycles. The homogenized sample was measured by X-ray sedimentation with the Micrometrics SediGraph 5100 and analyzed with the software SediGraph III Plus V1.02. This method is based on Stokes Law by calculating the equivalent grain size diameter with the settling velocity in the surrounding medium (see Equation 3).

Equation 3: Settling velocity

$$v = \frac{2}{9} * (\rho_k - \rho_m)\, r^2 \frac{g}{\eta}$$

ρ_k = *density of the grains (g cm^{-3})*

ρ_m = *density of the surrounding medium (g cm^{-3})*

r = *radius of the grains (cm)*

g = *gravity acceleration (cm s^{-2})*

η = *viscosity (g cm^{-1} s^{-1})*

3.4.4 SOIL TEXTURE CLASS

The particle-size classes and textural classes were determined according to Jahn et al. (2006). The fine earth fraction was divided into fine clay (< 1 µm), coarse clay (1–2 µm), fine silt (2–6 µm), medium silt (6–20 µm), coarse silt (20–63 µm), very fine sand (63–125 µm), fine sand (125–250 µm), medium sand (250–500 µm), coarse sand (500–1000 µm) and very coarse sand (1000–2000 µm).

3.4.5 MUNSELL SOIL COLOR

The color of the soil matrix of each horizon was determined in moist and dry conditions using the notations for hue, value and chroma as given in the Munsell Soil Color Charts (Munsell Color Company 1975).

3.5 CHEMICAL SOIL PROPERTIES

3.5.1 pH

5 g of dried and sieved soil (≤ 2 mm) and 12.5 ml of a 0.01 mol/l $CaCl_2$ solution were put in a beaker, stirred for 30 minutes, and then let it rest for 30 minutes. The pH was measured in the supernatant with a Metrohm 692 pH/Ion Meter electrode.

3.5.2 ORGANIC MATTER CONTENT

The organic matter content was determined by loss on ignition (LOI) according to Pansu & Gautheyrou (2006). 2 g of dried soil in a crucible was heated at 550 °C in a muffle oven for 6 hours. The crucible was cooled down in a desiccator and weighed again. The loss of weight represents the organic, and the residue on ignition the inorganic material.

3.5.3 TOTAL ELEMENT COMPOSITION WITH X-RAY FLUORESCENCE

The total elemental content was measured using X-ray fluorescence (XRF) (Brouwer 2006). The dried and sieved (≤ 2 mm) soil sample was fine milled for 30 minutes at 30 rps in a Retsch Mixer Mill MM200 with tungsten carbide jars and balls. The fine milled sample was measured in a SPECTRO XEPOS and evaluated with the Software X-LabPro by Spectro Analytical Instruments GmbH.

3.5.4 OXIDE CALCULATION

The concentration of elements is multiplied with the molecular weight of their respective oxide (see Table 2). The sum of oxides and organic matter was then normalized to 100 %.

3.5.5 ELEMENT FRACTION WITH OXALATE EXTRACTION

The amorphous forms of iron (Fe_o) and aluminium (Al_o) are extracted with an oxalate solution (Borggaard 1988; Dahlgren & Ugolini 1991; Parfitt & Henmi 1982; Tamm 1922; Wada 1977). 2 g of dried and sieved soil (≤ 2 mm) and 100 ml oxalate solution at pH 3 are mixed in a flask and shaken in the dark at 150 rpm for 2 hours. After shaking, the suspension is filtered and 50 ml of the filtered solution are analyzed for iron and aluminium using atomic absorption spectrometry (AAS) (Bashour & Sayegh 2007) with a Analytik Jena ContrAA 700 and evaluated with the Software Aspect CS also by Analytik Jena.

Table 2: Mass of molecules

Atom	Molar mass g/mol	Molecule	Molar mass g/mol
Na	22.99	Na_2O	61.98
Mg	24.305	MgO	40.305
Al	26.982	Al_2O_3	101.964
Si	28.086	SiO_2	60.086
P	30.97	P_2O_5	141.94
S	32.06	SO_3	80.06
K	39.098	K_2O	94.196
Ca	40.08	CaO	56.08
Ti	47.88	TiO_2	79.88
Mn	54.938	MnO	70.938
Fe	55.847	Fe_2O_3	159.694

3.6 WEATHERING INDICES

Weathering indices were used to assess the degree of weathering of soils and sediments or to assess soil development (Delvaux *et al.* 1989). To calculate weathering indices, the oxides of the elemental composition are used.

3.6.1 CHEMICAL INDEX OF ALTERATION (CIA)

The Chemical Index of Alteration (CIA) is based on the relative abundance of alumina to other major cations like calcium, sodium and potassium (Nesbitt & Young 1982). It assumes that Na, Ca, and K are lost during weathering and Al is immobile. Since the CIA values increase with the removal of more mobile cations (such as Na and Ca) and the relative enrichment of Al due to the formation of clay minerals, it can effectively indicate the extent of weathering and clay mineral formation in a soil profile developed from sandstone. It can be used as a measure of the extent of conversion of feldspar minerals to clay minerals (Nesbitt & Young 1984, 1989). This index is advantageous for assessing the chemical weathering degree of silicate rocks, including sandstones (Price & Velbel 2003).

Equation 4: Chemical Index of Alteration (CIA)

$$CIA = 100 \left[\frac{Al_2O_3}{Al_2O_3 + CaO + Na_2O + K_2O} \right]$$

CIA = Chemical Index of Alteration

3.6.2 Chemical Index of Weathering (CIW)

The Chemical Index of Weathering (CIW) is similar to the CIA but excludes K_2O (Harnois 1988). It assumes that Al remains and accumulates in residual products, while Ca and Na are dissolved or consumed. Like the CIA, the CIW is also essentially a measure of the extent of conversion of feldspar minerals to clay minerals (Price & Velbel 2003). Its value increases with the increase of weathering degree. The value of fresh material is <50, while the maximum CIW of weathered material is 100 (Duzgoren-Aydin *et al.* 2002; Price & Velbel 2003).

Equation 5: Chemical Index of Weathering (CIW)

$$CIW = 100\left[\frac{Al_2O_3}{Al_2O_3 + CaO + Na_2O}\right]$$

CIW = Chemical Index of Weathering

3.6.3 Weathering Index of Parker (WIP)

The Weathering Index of Parker (WIP) is used for silicate rocks (Parker 1970). It is determined by the ratio of alkali and alkaline earth metals Na, K, Ca, and Mg (see Equation 6). The individual mobility is considered based on the bond strengths with oxygen. With increasing weathering, the WIP value decreases to a minimum of zero (Parker 1970; Price & Velbel 2003).

Equation 6: Weathering Index of Parker (WIP)

$$WIP = 100\left[\frac{2Na_2O}{0.35} + \frac{MgO}{0.9} + \frac{2K_2O}{0.25} + \frac{CaO}{0.7}\right]$$

WIP = Weathering Index of Parker

3.6.4 [(Ca+K)/Ti]

The ratio of the mobile cations calcium and potassium to the immobile cation titanium is used to establish their leaching rates (Dorn 1983). It provides a relative age indicator which decreases with weathering time (Harrington & Whitney 1987).

Equation 7: Ratio of calcium and potassium to titanium

$$I = \frac{CaO + K_2O}{TiO_2}$$

3.6.5 [(Na+K)/Ti]

The molar ratio of sodium and potassium to titanium is used to better characterize silicate weathering (Egli *et al.* 2020; Egli & Fitze 2000; Stiles *et al.* 2003). It can also be used to exclude calcium in carbonate-rich material to prevent bias from carbonate leaching, which is however not an issue at this study sites. The index decreases with weathering time.

Equation 8: Ratio of sodium and potassium to titanium

$$I = \frac{Na_2O + K_2O}{TiO_2}$$

3.7 Infrared and Optical Stimulated Luminescence

The samples shielded from light were measured with infrared and optical stimulated luminescence (IR/OSL). In this study the Scottish Universities Environmental Research Centre (SUERC) portable IR/OSL-Reader was used (Sanderson & Murphy 2010). From each of the 31 samples, which were kept in steel cylinders in the fridge, the outermost parts were discarded. Several grams of the inner sample material were placed in disposable 5 cm diameter plastic petri dishes, which were then introduced in the light-tight sample chamber drawer of the IR/OSL-Reader. The sample preparation, input and measuring were undertaken under subdued redlight.

The samples were stimulated with photons from light-emitting diodes in the blue (470 nm) and infrared (880 nm) electromagnetic spectrum with 60 seconds of stimulation in the infrared band (IRSL) followed by 60 seconds in the blue stimulation band (BLSL).

3.8 Pu-Activity

3.8.1 Sample preparation

The samples were prepared at the Physical Geography Laboratories of the University of Zurich using the method modified after Ketterer et al. (2004, 2002) and Ketterer (2015).

Each soil sample was sieved to a fraction less than 1 mm and milled to fine powder. Around 5.0 g of the sample powder was precisely weighed into a 40 ml glass vial and ashed for at least 16 hours at 550 °C to ignite the organic matter. Afterwards, 10 ml of 65 % HNO_3 was added to the sample and the sample vial cooled down for 0.5–2 hours while regularly swirling. Then a ^{242}Pu spike solution

(0.0042–0.0044 Bq) of 1.0 ml 2 M HNO_3 was added to the sample. The optimal amount of ^{242}Pu to add is about 30 picograms (0.0044 Bq). The sample was agitated at 150 rpm for 30 minutes, heated at 80°C for 16 hours and agitated again to extract plutonium isotopes into a leachate solution. Finally, 10 ml H_2O was added and the sample mixed.

After the extraction, the plutonium containing leachate was separated from the solid sample by centrifugation at 2'000 rpm for 2–3 minutes. The leachate was filtered through a filtration column stuffed with cotton wool into a 50 ml centrifuge tube (CT). The solid sample was washed with 4 ml of H_2O while shaking at 100 rpm for about 5 minutes. This solution was centrifuged at 2000 rpm and filtered into the same 50 ml CT to combine it with the leachate. The filtration column was washed with 2 ml of 2 M HNO_3 also into the same CT.

To change the plutonium valence to +IV, 1 ml of a 50 mg ml^{-1} $FeSO_4 * 7\ H_2O$ solution and 1 ml of a 500 mg ml^{-1} $NaNO_2$ solution were added to the sample. After the initial NO_2 fume had been evacuated, the sample was mixed with a vortex shaker and heated at 75 °C for 2 hours. After cooling and mixing again, 1 ml of a 50 mg ml^{-1} TEVA suspension was added to the sample. To ensure that the plutonium is retained on the TEVA resin, the sample was shaken at 100 rpm for 30 minutes.

Afterwards the resin was collected on a glass wool filtration column and rinsed with 8 ml of 2 M HNO_3, 5 ml of 8 M HCl, and 3 ml of 2 M HNO_3 to remove U and Th. Finally, Pu was eluted from the resin by adding 0.4 ml H_2O, 0.4 ml of 0.05 M ammonium oxalate and 0.5 ml H_2O.

The sample preparation was done in four batches of 48 samples and one batch of 18 samples. Seven samples were repeated due to high organic matter content. A batch of 48 samples contained two preparation blanks, two soil standards IAEA-447 (International Atomic Energy Agency 2021), one negative control standard (rock powder) and three duplicates.

3.8.2 $^{239+240}Pu$ Isotope activity analysis

The measurement of the ^{239}Pu and ^{240}Pu concentration was done relative to the ^{242}Pu spike using an Agilent 8800 Triple Quadrupole ICP-MS equipped with an ESI Scientific Apex IR nebulizer at the Department of Chemistry of the University of Zurich. The instrument stability was checked with a solution of 250 ppt depleted Uranium and 25 ppt plutonium-242 in 2 % HNO_3 and 0.01 M oxalic acid, while the background was controlled with a solution of 2 % HNO_3.

The results were corrected to the $^{238}UH^{+}$ isobar and the background of the preparation blanks. The concentration of ^{239}Pu and ^{240}Pu in the samples were converted into the summed activity $^{239+240}Pu$. The extraction yield of the plutonium isotopes from the standard IAEA-447 gave an average of 86.45 %. The final sample activity was multiplied on a factor of 1.1567 to normalize the activity to the real value of the standard IAEA-447.

All processed duplicates did not show a statistically significant difference. The detection limit of the method derived from the preparation blanks is 0.001 Bq kg^{-1} $^{239+240}Pu$.

3.8.3 CALCULATION OF $^{239+240}PU$ INVENTORIES AND SOIL REDISTRIBUTION RATES

To quantify soil redistribution, the inventories of FRN of each sampling point was compared with the reference inventory. Thus, activities of $^{239+240}Pu$ (Bq kg^{-1}) were converted into inventories (Bq m^{-2}) with the sampled depth and the bulk density of the fine soil fraction. For each plot the cumulative inventory was calculated.

For further calculations the average Pu inventory per depth increment was used. Positive values in inventory change indicate deposition and negative values indicate erosion. The inventory change was calculated according to Meusburger et al. (2016) (see Equation 9).

Equation 9: Inventory change

$$\Delta I = \frac{I - I_{ref}}{I_{ref}} \times 100$$

ΔI = change in inventory (%)

I_{ref} = average reference total inventory (Bq m^{-2})

I = average total inventory at one sampling point (Bq m^{-2})

To calculate soil redistribution (erosion and accumulation) rates, isotope inventories from a site, that was influenced by erosion or accumulation, were compared with the inventory of a local reference site, where no redistribution is expected. Here the profile distribution model (PDM) by Walling and He (1999) and the inventory method (IM) by Lal et al. (2013) models were used. They are suitable for uncultivated sites and use a distinct function to describe the depth distribution of FRN in the soil.

The inventory of the $^{239+240}$Pu activities (Bq m^{-2}) was calculated using Equation 10 (Portes *et al.* 2018; Raab *et al.* 2018). The area *S* of the sampling core was 1.96325∗10^{-3} m^2.

Equation 10: Inventory of $^{239+240}$Pu activities

$$A(s) = \frac{1}{S}\sum_{i} M_{Ti}C_i$$

A(s) = *area of the horizontal cross-section (m^2)*

S = *area of the core (m^2)*

M_{Ti} = *total mass of the sample (kg)*

C_i = *activity of the subsample depth increment (Bq kg^{-1})*

To convert Pu into soil erosion rates, the profile distribution model (PDM) was used (Walling & He 1999; Walling & Quine 1990; Zhang *et al.* 1990). First the isotope inventory is calculated with Equation 11. As coefficient h_0 for uncultivated sites a factor of 55.59 was determined. The erosion rate was calculated with the Equation 12 (Walling & He 1999; Zhang *et al.* 1990). The sampling year *t* was 2022 and the reference year t_0 is 1963 estimated by Zhang et al. (1999).

Equation 11: Isotope inventory according to the profile distribution model (PDM) (Walling & He 1999)

$$A'(x) = A_{ref}\left(1 - e^{x/h_0}\right)$$

x = *soil mass between surface and sample depth*

A'(x) = *cumulative isotope inventory between surface and sample depth in Bq m^{-2}*

A_{ref} = *mean Pu inventory of all reference sites in Bq m^{-2}*

h_0 = *coefficient for describing the rate of exponential decrease of Pu with depth in kg m^{-2}*

Equation 12: Erosion rate according to the profile distribution model (PDM) (Walling & He 1999)

$$Y = \frac{10}{t - t_0} \times ln\left(1 - \frac{X}{100}\right) \times h_0$$

Y = *erosion rate in t ha^{-1} yr^{-1}*

t = *year the sampling took place*

t_0 = *reference year*

x = *reduction of the inventory in %*

h_0 = *coefficient for describing the rate of exponential decrease of Pu with depth in kg m^{-2}*

The other model that was used to calculate the soil erosion rates is the inventory method (IM) (Lal *et al.* 2013). The coefficient *α* was fitted after Alewell et al. (2014). The *P* factor was chosen according to Walling and He (1999) who recommend a particle size correction factor (*P* factor) of 1 and 1.2, whereas Lal et al. (2013) recommend a factor of 1.5. In this study an *α* of –0.117 and different *P* factors were used.

Equation 13: Soil erosion rates according to the inventory method (IM) (Lal *et al.* 2013)

$$L = -\frac{1}{(\alpha P)} \times ln\left(1 - \frac{I_{loss}}{I_{ref}}\right)$$

L = *loss of soil*

α = *coefficient of the least squares exponential fit of the profile depth to activity*

P = *particle size correction factor*

I_{ref} = *local reference inventory as mean of all reference sites in Bq m^{-2}*

I_{loss} = *actual inventory subtracted from the reference inventory (I_{ref}) in Bq m^{-2}*

3.9 MODELLING EROSION AND DEPOSITION RATES WITH MODERN

Additionally to the calculation methods above, the model by Arata et al. (2016) called MODERN (modelling deposition and erosion rates with Radionuclides) was used to convert inventories into soil redistribution rates. MODERN is a free to use open-source R package. It works iteratively and is able to describe specific depth distributions in a soil. MODERN creates the depth profile of the reference site, where no redistribution is expected, as a step function *g(x)*, which at each depth increment returns the Pu inventory. It also needs the total inventory of the sampling site, that was influenced by erosion or accumulation, for the total sampling depth in cm.

The model compares the FRN inventory of the reference site to the total FRN inventory of the sampling site. Therefore, it first needs to calculate the inventory (Equation 14).

To find possible solutions, simulated layers are integrated into the reference profile both below and above as potential soil loss or gain. The layer thickness is equal to the sampling depth increment, which is in this case 5 cm. For the estimation of sedimentation rates in MODERN, assumptions about the thickness of the horizons and the inventories are necessary, since a high inventory can be the result of a high deposition rate with low Pu activity or a low deposition rate with high Pu activity (Meusburger *et al.* 2016).

The new simulated depth profile is described by the integral function S (Equation 15) which can be solved through the primitive function G of the distribution function g(x) (Equation 16). MODERN calculates soil losses or gains return the results in cm or yearly rates (Equation 17). For that it needs the sampling year, which was 2018, and the reference year, which is estimated by Zhang et al. (1999) to be 1963.

Equation 14: Inventory of sampling site (Arata *et al.* 2016)

$$\int_{x^*}^{x^*+d} g(x)dx = I$$

I = FRN inventory at the sampling site in Bq m^{-2}

g(x) = function describing the FRN depth profile of the reference site in Bq m^{-2}

x = erosion or deposition rates in cm*

Equation 15: Simulated depth profile (Arata *et al.* 2016)

$$S(x) = \int_{x}^{x+d} g(x')dx'$$

S(x) = simulated total inventory of reference sites in Bq m^{-2}

x = required thickness in cm

g(x) = function describing the FRN depth profile of the reference site in Bq m^{-2}

d = depth increment of the sampling site in cm

Equation 16: Distribution function (Arata *et al.* 2016)

$$S(x) = G(x + d) - G(x)$$

S(x) = simulated total inventory of reference sites in Bq m^{-2}

G(x) = function describing the FRN depth profile of the reference site in Bq m^{-2}

x = required thickness in cm

d = total sampled depth at the sampling site in cm

Equation 17: Soil loss rates (Arata *et al.* 2016)

$$Y = 10 \times \frac{x^* \cdot x_m}{t - t_0}$$

Y = *erosion or deposition rates in t ha^{-1} yr^{-1}*

t = *sampling year*

t_0 = *reference year*

d = *total sampled depth at the sampling site in cm*

x_m = *mass depth of sampling site in kg m^{-2}*

*x** = *erosion or deposition in cm*

3.10 STATISTICS

The $^{239+240}$Pu-activities were checked for normal distribution by a Shapiro-Wilk test. To examine whether the central tendencies of several independent samples differ the $^{239+240}$Pu-inventories a one-way ANOVA (Kruskal-Wallis test) for non-parametric data, was applied. The correlation between variables was calculated pairwise with the Spearman rank coefficient.

4 RESULTS

4.1 SOIL PROFILES

4.1.1 SOIL TYPES

The most common soil types in the sampling area are Albic Podzols, found in various forms across the sampling sites P1, P2, P3, P4, P5 and P7 (see Table 3). At sampling site P6 a Stagnosol and at P8 a Gleysol were encountered.

All sites indicated podzolization to at least some degree. The soils at sampling site P1 (Histic Leptic Albic Podzol) and at site P8 (Spodic Histic Gleysol) have additional organic-rich layers and wet conditions (Histic horizon). At sampling sites P6 (Albic Stagnosol) and P7 (Albic Stagnic Podzol) the soils show features of water stagnation and poor drainage (Stagnic horizon). Continuous rock was exposed at sampling site P1 in a depth of 75 cm (Endoleptic). At the other sites, continuous rock was not reached. But the sampling sites P3 and P4 showed high skeletal content below a depth of 50 cm (Endoskeletic).

4.1.2 SOIL HORIZONS

All sites feature organic horizons (Oi, Oe, Oa) at the top, varying in thickness. The Oi horizon with a thickness of 2–3 cm, the Oe horizon with 4–10 cm and the Oa horizon with 2–9 cm.

Indicative of eluviation or leaching, the Ah and E horizons were found in all profiles, having a thickness from 4–31 cm (AhE horizon) and 4–30 cm (E horizon). The sampling site P4 showed the thickest leaching horizons with the AhE and E horizon combined thickness of 61 cm. The other sampling sites showed thinner AhE horizons from 4–16 cm. The E horizon also showed considerable variation with P2 and P4 having the thickest E horizons of 30 cm and P5, P6 and P7 having thinner horizons of 4–10 cm.

The B horizons had a thickness of 18–74 cm and showed accumulation of leached materials like organic matter (h) and sesquioxides (s) or the influence of stagnant water (g) or groundwater (l, r).

The transition to mineral layers (BC, CB, or C) was observed in 42 to > 100 cm depth. A change in parent material was observed in all soil profiles except in P2. In P1 the parent material changed from

peat to sandstone. In P3–P8 the parent material changes from colluvial sandy material to finer-grained marls and mudstones.

Table 3: Soil profiles with classification and horizon designation according to IUSS Working Group WRB (2022) (see Appendix 4 and Appendix 5).

Site	Name	Depth cm	Soil horizon	Thickness cm
P1	Histic Endoleptic Albic Podzol (Arenic, Epic)			
		8–6	Oi	2
		6–0	Oe	6
		0–6	Oa	6
		6–22	AhE	16
		22–45	2E	23
		45–65	2Bhs	20
		65–75	2Cs	10
P2	Albic Podzol (Arenic, Endic, Folic)			
		7–5	Oi	2
		5–0	Oe	5
		0–6	Oa	6
		6–15	AhE	9
		15–45	E	30
		45–75	BE	30
		75–90	BhsC	15
P3	Endoskeletic Albic Podzol (Arenic, Epic, Folic)			
		13–10	Oi	3
		10–0	Oe	10
		0–2	Oa	2
		2–15	AhE	13
		15–33	E	18
		33–38	Bh	5
		38–90	2BsC	52
P4	Endoskeletic Albic Podzol (Arenic, Endic, Folic)			
		8–5	Oi	3
		5–0	Oe	5
		0–4	Oa	4
		4–35	AhE	31
		35–65	E	30
		65–95	BhC	30
		95–100	2BhsC	5

Site	Name	Depth cm	Soil horizon	Thickness cm
P5	Albic Podzol (Loamic, Epic, Folic)			
		7–4	Oi	3
		4–0	Oe	4
		0–8	Oa	8
		8–18	E	10
		18–29	Bh	11
		29–46	2Bs	17
		46–65	2CB	19
P6	Albic Stagnosol (Loamic, Epic, Folic, Protospodic)			
		9–7	Oi	2
		7–0	Oe	7
		0–3	Oa	3
		3–7	AhE	4
		7–11	E	4
		11–28	2Bsvc	17
		28–42	2Bg	14
		42–85	2BCg	43
P7	Albic Stagnic Podzol (Loamic, Epic, Folic)			
		8–6	Oi	2
		6–0	Oe	6
		0–7	Oa	7
		7–16	AhE	9
		16–23	E	7
		23–50	2Bhsvc	27
		50–67	2Bg	17
P8	Spodic Histic Gleysol (Abruptic, Clayic, Inclinic)			
		9–7	Oi	2
		7–0	Oe	7
		0–9	Oa	9
		9–21	AhE	12
		21–36	El	15
		36–54	2Bl	18
		54–80	3Cr	26

4.2 SOIL PROPERTIES

4.2.1 BULK DENSITY

The mean bulk density across all profiles and depths was found to be 1.326 g cm^{-3} with a median of 1.407 g cm^{-3}. The surface horizons have the lowest bulk density with a minimum of 0.286 g cm^{-3} in profile P7 in a depth of 0–7 cm. The highest bulk density of 1.762 g cm^{-3} is in profile P8 in a depth of 21–36 cm.

Generally, the highest mean, median and maximum bulk densities are found in soil profiles P1 and P8. Soil profiles P4 and P6 showed intermediate bulk densities. The lowest mean bulk densities are presented in soil profiles P2, P3, P5 and P7.

The soil profiles P2, P6 and P7 show a continuous increase in bulk density with depth (see Figure 12). The other soil profiles show an inconsistency and have horizons with a higher bulk density than those directly below. These denser horizons are found at soil profiles P1 in 22–45 cm (2E horizon), P3 in 15–33 cm (E horizon), P4 in 35–95 cm (E and Bhc horizon), P5 in 8–18 cm (E horizon) and P8 in 21–54 cm (El and 2Bl horizon).

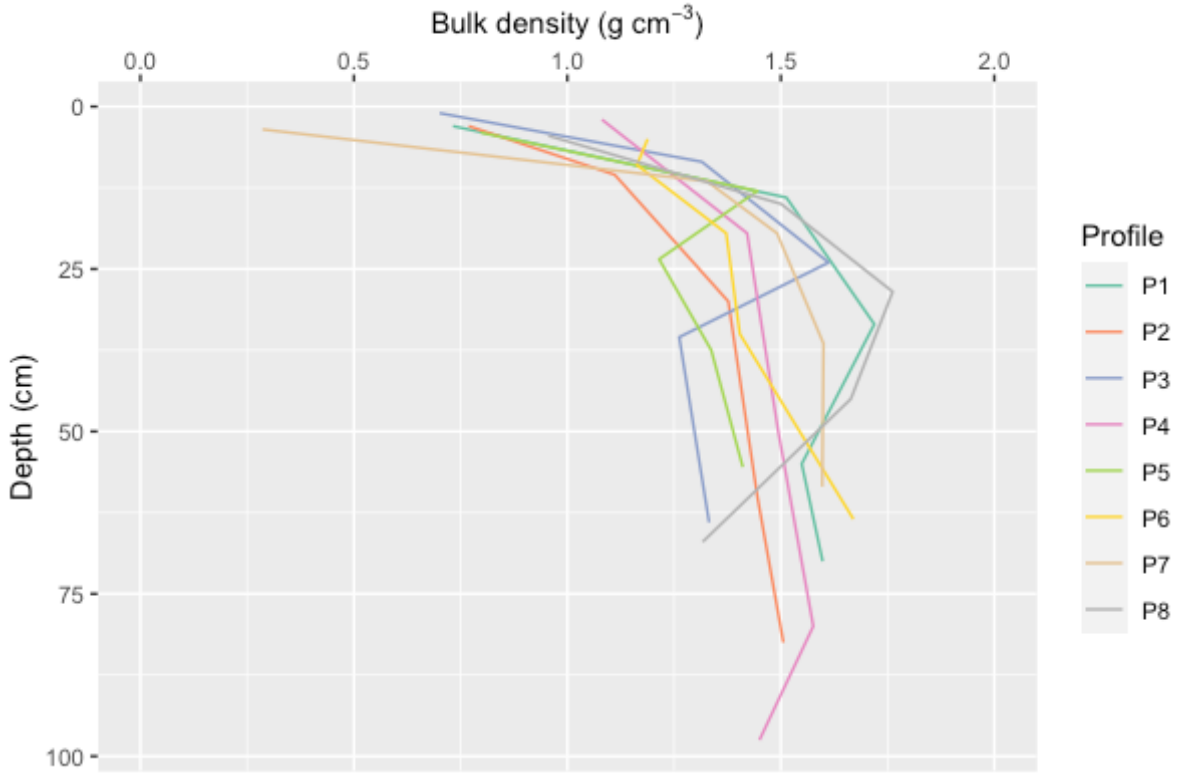

Figure 12: Bulk density as a function of depth in soil profiles P1–P8.

4.2.1 FRACTION OF ROCK FRAGMENTS (SOIL SKELETON)

The volumetric samples had a mean skeletal fraction of 16.4 % and a median of 10.2 %. The maximum skeletal fraction of up to 72.8 % was found in soil profile P4 at a depth of 95–100 cm. In contrast, there was no skeletal fraction in soil profile P6 at a depth of 42–85 cm, in soil profile P7 at a depth of 0–7 cm, in soil profile P8 at a depth of 36–54 cm.

Generally, the soil profiles showed an increase of the skeletal content with depth (see Figure 13). The exceptions were soil profile P2, P6 and P8. In soil profile P2 the skeletal fraction increases but was not collected with the volumetric cylinder due to the grain size. In soil profile P6, which is very profound, the skeletal fraction was generally low with no trend in decrease or increase up to a depth of 85 cm. In soil profile P8 the skeletal fraction dropped from 33.3 % to 0 %. Over all horizons a soil profile, P6 had the lowest (1.5 %) and P4 the highest (27.3 %) mean skeletal fraction.

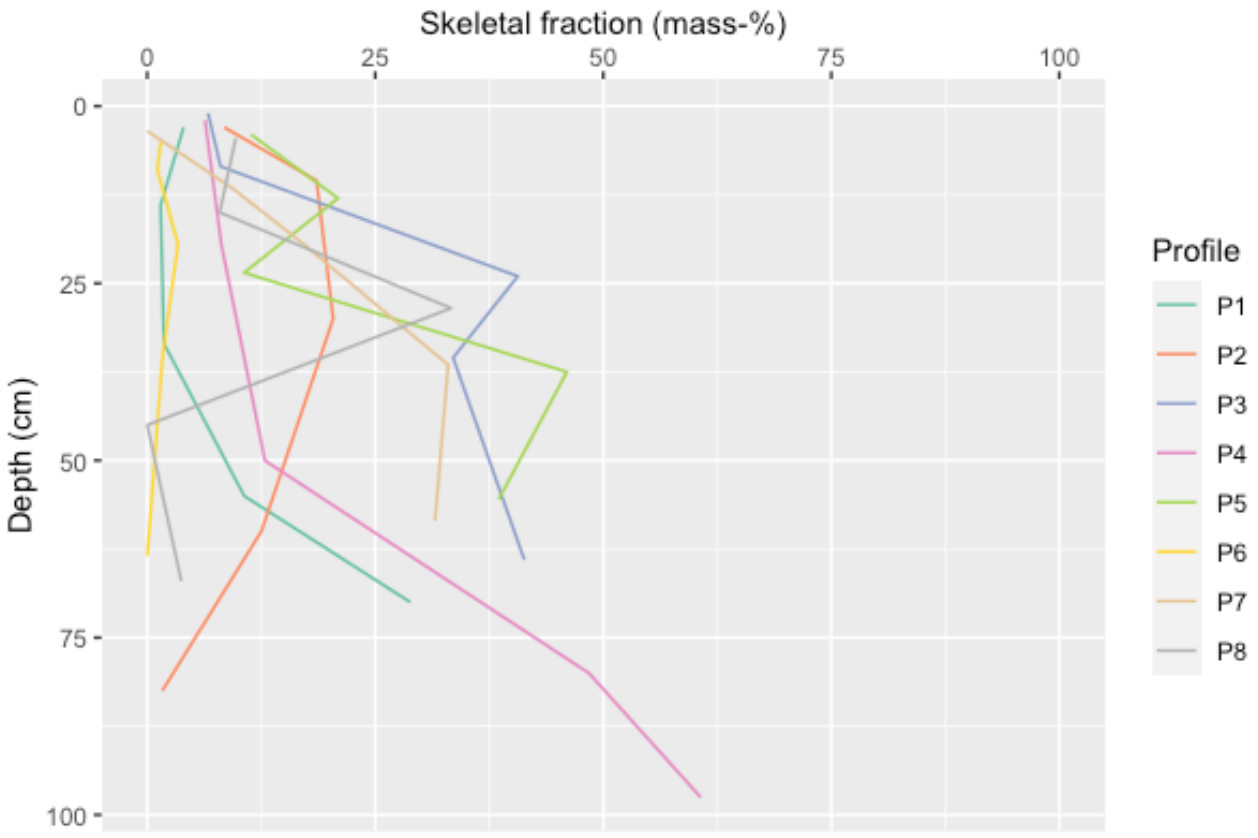

Figure 13: Skeletal fraction as a function of depth in soil profiles P1–P8.

4.2.2 GRAIN SIZE DISTRIBUTION

The grain size distribution showed a higher sand content compared to silt and clay contents. Especially the fine and very fine sand grain size were more common (see Figure 14). Only in soil profiles P6–P8, the clay and silt content together surpassed 50 % in certain horizons. In soil profile P8 in a depth of 54–80 cm, the fine clay made up 61 % of the fine earth.

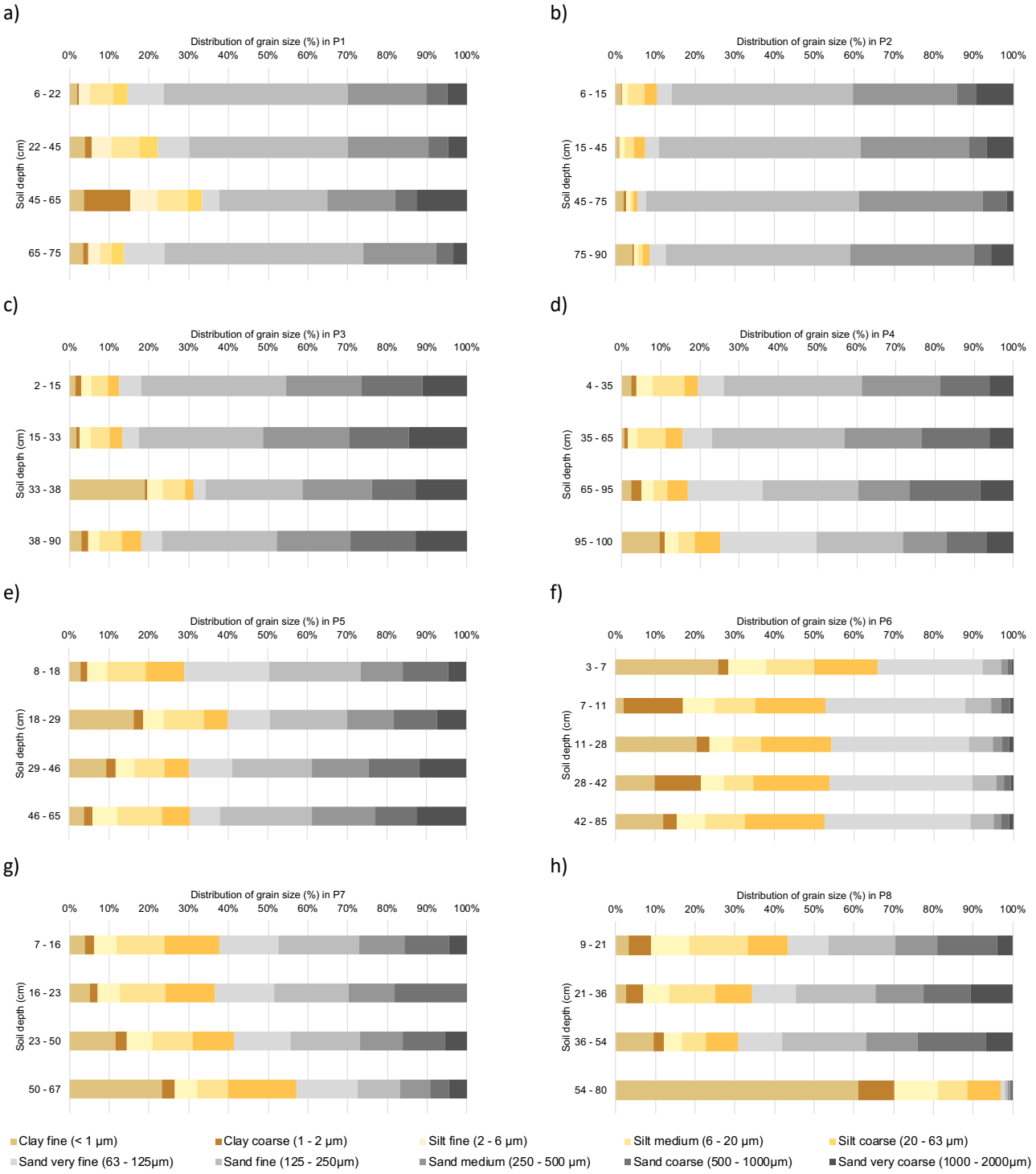

Figure 14: Fine earth grain size distribution as a function of depth in soil profiles P1–P8.

4.2.2.1 CLAY CONTENT

A mean clay content of approximately 11.8% across all soil profiles and horizons and a median of 7.1 % was observed. The distribution of clay content varied considerably (see Figure 15) with the highest concentration of 70.1% clay found in profile P8 within the deepest horizon (54-80 cm). Conversely, the lowest clay content measured was 0.9% in profile P2 within the 15-45 cm horizon.

The clay content increased with depth within the soil profiles and also with decreasing altitude (see Figure 14). So, the lowest clay contents were in the uppermost soil profiles, the highest clay content was in the lowest soil profiles.

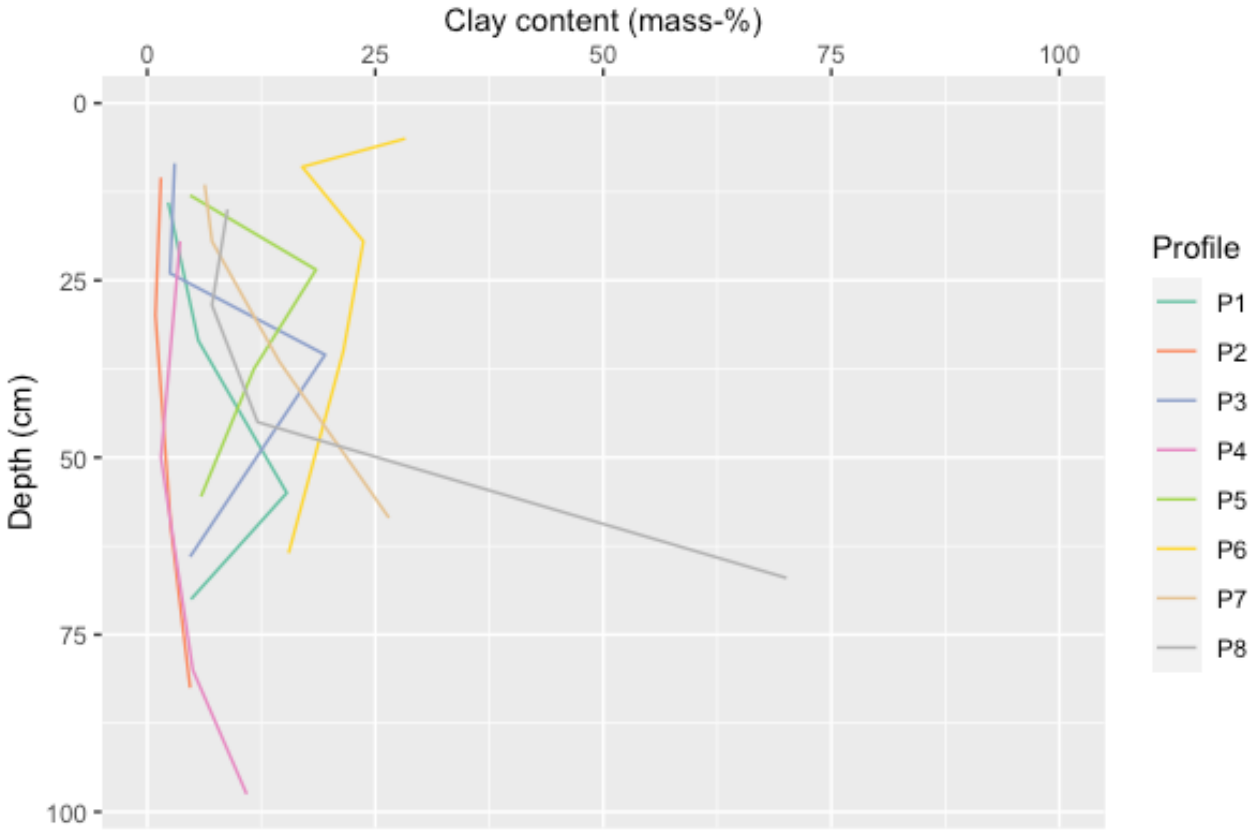

Figure 15: Clay content as a function of depth in soil profiles P1–P8.

4.2.2.2 SILT CONTENT

The mean silt content over all soil profiles and depths was 20.2 % with a median of 18.5 %. The lowest silt content of 2.8 % was found in soil profile P2 at 45–75 cm depth. P2 also had generally the lowest silt content of 2.8–8.9 %. The highest silt content of 37.7 % was measured in P6 at 3–7 cm depth, the highest silt content in soil profile P6 with a range of 30.5–37.7 %.

Within each soil profile, the silt content was roughly evenly distributed across the horizons (see Figure 16). The only soil profile with more than 10 percentage points difference in silt content over its horizons was P8.

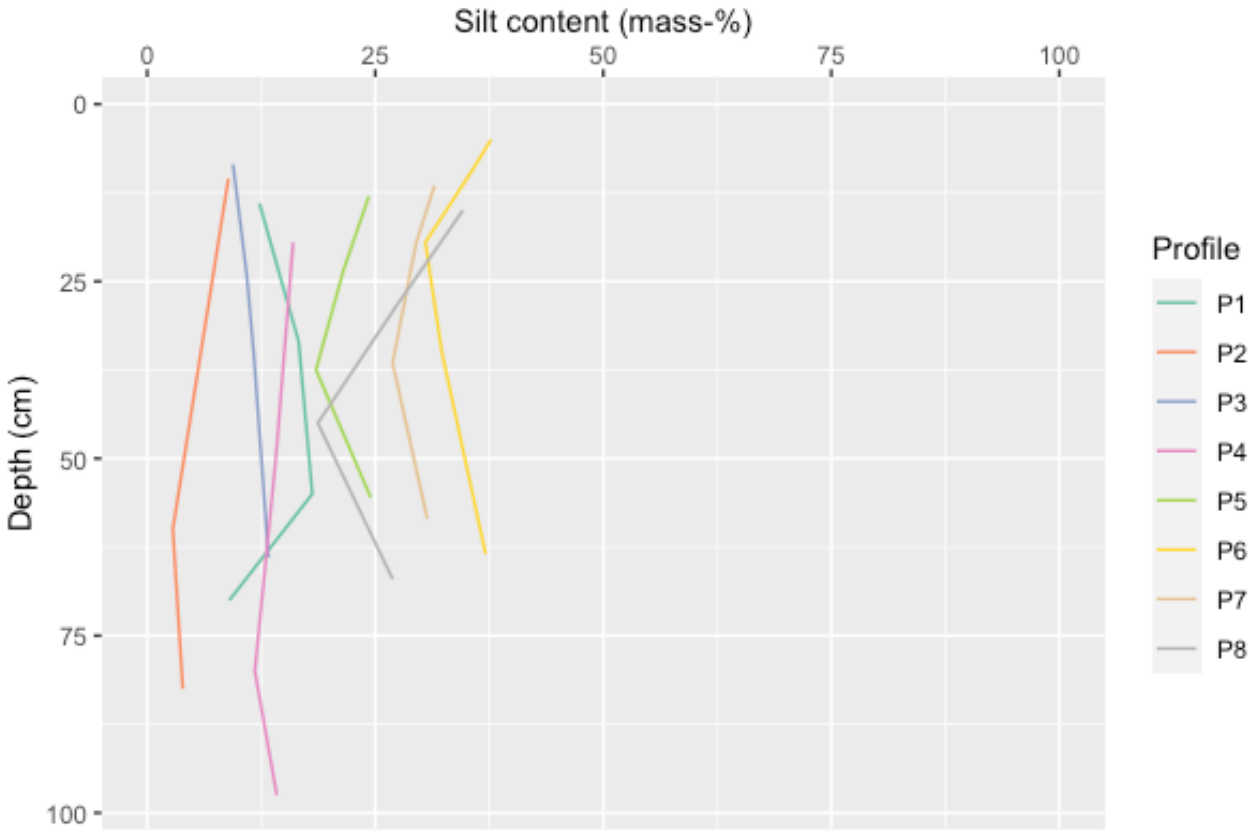

Figure 16: Silt content as a function of depth in soil profiles P1–P8.

4.2.2.3 SAND CONTENT

A mean sand content of 68.0 % and a median of 69.6 % was measured. The lowest sand content of 3.0 % was found in soil profile P8 at a depth of 54–80 cm and the highest sand content of 94.6 % in soil profile P2 at a depth of 45–75 cm. Soil profile P2 also had generally the highest sand content with 89.6–94.6 %. The lowest sand content of 34.0–47.4 % was found in soil profile P6.

In soil profiles P7 and P8, there was a decrease in sand content with depth. Within the others, there was no clear trend across the soil horizons of each profile. Three soil profiles had an intermediate horizon with a lower silt content, P1 in 45–65 cm depth (2Bhs horizon), P3 in 33–38 cm depth (Bh horizon) and P5 in 18–29 cm depth (Bh horizon).

In comparison the four upper soil profiles (P1–P4) had a higher sand content than the lower four (P5–P8) (see Figure 17).

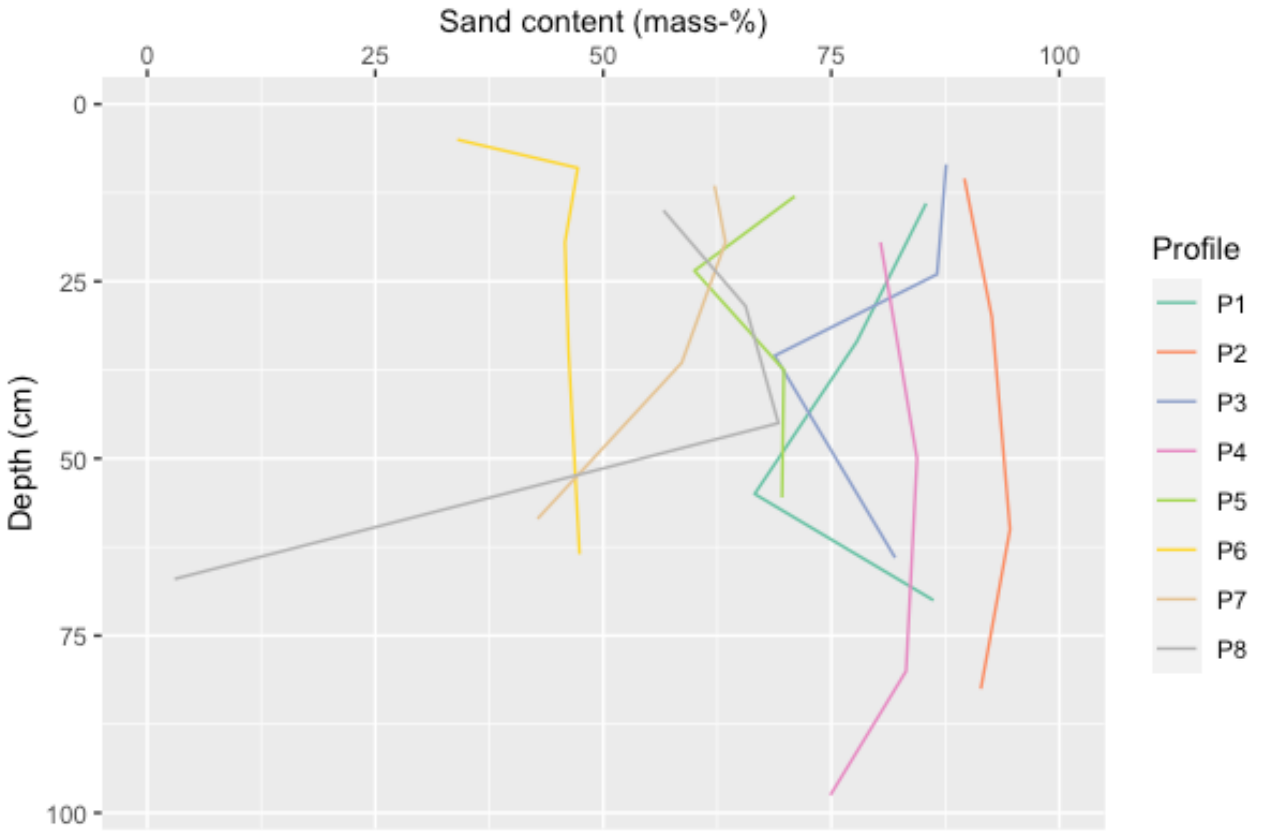

Figure 17: Sand content as a function of depth in soil profiles P1–P8.

4.2.3 SOIL TEXTURE CLASS

In the investigated soil profiles, six texture classes were identified: sand (S), loamy sand (LS), sandy loam (SL), loam (L), clay loam (CL) and clay (C) (see Figure 18).

Sandy loam was the most prevalent soil texture, identified 13 times across the soil profiles (in P1, P3, P4, P5, P7 and P8). Occurring seven times, loamy sand was the second most common texture (in P1, P3 and P4). A sand texture was identified in six instances (in P2 and P3) and loam was found five times (in P6 and P7). Less common in this study, clay loam (in P6) and clay (in P8) were each identified once.

In the individual soil profiles, P1 and P4 contained sandy loam and loamy sand, P2 consisted mainly of sand and P5 of sandy loam. The soil texture in P3 spread from sand to sandy loam, in P6 from loam to clay loam, in P7 from sandy loam to loam and in P8 from sandy loam to clay.

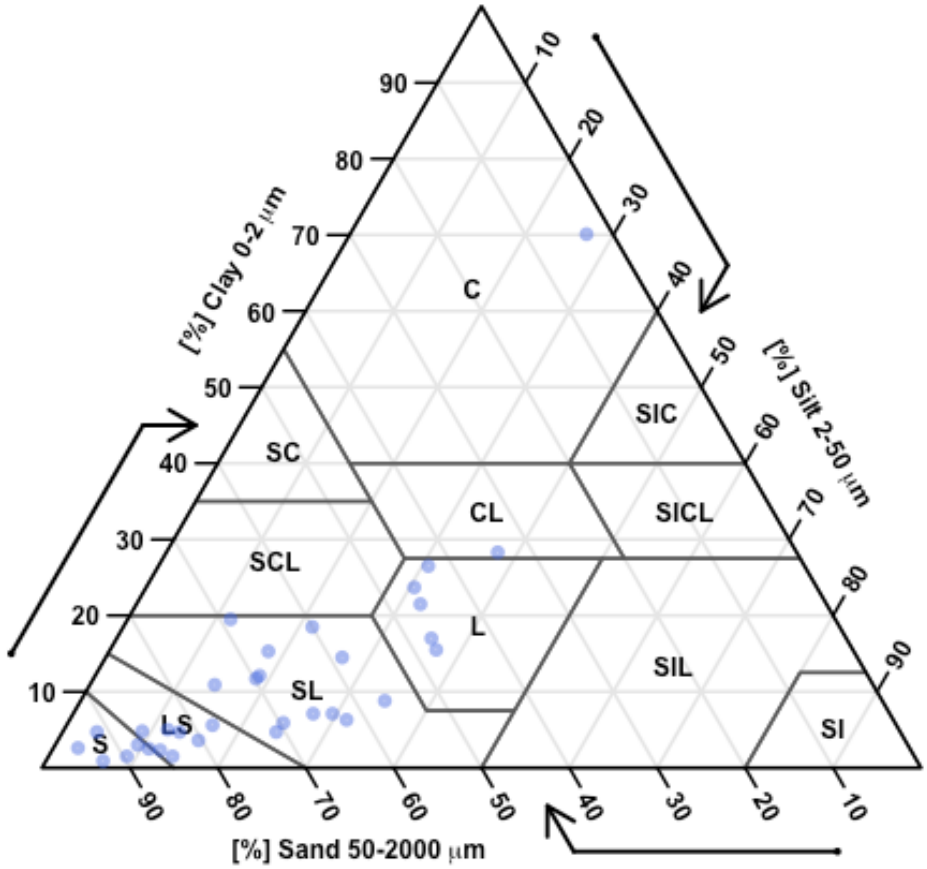

Figure 18: Soil texture diagram.

4.2.4 SOIL COLOR

The soil color in moist conditions had mainly a Munsell hue of 7.5YR and 10 YR (see Figure 19). Only in P2 and P8 other hues like 2.5YR and 5YR were found. In dry conditions, the Munsell hue was 10YR in almost all horizons. Exceptions are the three lowest horizons of P8, where hues of 2.5YR and 7.5Y were found (see Figure 20).

The Munsell value was generally lowest in the uppermost horizons and increased with depth. Exceptions were the horizons 2Bhs in P1, BE and BhsC in P2, Bh in P3, Bhc and 2BhsC in P4, Bh in P5 and 2Bl in P8, where the Munsell value decreased again.

The Munsell chroma was generally also lowest in the uppermost horizons and increased with depth. But the horizons 2E in profile P1, AhE in P2, Bh in P3, 2CB in P5, E and 2BCg in P6 and 3 Cr in P8 showed a lower chroma than the horizon above.

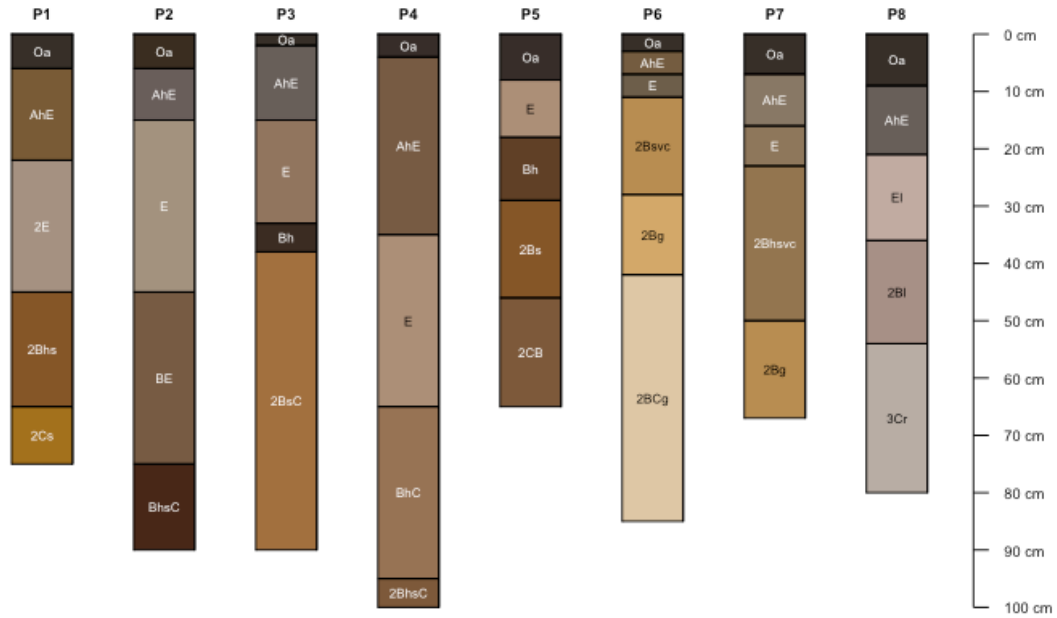

Figure 19: Moist soil profile horizon colors in different depths of soil profiles P1–P8

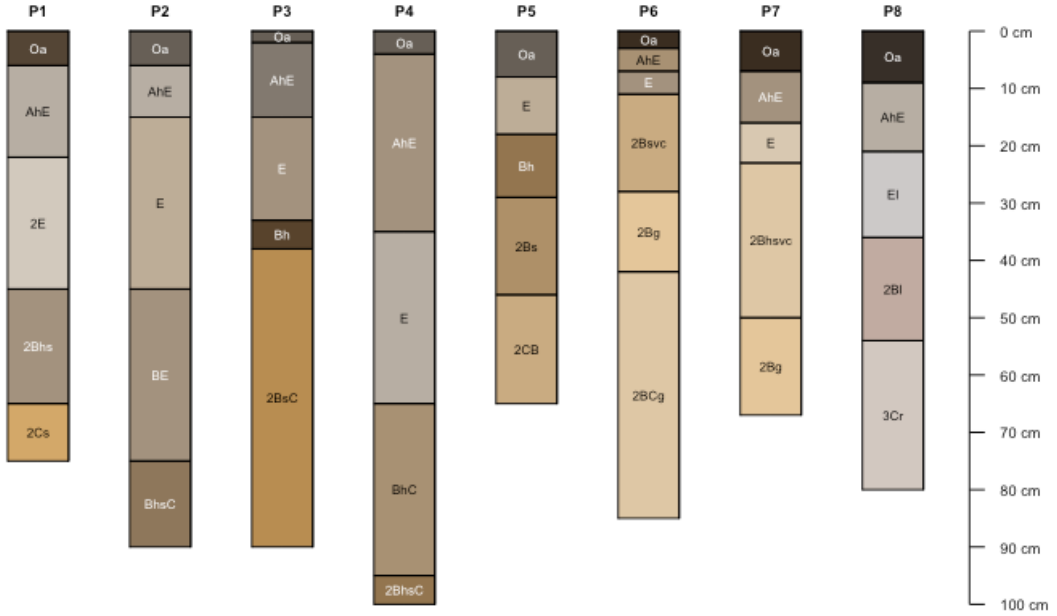

Figure 20: Dry soil profile horizon colors in different depths of soil profiles P1–P8

4.2.5 pH

The mean pH was 3.46 and the median pH was 3.19. The lowest pH of 2.57 was found at a depth of 0–6 cm (Oa horizon) in soil profile P2, which was also the profile with the lowest average pH over

its entire soil depth. The highest pH of 6.93 was measured in a depth of 21–36 cm (El horizon) in soil profile P8, which was also the profile with the highest average pH over all its horizons.

At the surface, the pH was lowest and ranges from 2.57 to 2.88. The pH increases with depth, in soil profiles P1–P7 the pH increased to 3.41–4.13 in their deepest horizon.

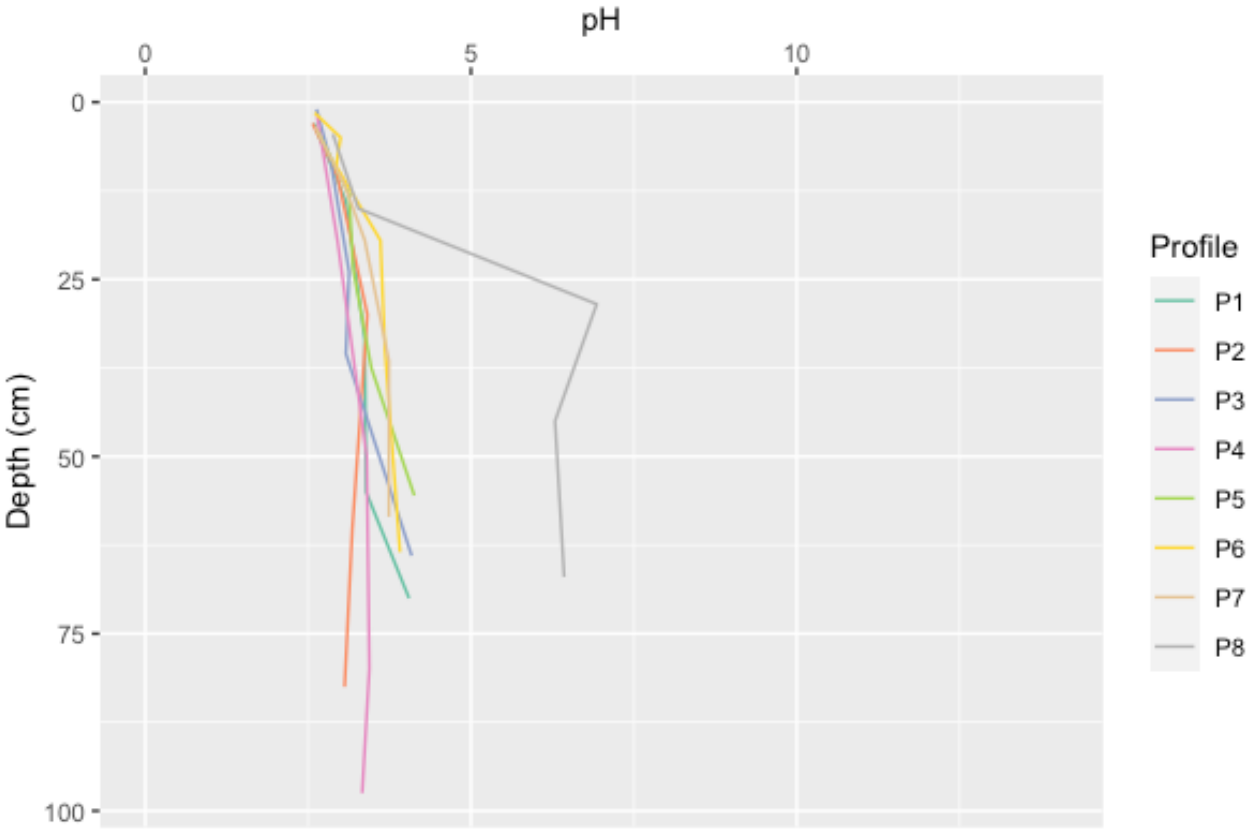

Figure 21: pH as a function of depth in soil profiles P1–P8.

4.2.6 ORGANIC MATTER CONTENT

The mean organic matter content (LOI) was 7.5 % with a median of 3.0 %. The lowest organic matter content was 0.3 % in soil profile P2 in the E horizon at a depth of 15–45 cm. The highest organic matter content was 52.7 % in soil profile P8 in the Oa horizon at a depth of 0–9 cm.

Generally, the organic matter content decreased with depth. Exceptions were found in E horizons, which were low in organic matter and Bh horizons, which showed a higher organic matter content than the overlying horizon. The groundwater influenced soil profile P8 had an increased organic matter content in the water-saturated Cr horizon.

In some of the soil horizons, distributed across all soil profiles and different depths, biochar was found.

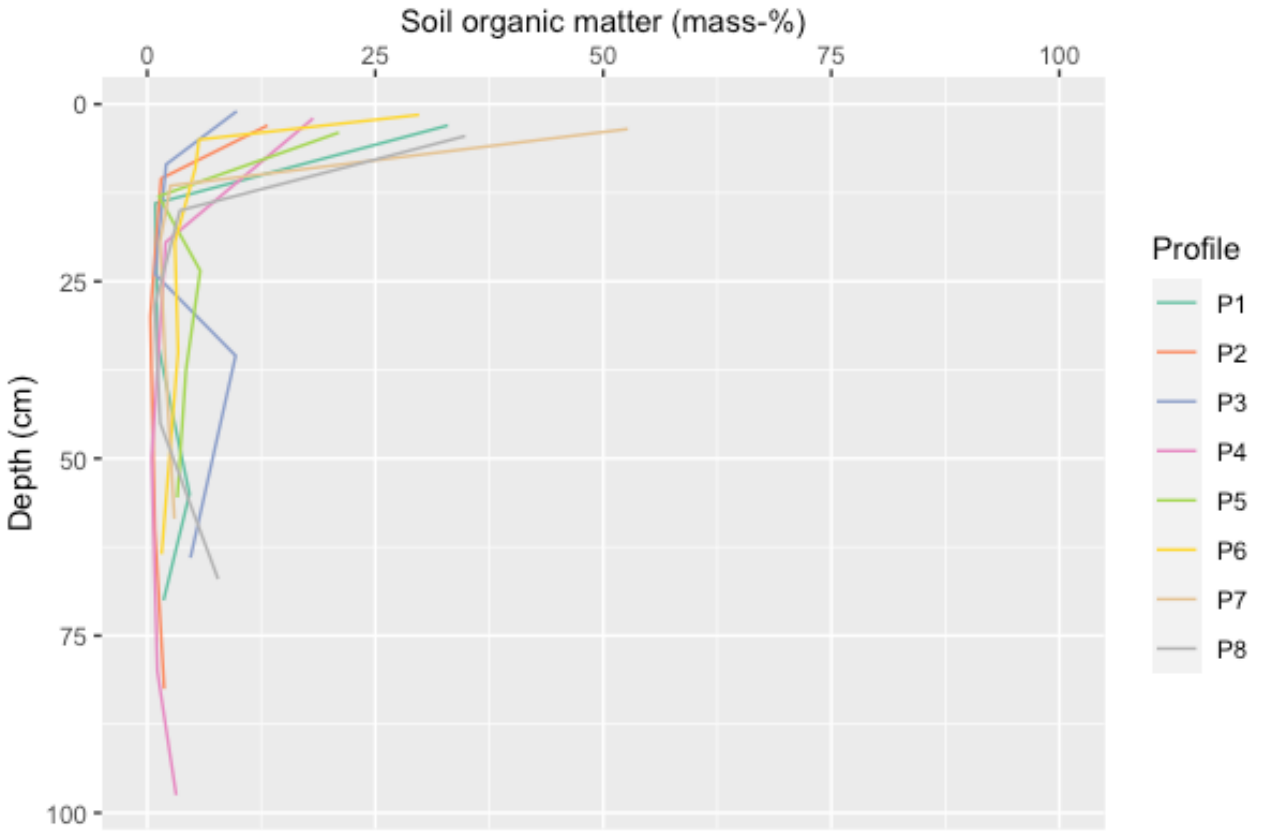

Figure 22: Soil organic matter as a function of depth in soil profiles P1–P8.

4.2.7 TOTAL ELEMENT COMPOSITION

The most abundant element in all soil horizons was silicon followed by aluminium, potassium, and iron. Other more frequent elements in order of abundance were sodium, magnesium, titanium, sulfur, calcium, zirconium, phosphorous, tungsten and manganese.

When assessing the soil profiles the Si content was low in organic horizons and high in eluvial horizons. Contrarily Al and Fe were low in eluvial horizons and higher in Bh, Bs and C horizons. The fraction of K, Ti, Ca, Mn, and Mg increased with depth within the soil profiles. In contrast S, P and W decreased with depth. For Na and Zr there was no clear trend within the individual soil profiles observable. When comparing the mean values of all soil profiles, K, Fe, Na, Mg, Ti, Ca, Mn and Zr seemed to be less abundant in upper four soil profiles (P1–P4) and more abundant in the lower four (P5–P8).

4.2.8 OXIDES

Oxide composition correlated closely with elemental abundance across soil profiles, with silicon dioxide (SiO_2) being the most prevalent oxide. Its concentration ranged from a low of 40.0 % in profile P7 (0–7 cm depth) to a high of 96.8 % in profile P1 (6–22 cm depth) exhibiting an average of 83 % and a median of 84.2 %.

Sodium oxide (Na_2O), sulfur trioxide (SO_3), and phosphorus pentoxide (P_2O_5) concentrations were highest at the surface in Oa horizons and decrease with depth.

Conversely, the concentrations of magnesium oxide (MgO), aluminum oxide (Al_2O_3), potassium oxide (K_2O), calcium oxide (CaO), titanium dioxide (TiO_2), manganese(II) oxide (MnO), and iron(III) oxide (Fe_2O_3) generally increased with depth. Al_2O_3, Fe_2O_3, K_2O, MgO, CaO and TiO_2 reached their maximal abundance in soil profile P8 in a depth of 54–80 cm. The minimal concentration of Al_2O_3 MgO was calculated in soil profile P2 in a depth of 6–15 cm, the minimum of Fe_2O_3 and K_2O in P1 in a depth of 6–22 cm and the one of CaO and TiO_2 in P2 in a depth of 45–75 cm. MnO had its maximum in soil profile P7 in a depth of 23–50 cm and its minimum in P2 in a depth of 45–75 cm.

a) Na_2O

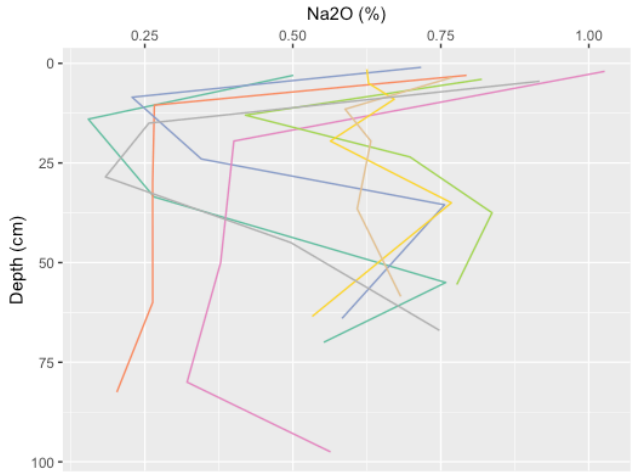

b) MgO

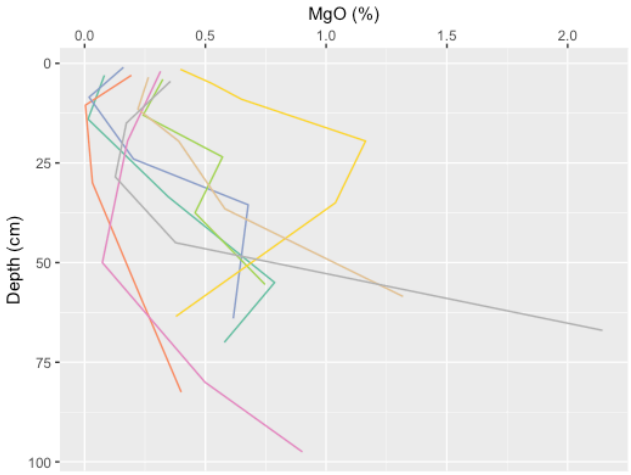

c) Al_2O_3

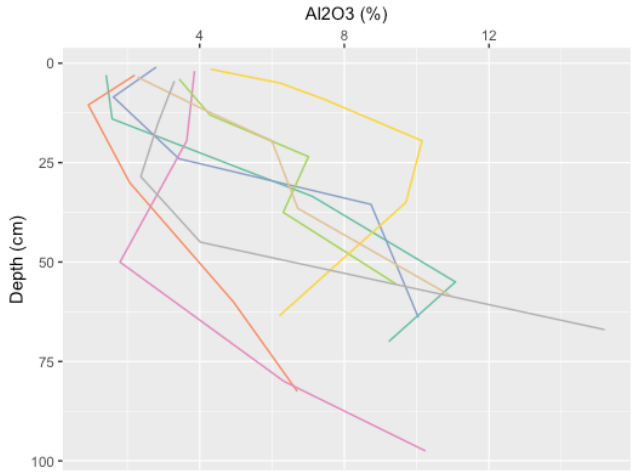

d) SiO_2

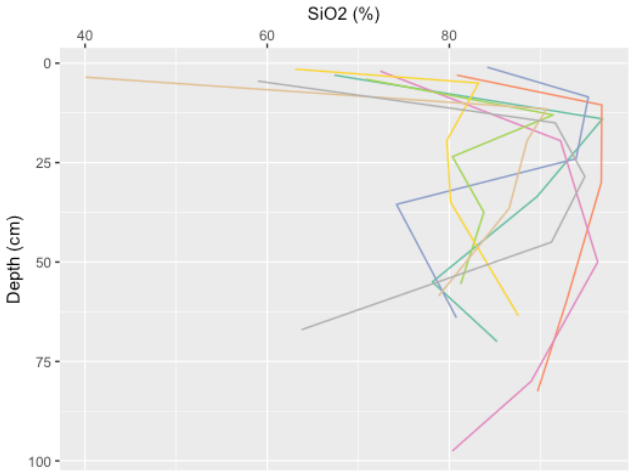

e) P_2O_5

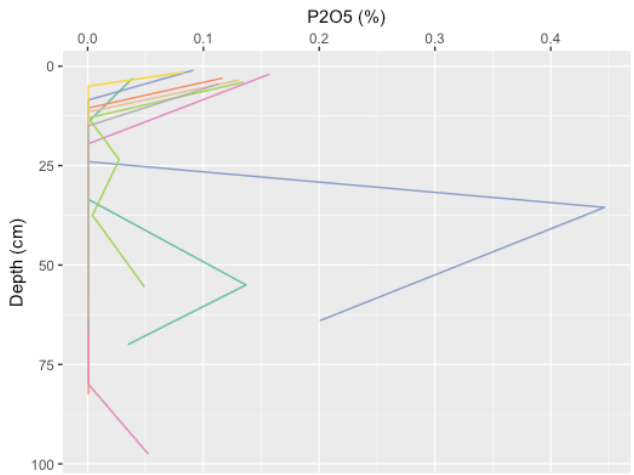

f) SO_3

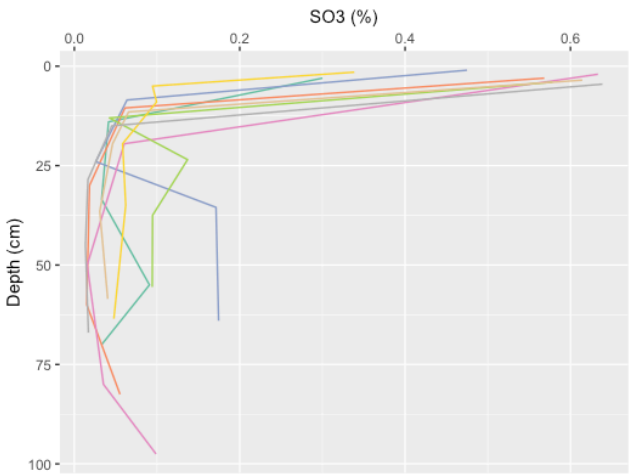

g) K_2O

h) CaO

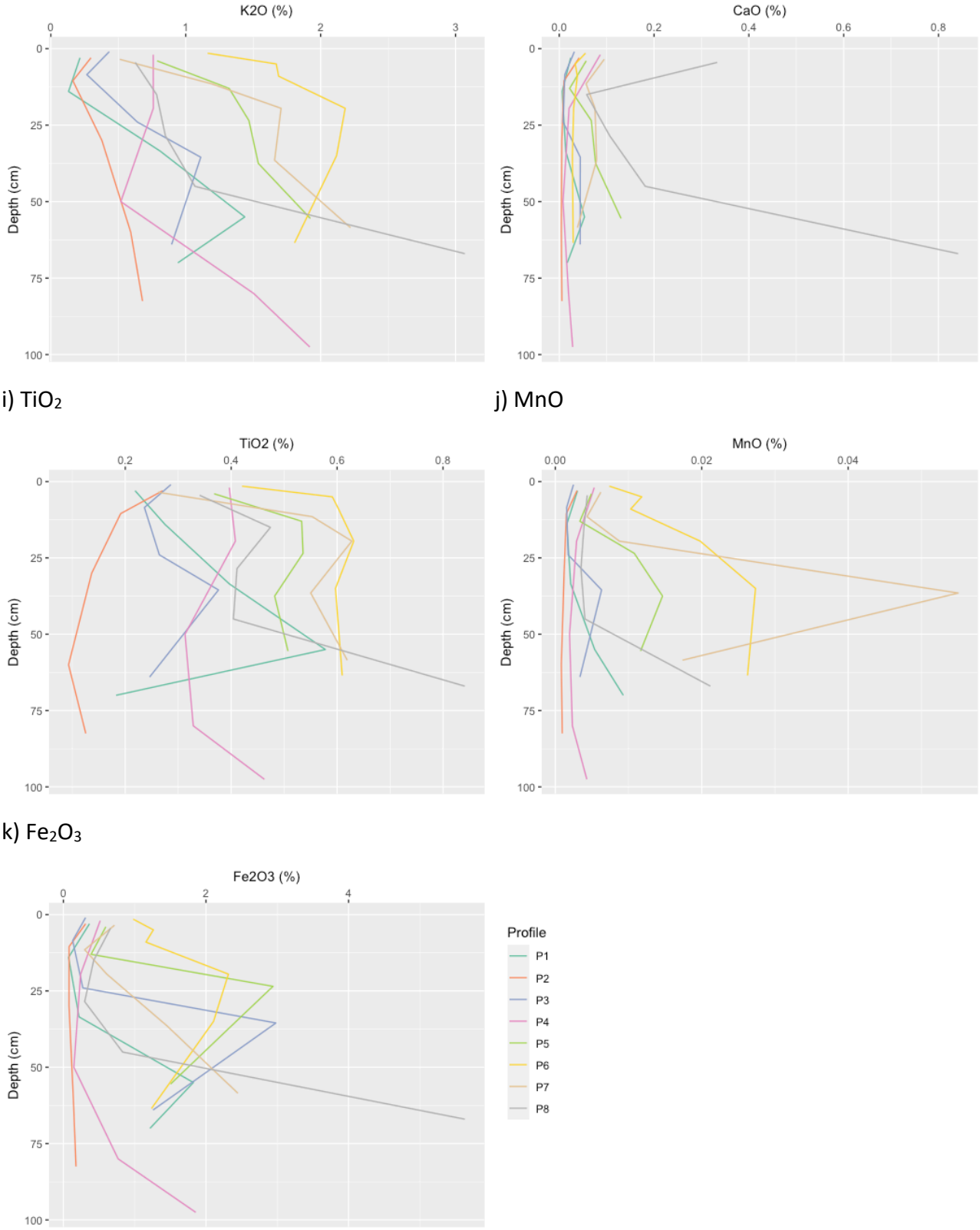

i) TiO_2

j) MnO

k) Fe_2O_3

Figure 23: The content of different oxides a)–k) as a function of depth in soil profiles P1–P8.

4.2.9 AMORPHOUS FORMS OF ALUMINIUM AND IRON

The analysis revealed a mean concentration of amorphous aluminum oxide (Al_o) across all soil profiles and horizons of 911 mg kg^{-1}, with a median value of 685 mg kg^{-1}. The lowest concentration of amorphous aluminum oxide was found in the E horizon of profile P2, at a depth of 15–45 cm, with a value of 16 mg kg^{-1}. Conversely, the highest concentration was observed in the 2BsC horizon of profile P3, at a depth of 38–90 cm, where the concentration reached 4'498 mg kg^{-1}.

The lowest concentrations of amorphous aluminum oxide were typically associated with the AhE and E horizons. In contrast, the highest concentrations were identified in the B and C horizons.

The investigation yielded a mean concentration of amorphous iron oxides (Fe_o) across all sampled soil profiles and horizons of 1'856 mg kg^{-1}, with a median concentration of 962 mg kg^{-1}. The lowest recorded concentration of amorphous iron oxides was 6.7 mg kg^{-1}, observed in the E horizon of profile P4, at a depth of 35–65 cm. Conversely, the highest concentration of amorphous iron oxides was measured at 9'766 mg kg^{-1} in the Bh horizon of profile P5, at a depth of 18–29 cm.

The analysis indicated that the lowest concentrations of amorphous iron oxides were typically found in the E horizons, which were more susceptible to leaching processes. In contrast, higher concentrations were identified in the Bh and Bs horizons, which are associated with the accumulation and enrichment of iron oxides.

The displacement ratio of Al_o+½Fe_o reaches from 0.002 % to 0.67 % with a mean of 0.18 % and a median of 0.12 %. It revealed generally lower ratios in eluvial horizons and higher in O, C and illuvial horizons (see Figure 24). The exceptions are the soil profile P2 and P6, in which uniformly low ratios occurs across all depths. The lowest ratio is in the E horizon in soil profile P2 and the highest ratio in the Bh horizon in soil profile P3.

a) amorphous Al

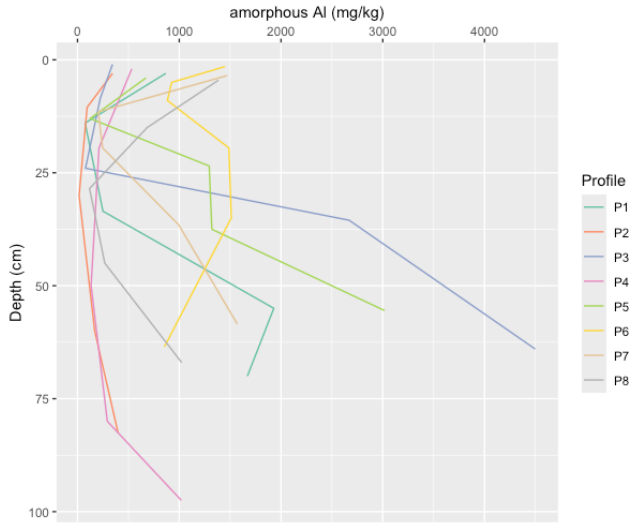

b) amorphous Fe

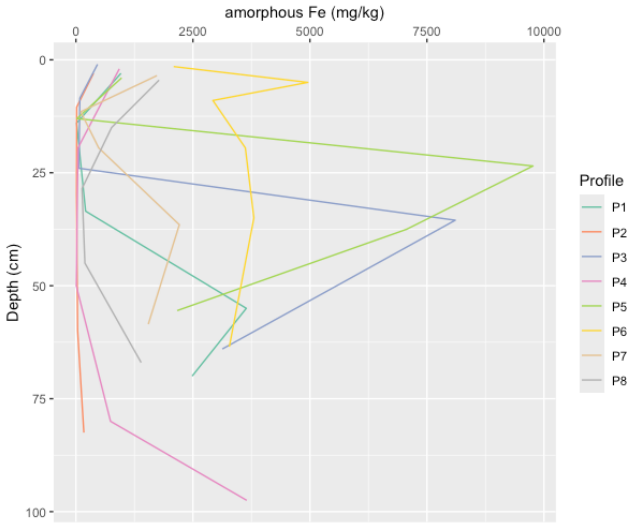

c) Displacement ratio of amorphous Al+1/2Fe

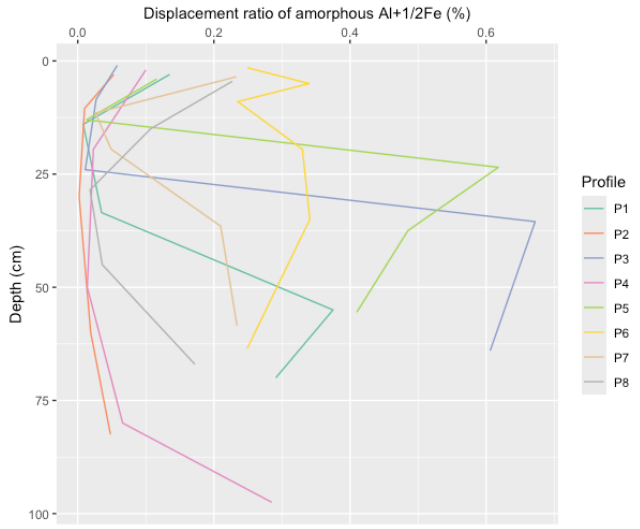

Figure 24: The content of a) amorphous Al and b) amorphous Fe and c) the displacement ratio of amorphous Al+1/2Fe as a function of depth in soil profiles P1–P8.

4.3 WEATHERING INDICES

4.3.1 CHEMICAL INDEX OF ALTERATION (CIA)

The calculated CIA spans from 53 (P7, 0–7 cm depth, Oa horizon) to 86 (P2, 75–90 cm depth, BhsC horizon) with a mean of 69 and median of 70. A general trend of increasing value with depth was observed in all soil profiles except P6. While the soil profiles P2, P3 and P7 revealed a continuous increase with depth, the others (P1, P4, P5 and P8) showed and a sudden decrease in a depth of 20–65 cm. The upper three soil profiles (P1–P3) and P6 had a higher mean CIA than the other four soil profiles (P4, P5, P7 and P8). The lowest mean CIA per soil profile was determined in P8, the highest in P1.

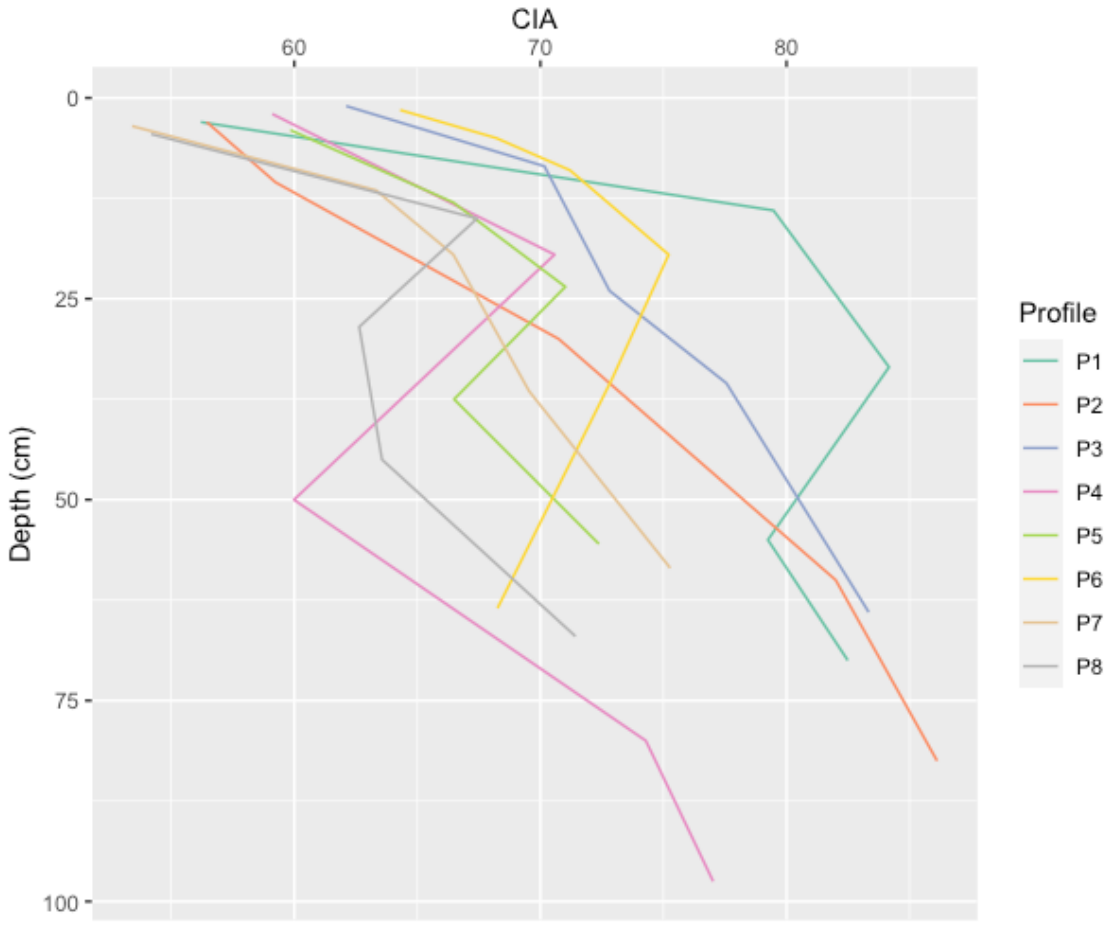

Figure 25: The Chemical Index of Alteration (CIA) as a function of depth in soil profiles P1–P8.

4.3.2 Chemical Index of Weathering (CIW)

The CIW also has trend of increasing with depth in all soil profiles and shows a similar behavior than the CIA. Soil profiles P4, P5 and P8 also showed a sudden CIW-decrease in a depth of 20–65 cm, while the index in P2, P3 and P7 increased continuously. The CIW ranged from 61 (P8, 0–9 cm depth, Oa horizon) to 95 (P2, 75–90 cm depth, BhsC horizon) with a mean of 82 and a median of 85. The soil profile with lowest mean CIW is P8 and the one with the highest is P6.

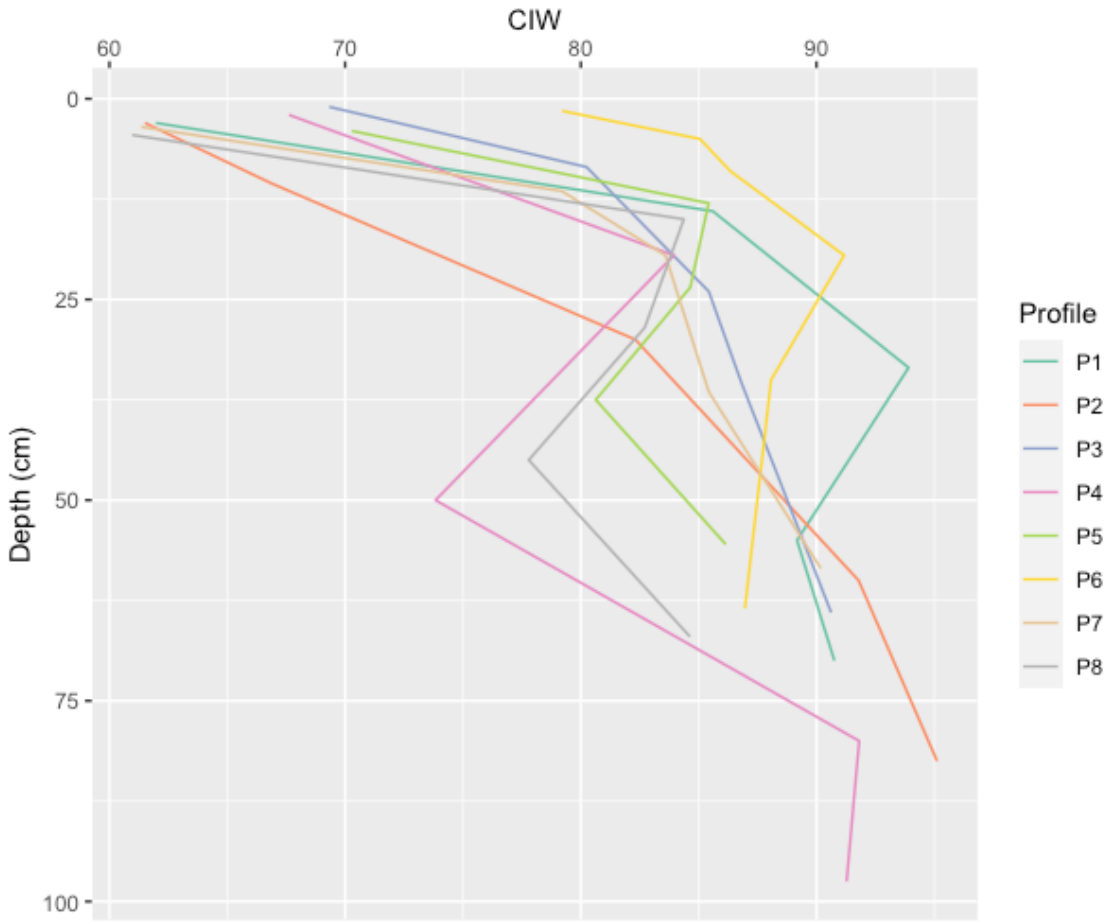

Figure 26: The Chemical Index of Weathering (CIW) as a function of depth in soil profiles P1–P8.

4.3.3 Weathering Index of Parker (WIP)

The WIP ranges from 2.6 (P1, 6–22 cm depth, AhE horizon) to 41 (P8, 54–80 cm depth, 3Cr horizon) with a mean and median of 16. The index in soil profiles P5 and P7 continuously increases with depth. The WIP of soil profiles P1, P3 has an S-form, it decreases at first in a depth of 2–22 cm, increases in a depth of 33–65 cm and below that decreases again. In soil profiles P2, P4 and P8 the values are lower in the second and third horizon. In soil profile P6 the index decreases below a depth of 42 cm. The mean WIP per site is lower in the upper four soil profiles (P1–P4) and higher in the lower four (P5–P8).

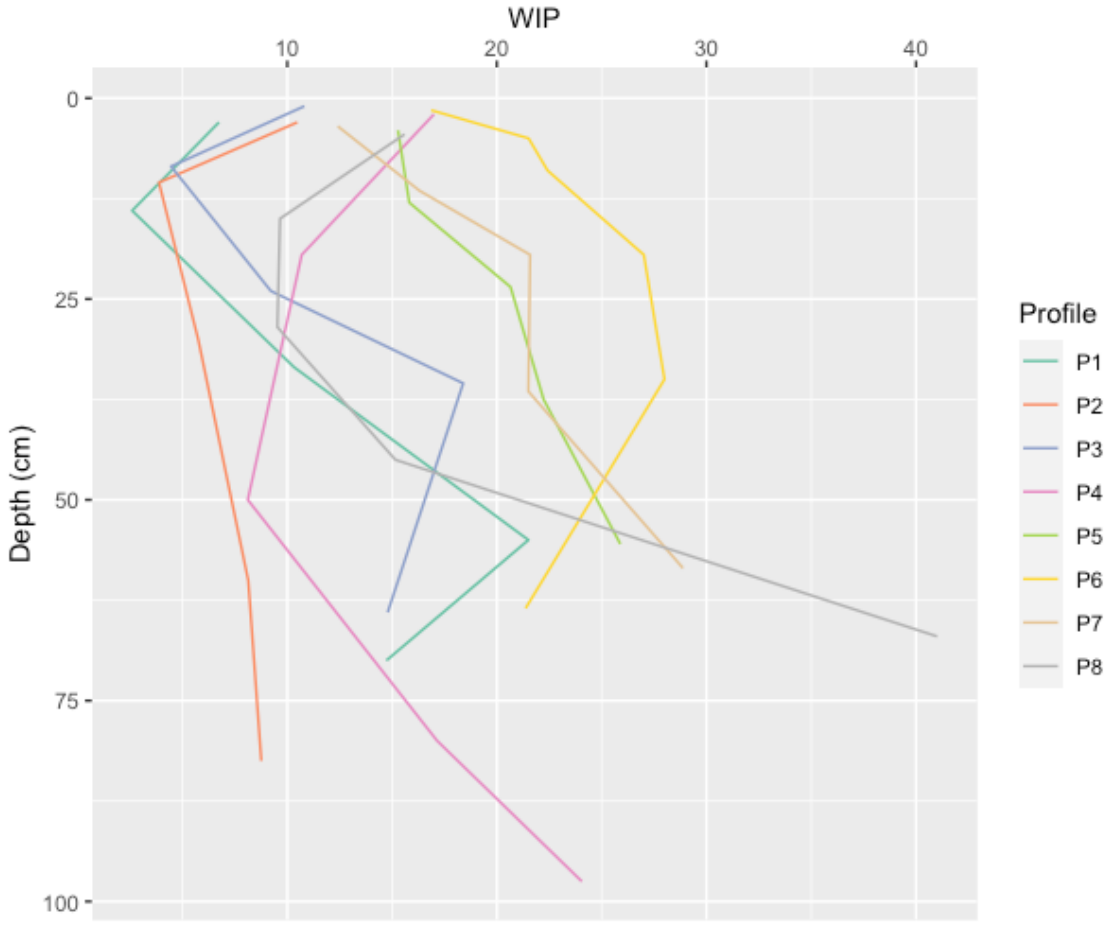

Figure 27: The Weathering Index of Parker (WIP) as a function of depth in soil profiles P1–P8.

4.3.4 [(Ca+K)/Ti] Index

This index ranges from 0.8 (P1, 6–22 cm depth, AhE horizon) to 10.9 (P2, 45–75 cm depth, BE horizon) with a mean and median of 4.8. The index generally increases with depth in a profile. But while the soil profile P5 is the only with a continuous increase of the index across all sampling depths, the others (P1, P2, P3, P4, P6, P7, P8) have decreasing values in their second-highest horizon before increasing again. P2, P4 and P6 even show a decreasing index again in their lowest horizon. The highest mean index per site was calculated for soil profile P2 and the lowest for P1.

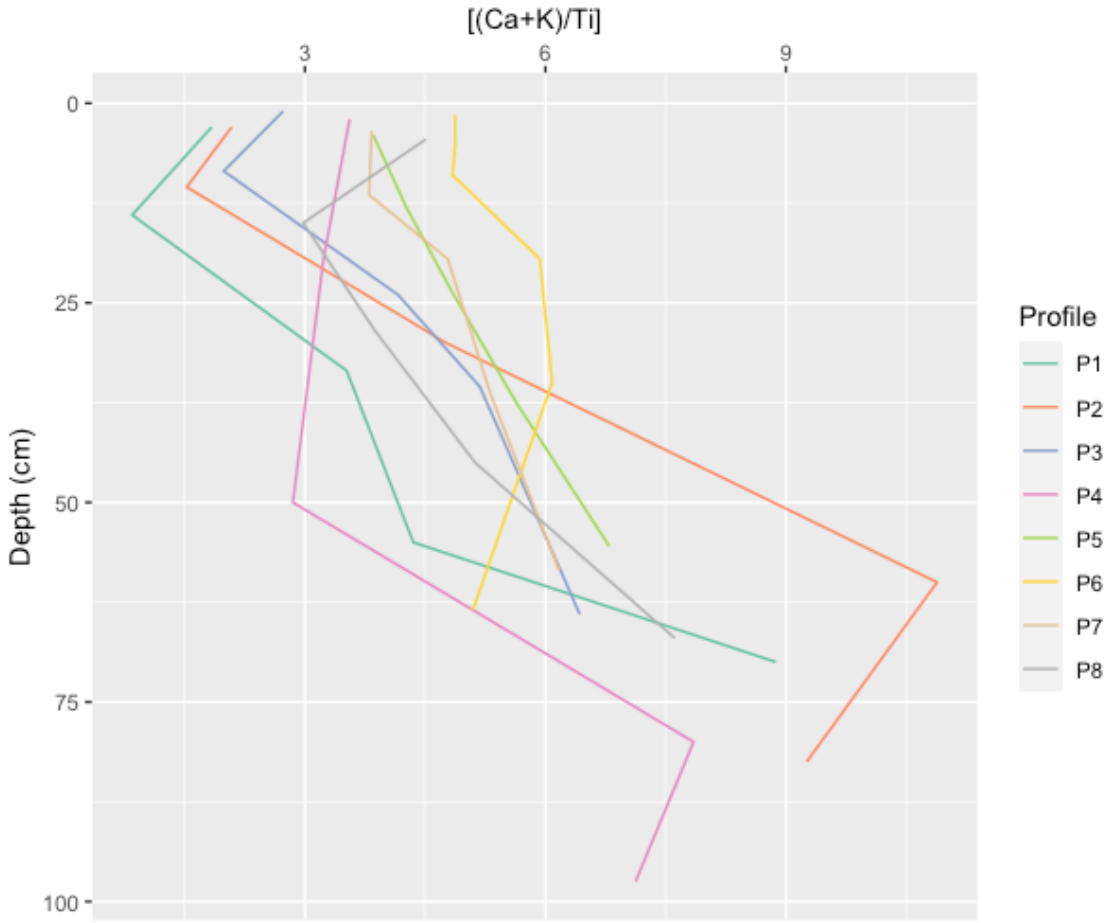

Figure 28: (Ca+K)/Ti-Index as a function of depth in soil profiles P1–P8.

4.3.5 [(Na+K)/Ti] Index

This index shows a similar behavior as the [(NA+K)/TI] ratio. The index ranges from 2.3 (P1, 6–22 cm, AhE horizon) to 18.1 (P2, 45–75 cm, BE horizon) with a mean of 8.5 and a median of 8.2. The highest mean index per site was calculated for soil profile P2 and the lowest for P8.

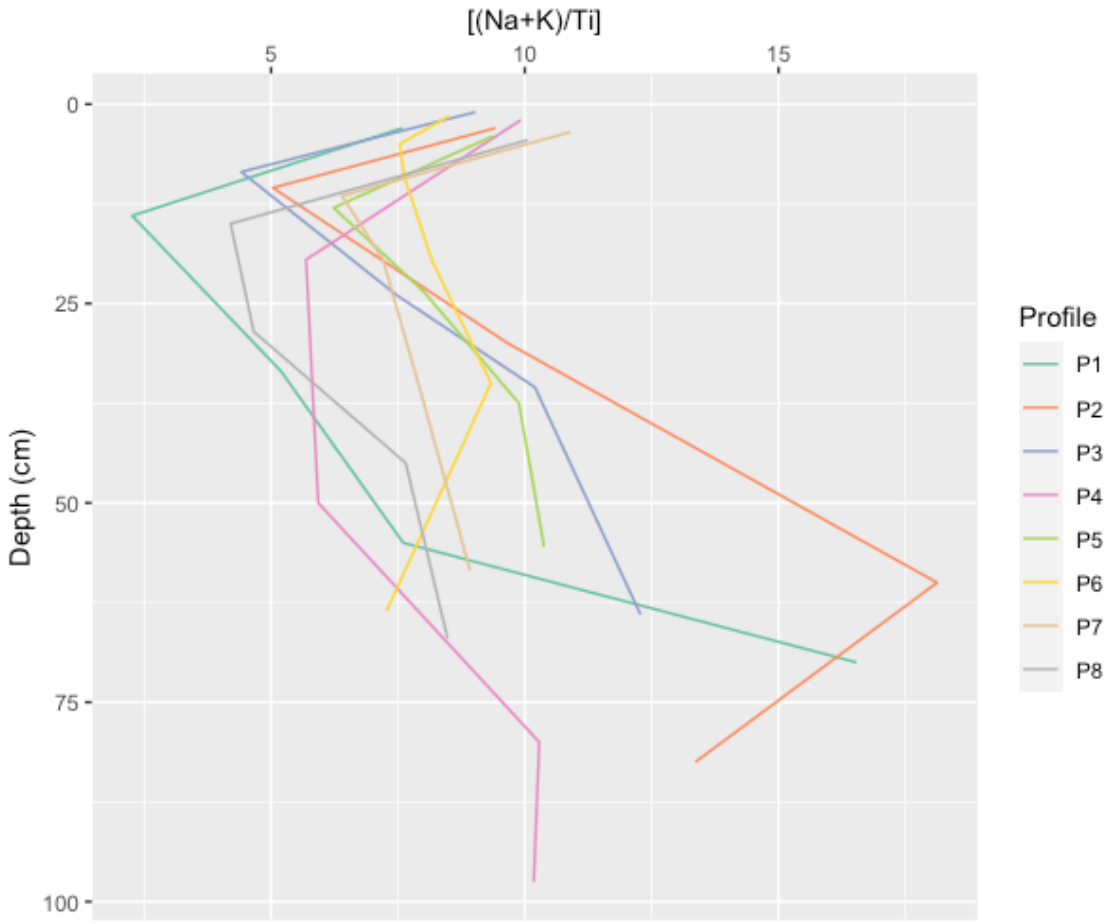

Figure 29: (Na+K)/Ti-Index as a function of depth in soil profiles P1–P8.

4.4 LUMINESCENCE

4.4.1 INFRARED STIMULATED LUMINESCENCE

The lowest counts of Infrared Stimulated Luminescence (IRSL) were found in the uppermost horizons (see Figure 30). The measurements for the soil profiles P1, P2, P3, P4, P5 and P8 showed low values in the uppermost layer, an increase with depth, and then again lower values in the deepest measurement. For soil profiles P6 and P7 a continuous increase in net counts was detected.

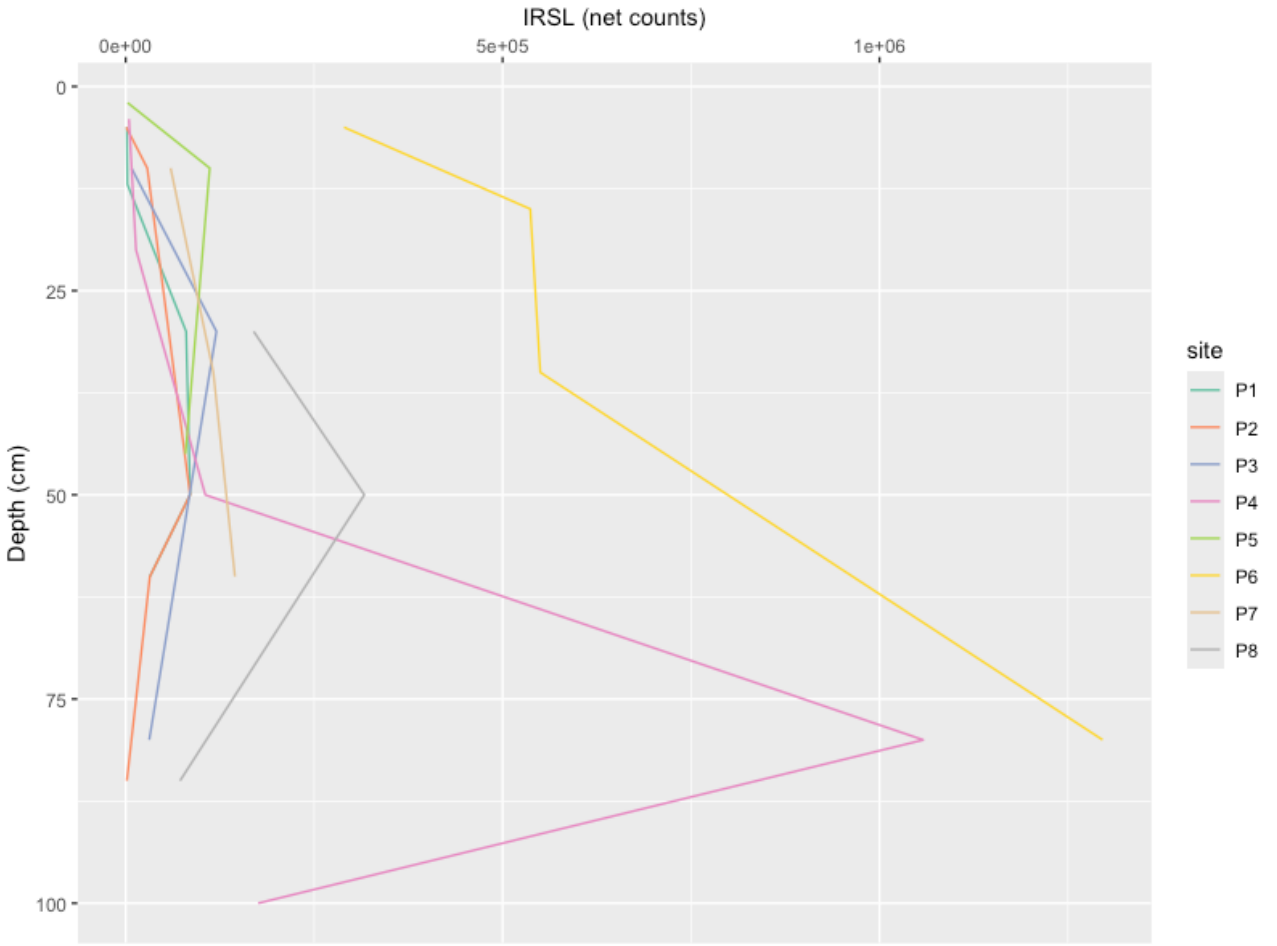

Figure 30: Infrared Stimulated Luminescence (IRSL) as a function of depth in soil profiles P1–P8.

4.4.2 Optical Stimulated Luminescence

The measurements of the different depths with Optical Stimulated Luminescence (OSL) revealed a similar behavior as with IRSL. The OSL net counts in soil profiles P6 and P7 show a continuous increase with depth. While in the other soil profiles (P1, P2, P3, P4, P5 and P8) an increase in net counts can be observed first, followed by a decrease at greater depths (see Figure 31).

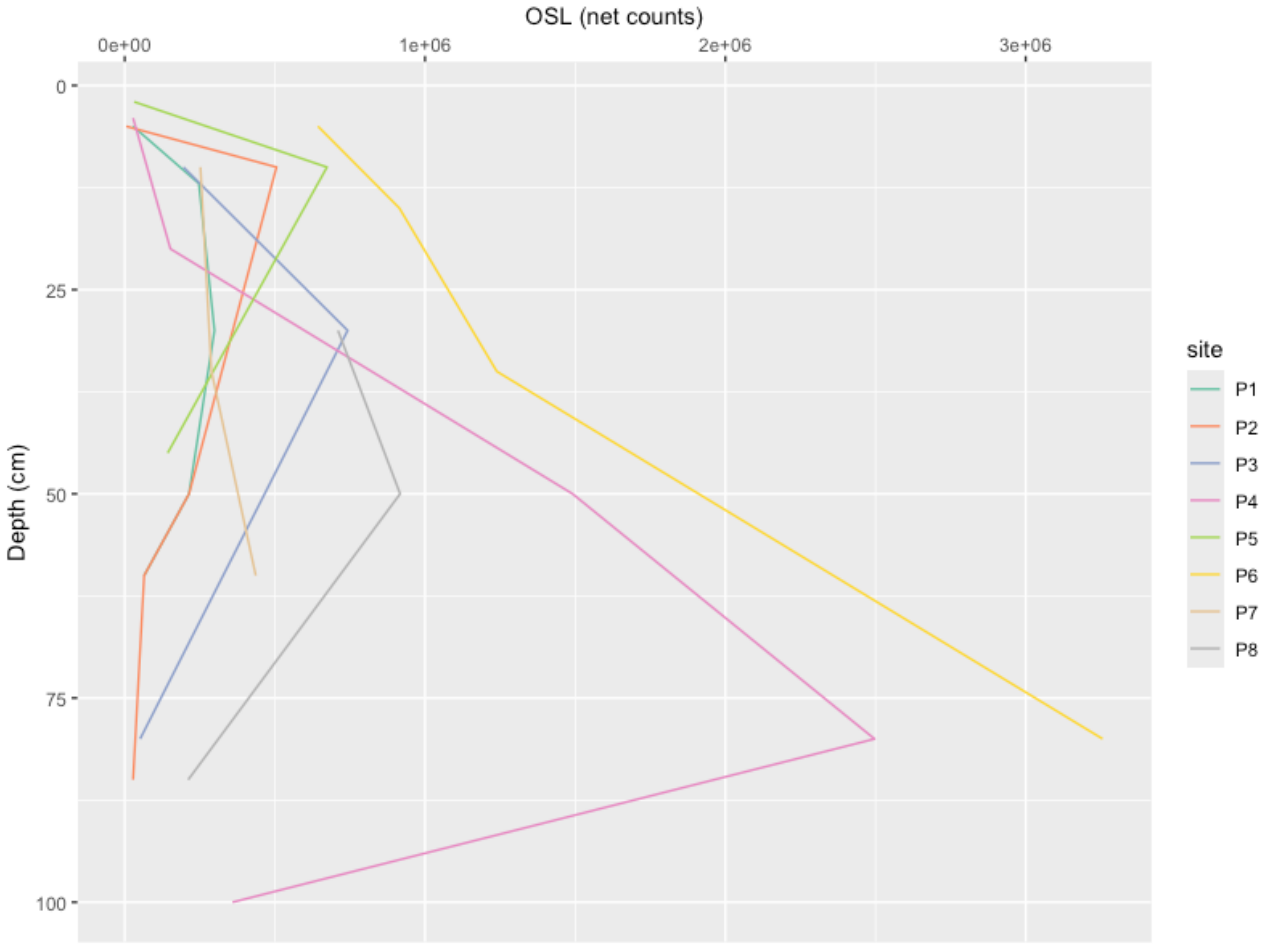

Figure 31: Optical Stimulated Luminescence (OSL) as a function of depth in soil profiles P1–P8.

4.4.3 IRSL/OSL

The ratio of IRSL to OSL ranged from 0.009 to 0.608. The ratios showed a trend of increasing with depth in soil profiles P3 and P5(see Figure 32). Furthermore, the soil profiles P1, P4 and P8 also have low ratios in the topmost layer and high ratios in the lowermost layer, but they do not increase continuously. However, the IRSL to OSL ratio in soil profiles P2, P6 and P7 gave an no clear trend with depth.

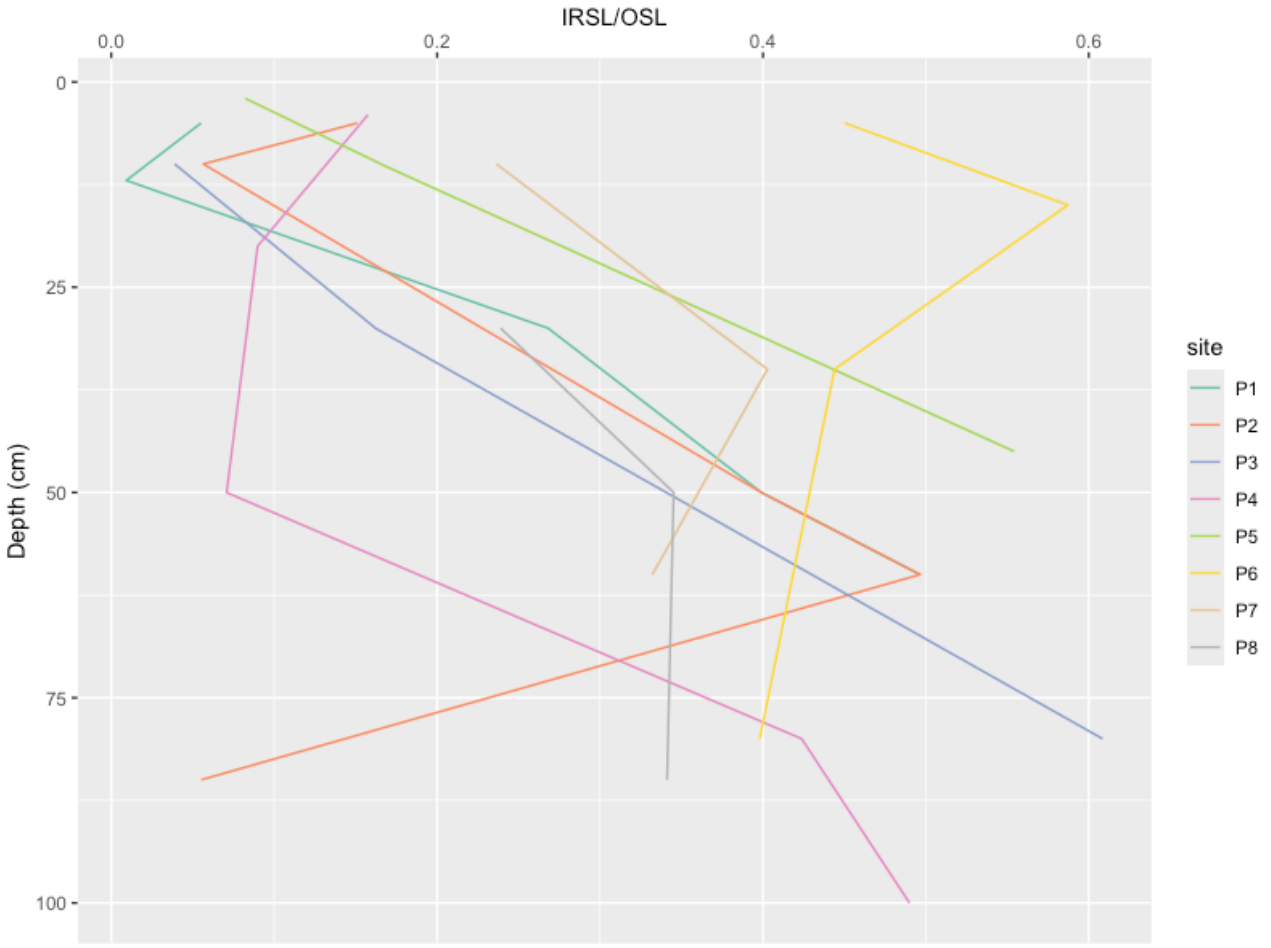

Figure 32: The ratio of IRSL to OSL (IRSL/OSL) as a function of depth in soil profiles P1–P8.

4.5 $^{239+240}$Pu

4.5.1 $^{239+240}$Pu ACTIVITIES

Measured $^{239+240}$Pu activities ranged from the detection limit up to 5.80 Bq kg^{-1} with a mean of 0.54 Bq kg^{-1} ± 0.95 (sd) with a median of 0.11 Bq kg^{-1}. Most samples (174 out of 176) exhibited the detectable levels of $^{239+240}$Pu. However, Pu activities of two samples (P4-11 and P5-11) were below the detection limit of 0.001 Bq kg^{-1}. For further calculations these six values were substituted with the method recommended by Verbovšek (2011), where the limit of detection (LOD) is divided through the square root of 2.

Equation 18: Substitution method for parameters below the limit of detection.

$$x = LOD/\sqrt{2}$$

x = substitution for values < LOD

LOD = Limit of detection

Pu activity normally decreased with increasing soil depth. At profile site P2, there was an increase in Pu activity within the 5–10 cm depth increment compared to the overlying increment. At profile site P5, while an increase in Pu activity was observed within the 5–10 cm depth increment, this increase did not reach statistical significance. Analysis of profile site P3 revealed no significant variation in Pu activity between the 5–10 cm and 10–15 cm depth increments. And in profile sites P4, P5 and P7 was no significant difference between the 10–15 cm and 15–20 cm depth increments although there was a slight decrease in average Pu activity with depth. The highest Pu activity was measured in the uppermost layer at profile sites P1 and P6, the lowest in the lowermost sampling depth at profile sites P1 and P2

AT the reference site R1 the average Pu activity was decreasing with depth. At reference site R2 the Pu activity showed a small increase from the 0–5 to the 5–10 cm depth increment.

The measured ^{240}Pu/^{239}Pu atomic ratios vary from 0.0006 to 0.3419 with an average of 0.1853 and a median of 0.1906. A comparison of the ^{240}Pu/^{239}Pu atomic ratios of the samples with the known global fallout of 0.180 ± 0.014 (Kelley *et al.* 1999) showed that the Pu source can be explained as FRN. The source can thus be mainly attributed to tests with nuclear weapons and compared with the reference year 1963.

4.5.2 $^{239+240}$Pu INVENTORIES

For each sampling site and depth increment the average $^{239+240}$Pu inventory as well as the average cumulative $^{239+240}$Pu inventory was calculated (see Table 4). The $^{239+240}$Pu inventories of all samples varied between 1.30 Bq m^{-2} (P2, 15–20 cm depth) and 48.09 Bq m^{-2} (P8, 5–10 cm depth) with a mean of 21.98 Bq m^{-2} ± 20.11 (sd) and a median of 9.72 Bq m^{-2}. The $^{239+240}$Pu inventories decreased with depth and with distance to the rock escarpment. The depth distribution of the inventories resembled the distribution of the activities (see Figure 33).

The cumulative $^{239+240}$Pu inventories for each site ranged from 29.55 Bq m^{-2} at soil profile site P2 to 114.14 Bq m^{-2} at P8. The highest $^{239+240}$Pu inventories were found in the lower soil profile sites P6 and P8. In contrast, the sites with the lowest $^{239+240}$Pu inventories were P2 and P3. Considering the relative standard deviation, the inventory in the two upper sampling depths at soil profile sites P2–P5 was highly variable (see Figure 33).

Table 4: Average and cumulative $^{239+240}$Pu inventories per depth increment of sampling sites P1–P8 and reference sites R1–R2.

Sampling site	Depth increment cm	Average $^{239+240}$Pu inventory Bq m^{-2}	relative standard deviation Bq m^{-2}	Average cumulative $^{239+240}$Pu inventory Bq m^{-2}	relative standard deviation Bq m^{-2}
P1	0–5	33.63	± 14.40	54.04	± 24.03
	5–10	15.92	± 11.12		
	10–15	3.07	± 1.11		
	15–20	1.41	± 0.60		
P2	0–5	7.35	± 6.11	29.55	± 12.61
	5–10	15.48	± 11.21		
	10–15	5.42	± 4.87		
	15–20	1.30	± 0.89		
P3	0–5	30.52	± 30.60	42.84	± 32.56
	5–10	4.60	± 3.80		
	10–15	5.64	± 5.03		
	15–20	2.08	± 2.44		
P4	0–5	27.51	± 28.39	60.18	± 45.35
	5–10	26.42	± 21.37		
	10–15	4.17	± 1.70		
	15–20	2.07	± 1.43		
P5	0–5	16.08	± 17.09	46.95	± 17.78
	5–10	22.02	± 22.71		
	10–15	4.97	± 2.08		
	15–20	3.88	± 2.75		
P6	0–5	44.37	± 31.03	102.63	± 40.26
	5–10	43.72	± 38.00		

	10–15	9.28	± 7.23		
	15–20	5.25	± 4.37		
P7	0–5	30.26	± 19.81	50.15	± 22.19
	5–10	10.18	± 5.85		
	10–15	5.11	± 1.70		
	15–20	4.60	± 1.22		
P8	0–5	47.05	± 20.20	114.14	± 43.04
	5–10	48.09	± 42.71		
	10–15	12.03	± 2.31		
	15–20	6.96	± 4.94		
R1	0–5	22.11	± 4.01	50.00	± 14.30
	5–10	18.86	± 9.71		
	10–15	7.40	± 6.34		
	15–20	1.64	± 1.24		
R2	0–5	20.07	± 6.64	59.22	± 1.03
	5–10	27.44	± 0.90		
	10–15	6.47	± 0.65		
	15–20	5.24	± 5.85		

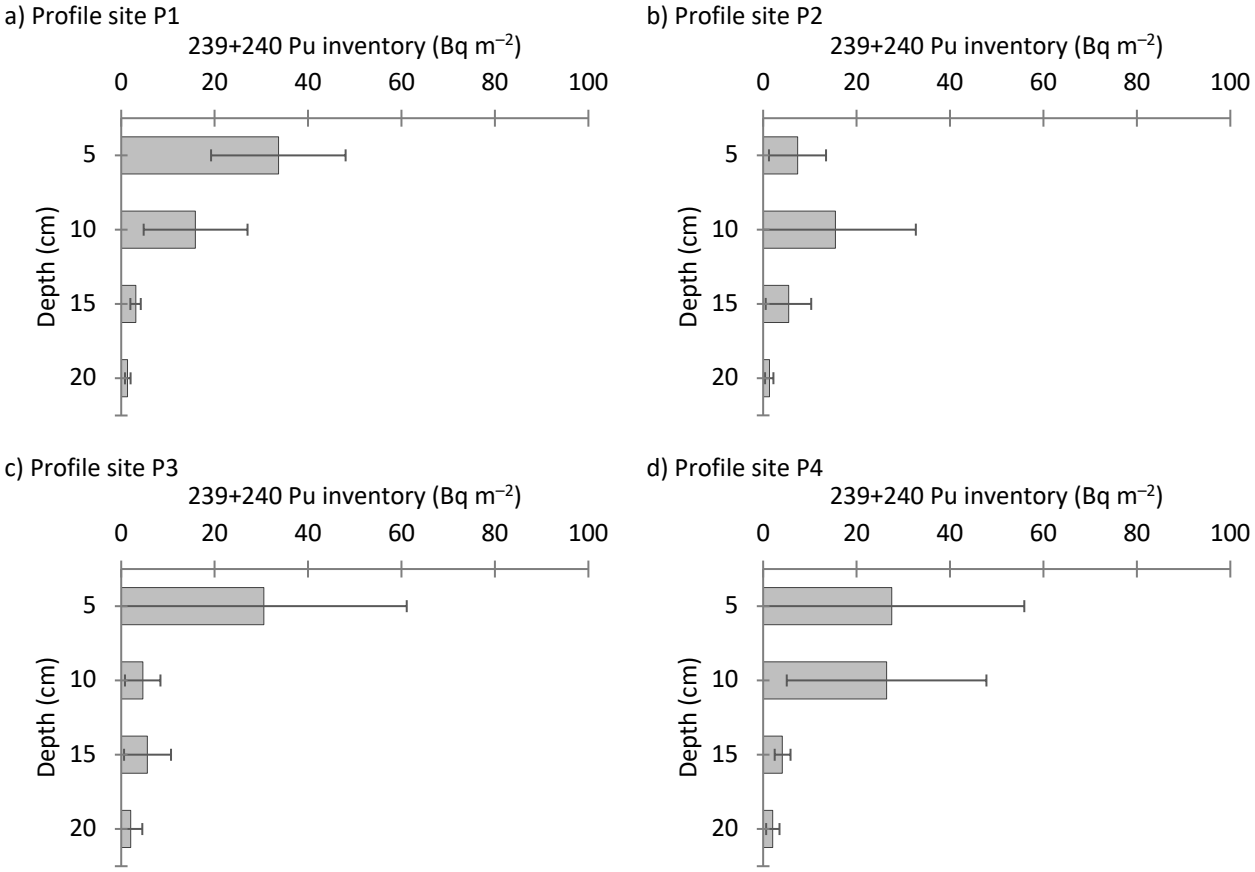

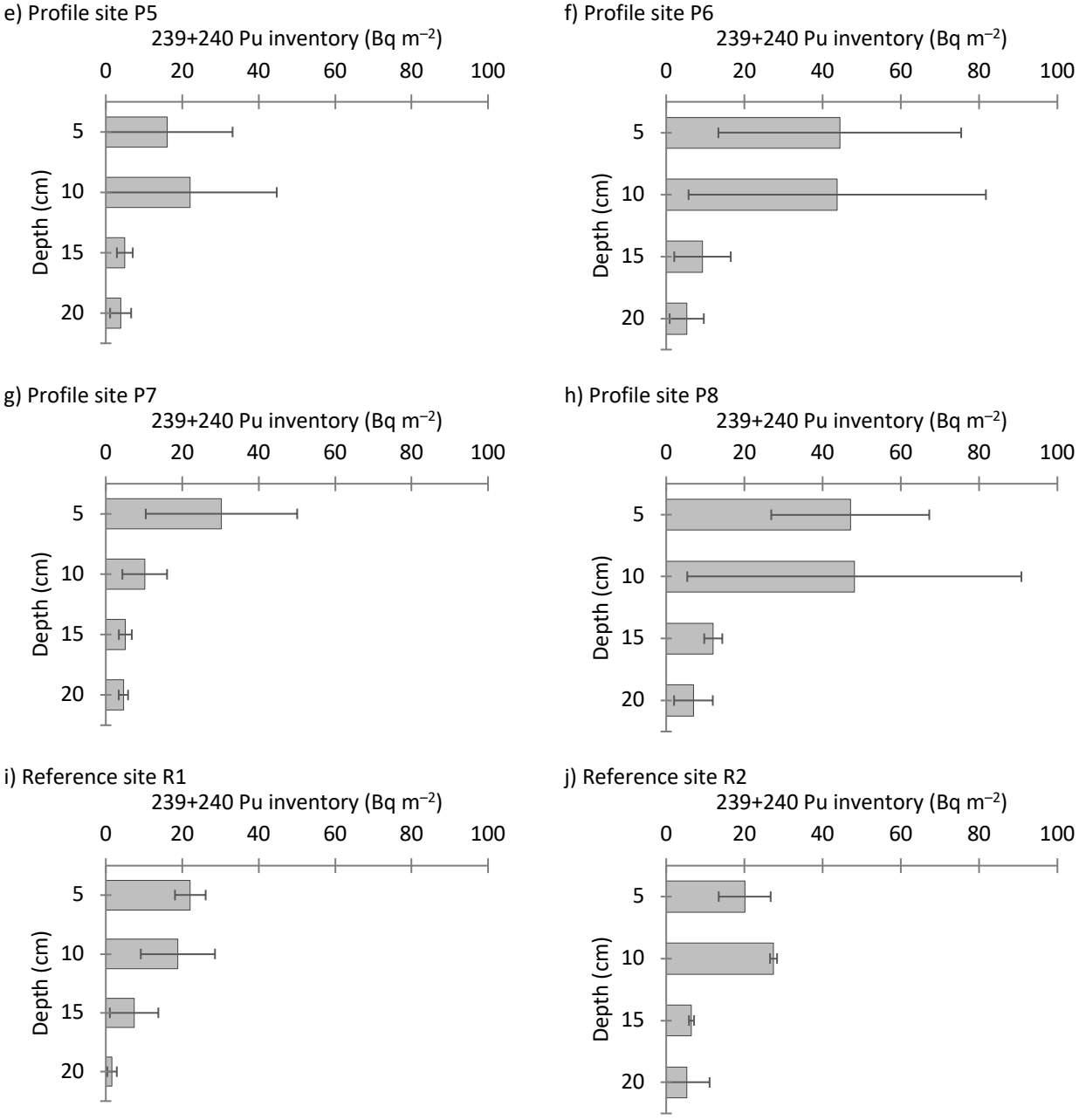

Figure 33: Distribution of $^{239+240}$Pu inventory with depth on eight sampling sites P1–P8 (a – h) and the reference sites R1 and R2 (i – j). The error bars indicate standard deviation.

a) Depth 0–5 cm

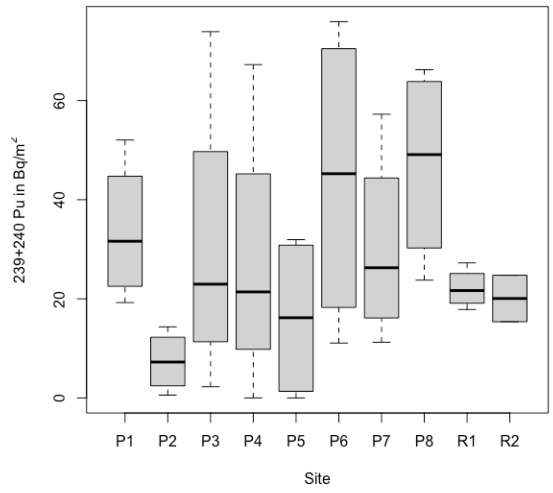

b) Depth 5–10 cm

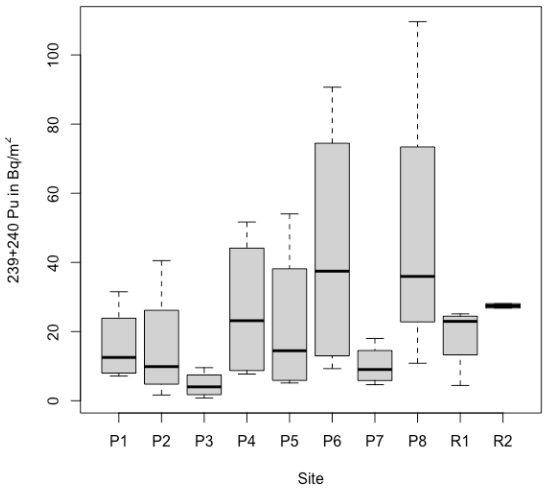

c) Depth 10–15 cm

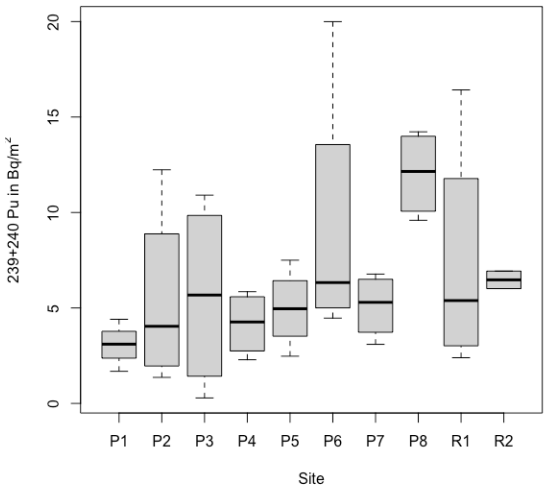

d) Depth 15–20 cm

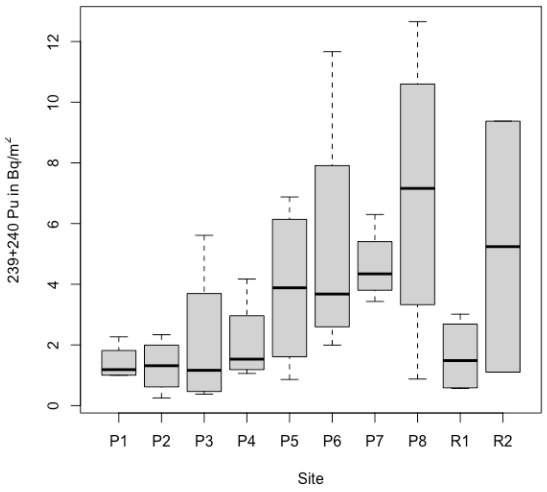

e) Depth 0–20 cm

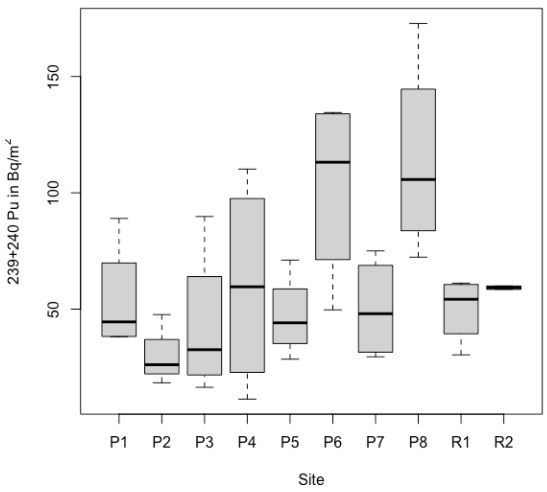

Figure 34: Boxplot of $^{239+240}$Pu inventories of sampling sites P1–P8 and the reference site R1–R2 in four depths a) 0 to 5 cm, b) 5 to 10 cm, c) 10 to 15 cm, d) 15 to 20 cm and the e) average cumulative inventories. The error bars indicate standard deviation.

Almost all inventory samples were normally distributed (Shapiro-Wilk test, confidence level 95%). Only the inventories of reference site R1 in depth of 5–10 cm (p-value = 0.034) and all depths in reference site R2 could not be confirmed as normally distributed.

For depths 0–5 cm, 5–10 cm, 10–15 cm, and 15–20 cm, the p-values were 0.265, 0.205, 0.154 and 0.091, respectively. These results suggest that there are no statistically significant differences in $^{239+240}$Pu inventories between the different sites at individual depth intervals since the p-values are above the typical alpha level of 0.05 (see Figure 34a-d). However, for the sum of $^{239+240}$Pu inventories per site (see Figure 34a) the p-value is 0.009, indicating statistically significant differences between the sites when considering the inventories over all depth intervals.

4.6 SOIL EROSION AND ACCUMULATION RATES

While the calculation methods IM and PDM provide numerical results of soil loss and soil erosion rates directly, MODERN creates depth profiles, where eroded and accumulated layers are estimated. The estimated soil loss and gain (soil redistribution) in cm or yearly rates on the different sampling sites vary, depending on the used calculation model (see Table 5 and Table 6).

The highest erosion rates were found at soil profile site P2. They range from −5.16 t ha^{-1} yr^{-1} ± 3.84 (IM with P factor 1.5) to −8.62 t ha^{-1} yr^{-1} ± 2.44 (MODERN). The highest deposition rates were estimated at site P8. There, the models estimated rates of 4.92 t ha^{-1} yr^{-1} ± 0.19 (MODERN) to 9.47 t ha^{-1} yr^{-1} ± 4.42 (IM). Comparing the soil redistribution rates of MODERN with the results of IM and PDM (see Figure 43), IM with a *P* factor of 1.2 gave the closest values to MODERN.

The models IM and MODERN calculated a soil gain at sites P1, P6 and P8, with the maximum at site P8 with 2.85 cm ± 0.11 (MODERN) resp. 5.31 cm ± 2.43 (IM). On the other hand, a soil loss was estimated at sites P2, P3 and P5, with the maximum loss at site P2 with −5 cm ± 1.41 (MODERN) resp. −3.89 cm ± 2.62 (IM). However, the two models differ at sites P4 and P7, where IM calculates a soil loss and MODERN a soil gain. The soil loss estimations of IM and MODERN correspond well (see Figure 44), but absolute values differ increasingly with a linear regression slope of 0.8149.

Generally, the different Inventory Methods the different methods give relatively similar values. The highest rates were estimated by IM with a *P* factor of 1, both for erosion and deposition. Only at soil profile site P2 MODERN estimates a higher erosion rate.

When calculating the sum of soil redistribution rates of each site with the different models, PDM gives an excess of 1.68 t ha^{-1} yr^{-1} while MODERN gives a deficit of –1.77 t ha^{-1} yr^{-1}. For all IM models, the result is an almost even balance of 0.02–0.03 t ha^{-1} yr^{-1}. The average soil redistribution across all models ranges from –6.92 to 7.7277 t ha^{-1} yr^{-1}.

Table 5: Soil redistribution rates from IM (Lal *et al.* 2013), PDM (Walling & He 1999) and MODERN (Arata *et al.* 2016) in t ha^{-1} yr^{-1}. Negative values indicate soil erosion (loss) and positive values accumulation (gain).

Site	IM								PDM		MODERN		Mean	
			P factor 1		*P factor 1.2*		*P factor 1.5*							
	t ha^{-1} yr^{-1}	sd	t ha^{-1} yr^{-1}	sd	t ha^{-1} yr^{-1}	sd	t ha^{-1} yr^{-1}	sd	t ha^{-1} yr^{-1}	sd	t ha^{-1} yr^{-1}	sd	t ha^{-1} yr^{-1}	sd
P1	0.17	± 4.29	0.18	± 4.37	0.15	± 3.64	0.12	± 2.91	0.14	± 4.02	0.61	± 0.19	0.23	± 8.68
P2	–7.60	± 5.65	–7.74	± 5.75	–6.45	± 4.79	–5.16	± 3.84	–5.94	± 4.01	–8.62	± 2.44	–6.92	± 11.17
P3	–4.74	± 9.62	–4.83	± 9.80	–4.03	± 8.16	–3.22	± 6.53	–3.58	± 7.24	–3.11	± 5.04	–3.92	± 19.38
P4	–1.92	± 12.74	–1.96	± 12.98	–1.63	± 10.82	–1.31	± 8.65	–1.37	± 10.41	1.49	± 5.16	–1.12	± 25.65
P5	–1.53	± 3.90	–1.56	± 3.98	–1.30	± 3.31	–1.04	± 2.65	–1.17	± 3.80	–1.26	± 1.28	–1.31	± 8.07
P6	7	± 5.07	7.13	± 5.16	5.94	± 4.30	4.75	± 3.44	6.53	± 4.73	4.18	± 0.13	5.92	± 10.25
P7	–0.82	± 5.45	–0.83	± 5.55	–0.69	± 4.62	–0.55	± 3.70	–0.75	± 4.64	0.02	± 0.26	–0.60	± 10.82
P8	9.47	± 4.42	9.64	± 4.50	8.04	± 3.75	6.43	± 3.00	7.82	± 3.71	4.92	± 0.19	7.72	± 8.75
Σ	0.03	± 19.88	0.03	± 20.25	0.03	± 16.87	0.02	± 13.5	1.68	± 16.28	–1.77	± 7.73	0.003	± 39.97

Table 6: Soil loss and gain from IM (Lal *et al.* 2013) and MODERN (Arata *et al.* 2016) in cm. Negative values indicate soil erosion (loss) and positive values accumulation (gain).

Site	IM		MODERN		Mean	
	cm	sd	cm	sd	cm	sd
P1	0.09	± 2.64	0.38	± 0.12	0.24	± 2.64
P2	–3.89	± 2.62	–5.00	± 1.41	–4.45	± 2.98
P3	–2.34	± 4.74	–1.75	± 2.84	–2.05	± 5.53
P4	–0.90	± 6.82	0.87	± 3.01	–0.02	± 7.45
P5	–0.77	± 2.49	–0.75	± 0.75	–0.76	± 2.60
P6	4.28	± 3.10	2.61	± 0.08	3.45	± 3.10
P7	–0.49	± 3.04	0.01	± 0.15	–0.24	± 3.04
P8	5.31	± 2.43	2.85	± 0.11	4.08	± 2.43
Σ	1.29	± 10.67	–0.78	± 4.44	0.26	± 11.55

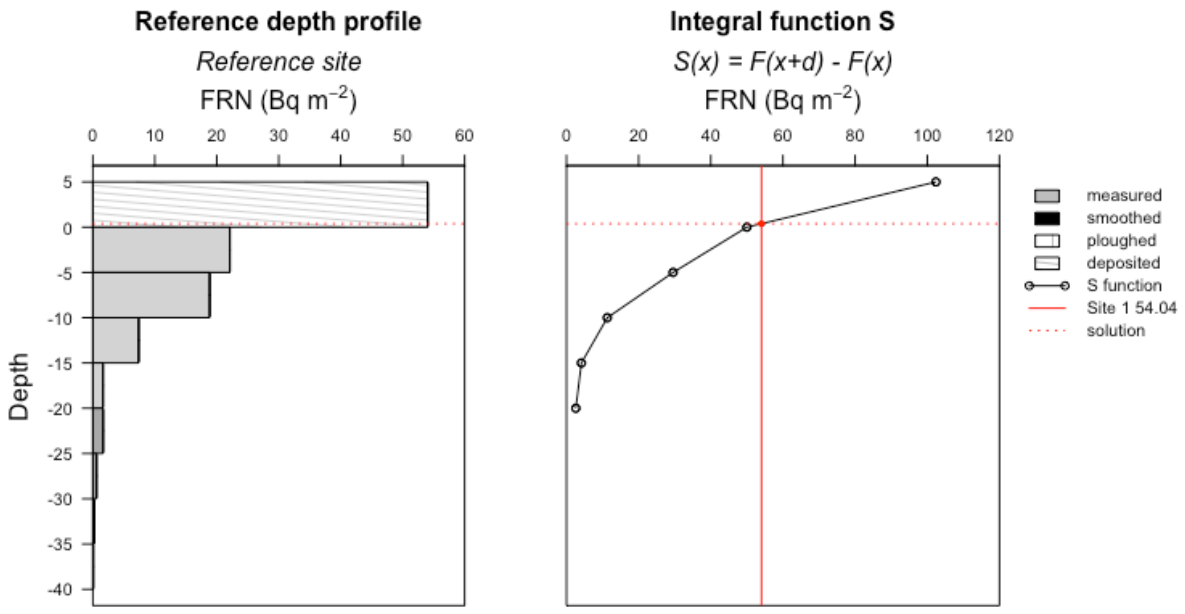

Figure 35: With MODERN created depth profiles of sampling site P1.

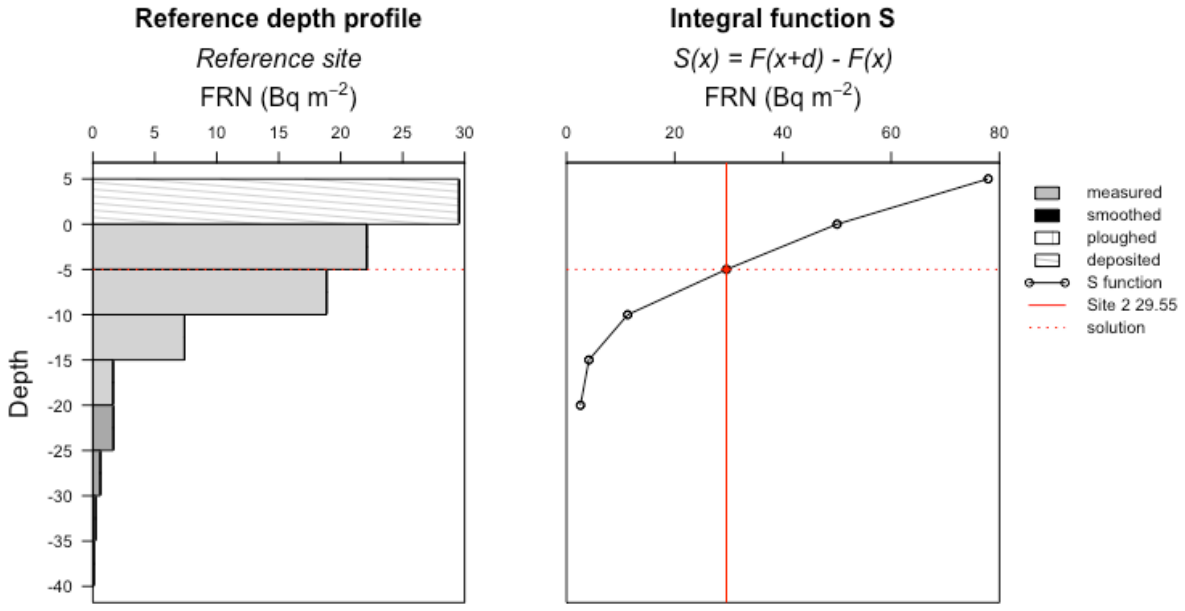

Figure 36: With MODERN created depth profiles of sampling site P2.

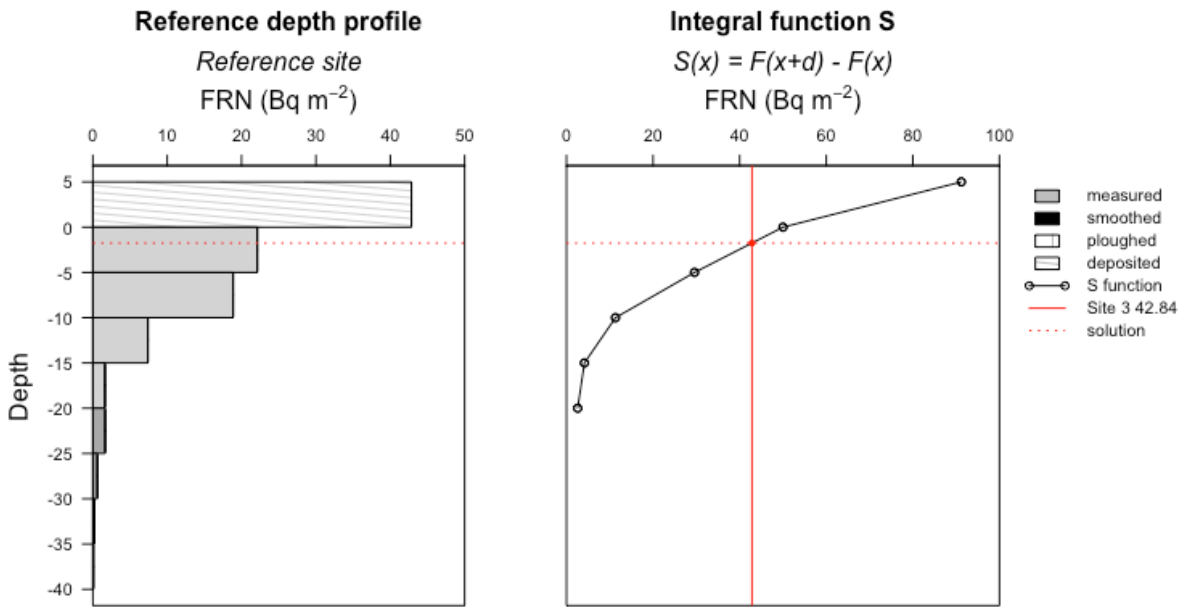

Figure 37: With MODERN created depth profiles of sampling site P3.

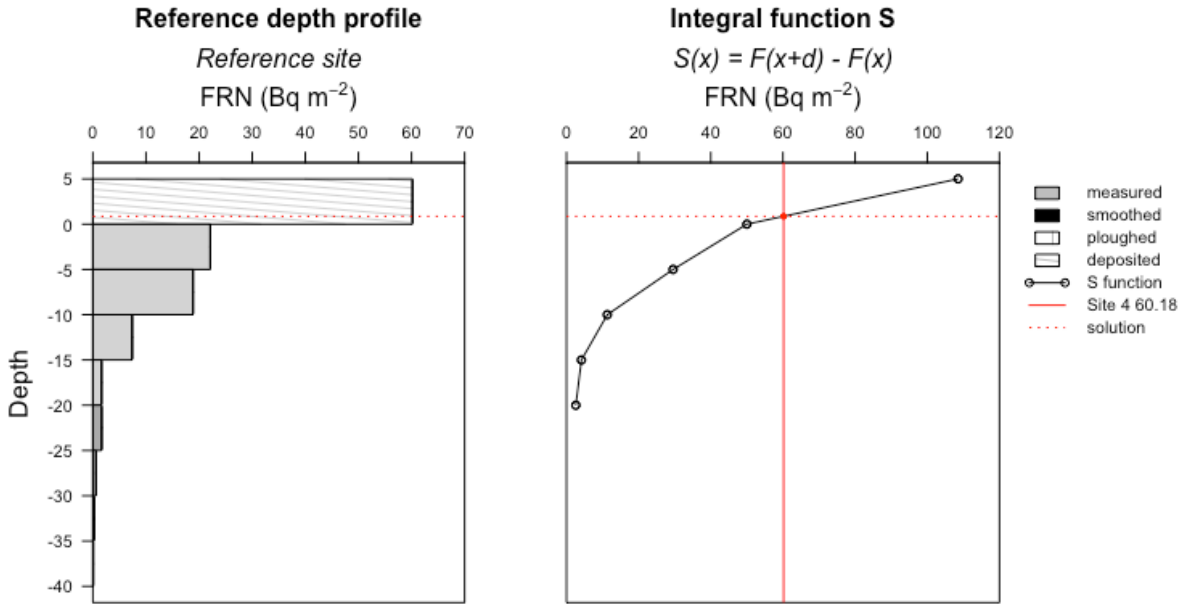

Figure 38: With MODERN created depth profiles of sampling site P4.

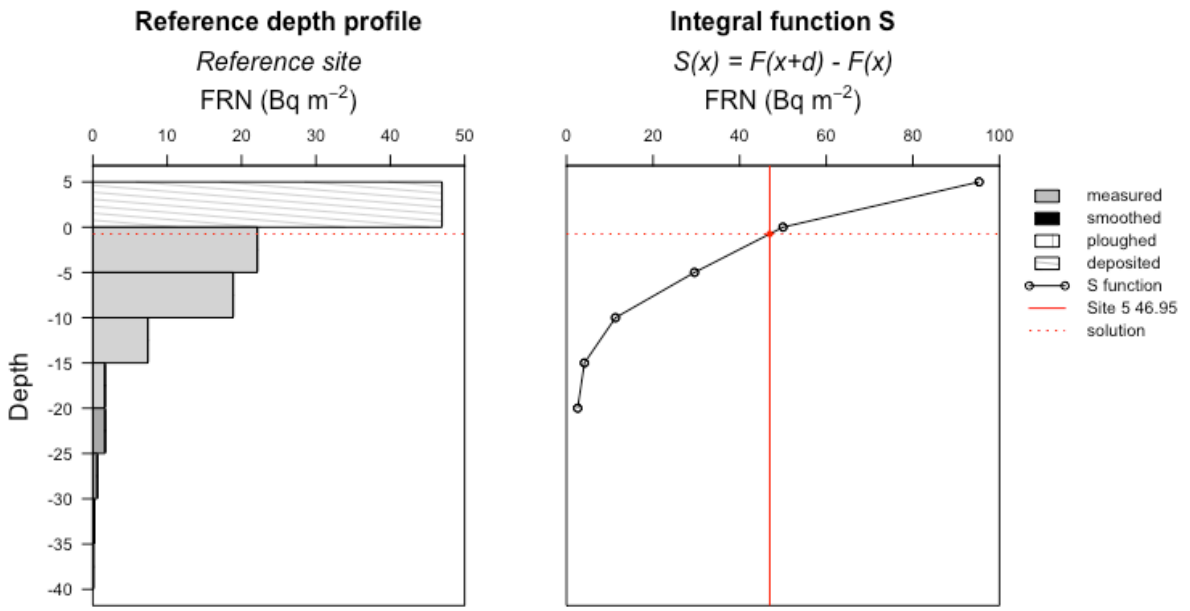

Figure 39: With MODERN created depth profiles of sampling site P5.

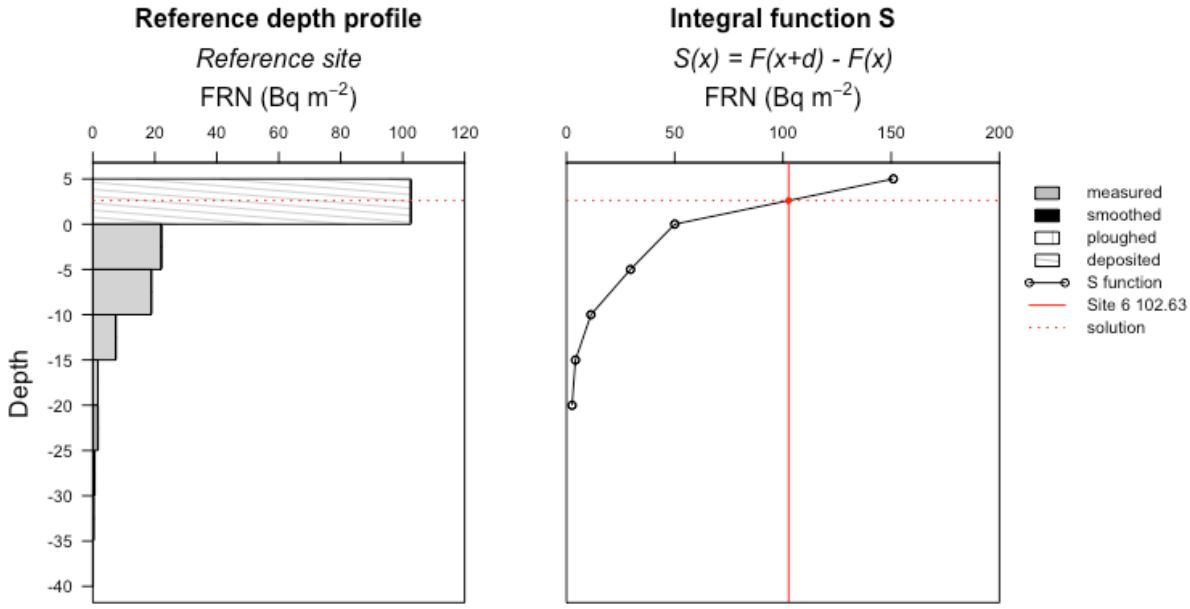

Figure 40: With MODERN created depth profiles of sampling site P6.

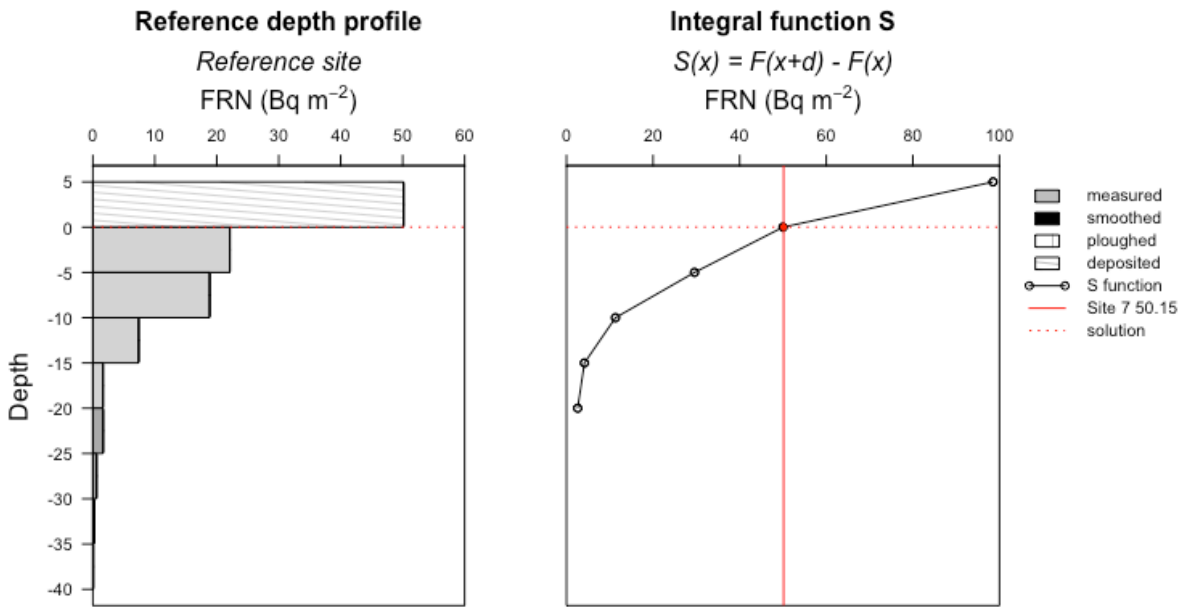

Figure 41: With MODERN created depth profiles of sampling site P7.

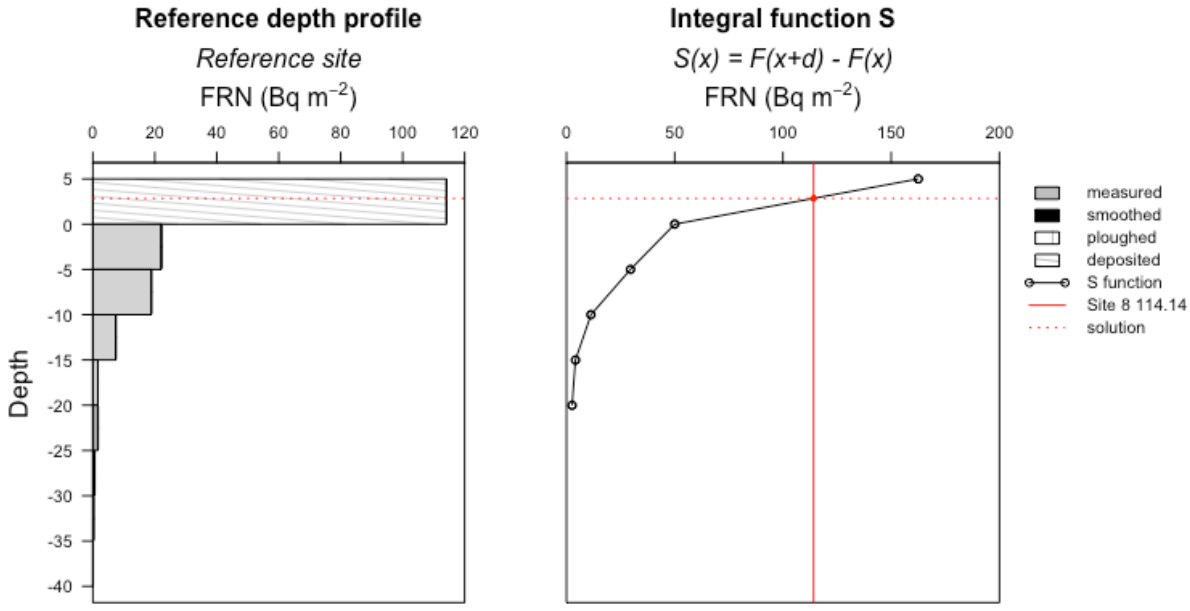

Figure 42: With MODERN created depth profiles of sampling site P8.

a) PDM

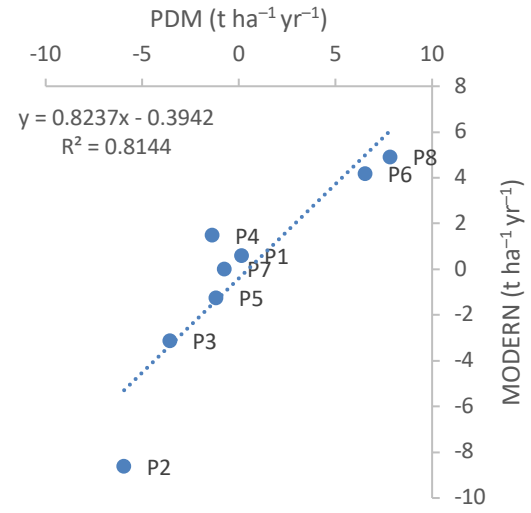

b) IM

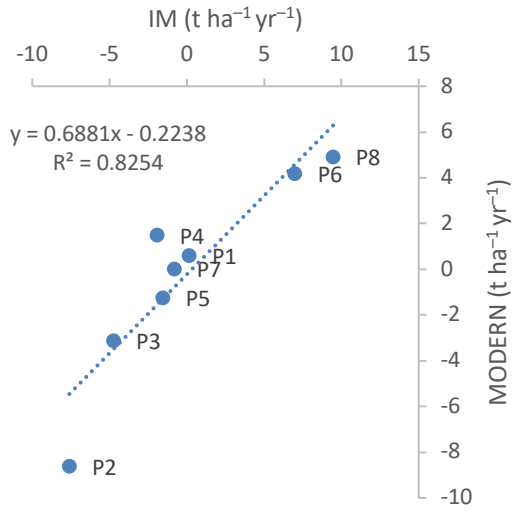

c) IM p factor 1

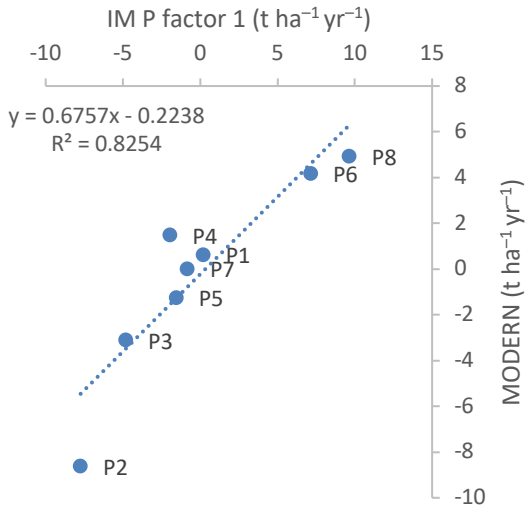

d) IM p factor 1.2

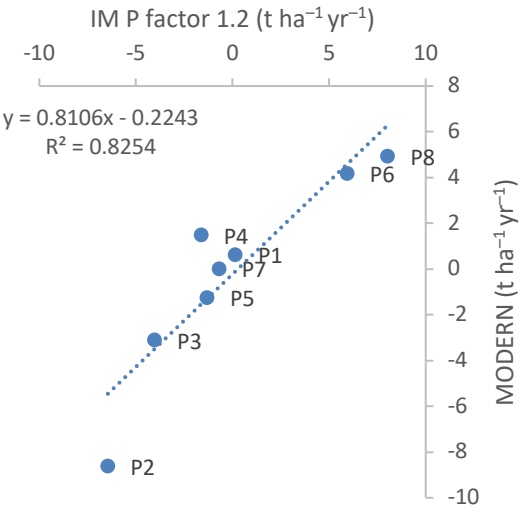

e) IM p factor 1.5

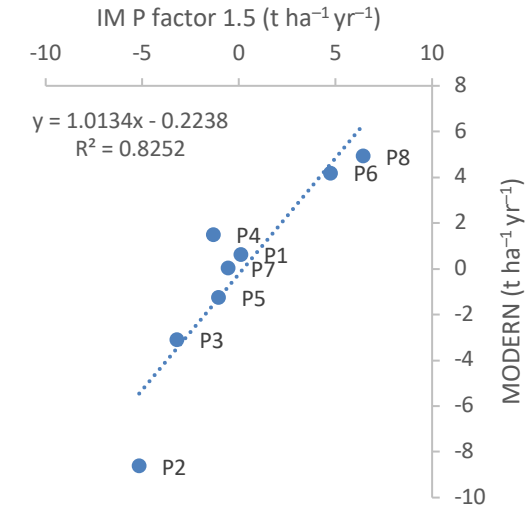

Figure 43: Comparison and linear regression of soil redistribution rates between PDM, IM and MODERN a)–e).

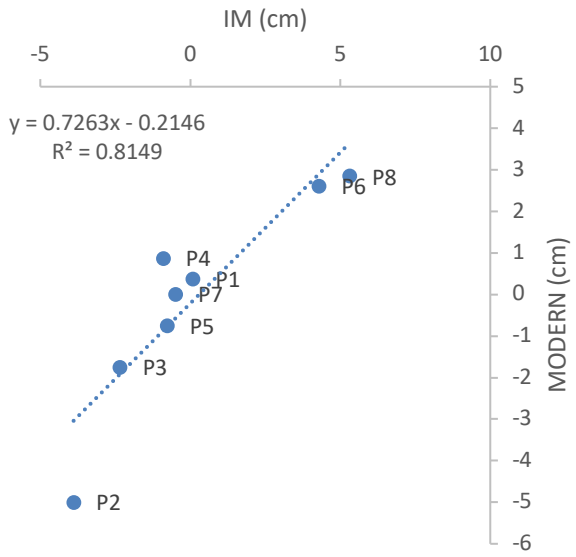

Figure 44: Comparison and linear regression of soil loss between IM and MODERN.

4.7 CORRELATIONS

Many variables correlate with their position on the slope, the altitude of the sites or the distance from the cliffside respectively (see Figure 45). With increasing distance, the average pH increases significantly (correlation 0.72, p-value 0.04). Both the content of clay (correlation 0.84, p-value 0.0086) and silt (correlation 0.61, p-value 0.11) increases with the descent, while the sand content decreases (correlation -0.61, p-value 0.11). The soil organic matter shows also a correlation depending on the position along the slope, (correlation 0.62, p-value 0.1007). But the correlation p-value for silt, sand and soil organic matter is ≤ 0.05 and therefore not significant.

With horizon depth both rock fragment fraction (correlation 0.56, p-value 7.21×10^{-4}) and bulk density (correlation 0.37, p-value 0.04) show a significant positive correlation. For soil organic matter, there are significant correlations with clay content (correlation 0.74, p-value 0.03), iron oxide (correlation 0.84, p-value 0.01) and bulk density (correlation -0.56, p-value 7.74×10^{-4}). And for clay content exists a significant positive correlation also with pH (correlation 0.79, p-value 0.02).

The erosion rates correlate with slope position and grain size distribution. With higher clay (correlation 0.89, p-value 0.003) and silt content (correlation 0.84, p-value 0.009) the deposition rate

increases significantly. With lower sand content (correlation -0.65, p-value 0.08) and with the descent (correlation 0.66, p-value 0.08) the erosion rate is decreases, but with no significant correlation.

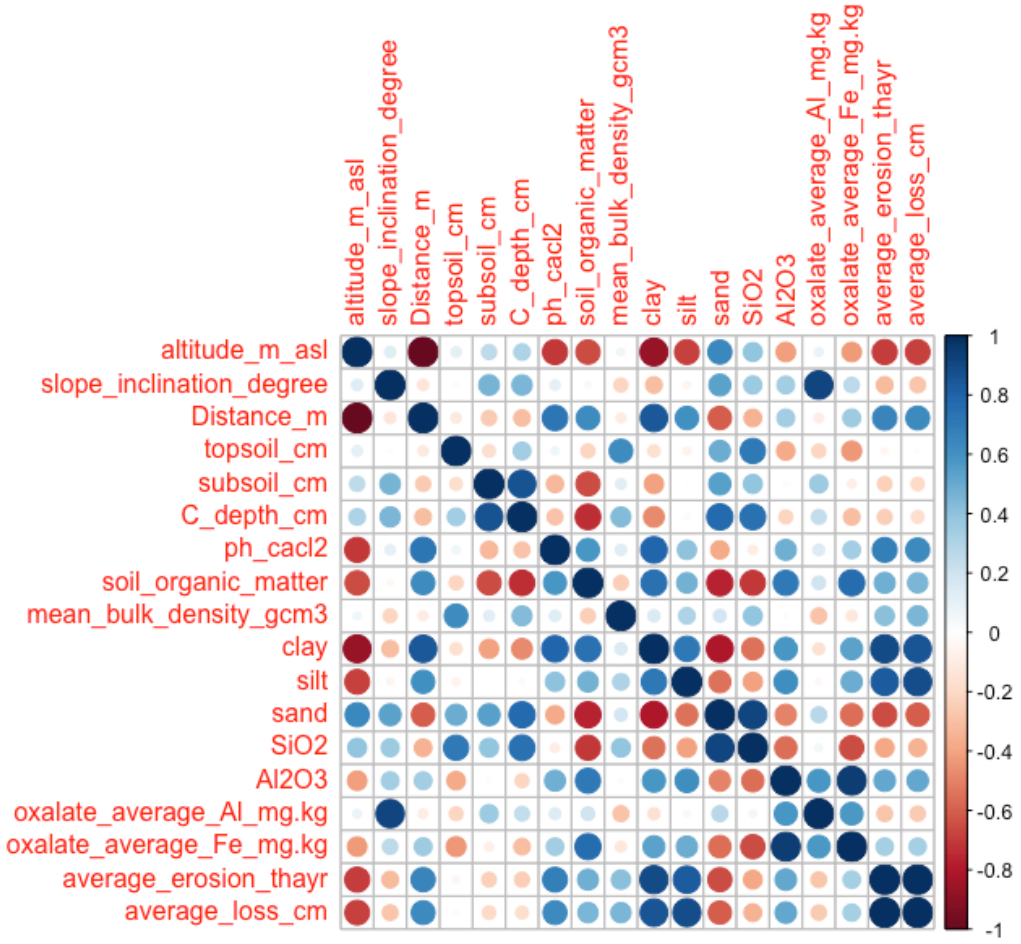

Figure 45: Correlation coefficient matrices showing relationships between properties of the sites of soil profiles P1–P8. The Spearman rank coefficient was applied.

When comparing the parameters within the horizons (see Figure 46). Aluminium oxide (Al_2O_3), iron(III) oxide (Fe_2O_3) and silicon dioxide (SiO_2) correlate with each other (see Appendix 18). The same applies to the correlation between pH, clay content and iron(III) oxide. Also, the amorphous forms of Fe_o and Al_o correlate significantly (correlation 0.5673052, p-value 5.76×10^{-4}). There is a positive correlation between clay content and Al_2O_3 (correlation 0.6890981, p-value 9.23×10^{-6}) and between sand content and SiO2 (correlation 0.702656, p-value 5.14×10^{-6}), which is clear due to the mineral composition of clay and sand. Another expected correlation is with the color, while the

Munsell value correlates with soil organic matter (correlation -0.3671248, p-value 0.0356), Munsell chroma correlates with Al_2O_3 (correlation 0.5623037, p-value 6.60×10^{-4}).

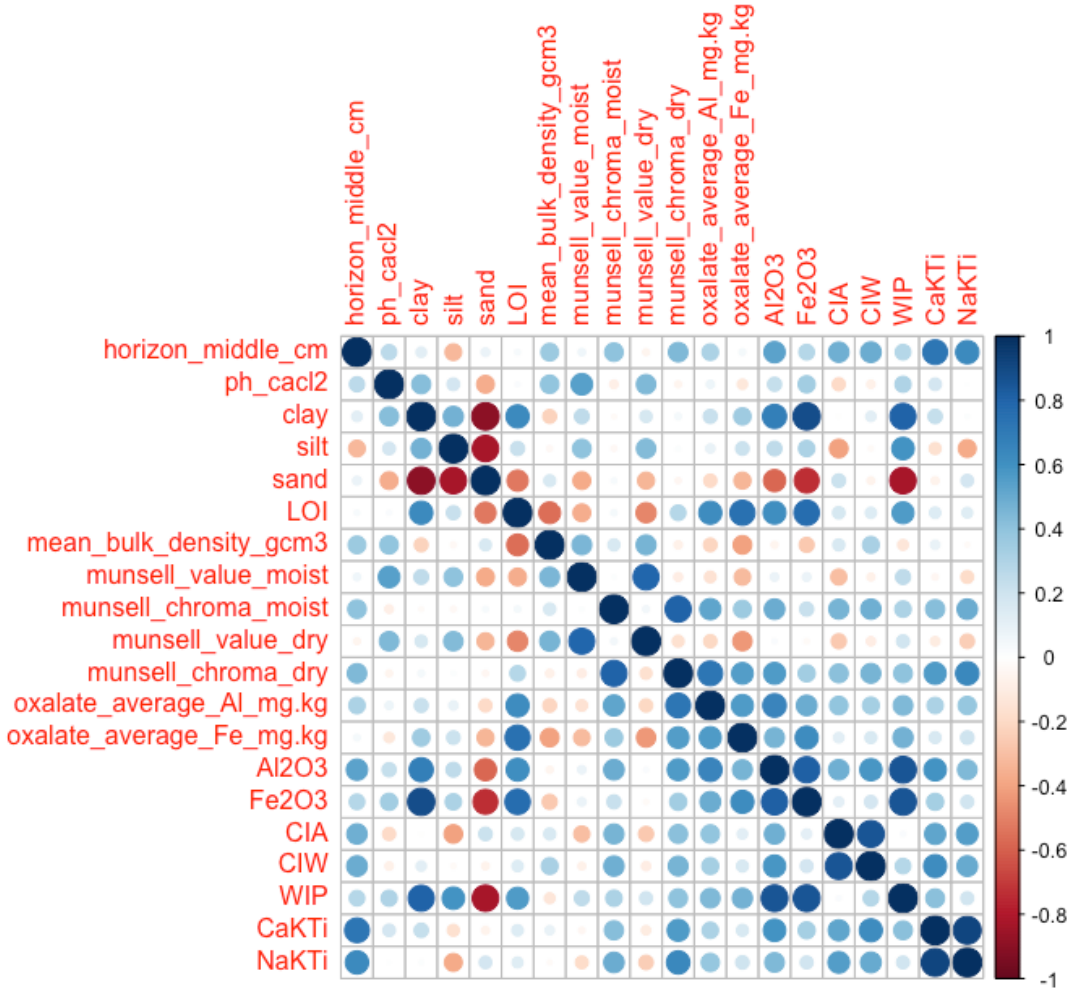

Figure 46: Correlation coefficient matrices showing relationships between properties of soil horizons in soil profiles P1–P8. The Spearman rank coefficient was applied.

5 DISCUSSION

5.1 DISTRIBUTION OF SOIL PROPERTIES

The catena showed a high influence of podzolization processes in the area, as eluvial soil horizons were found in all soil profiles. The distribution of similar horizons across different soil profiles reveals consistency in soil formation processes. But the differences in horizon depths, thickness and composition are showing considerable local variations in soil development stages.

The soilscape (pedochore) (Blume *et al.* 2016) shows a clear vertical zonality of soil development, which can be divided into 5 zones: First Podzols with histic properties on the caprock top, second Podzols along the escarpment with high skeletal fraction, third in upper mid-slope with arenic to loamic Podzols, fourth in lower mid-slope soils with stagnic properties and fifth at the toe-slope soils with gleyic properties

The peat-containing soils on top of the caprock (Histic Podzols) are influenced by the hydrological balance of the poorly draining sandstone. Along the escarpment Podzols with different eluvial and illuvial horizons and rock fragment fractions being higher in the upper slope and lower in the mid-slope (Endoskeletic and Albic Podzols). On the lower slope stagnic horizons (Albic Stagnosol and Stagnic Podzol) highlight the impact of water stagnation on soil development. And at the foot slope the Gleysols are groundwater-dominated.

The soil types and properties are comparable with other studies (Migoń & Kacprzak 2014; Pawlik *et al.* 2013, 2017; Waroszewski *et al.* 2013, 2015b, a). Waroszewski et al. (2015a) described a similar sequence in soil types along the slope with Podzols and Stagnosols. But they found Arenosols and Regosols in the upper slope. Although the soil profiles P1–P4 showed arenic and P3–P4 skeletic properties, these were less dominant. At the foot slope, Waroszewski et al. (2015a) found Planosols and even Cambisols, whereas this study met Gleysols (see Figure 47). In a lateral cross-section Migoń & Kacprzak (2014) found Podzols and Leptosols in a mid-slope position along a 1600 m long and 2–4 m high outcrop at 720–750 m a.s.l. 15–20° slope inclination, which is comparable with soil profile P5.

On mudstones in the central part of the Stołowe Mountains Eutric Cambisols were found on steep slopes and Stagnic Luvisols on level surfaces (Galka *et al.* 2014; Kabala *et al.* 2011; Waroszewski *et*

al. 2015b). Both soil types have the texture of loam and silt loam. On sandstones, in several varieties depending on slope morphology, regolith texture and drainage.

Podzols dominate with sandy and sandy loam textures. (Galka *et al.* 2014; Kabala *et al.* 2011; Waroszewski *et al.* 2015b). Pawlik *et al.* (2013) found shallow Cambisols on the steep slopes at the nearby Mount Rogowa Kopa with a soil texture of loam and silt loam in the Bw horizon and sandy loam to clay loam in the BC and C horizons. The fine earth contains ca. 15 % clay in the upper horizons, but in lowermost horizons clay more than 30%. There he documented redoximorphic features from periodical excess of water due to throughflow and limited permeability of bedrock. Waroszewski *et al.* (Waroszewski *et al.* 2015a) Cambisols that prevail on mudstones have a silt loam texture,

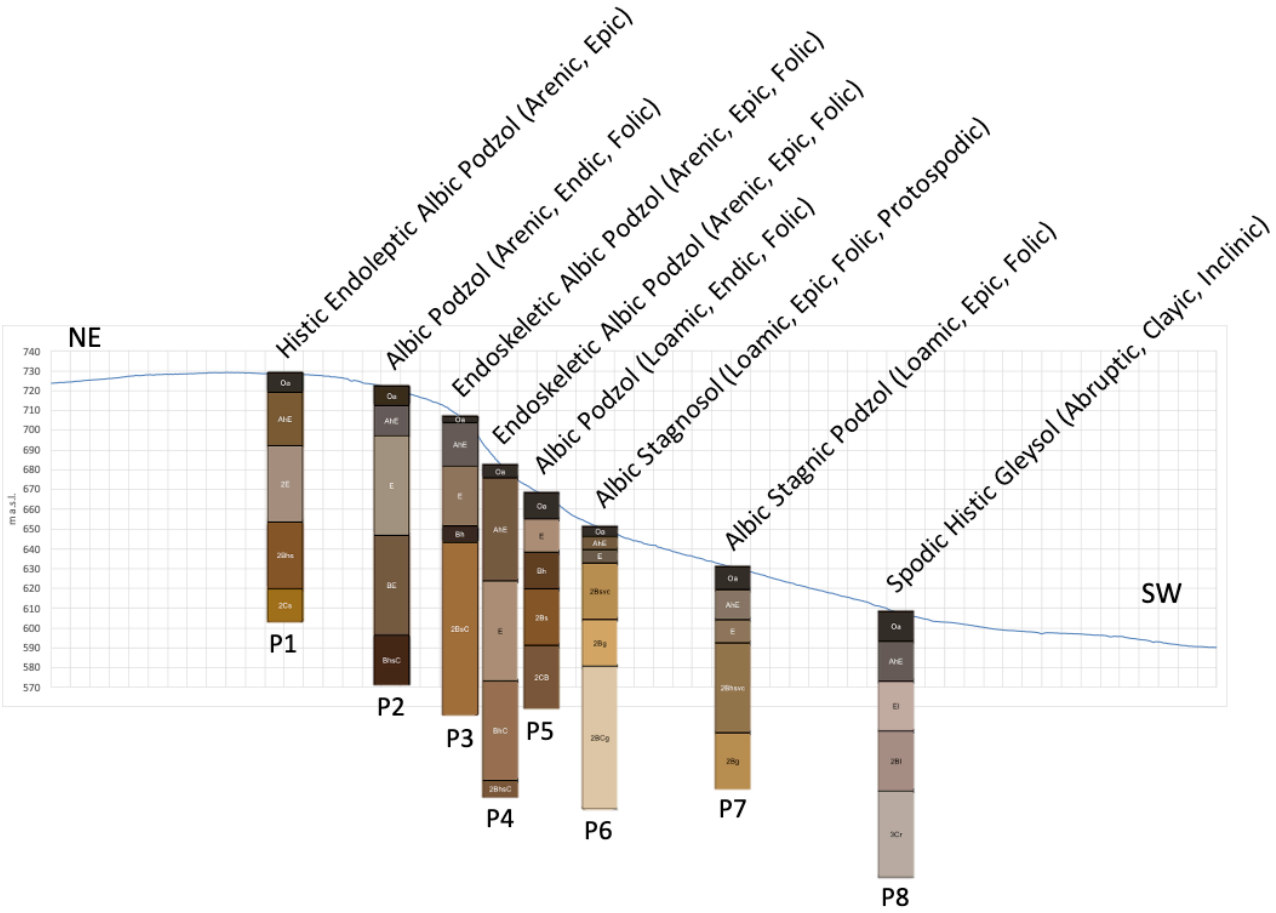

Figure 47: Relief cross-section with relative position of soil profiles P1–P8 at the southwestern slope of Urwisko Batarowskie (relief height exaggerated 2:1, soil profiles are not in scale).

In most horizons a very low pH was measured (2.6–4.1), which is consistent with the formation of Podzols (Lundström *et al.* 2000; Sauer *et al.* 2007). Similarly low pH values (2.7–5.6) were found by various studies in the region (Drewnik 2006; Migoń & Kacprzak 2014; Waroszewski *et al.* 2013, 2015a). An exception is the increase in pH in soil profile P8 at depth of 21 cm. Pawlik *et al.* (2013) found a similar situation with a significant increase in soil pH around or below the depth of 50 cm in the Cr horizons at the foot of the slope in the Stołowe Mountains. Although they did not observe free carbonates in the fine earth, calcium carbonate did occur in the mudstone beds or in the rock clasts. The carbonate-rich material indicates a relatively small degree of chemical weathering, as the lower limit of the B horizon is thought to be the depth of carbonate leaching (Schaetzl & Anderson 2005).

Along the catena organic litter horizons of 12–18 cm and organo-mineral horizons of 4–31 cm thickness were measured. The soil organic matter content of up to 53 % in Oa horizons and 1.5–5.7 % in Ah horizons is comparable to humus rich Ah horizons which reach up to 30% in forest soils (Jahn 1989; Jamroz *et al.* 2014; Pawlik *et al.* 2013). In peatland soils in the Stołowe Mountains Bogacz (2018) found organic horizons with a depth of 30–55 cm, which is comparable with the thickness of O and A horizons (30 cm) in soil profile P1. percentage of humus varies considerably. Differences in thickness of organic horizons are due to differences in accumulation or inhibited degradation of collected litter, which can be caused by topographic situation (Pawlik *et al.* 2013).

Strictly speaking, only the Oa horizons of soil profiles P1, P7 and P8 count as Oa according to the WRB (IUSS Working Group WRB 2022). The Oa horizons of the other soil profiles have less than 30 % organic material and would therefore count as Ah horizons.

5.2 Lithological Discontinuities

Along the whole catena, a high sand and SiO_2 content was found in the near-surface mineral horizons. The soil formation processes are therefore strongly influenced by the autochthonous sandstone in the upper sampling sites and probably allochthonous sandy cover material in the mid-slope and lower slope sites. Only in the lowermost soil profile the parent material of the fine-grained heterolithic complex was found, which is probably a mudstone. Besides the higher clay content, the lowermost horizon in soil Profile P8 also shows the highest bulk density, which indicates a poorly permeable material and a low porosity structure. Comparably, Waroszewski *et al.* (2013) measured

a high bulk density of 1.56–1.69 g cm^{-3} in a BC horizon. But they found no redoximorphic features, while the soil profile P8 showed an accumulation of reduced iron.

Pawlik *et al.* (2013) found Endoleptic or Haplic Cambisols on mudstone at a similar altitude in the Stołowe Mountains. It can be assumed that if the material in soil profile P8 had been more permeable, a Cambisol or a Podzol could have developed instead of a Gleysol.

In many middle altitude mountain ranges in Central Europe a stratified tripartite periglacial cover-bed series with a basal layer, an intermediate layer and an upper layer is present (Kleber *et al.* 2013). The composition, thickness and occurrence of such cover-beds is influenced by periglacial weathering, frost-induces transformations and denudation (Migoń *et al.* 2011). This results in a hillslope morphology with periglacial components (Jahn 1969; Traczyk & Migoń 2003), which can be stony material as possible residuum of Pleistocene solifluction (Phillips *et al.* 2005; Poesen & Lavee 1994) although this can be also caused by tree throw (Pawlik *et al.* 2013; Small *et al.* 1990). Periglacial material from solifluction is often strongly consolidated which leads to a high bulk density (Van Vliet-Lanoë 1998) as found in soil profile P8. In some parts of the Sudetes this series is composited of the basal periglacial layer formed by solifluction (Altermann *et al.* 2008; Waroszewski *et al.* 2013), the intermediate layer cryoturbated transitional zone or periglacial material (Raab & Völkel 2003; Waroszewski *et al.* 2013), and instead of the upper periglacial layer, there is a Holocene cover sand layer (Waroszewski *et al.* 2013). The deposition of these sandy sediment covers are attributed to heavy rainfall events (Waroszewski *et al.* 2013; Wicik 1986). Waroszewski *et al.* (2013, 2015b) found the sandy topsoil material to probably originate from the Holocene and the subsoil material from the Pleistocene. In other regions of the Sudetes no allochthonous three-part periglacial layering was found and discontinuities were rather attributed to in-situ weathering and pedogenetic processes (Migoń & Kacprzak 2014).

The Holocene cover sand layer was encountered in the uppermost 50–100 cm at Urwisko Batorowskie. A lithological discontinuity between the basal layer and the overlying sandy cover was also found by Waroszewski *et al.* (2013). Lithological discontinuities can influence the vertical differentiation of soil properties leading to horizons (Lorz 2008; Lorz *et al.* 2011; Lorz & Phillips 2006; Migoń & Kacprzak 2014; Phillips & Lorz 2008). Indicators for different parent material at horizon boundaries are abrupt changes in gravel and stone content (Waroszewski *et al.* 2015b) or soil texture and bulk density, which may lead to water stagnation (Phillips 2007). On the other hand, water

throughflow influences the properties soil properties through enhanced chemical weathering and washing of finer material, and may lead to contrasts in parent material (Migoń & Kacprzak 2014).. So, changes in parent material are not always easy to recognize.

Lithological discontinuities can lead to different pedogenesis in the different regolith layers (Phillips & Lorz 2008). So, the pedogenic horizons formed by podzolization and lithological stratification often overlap (Kabala 2007; Kabala *et al.* 2008).

Possible evidence of lithological discontinuities were found in all soil profiles except P2. in soil profile P5 the 2Bs horizon inherits a lower rock fragment fraction and lower luminescence than the overlying Bh horizon. In soil profile P7 the 2Bg horizon has a lower rock fragment fraction and sand content but which could also be attributed to leaching processes 2Bhsvc so the designated 2Bg horizon might even be actually the 3Bg horizon.

There are even two discontinuities in soil profile P8. The first one at the boundary between the horizons El and 2Bl, and the second between the horizons 2Bl and 3Cr. Here the discontinuities can be identified on the basis of the jump in rock fragment fraction and grain size distribution towards a fine-grained soil. Furthermore, there was a lower luminescence measured in the lowermost horizon 3Bg.

Through such a catena the regolith variability is examined representatively (Schaetzl & Anderson 2005), but there doesn't have to be a consistent relationship between regolith sequence and slope relief (Migoń & Kacprzak 2014). Migoń & Kacprzak (2014) found a wide variability of parent material in the upper regolith layer and concluded, that the variability of slope covers might even be underestimated and that the regolith characteristics are influenced by topography and bedrock structure which controls groundwater movement.

In soil profiles P6–P8 the higher silt content might indicate cover material which was transported by aeolian long-distance transport (loess). Generally, there is the possibility of loess deposits, as the upper border of loess-like deposits is recognized at about 700–750 m a.s.l. (Waroszewski *et al.* 2013). But a the aeolian entry is considered unlikely at Urwisko Batarowskie for several reasons. Aeolian input is indicated by a surface Increase in Al and K (Waroszewski *et al.* 2016), which was not found here. The inner part of the Sudetes were never covered by aeolian deposits or any aeolian cover has been completely removed (Migoń *et al.* 2011). Migoń & Kacprzak (2014) found the upper regolith to be a product of in-situ weathering. Furthermore, the development of spodic horizons

would be unlikely, as podzolization is typically hindered by loess-enriched parent material (Kleber 1997). In the case of this study, the differences in silt content are rather attributed to the short-range deposition of colluvial material, as the soil profile P6 is also the one with the highest depositional input determined with $^{239+240}$Pu inventories.

A possibility to check for allochthonous input is the use elements as proxies, like Ti, Zr, Nb, Ce or Y, which are considered to be chemically immobile under most near-surface environments (Hutton 1977; Muhs & Benedict 2006; Taylor & McLennan 1985). For example the Ti/Zr ratio as indicator for long distance aeolian input (Dahms & Egli 2016; Kowalska *et al.* 2022), the K/Rb ratio to determine lithogenic sources (Buggle *et al.* 2011) or the Zr/Rb ratio which is used as corresponding proxy for loess (Liu *et al.* 2002).

Silt-enriched layers would be more prone to develop Luvisols while sand cover facilitates the formation of Podzols (Kleber 1997). Although the podzolization process is less distinctive in the soil profile P6, there was no clear evidence of lessivation.

5.3 WEATHERING STATES

For fresh parent material, the CIA value is below 50, while for secondary clay minerals like montmorillonite, the CIA value falls between 75 and 85 (Nesbitt & Young 1982). This applies similarly to the CIW (Harnois 1988). Both indices are measures of the extent of conversion of feldspars to clay minerals (Fedo *et al.* 1995; Maynard *et al.* 1995). The caprock is mainly quartz arenite sandstone, but lower layers are arkosic sandstones. Given that arkosic sandstone contains feldspar, the CIA and CIW could provide insights into the specific weathering dynamics of feldspar minerals within the soil profile, if such layers had been reached, as found by Weber *et al.* (2012).

For soil profiles P1–P8 the CIA and CIW show inverse weathering, with hardly weathered material on the topmost horizons and highly weathered material in the lowermost horizons. This could be only the case if unweathered parent material was continuously deposited on top, for example through aeolian or mass movement processes. In comparison with the other indices, the soil properties described in the field and from the perspective of soil formation this does not seem plausible. Both, CIA, and CIW, use Al_2O_3 as a normalization factor. Due to the podzolization and therefore eluviation and illuviation of aluminium, these indices are probably not applicable as they assume aluminium immobility (Price & Velbel 2003).

The [CaKTi]- and [NaKTi]-index indicate a normal weathering profile. Both show similar behavior with highly weathered surface horizons and decreasing signs of weathering with depth. In soil profiles P2, P4 and P6, the lowermost horizon seems to be more weathered than the one above. WIP shows similar results for soil profiles P1, P3 and P6. There, weathering also increases again in the deepest horizon. According to Price & Velbel (2003) the WIP is the most appropriate index of alteration for application to felsic heterogeneous weathered regolith. These lowermost less weathered horizons are indicators for buried older horizons.

5.4 PODZOLIZATION PROCESSES ALONG THE SLOPE

The variation in thickness of illuvial and eluvial horizons in all soil profiles indicate different rates of leaching affected by local topography, parent material, vegetation, and hydrology (Lundström *et al.* 2000; Musielok *et al.* 2022; Sauer *et al.* 2007). Waroszewski *et al.* (2015b) found indications for lateral podzolization in the Stołowe Mountains. Lateral podzolization is the process of downslope translocation of soil solutions (Sommer *et al.* 2000), also known as intrapedon translocation (Schlichting & Schweikle 1980). This process can occur in different parent material including sandstone (Sommer *et al.* 2001) and was described at several sites in temperate climate (Bower *et al.* 2023; Jankowski 2014). When comparing the altitude, distance or inclination and thickness of illuvial or eluvial horizons, possible lateral podzolization. The soil profile P2 shows profound eluvial horizons and seemingly shallow illuvial horizons, compared to the 24 m lower and 59 m further soil profile P3 with a comparingly shallow eluvial horizon and profound illuvial horizons. The same applies for soil profile P4 and P5 which are 11 m in vertical and 38 m in horizontal distance. However, a correlation between slope position and thickness of illuvial or eluvial horizons was not found. So, there is no evidence for a lateral podzolization over all soil profiles P1 to P8 along the whole catena.

Podzolization can occur through vertical or lateral flux of water transporting organic substances, Al and Fe (Sauer *et al.* 2007; Sommer *et al.* 2001). While the vertical podzolization can be determined within a single soil profile, the lateral podzolization can cause thicker eluvial horizons in the upper slope and thicker illuvial horizons in the lower slope (Jankowski 2014). Despite the differences in pH and grain size distribution in relation to the position along the slope, there is no clear relationship between the thickness of E or Bhs horizons and location (Waroszewski *et al.* 2013).

The displacement ratio of Al_o and Fe_o (Al_o + ½Fe_o) can be used to recognize illuviation processes (McKeague *et al.* 1971). According to IUSS Working Group WRB (2022) a potential definition criteria for a spodic horizon is a subhorizon with a displacement ratio of ≥ 0.5%, which is also ≥ 2 times the ratio of the lowest of all the mineral layers above the spodic horizon. This is only the case in the Bh and 2BsC horizon in soil profile P3 and in the Bh horizon in soil profile P5 (see Figure 48). Waroszewski *et al.* (2013) and Pawlik *et al.* (2023) found similar concentrations in Al_o and Fe_o and ratios in Podzols in the Sudetes. They also had illuvial horizons, that did not exceed 0.5 %. In contrast, Kowalska *et al.* (2021) found about 10 times higher values in Al_o and Fe_o in Podzols. But their study was conducted in the Tatra Mountains, which are about 1'100 m higher than the Stołowe Mountains.

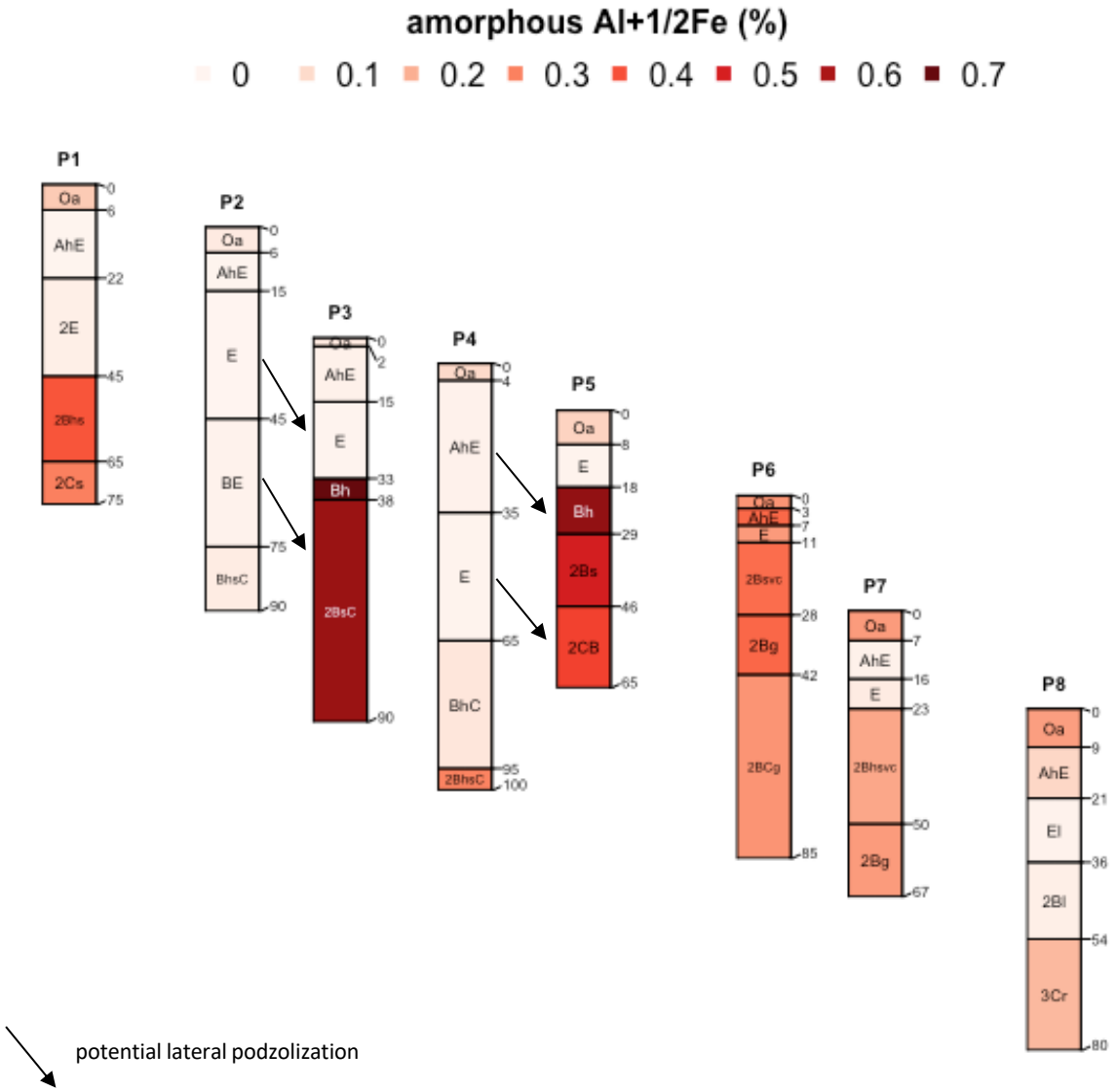

Figure 48: Amorphous Al+1/2Fe in soil profiles P1–P8 in relative topographical position with indicated potential lateral podzolization.

The distribution of oxides are also eligible indicators of pedogenic processes (Jenny 1941). Across all oxides we find a similar distribution and in the same order of magnitude as other studies (Caspari *et al.* 2006; Waroszewski *et al.* 2016). In illuvial horizons higher proportions of Al_2O_3 and Fe_2O_3 were measured compared to eluvial horizons. This supports the assumption that podzolization processes were occurring.

Amorphous inorganic Al and Fe phases such as imogolite, allophane and ferrihydrite potentially stabilize soil organic carbon because of their reactivity and large specific surface area (Eusterhues *et al.* 2005). This may be one of the reasons for the correlation between amorphous Al and Fe and soil organic matter.

5.5 TRACE ELEMENTS AND ANTHROPOGENIC POLLUTION

The distribution of trace elements such as heavy metals can be an indicator for anthropogenic soil pollution (Kabała & Szerszeń 2002; Kowalska *et al.* 2016). In the uppermost horizon in a depth of approximately 0–6 cm values of Cu (4–16 mg kg^{-1}), Pb (40–142 mg kg^{-1}), Zn (9–36 mg kg^{-1}), Cd (0.2–1.3 mg kg^{-1}). These are similar to Glina *et al.* (2017b) who found values of Cu 6–12 mg kg^{-1}, Pb 40–180 mg kg^{-1} , Zn 20–140 mg kg^{-1} and Cd of 0.5–3 mg kg^{-1} in depth increments of 10 cm up to a depth of 0–30 cm. But in the case of our study, the concentrations decrease abruptly in the horizons below by a factor 5 to 10. This might be caused through podzolization processes as the trace element content slightly increases again in the illuvial horizons, such as described by Kowalska *et al.* (2021) who found an accumulation of trace elements in Bs and BsC horizons. Glina *et al.* (2017b) attributed the relatively high concentration of these heavy metals to air deposition and groundwater interflow. Although we can attribute the distribution to superficial air deposition, it shows no indication of groundwater interflow, which should show in the stagnic or gleyic horizons. Since the content of lead is exceeding the content of zinc, this indicates an imbalance of natural proportions between trace elements and anthropogenic accumulation (Waroszewski *et al.* 2009). A possible anthropogenic source of heavy metals is the "black triangle", a region of high industrial activity including mining and metallurgy at the border of Germany, Poland and the Czech Republic which led to high levels of pollution (Markert *et al.* 1996). Many studies attributed the elevated content of heavy metals in the uppermost layers of soils to atmospheric input from this region (Ettler & Mihaljevic 1999; Glina & Bogacz 2013; Karczewska *et al.* 2006; Szopka *et al.* 2013).

Difficulties arose when preparing soil samples and measuring them using XRF for elemental analysis. Due to the hardness of quartz sand, the milling process of the soil samples with 15 min at 30 rps seemed partially insufficient for the subsequent XRF analysis. Although the milling duration as recommended by Locock et al. (2012), a repetition with an additional 15 min was needed to reach the necessary fine grain size. Ultimately, an accuracy of ± 10 % was achieved for calculating the oxides. Other elements like Ba, W und Zr, that have a higher abundance than e.g. Mn or P, may need to be included in the calculation of oxides to reach a higher accuracy.

5.6 RELATIVE DEPOSITION AGES

The relative dating with luminescence indicates the youngest depositional layers at the topmost horizon in each soil profile. While in soil profiles P6 and P7 a continuous covering age can be assumed, in soil profiles P1–P5 and P8 a former surface layer seems to be covered (see Figure 49). Latocha & Migoń (2006) found colluvial depositions in 60–75 cm depth, which they attributed to surface wash or solifluction. The depth of these colluvial depositions would correspond well with the discovery of a former surface layer in 29–95 cm depth at Urwisko Batarowskie. Although solifluction depositions are widely reported in the Sudetes (Jahn 1969; Traczyk & Migoń 2003), the study site probably shows Holocene sandy cover layers (Waroszewski *et al.* 2013) and therefore the colluvial depositions are rather attributable to surface wash. With radiocarbon dating, Latocha & Migoń (2006) received a deposition age of 310–330 years BP ± 30 (calibrated 1480–1650). This might indicate, that the depositions originate in times of higher anthropogenic impact and possibly deforestation (Latocha *et al.* 2016).

The existence of buried older horizons in the Sudetes was also described based on pollen and micromorphological analyses (Waroszewski *et al.* 2012). Waroszewski (2013) found present-day Bh horizons that were surface mineral horizons in the past and now covered by sandy sediments. This leads to the assumption that polygenetic soils are present at Urwisko Batarowskie. Such polygenetic soils on sandstone in the Stołowe Mountains were also found by Kabala (2007).

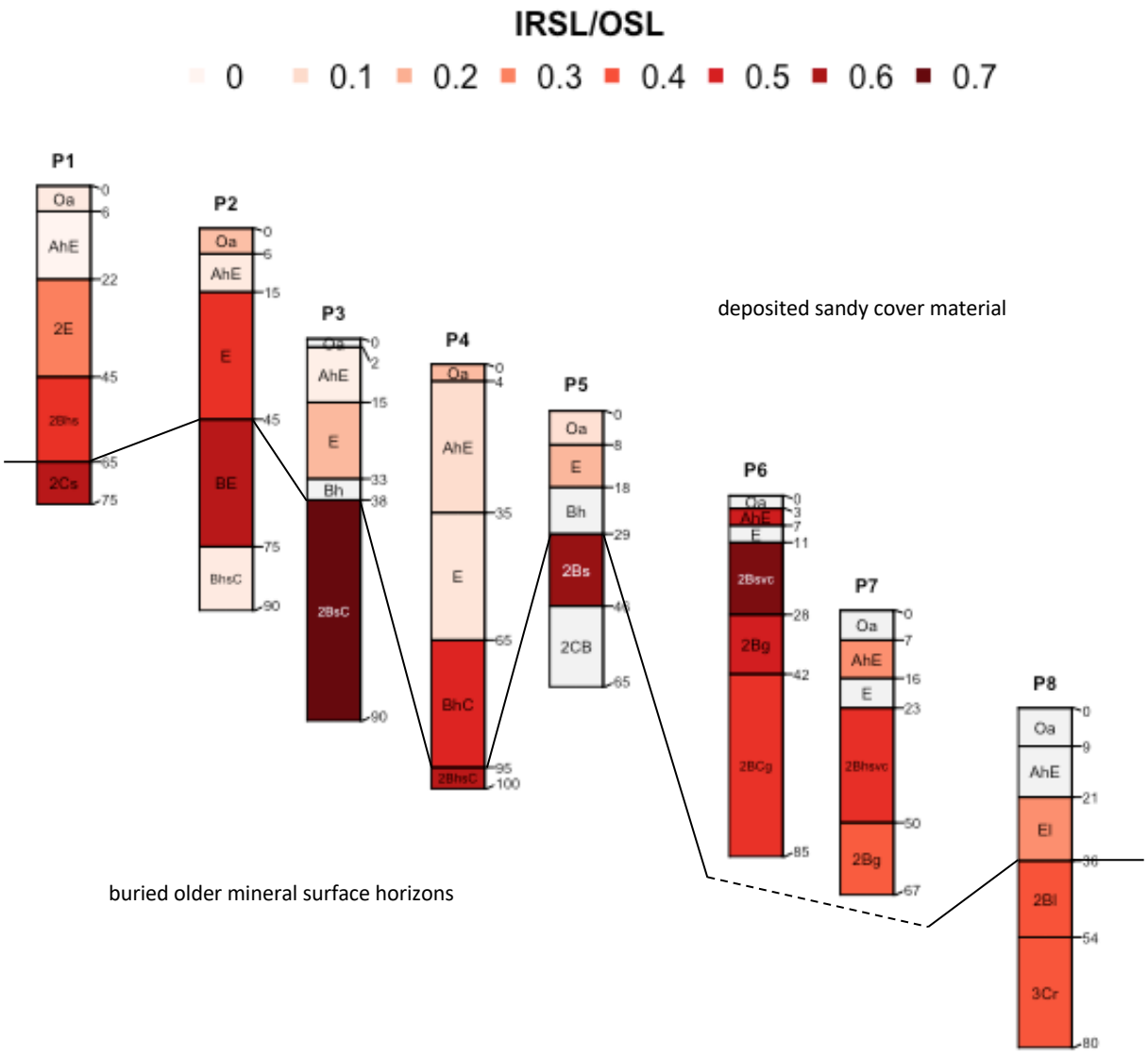

Figure 49: Ratio of Infrared Stimulated Luminescence (IRSL) to Optical Stimulated Luminescence (OSL) in soil profiles P1–P8 in relative topographical position with boundary of older mineral surface and later deposited cover material.

5.7 SOIL REDISTRIBUTION

In this study, the soil redistribution across all models (IM, PDM and MODERN) ranges from –6.9 to 7.7 t ha^{-1} yr^{-1} along the slope. The erosion rates at sites P2, P3, P4, P5 and P6 range from –0.6 to –6.9 t ha^{-1} yr^{-1} (60–690 t km^{-2} yr^{-1}) and the deposition rates at sites P1, P6 and P8 range from 0.23 to 7.72 t ha^{-1} yr^{-1} (23–772 t km^{-2} yr^{-1}). Although the values should be viewed with caution, as the measurements of $^{239+240}Pu$ activities showed a high variance and RSD. No significant correlation

between soil redistribution rates and slope inclination was found. And although soil redistribution is a possible cause for differences in thickness of eluvial and illuvial horizon, as erosion degrades a Podzol soil profile and deposition aggrades it (Waroszewski *et al.* 2015b), there was no significant correlation between redistribution rates and the thickness of illuvial and eluvial horizons.

The highest erosion rate was determined for site P2 on top of the escarpment at an exposed position. Therefore, it is probably more prone to enhanced weathering and erosion. The highest deposition rate was found in soil profile P8, located at the flatter foot slope. The soil redistribution along the slope is not continuous. Rather, it shows several stages of erosion and deposition. The first stage spreads from site P2 with high erosion to site P6 with high deposition. The site in between shows a discontinuous decrease in erosion. Site P4 even appears to be in equilibrium between erosion and deposition. The second stage ranges from soil profile P7 to P8. A forest road between soil profile P6 and P7 separates the two soil redistribution stages. The distribution of erosion and deposition along the slope suggests, that there is not necessarily a high soil loss out of the catchment.

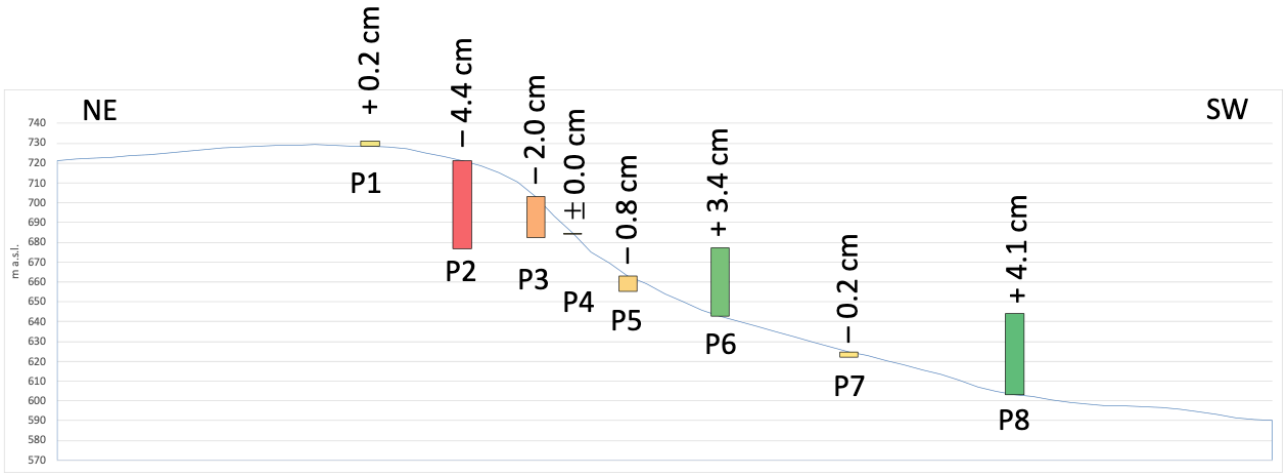

Figure 50: Relief cross-section with calculated average soil erosion and deposition rates since 1963 on sampling sites P1–P8 at the southwestern slope of Urwisko Batarowskie (relief height exaggerated 2:1).

Latocha *et al.* (2016) observed a substantial reduction in erosion rates over the last 150 years in the Sudetes Mountains, from 4.03 t ha^{-1} yr^{-1} in the 19th century to 0.96 t ha^{-1} yr^{-1} in present day, largely due to land abandonment and subsequent vegetation succession, which stabilized the soil and reduced erosion. Based on meteoric ^{10}Be in loess-mantled soils Kowalska *et al.* (2023) estimated

long-term erosion rates ranging from 0.1 to 3 t ha^{-1} yr^{-1} depending on environmental conditions and soil properties. These values are within the magnitude of the erosion rates at Urwisko Batarowskie.

In other forested mountainous areas around the world similar erosion rates were found with 90–700 t km^{-2} yr^{-1} in South Korea (Meusburger *et al.* 2013) and 200–300 t km^{-2} yr^{-1} in the Sila Mountains in Italy (Raab *et al.* 2018). Portenga & Bierman (2011) calculated erosion rates of up to 320 t km^{-2} yr^{-1} in mountain ranges, where a continuous soil cover cannot develop due to slightly more rapid erosion. In the Wind River Range (USA) erosion rates of soils on younger moraines under tundra vegetation range from 257–517 t km^{-2} yr^{-1} (Portes *et al.* 2018). There soils on older, forested moraines showed erosion rates close to zero or even net accumulation rates of 15–48 t km^{-2} yr^{-1} where aeolian input lead to a net positive rate (Dahms & Rawlins 1996), which can be indicated with change in silt and clay content even in lower soil horizons (Birkeland 1984). In the Sila Mountains erosion rates on steeper slopes even reached 1'000–3'500 t km^{-2} yr^{-1} (Raab *et al.* 2018) and in Swiss alpine areas soil erosion rates from 600–3'000 t km^{-2} yr^{-1} were determined (Alewell *et al.* 2015). These are much higher compared with erosion rates found on the slope of Urwisko Batarowskie. Erosion rates higher than 1'000 t km^{-2} yr^{-1} are probably linked to anthropogenic activities like disturbance in vegetation and decreasing vegetation cover, which induces an exponential increase in total erosion rates (Vanacker *et al.* 2014). Bajard et al. (2017) found erosion of 1'000 t km^{-2} yr^{-1} in the Norther French Alps and stated, that the tolerable erosion limit is 25–30 t km^{-2} yr^{-1}.

Humic layers are vulnerable to slope surface wash and thereby easily eroded (Latocha & Migoń 2006). Klementowski & Jahn (1996) attributed an erosion rate of 0.002–0.025 t ha^{-1} yr^{-1} to slope surface wash in forests, in contrast to 0.58–2.3 t ha^{-1} yr^{-1} on cultivated slopes, and 100 t ha^{-1} yr^{-1} on arable fields in the Śnieżnik Massif, a part of the Czech Sudetes. In the Sudetes, the erosion on steep and high slopes, which were transformed from arable land to forests and grassland experienced a huge decrease by 8 to 16 t ha^{-1} yr^{-1} in erosion (Latocha *et al.* 2016).

A decrease of human impact generally leads to reduction of soil erosion (Latocha & Migoń 2006). According to Latocha *et al.* (2016), changes in land us and land cover have a much larger impact on soil erosion than climate change. As single-plant forestry is often involved in high erosion rates (Klementowski 2002; Parzóch 2001) and therefore a renaturation of the forest-managed slopes could be beneficial for higher slope stability (Latocha & Migoń 2006). Studies in the Carpathians

have shown that access roads are the main source of sediment transport and contribute up to 90 % of the suspended load (Froehlich 1982, 1991; Froehlich & Walling 1997). But erodibility in the Stołowe Mountains is probably smaller due to its sandstone bedrock and the finer-grained sediment, in contrast to the flysch sediments of the Carpathians. A natural vegetation community would include *Abies alba* (Jędryszczak & Miscicki 2001). And according to (Filipiak *et al.* 2003) the best for regeneration are medium-textured soils, containing a few percent of the clay fraction and 50 to 60 % of sand. In contrast, silty soils have the poorest regeneration potential. The soils along the escarpment at Urwisko Batarowskie appears to meet these conditions, except at the foot slope where higher silt and clay contents could negatively influence the growth of European silver fir.

The $^{239+240}$Pu activity and the subsequent calculation of erosion rates show a wide variance and high standard deviation. However, MODERN provides relatively low standard deviations for modelled soil redistribution rates in. When analyzing soil properties the main source of error is the soil sampling design and process (Cline 1944; Edwards 2010). The sample size with four repetitions per site and depth lies within the margin of 3–17 samples estimated by Han et al. (2016). As a comparison Alewell et al. (2014) used 3 cores per site and sampling depths and received also unusually high standard deviations. Possible errors could be the small-scale variation of soil redistribution, differences in horizon thicknesses. Cross-contamination from site to site seems rather unlikely due to the relatively large amount of material per sample taken from each location.

The Pu activity distribution in reference site R1 was as expected for a soil profile with assumably negligible soil erosion or deposition. The distribution in reference site R2 however, indicated a disturbed soil, therefore R2 was excluded.

5.8 ESCARPMENT RETREAT AND EVOLUTION OF SLOPE

The large-scale evolution of the landscape is influenced by denudation, a natural process and driven by topography, climate, tectonic activity, geology and anthropogenic and biotic activities (Smithson *et al.* 2013). Portenga & Bierman (2011) estimated worldwide denudation rates ranging from 5 to 11’800 t km^{-2} yr^{-1} based on 87 sites, with a median at 80 t km^{-2} yr^{-1}. For the primal forest Boubínský prales in the Czech Republic, the maximum net denudation rate reaches up to 92 t km^{-2} yr^{-1} (Šamonil *et al.* 2019) and the denudation rates in the Sudetes was estimated by Jahn (1968) to be around 0.01–0.05 mm yr^{-1} (approximately 13–65 t km^{-2} yr^{-1} with a bulk density of 1.3 g cm^{-3}). Sandstone

rock however, shows an uneven rate of denudation (Duszyński 2024). For example the stratigraphically lower arkosic sandstone is more easily weatherable than the higher quartz sandstone (arenite) (Piccini & Mecchia 2009). Although arenite is very resistant, due to its joints and high primary porosity it is prone to increased subsurface moisture and therefore selective weathering processes (Duszyński & Migoń 2022b; Walczak 1963; Wojewoda *et al.* 2011). This results in cliff reduction, in contrast to high cliffs in arid climatic conditions (Burnett *et al.* 2008). Contrarily, the fine-grained sediments below the caprock show low porosity and low permeability but also low resistance to weathering, resulting in less steep terrain (Duszyński 2024).

With this background a landslide-controlled parallel retreat and decline (Pain 1986) or the in situ cliff disintegration (Duszyński & Migoń 2015). The exact mechanism of slope lowering in neither defined, but might be approximated by denudation rates (Saunders & Young 1983). Thus, slope development processes may include deformation, subsidence and mass movement like rock fall and landslides (Migoń & Kasprzak 2011).

Literature on escarpment retreat shows a range from 0.006 to 200 m ka^{-1} (Duszyński 2019). More likely is the assumption by Curry & Morris (2004) of 0.1–1.2 m ka^{-1} for a temperate climate. However, the extent of the long-term retreat of the escarpment is uncertain (Migoń & Kasprzak 2016). Additionally, the effect of climate change on geomorphical processes will likely change the development and bring the escarpment out of the presumed equilibrium (Błaś & Ojrzyńska 2024).

6 CONCLUSION

The soil profiles on the caprock, the upper slope and mid-slope are strongly influenced by the sand content. The lower along the slope, the more the influence of fine-grained sediments are visible through a loam or clay texture or the influence of backwater or capillary rising water.

Vertical and lateral Podzolization and other soil formation processes are evident down to a minimal depth of 50 cm. The soilscape (pedochore) can be divided into 5 vertical zonalities with significant variations in horizon thickness, organic matter accumulation, vertical and lateral leaching processes, and material deposition: On the caprock are soils with histic properties, along the escarpment Podzols with high skeletal fraction, in the upper mid-slope arenic to loamic Podzols, in lower mid-slope soils with stagnic properties and at the foot slope soils with gleyic properties.

Several parameters, such as weathering indices and luminescence dating, imply the covering of former surface horizons. Also, the abrupt changes in rock fragment fractions, soil texture and pH indicate lithological discontinuities. This leads to the assumption that soils at Urwikso Batarowskie are polygenetic. Which means that layers of parent material of different deposition ages lead to lithological discontinuities, which influences the

The erosion rates are within ranges of other mountainous forests in temperate climate zones. The soil redistribution is not continuous along the slope. Rather, it shows several stages of erosion and deposition. In addition, soils that show an even mass balance were found in steep mid-slope positions. It is possible that the eroded material remains largely within the catchment.

To address the hypotheses of the study: (i) Although sand and SiO_2 content decrease with distance to the sandstone plateau, both show no significant correlation with the position on the slope, (ii) the deepest weathering and most profound soil profile was found in mid-slope position which can probably be attributed to the accumulation of upslope material, (iii) there is no continuous increase in depositional age with soil horizon depth as the relative depositional age show buried former mineral surface horizons and (iv) although the erosion rates are higher in steeper parts of the hillslope, they do not continuously increase with decreasing slope. The distribution of erosion and deposition along the slope rather seems to be bipartite.

Altogether, the soil dynamics at Urwisko Batarowskie show a complex system that influences the further development of the escarpment.

7 OUTLOOK

From all the collected samples, data and conclusions, several directions of additional studies and advancing research questions are possible. To refine the collected data the new allocation of Oa horizons with < 30 % of soil organic matter as Ah horizons could be considered. Additionally, the designations of horizons that show a lithological change should be checked. To have a better overview of the composition and influence of the parent material, the determination of the quartz content or general mineral composition in the soil could be useful.

The determination of free aluminium and iron with dithionite extraction could help to examine weathering and podzolization processes in more detail. And since biochar was found in several horizons in different depths, the age could be determined with radiocarbon dating, which could also help to understand the geomorphic history of the escarpment.

Apart from uranium-239 and -240, the use of cesium-137 as soil erosion proxy might be interesting due to the proximity to the former nuclear power plant of Chernobyl. Although the application is probably limited by the shorter half-life of ^{137}Cs.

In order to better understand the development of the escarpment retreat, the estimation of denudation should also be carried out over large areas and parallel to the cliff to better cover the variability.

Future research should integrate these findings to further describe the complex ecological and geomorphic processes of the Stołowe Mountains.

8 REFERENCES

Aitken, M.J. (1998). *Introduction to optical dating: the dating of Quaternary sediments by the use of photon-stimulated luminescence*. Clarendon Press.

Alewell, C., Egli, M. & Meusburger, K. (2015). An attempt to estimate tolerable soil erosion rates by matching soil formation with denudation in Alpine grasslands. *Journal of Soils and Sediments*, 15, 1383–1399.

Alewell, C., Meusburger, K., Juretzko, G., Mabit, L. & Ketterer, M.E. (2014). Suitability of 239+240Pu and 137Cs as tracers for soil erosion assessment in mountain grasslands. *Chemosphere*, 103, 274–280.

Altermann, M., Jäger, K.-D., Kopp, D., Kowalkowski, A., Kühn, D. & Schwanecke, W. (2008). Zur Kennzeichnung und Gliederung von periglaziär bedingten Differenzierungen in der Pedosphäre. *Waldökologie, Landschaftsforschung und Naturschutz*, 6, 5–42.

Arata, L., Meusburger, K., Frenkel, E., A'Campo-Neuen, A., Iurian, A.-R., Ketterer, M.E., *et al.* (2016). Modelling Deposition and Erosion rates with RadioNuclides (MODERN) – Part 1: A new conversion model to derive soil redistribution rates from inventories of fallout radionuclides. *Journal of Environmental Radioactivity*, 162–163, 45–55.

Armson, K.A. & Fessenden, R.J. (1973). Forest Windthrows and Their Influence on Soil Morphology. *Soil Science Society of America Journal*, 37, 781–783.

Bajard, M., Poulenard, J., Sabatier, P., Develle, A.-L., Giguet-Covex, C., Jacob, J., *et al.* (2017). Progressive and regressive soil evolution phases in the Anthropocene. *CATENA*, 150, 39–52.

Bashour, I.I. & Sayegh, A.H. (2007). *Methods of analysis for soils of arid and semi-arid regions*. Food and agriculture organization of the United Nations.

Birkeland, P.W. (1984). *Soils and geomorphology*. Oxford University Press, New York.

Błaś, M. & Ojrzyńska, H. (2024). The Climate of Poland. In: *Landscapes and Landforms of Poland*, World Geomorphological Landscapes (eds. Migoń, P. & Jancewicz, K.). Springer International Publishing, Cham, pp. 33–51.

Blume, H.-P., Brümmer, G.W., Fleige, H., Horn, R., Kandeler, E., Kögel-Knabner, I., *et al.* (2016). Soil Geography. In: *Scheffer/SchachtschabelSoil Science* (eds. Blume, H.-P., Brümmer, G.W., Fleige, H., Horn, R., Kandeler, E., Kögel-Knabner, I., et al.). Springer, Berlin, Heidelberg, pp. 391–408.

Bogacz, A. (2018). The effect of long-term peatlands drainage on the properties of soils in microrelief in the Długie Mokradło bog (Central Sudetes–SW Poland). *Polish Journal of Soil Science*, 50, 237.

Boratyńska, K., Gołąb, Z., Łabiszak, B., Niemczyk, W., Sobierajska, K.I., Ufnalski, K., *et al.* (2021). Are there any traces of Pinus uliginosa in the Stołowe Mountains Outside the Wielkie Torfowisko Batorowskie and Błędne Skały? *Acta Soc Bot Pol*, 90, 904.

Borggaard, O.K. (1988). Phase Identification by Selective Dissolution Techniques. In: *Iron in Soils and Clay Minerals*, NATO ASI Series (eds. Stucki, J.W., Goodman, B.A. & Schwertmann, U.). Springer Netherlands, Dordrecht, pp. 83–98.

Bower, J.A., Ross, D.S., Bailey, S.W., Pennino, A.M., Jercinovic, M.J., McGuire, K.J., *et al.* (2023). Development of a lateral topographic weathering gradient in temperate forested podzols. *Geoderma*, 439, 116677.

Brázdil, R. (1998). Meteorological extremes and their impacts on forests in the czech republic. In: *The Impacts of Climate Variability on Forests* (eds. Beniston, M. & Innes, J.L.). Springer, Berlin, Heidelberg, pp. 19–47.

Brouwer, P. (2006). Theory of XRF. *Almelo, Netherlands: PANalytical BV*.

Buggle, B., Glaser, B., Hambach, U., Gerasimenko, N. & Marković, S. (2011). An evaluation of geochemical weathering indices in loess–paleosol studies. *Quaternary International*, 240, 12–21.

Burliga, S., Kasprzak, M., Sobczyk, A. & Niemczyk, W. (2023). Geomorphometric and Geophysical Constraints on Outlining Drained Shallow Mountain Mires. *Geosciences*, 13, 43.

Burnett, B.N., Meyer, G.A. & McFadden, L.D. (2008). Aspect-related microclimatic influences on slope forms and processes, northeastern Arizona. *Journal of Geophysical Research: Earth Surface*, 113.

Caspari, T., Bäumler, R., Norbu, C., Tshering, K. & Baillie, I. (2006). Geochemical investigation of soils developed in different lithologies in Bhutan, Eastern Himalayas. *Geoderma*, 136, 436–458.

Čech, S. & Gawlikowska, E. (1999). *Góry Stołowe: mapa geologiczno-turystyczna [Stołowe Mountains: geological and tourist map]: 1:50'000*. Państwowy Instytut Geologiczny.

Cline, M.G. (1944). Principles of soil sampling. *Soil Science*, 58, 275.

Clinton, B.D. & Baker, C.R. (2000). Catastrophic windthrow in the southern Appalachians: characteristics of pits and mounds and initial vegetation responses. *Forest Ecology and Management*, 126, 51–60.

Curry, A.M. & Morris, C.J. (2004). Lateglacial and Holocene talus slope development and rockwall retreat on Mynydd Du, UK. *Geomorphology*, 58, 85–106.

Cymerman, Z. (2019). *Objaśnienia do szczegółowej mapy geologicznej Polski 1:50 000. 899 i 900, Arkusz Kudowa Zdrój i arkusz Duszniki Zdrój*. PIG-PIB, Warszawa.

Dahlgren, R. & Ugolini, F. (1991). Distribution and characterization of short-range-order minerals in Spodosols from the Washington Cascades. *Geoderma*, 48, 391–413.

Dahms, D. & Egli, M. (2016). Carbonate and elemental accumulation rates in arid soils of mid-to-late Pleistocene outwash terraces, southeastern Wind River Range, Wyoming, USA. *Chemical Geology*, Deciphering time-dependent processes in soil and weathering profile evolution, 446, 147–162.

Dahms, D.E. & Rawlins, C.L. (1996). A Two-Year Record of Eolian Sedimentation in the Wind River Range, Wyoming, U.S.A. *Arctic and Alpine Research*, 28, 210–216.

Delvaux, B., Herbillon, A.J. & Vielvoye, L. (1989). Characterization of a weathering sequence of soils derived from volcanic ash in Cameroon. Taxonomic, mineralogical and agronomic implications. *Geoderma*, 45, 375–388.

Derakhshan-Babaei, F., Nosrati, K., Tikhomirov, D., Christl, M., Sadough, H. & Egli, M. (2020). Relating the spatial variability of chemical weathering and erosion to geological and topographical zones. *Geomorphology*, 363, 107235.

Digital Terrain Model. (2023). .

Dorn, R.I. (1983). Cation-Ratio Dating: A New Rock Varnish Age-Determination Technique. *Quat. res.*, 20, 49–73.

Drewnik, M. (2006). The effect of environmental conditions on the decomposition rate of cellulose in mountain soils. *Geoderma*, 132, 116–130.

Dubicki, A. & Głowicki, B. (2008). Klimat [Climate]. In: *Przyroda Parku Narodowego Gór Stołowych [Nature of the Stołowe Mountains National Park]*. Wydawnictwo Parku Narodowego Gór Stołowych, Kudowa-Zdrój, pp. 101–113.

Dumanowski, B. (1961). Zagadnienie rozwoju stoku na przykładzie Gór Stołowych [The dependence of slope evolution on the example of the Stołowe Mountains]. *Czasopismo Geograficzne*, 32, 311–324.

Dumanowski, B., M. (1961). Forms of spherical cavities in the Stołowe Mountains (Heuscheur Gebirge). *Acta Universitatis Wratislaviensis*, B, 123–137.

Duszyński, F. (2024). The Stołowe Mountains—A Unique Sandstone Tableland. In: *Landscapes and Landforms of Poland*, World Geomorphological Landscapes (eds. Migoń, P. & Jancewicz, K.). Springer International Publishing, Cham, pp. 191–210.

Duszyński, F., Clifford, F., Goudie, A. & Migoń, P. (2021). Rock properties and rock-controlled landforms. *Geological Society, London, Memoirs*, 58, M58-2021.

Duszyński, F., Jancewicz, K., Kasprzak, M. & Migoń, P. (2017). The role of landslides in downslope transport of caprock-derived boulders in sedimentary tablelands, Stołowe Mts, SW Poland. *Geomorphology*, 295, 84–101.

Duszyński, F., Jancewicz, K. & Migoń, P. (2018). Evidence for subsurface origin of boulder caves, roofed slots and boulder-filled canyons (Broumov Highland, Czechia). *International Journal of Speleology*, 47, 343–359.

Duszyński, F. & Migoń, P. (2015). Boulder aprons indicate long-term gradual and non-catastrophic evolution of cliffed escarpments, Stołowe Mts, Poland. *Geomorphology*, 250, 63–77.

Duszyński, F. & Migoń, P. (2017). Zespół skalny Dziedzińca na płaskowyżu Skalniaka w Górach Stołowych [The courtyard rock complex on the Skalniaka plateau in the Stołowe Mountains]. *Przyroda Sudetów*, 20, 199–218.

Duszyński, F. & Migoń, P. (2018). The origin of 'rock cities' on sandstone plateaus [Geneza skalnych miast na płaskowyżach piaskowcowych]. *Przegląd Geograficzny*, 90, 379–402.

Duszyński, F. & Migoń, P. (2022a). Geomorphological heritage of cretaceous sandstone terrains in SW Poland: diversity, conservation and interpretation issues. *Geoheritage*, 14, 31.

Duszyński, F. & Migoń, P. (2022b). Skalne grzyby w Polsce i na świecie–terminologia, rozmieszczenie, poglądy na rozwój [Rock mushrooms in Poland and the world–terminology, distribution, views evolution]. *Przegląd Geograficzny*, 94, 5–30.

Duszyński, F., Migoń, P. & Kasprzak, M. (2016). Underground erosion and sand removal from a sandstone tableland, Stołowe Mountains, SW Poland. *CATENA*, 147, 1–15.

Duszyński, F., Migoń, P. & Strzelecki, M.C. (2015). The origin of sandstone boulder aprons along the escarpments of the Stołowe Mountains: are they all rockfall-derived? A new insight into an old problem using the CONEFALL 1.0 software. *Bulletin of Geography. Physical Geography Series*, 8, 19–32.

Duszyński, F., Migoń, P. & Strzelecki, M.C. (2019). Escarpment retreat in sedimentary tablelands and cuesta landscapes – Landforms, mechanisms and patterns. *Earth-Science Reviews*, 196, 102890.

Duzgoren-Aydin, N.S., Aydin, A. & Malpas, J. (2002). Re-assessment of chemical weathering indices: case study on pyroclastic rocks of Hong Kong. *Engineering Geology*, 63, 99–119.

Edwards, A.C. (2010). Soil Sampling and Sample Preparation. In: *Trace Elements in Soils*. John Wiley & Sons, Ltd, pp. 39–51.

Egli, M. & Fitze, P. (2000). Formulation of pedologic mass balance based on immobile elements: A revision. *Soil Science*, 165, 437–443.

Egli, M., Plötze, M., Tikhomirov, D., Kraut, T., Wiesenberg, G.L.B., Lauria, G., *et al.* (2020). Soil development on sediments and evaporites of the Messinian crisis. *CATENA*, 187, 104368.

Ettler, V. & Mihaljevic, M. (1999). Distribution of trace elements in several ombrotrophic peatbogs in the Bohemian Massif. *Rostlinna Vyroba*, 45.

Eusterhues, K., Rumpel, C. & Kögel-Knabner, I. (2005). Organo-mineral associations in sandy acid forest soils: importance of specific surface area, iron oxides and micropores. *European Journal of Soil Science*, 56, 753–763.

Fedo, C.M., Wayne Nesbitt, H. & Young, G.M. (1995). Unraveling the effects of potassium metasomatism in sedimentary rocks and paleosols, with implications for paleoweathering conditions and provenance. *Geology*, 23, 921–924.

Fiantis, D., Nelson, M., Shamshuddin, J., Goh, T.B. & Van Ranst, E. (2010). Determination of the geochemical weathering indices and trace elements content of new volcanic ash deposits from Mt. Talang (West Sumatra) Indonesia. *Eurasian Soil Sc.*, 43, 1477–1485.

Filipiak, M., Komisarek, J. & Nowinski, M. (2003). Natural regeneration of the European silver fir in the Sudety Mountains on soils with different particle size distribution. *Dendrobiology*.

Filippi, M., Slavík, M., Bruthans, J., Weiss, T. & Řihošek, J. (2021). Accelerated disintegration of in situ disconnected portions of sandstone outcrops. *Geomorphology*, 391, 107897.

Froehlich, W. (1982). *Mechanizm transportu fluwialnego i dostawy zwietrzelin do koryta w górskiej zlewni fliszowej [Mechanism of fluvial transport and supply of weathered material to the riverbed in a mountain flysch catchment]*. IGiPZ PAN.

Froehlich, W. (1991). Sediment production from unmetalled road surfaces. In: *Sediment and stream water quality in a changing environment: trends and explanation*. Presented at the XXth General Assembly of the International Union of Geodesy and Geophysics, IAHS Publication, Vienna, Austria, pp. 21–30.

Froehlich, W. & Walling, D. (1997). The role of unmetalled roads as a sediment source in the fluvial systems of the Polish Flysch Carpathians. *IAHS Publication*, 245, 159–168.

Galka, B., Labaz, B., Bogacz, A., Bojko, O. & Kabala, C. (2014). Conversion of Norway spruce forests will reduce organic carbon pools in the mountain soils of SW Poland. *Geoderma*, 213, 287–295.

Gallaway, J.M., Martin, Y.E. & Johnson, E.A. (2009). Sediment transport due to tree root throw: integrating tree population dynamics, wildfire and geomorphic response. *Earth Surface Processes and Landforms*, 34, 1255–1269.

Glina, B. & Bogacz, A. (2013). Concentration and pools of trace elements in organic soils in the Izera Mountains. *Journal of Elementology*, 18.

Glina, B., Malkiewicz, M., Mendyk, Ł., Bogacz, A. & Woźniczka, P. (2017a). Human-affected disturbances in vegetation cover and peatland development in the late Holocene recorded in shallow mountain peatlands (Central Sudetes, SW Poland). *Boreas*, 46, 294–307.

Glina, B., Piernik, A., Hulisz, P., Mendyk, Ł., Tomaszewska, K., Podlaska, M., *et al.* (2019). Water or soil—What is the dominant driver controlling the vegetation pattern of degraded shallow mountain peatlands? *Land Degrad Dev*, 30, 1437–1448.

Glina, B., Spychalski, W., Zawieja, B. & Kaczmarek, T. (2017b). Spatial distribution of trace elements in shallow mountain peatlands, the Stołowe Mountains (SW Poland). *J. Elem.*

Han, Y., Zhang, J., Mattson, K.G., Zhang, W. & Weber, T.A. (2016). Sample Sizes to Control Error Estimates in Determining Soil Bulk Density in California Forest Soils. *Soil Science Society of America Journal*, 80, 756–764.

Harnois, L. (1988). The CIW index: a new chemical index of weathering. *Sedimentary geology*, 55, 319–322.

Harrington, C.D. & Whitney, J.W. (1987). Scanning electron microscope method for rock-varnish dating. *Geology*, 15, 967.

He, Q. & Walling, D.E. (1996). Use of fallout Pb-210 measurements to investigate longer-term rates and patterns of overbank sediment deposition on the floodplains of lowland rivers. *Earth Surface Processes and Landforms*, 21, 141–154.

He, Q. & Walling, D.E. (1997). The distribution of fallout 137Cs and 210Pb in undisturbed and cultivated soils. *Applied Radiation and Isotopes*, 48, 677–690.

Hutton, J.T. (1977). Titanium and zirconium minerals. In: *Minerals in Soil Environments* (eds. Dixon, J.B. & Weed, S.B.). Soil Science Society of America, Madison, Wisconsin, pp. 673–688.

International Atomic Energy Agency. (2021). Natural and anthropogenic radionuclides in moss-soil. Certified reference material, Certificate IAEA-447 Rev.01.

IUSS Working Group WRB. (2022). *World Reference Base for Soil Resources. International soil classification system for naming soils and creating legends for soil maps*. 4th edition. International Union of Soil Sciences (IUSS), Vienna, Austria.

Jahn, A. (1968). Geomorfologiczne wnioski z obserwacji dna jeziora zaporowego [Geomorphological conclusions from observations of the bottom of a damm lake]. *Czas. Geogr*, 39, 117–123.

Jahn, A. (1969). Some problems concerning slope development in the Sudetes. *Biuletyn peryglacjalny*, 8, 331–348.

Jahn, A. (1977). The permafrost active layer in the Sudety Mountains during the last glaciation. *Quaestiones Geographicae*, 4, 29–42.

Jahn, A. (1989). The Soil Creep on Slopes in Different Altitudinal and Ecological Zones of Sudetes Mountains. *Geografiska Annaler. Series A, Physical Geography*, 71, 161.

Jahn, R., Blume, H.P., Asio, V.B., Spaargaren, O. & Schad, P. (2006). *Guidelines for soil description, 4th edition*. FAO, Rome.

Jamroz, E., Kocowicz, A., Bekier, J. & Weber, J. (2014). Properties of soil organic matter in Podzols under mountain dwarf pine (Pinus mugo Turra) and Norway spruce (Picea abies (L.) Karst.) in various stages of dieback in the East Sudety Mountains, Poland. *Forest Ecology and Management*, 330, 261–270.

Jancewicz, K., Migoń, P. & Kasprzak, M. (2019). Connectivity patterns in contrasting types of tableland sandstone relief revealed by Topographic Wetness Index. *Science of the Total Environment*, 656, 1046–1062.

Jancewicz, K. & Porębna, W. (2022). Point cloud does matter. Selected issues of using airborne LiDAR elevation data in geomorphometric studies of rugged sandstone terrain under forest – Case study from Central Europe. *Geomorphology*, 412, 108316.

Jankowski, M. (2014). The evidence of lateral podzolization in sandy soils of Northern Poland. *CATENA*, Landscapes and Soils through Time, 112, 139–147.

Jędryszczak, E. & Miscicki, S. (2001). Forests of the Stołowe Mountains National Park. *Szczeliniec*, 5, 79–103.

Jenny, H. (1941). *Factors of soil formation: a system of quantitative pedology*. McGraw–Hill, New York.

Jerzykiewicz, T. (1968a). Sedymentacja górnych piaskowców ciosowych niecki śródsudeckiej (górna kreda) [Sedimentation of the upper ashlar sandstones of the Intra-Sudetic Basin (Upper Cretaceous)]. *Geologia Sudetica*, 4, 409–462.

Jerzykiewicz, T. (1968b). Uwagi o orientacji i genezie ciosu w skałach kredowych niecki śródsudeckiej [Remarks on the orientation and genesis of the rock formation in the Cretaceous rocks of the Intra-Sudetic Basin]. *Geologia Sudetica*, 4, 465–468.

Jewula, E. (1974). Rejonizacja szkód powodowanych przez wiatry w drzewostanach górskich i podgórskich Południowej Polski. *Sylwan*, 118.

Kabala, C. (2007). The sequence of polygenetic soils developed from sandstone in the Góry Stołowe Mountains (Poland). *Sandstone Landscapes. Academia, Praha*, 127–133.

Kabala, C., Bogacz, A., Waroszewski, J. & Ochyra, S. (2008). Influence of slope cover-beds structure on the morphology and properties of podzols in subalpine zone of the Karkonosze Mts.[Poland]. *Roczniki Gleboznawcze (Poland)*, 59.

Kabala, C., Chodak, T., Bogacz, A., Labaz, B., Jezierski, P., Galka, B., *et al.* (2011). Spatial variability of soils and habitats in the Stolowe Mountains. In: *Geo-ecological Conditions of the Stolowe Mountains National Park* (ed. Chodak, T.). WIND, Wrocław, Poland, pp. 141–167.

Kabała, C. & Szerszeń, L. (2002). Profile Distributions of Lead, Zinc, and Copper in Dystric Cambisols Developed from Granite and Gneiss of the Sudetes Mountains, Poland. *Water, Air, & Soil Pollution*, 138, 307–317.

Kacprzak, A. & Migoń, P. (2013). Using soil properties as a tool to differentiate landslide generations and constrain their ages-Rogowiec landslide, Sudetes (SW Poland). Presented at the EGU General Assembly Conference Abstracts, pp. EGU2013-10132.

Karczewska, A., Bogda, A., Ga, B., Szulc, A., Czwarkiel, D. & Duszyñska, D. (2006). Natural and anthropogenic soil enrichment in heavy metals in areas of former metallic ore mining in the Sudety Mts. *Polish Journal of Soil Science*, 39.

Kasprzak, M. & Migoń, P. (2015a). DEM-based analysis of geomorphology of a stepped sandstone plateau, Stołowe Mountains (SW Poland) Stołowe Mountains (SW Poland). *zfg_suppl*, 59, 245–268.

Kasprzak, M. & Migoń, P. (2015b). DEM-based analysis of geomorphology of a stepped sandstone plateau, Stołowe Mountains (SW Poland) Stołowe Mountains (SW Poland). *zfg_suppl*, 59, 245–268.

Kasprzak, M. & Migoń, P. (2015c). Geomorphology and geomorphometry of a stepped sandstone plateau, Stołowe Mountains (SW Poland). *Zeitschrift für Geomorphologie, Supplementary Issues*, 59, 247–270.

Kelley, J.M., Bond, L.A. & Beasley, T.M. (1999). Global distribution of Pu isotopes and 237Np. *Science of The Total Environment*, 237–238, 483–500.

Ketterer, M.E. (2015). Standard Operating Procedure for Preparation of Soils and Sediments for 239+240Pu Activity and 240Pu/239Pu Atom Ratio Measurements – Acid Leaching and Quadrupole ICPMS.

Ketterer, M.E., Hafer, K.M., Jones, V.J. & Appleby, P.G. (2004). Rapid dating of recent sediments in Loch Ness: inductively coupled plasma mass spectrometric measurements of global fallout plutonium. *Science of The Total Environment*, 322, 221–229.

Ketterer, M.E., Watson, B.R., Matisoff, G. & Wilson, C.G. (2002). Rapid Dating of Recent Aquatic Sediments Using Pu Activities and 240Pu/239Pu As Determined by Quadrupole Inductively Coupled Plasma Mass Spectrometry. *Environ. Sci. Technol.*, 36, 1307–1311.

Ketterer, M.E., Zheng, J. & Yamada, M. (2012). Applications of Transuranics as Tracers and Chronometers in the Environment. In: *Handbook of Environmental Isotope Geochemistry: Vol I*, Advances in Isotope Geochemistry (ed. Baskaran, M.). Springer, Berlin, Heidelberg, pp. 395–417.

Kleber, A. (1997). Cover-beds as soil parent materials in midlatitude regions. *CATENA*, 30, 197–213.

Kleber, A., Terhorst, B., Bullmann, H., Hülle, D., Leopold, M., Müller, S., *et al.* (2013). Chapter 2 - Subdued Mountains of Central Europe. In: *Developments in Sedimentology*, Mid-Latitude Slope Deposits (Cover Beds) (eds. Kleber, A. & Terhorst, B.). Elsevier, pp. 9–93.

Klementowski, J. (2002). Spłukiwanie i erozja żłobinowa na stokach Śnieżnika Kłodzkiego (Sudety Wschodnie) [Flushing and gully erosion on the slopes of Śnieżnik Kłodzki (Eastern Sudetes)]. *Zeszyty Problemowe Postępów Nauk Rolniczych*.

Klementowski, J. & Jahn, A. (1996). Degradacja pokryw stokowych w warunkach antropopresji. Procesy kriogeniczne, spłukiwanie i erozja żłobinowa. [Degradation of slope covers under anthropocene pressure conditions. Cryogenic processes, flushing and gouge erosion.]. In: *Masyw Śnieżnika. Zmiany w środowisku przyrodniczym [Śnieżnik Massif. Changes in the natural environment]*. Wydawnictwo PAE, Warszawa, pp. 121–142.

Kowalska, J., Mazurek, R., Gąsiorek, M., Setlak, M., Zaleski, T. & Waroszewski, J. (2016). Soil pollution indices conditioned by medieval metallurgical activity – A case study from Krakow (Poland). *Environmental Pollution*, 218, 1023–1036.

Kowalska, J.B., Egli, M., Vögtli, M., Tikhomirov, D., Łabaz, B., Christl, M., *et al.* (2023). Meteoric 10Be as a tracer of soil redistribution rates and reconstruction tool of loess–mantled soils (SW, Poland). *Geoderma*, 433, 116451.

Kowalska, J.B., Gąsiorek, M., Zadrożny, P., Nicia, P. & Waroszewski, J. (2021). Deep subsoil storage of trace elements and pollution assessment in mountain Podzols (Tatra Mts., Poland). *Forests*, 12, 291.

Kowalska, J.B., Vögtli, M., Kierczak, J., Egli, M. & Waroszewski, J. (2022). Clay mineralogy fingerprinting of loess-mantled soils on different underlying substrates in the south-western Poland. *CATENA*, 210, 105874.

Kowalski, S. (1980). Charakterystyka hydrogeologiczna źródeł Gór Stołowych [Hydrogeological characteristics of the water sources of the Stołowe Mountains]. *Geological Quarterly*, 24.

Lal, R. & Elliot, W. (1994). Erodibility and erosivity. In: *Soil erosion research methods*. St. Lucie Press ; Soil and Water Conservation Society, Delray Beach, Fla. : Ankeny, IA, pp. 181–210.

Lal, R., Tims, S.G., Fifield, L.K., Wasson, R.J. & Howe, D. (2013). Applicability of 239Pu as a tracer for soil erosion in the wet-dry tropics of northern Australia. *Nuclear Instruments and Methods in Physics Research Section B: Beam Interactions with Materials and Atoms*, Proceedings of the Twelfth International Conference on Accelerator Mass Spectrometry, Wellington, New Zealand, 20-25 March 2011, 294, 577–583.

Latocha, A. & Migoń, P. (2006). Geomorphology of medium-high mountains under changing human impact, from managed slopes to nature restoration: a study from the Sudetes, SW Poland. *Earth Surface Processes and Landforms*, 31, 1657–1673.

Latocha, A., Szymanowski, M., Jeziorska, J., Stec, M. & Roszczewska, M. (2016). Effects of land abandonment and climate change on soil erosion—An example from depopulated agricultural lands in the Sudetes Mts., SW Poland. *CATENA*, 145, 128–141.

Liu, L., Chen, J., Chen, Y., Ji, J. & Lu, H. (2002). Variation of Zr/Rb ratios on the Loess Plateau of Central China during the last 130000 years and its implications for winter monsoon. *Chinese Science Bulletin*, 47, 1298–1302.

Locock, A.J., Chesterman, D., Caird, D. & Duke, M.J.M. (2012). Miniaturization of mechanical milling for powder X-ray diffraction. *Powder Diffraction*, 27, 189–193.

Lorz, C. (2008). Lithological Discontinuous Soils Archives for the Pedo-Geochemical Genesis of the Soil-Regolith-Complex? *zfg_suppl*, 52, 119–132.

Lorz, C., Heller, K. & Kleber, A. (2011). Stratification of the Regolith Continuum - a Key Property for Processes and Functions of Landscapes. *Zeitschrift fur Geomorphologie Supplement*, 55, 277–292.

Lorz, C. & Phillips, J.D. (2006). Pedo-ecological consequences of lithological discontinuities in soils—examples from Central Europe. *Journal of Plant Nutrition and Soil Science*, 169, 573–581.

Lundström, U.S., van Breemen, N. & Bain, D. (2000). The podzolization process. A review. *Geoderma*, 94, 91–107.

Lyford, W.H. & MacLean, D.W. (1966). Mound and pit microrelief in relation to soil disturbance and tree distribution in New Brunswick, Canada. *Harvard Forest Paper*, 1–18.

Marek, S. (1998). Development of the Wielkie Torfowisko Batorowskie mountain mire as shown by palynological study. *Szczeliniec*, 2, 49–88.

Markert, B., Herpin, U., Berlekamp, J., Oehlmann, J., Grodzinska, K., Mankovska, B., *et al.* (1996). A comparison of heavy metal deposition in selected Eastern European countries using the moss monitoring method, with special emphasis on the 'Black Triangle.' *Science of The Total Environment*, 193, 85–100.

Matisoff, G. & Whiting, P.J. (2012). Measuring Soil Erosion Rates Using Natural (7Be, 210Pb) and Anthropogenic (137Cs, 239,240Pu) Radionuclides. In: *Handbook of Environmental Isotope Geochemistry: Vol I*, Advances in Isotope Geochemistry (ed. Baskaran, M.). Springer, Berlin, Heidelberg, pp. 487–519.

Maynard, J.B., Sutton, S.J., Robb, L.J., Ferraz, M.F. & Meyer, F.M. (1995). A paleosol developed on hydrothermally altered granite from the hinterland of the Witwatersrand Basin: characteristics of a source of basin fill. *The Journal of Geology*, 103, 357–377.

Mazur, S. (2024). An Outline of the Geology of Poland. In: *Landscapes and Landforms of Poland*, World Geomorphological Landscapes (eds. Migoń, P. & Jancewicz, K.). Springer International Publishing, Cham, pp. 3–17.

McKeague, J.A., Brydon, J.E. & Miles, N.M. (1971). Differentiation of Forms of Extractable Iron and Aluminum in Soils. *Soil Science Society of America Journal*, 35, 33–38.

Meusburger, K., Mabit, L., Ketterer, M., Park, J.-H., Sandor, T., Porto, P., *et al.* (2016). A multi-radionuclide approach to evaluate the suitability of 239+240Pu as soil erosion tracer. *Science of The Total Environment*, 566–567, 1489–1499.

Meusburger, K., Mabit, L., Park, J.-H., Sandor, T. & Alewell, C. (2013). Combined use of stable isotopes and fallout radionuclides as soil erosion indicators in a forested mountain site, South Korea. *Biogeosciences*, 10, 5627–5638.

Michniewicz, A., Jancewicz, K. & Migoń, P. (2020). Large-scale geomorphological mapping of tors – Proposal of a key and landform interpretation. *Geomorphology*, 357, 107106.

Migoń, P. (2008). Rzeźba i rozwój geomorfologiczny Gór Stołowych [Relief and geomorphological development of the Stołowe Mountains]. In: *Przyroda Parku Narodowego Gór Stołowych [Nature of the Stołowe Mountains National Park]*. Wydawnictwo Parku Narodowego Gór Stołowych, Kudowa-Zdrój, pp. 49–69.

Migoń, P. (2011). Geomorphic diversity of the Sudetes - effects of structure and global change superimposed. *Geographia Polonica*, 84, 75–92.

Migoń, P. (2017). Extreme geomorphic events in the contemporary evolution of forested slopes in a Central European mountain range, the Sudetes. *Revista de Geomorfologie*, 19, 17–28.

Migoń, P. (2021). Sandstone geomorphology – Recent advances. *Geomorphology*, 373, 107484.

Migoń, P. & Duszyński, F. (2017). Process-form relationship in the Stołowe Mountains tableland (Central Europe)-an example of strong lithostructural control on geomorphic systems of medium-altitude mountains. *Studia Geomorphologica Carpatho-Balcanica*, 51(52), 155–178.

Migoń, P., Duszyński, F. & Goudie, A. (2017a). Rock cities and ruiniform relief: Forms–processes–terminology. *Earth-Science Reviews*, 171, 78–104.

Migoń, P., Duszyński, F., Kasprzak, M. & Różycka, M. (2017b). Evolving slope instability zone at Mt. Turzyna (Sudetes, SW Poland) – An example of incipient deep-seated gravitational slope deformation. *Zeitschrift für Geomorphologie*, 61.

Migoń, P. & Jancewicz, K. (Eds.). (2024). *Landscapes and Landforms of Poland*. World Geomorphological Landscapes. Springer International Publishing, Cham.

Migoń, P. & Kacprzak, A. (2014). Lateral diversity of regolith and soils under a mountain slope — implications for interpretation of hillslope materials and processes, Central Sudetes, SW Poland. *Geomorphology*, 221, 69–82.

Migoń, P. & Kasprzak, M. (2011). Morfologiczny zapis ruchów masowych na progach morfologicznych Gór Stołowych w świetle numerycznego modelu wysokości o dużej rozdzielczości. *Przyroda Sudetów*.

Migoń, P. & Kasprzak, M. (2016). Pathways of geomorphic evolution of sandstone escarpments in the Góry Stołowe tableland (SW Poland) — Insights from LiDAR-based high-resolution DEM. *Geomorphology*, 260, 51–63.

Migoń, P., Kasprzak, M. & Traczyk, A. (2013). How high-resolution DEM based on airborne LiDAR helped to reinterpret landforms – examples from the Sudetes, SW Poland. *Landform Analysis*, 22, 89–101.

Migoń, P. & Latocha, A. (2013). Human interactions with the sandstone landscape of central Sudetes. *Applied Geography*, 42, 206–216.

Migoń, P., Latocha, A., Parzóch, K., Kasprzak, M., Owczarek, P., Witek, M., *et al.* (2011). Współczesny system morfogenetyczny gór stołoWych [Contemporary geomorphic system of the Stołowe Mountains]. In: *Geoekologiczne warunki środowiska przyrodniczego Gór Stołowych [Geoecological conditions of the Stołowe Mountains National Park]*. WIND, Wrocław, pp. 1–52.

Migoń, P. & Parzóch, K. (2021). Enigmatic clusters of sandstone boulders on plateaus of the Stołowe Mountains (Sudetes, south-west Poland) – their geoheritage and geotouristic value. *Geologos*, 27, 141–155.

Muhs, D.R. & Benedict, J.B. (2006). Eolian additions to late quaternary alpine soils, Indian peaks wilderness area, Colorado front range. *Arctic, Antarctic, and Alpine Research*, 38, 120–130.

Munsell Color Company (Ed.). (1975). *Munsell soil color charts*. Munsell Color Company, Baltimore, MD.

Munyikwa, K., Kinnaird, T.C. & Sanderson, D.C.W. (2021). The potential of portable luminescence readers in geomorphological investigations: a review. *Earth Surface Processes and Landforms*, 46, 131–150.

Musielok, Ł., Buczek, K. & Karcz, T. (2022). Relief-induced feedback mechanisms controlling local podzolization occurrence on flysch slopes–Examples from Outer Western Carpathians (southern Poland). *CATENA*, 213, 106124.

Nesbitt, Hw. & Young, G.M. (1982). Early Proterozoic climates and plate motions inferred from major element chemistry of lutites. *nature*, 299, 715–717.

Nesbitt, H.W. & Young, G.M. (1984). Prediction of some weathering trends of plutonic and volcanic rocks based on thermodynamic and kinetic considerations. *Geochimica et Cosmochimica Acta*, 48, 1523–1534.

Nesbitt, H.W. & Young, G.M. (1989). Formation and Diagenesis of Weathering Profiles. *The Journal of Geology*, 97, 129–147.

Norton, D.A. (1989). Tree windthrow and forest soil turnover. *Can. J. For. Res.*, 19, 386–389.

Ortofotomapa. (2023). .

Pain, C. (1986). Scarp retreat and slope development near picton, New South Wales, Australia. *Catena*, 13, 227–239.

Pansu, M. & Gautheyrou, J. (2006). *Handbook of Soil Analysis*. Springer, Berlin, Heidelberg.

Parfitt, R. & Henmi, T. (1982). Comparison of an oxalate-extraction methon and an infrared spectroscopic method for determining allophane in soll clays. *Soil Science and Plant Nutrition*, 28, 183–190.

Parker, A. (1970). An index of weathering for silicate rocks. *Geological Magazine*, 107, 501–504.

Parzóch, K. (2001). Współczesne procesy geomorfologiczne w Karkonoszach w warunkach antropopresji [Contemporary geomorphic processes in the Karkonosze Mts under human impact].

Parzóch, K. & Migoń, P. (2015). Deciphering the origin of allochthonous sandstone boulder trains within a mudstone escarpment, Stołowe Mountains, SW Poland. *zfg_suppl*, 59, 103–122.

Pawlak, W., Anioł-Kwiatkowska, J., Pawlak, J., Nowak-Ferdhus, E., Migoń, P., Malicka, A., *et al.* (2008). Atlas of Lower and Opole Silesia. *Wrocław: University of Wrocław*.

Pawlik, Ł. (2013). The role of trees in the geomorphic system of forested hillslopes — A review. *Earth-Science Reviews*, 126, 250–265.

Pawlik, Ł. (2014). Biogenic Imprint on Hillslopes in the Sudety Mts. — Origin and Consequences of the Tree Uprooting Process. *Studia Geomorphologica Carpatho-Balcanica*, 48.

Pawlik, Ł., Gruba, P., Gałązka, A., Marzec-Grządziel, A., Kupka, D., Szopa, K., *et al.* (2023). Weathering and soil production under trees growing on sandstones – The role of tree roots in soil formation. *Science of The Total Environment*, 902, 166002.

Pawlik, Ł. & Kasprzak, M. (2015). Electrical resistivity tomography (ERT) of pit-and-mound microrelief, Mt Rogowa Kopa case study, the Stołowe Mountains, SW Poland. *Landform Analysis*, 29, 41–47.

Pawlik, Ł., Migoń, P., Owczarek, P. & Kacprzak, A. (2013). Surface processes and interactions with forest vegetation on a steep mudstone slope, Stołowe Mountains, SW Poland. *CATENA*, 109, 203–216.

Pawlik, Ł., Migoń, P. & Szymanowski, M. (2016). Local- and regional-scale biomorphodynamics due to tree uprooting in semi-natural and managed montane forests of the Sudetes Mountains, Central Europe: Biomorphodynamics due to tree uprooting. *Earth Surf. Process. Landforms*, 41, 1250–1265.

Pawlik, Ł., Musielok, Ł., Migoń, P., Wrońska-Wałach, D., Duszyński, F. & Kasprzak, M. (2017). Deciphering the history of forest disturbance and its effects on landforms and soils – lessons from a pit-and-mound locality at Rogowa Kopa, Sudetes, SW Poland. *Bulletin of Geography. Physical Geography Series*, 12, 59–81.

Pawlik, Ł. & Šamonil, P. (2018). Soil creep: The driving factors, evidence and significance for biogeomorphic and pedogenic domains and systems – A critical literature review. *Earth-Science Reviews*, 178, 257–278.

Peterson, C.J. & Pickett, S.T.A. (1990). Microsite and elevational influences on early forest regeneration after catastrophic windthrow. *Journal of Vegetation Science*, 1, 657–662.

Phillips, J.D. (2007). Development of texture contrast soils by a combination of bioturbation and translocation. *CATENA*, 70, 92–104.

Phillips, J.D. & Lorz, C. (2008). Origins and implications of soil layering. *Earth-Science Reviews*, 89, 144–155.

Phillips, J.D., Luckow, K., Marion, D.A. & Adams, K.R. (2005). Rock fragment distributions and regolith evolution in the Ouachita Mountains, Arkansas, USA. *Earth Surface Processes and Landforms*, 30, 429–442.

Phillips, J.D., Šamonil, P., Pawlik, Ł., Trochta, J. & Daněk, P. (2017). Domination of hillslope denudation by tree uprooting in an old-growth forest. *Geomorphology*, 276, 27–36.

Piccini, L. & Mecchia, M. (2009). Solution weathering rate and origin of karst landforms and caves in the quartzite of Auyan-tepui (Gran Sabana, Venezuela). *Geomorphology*, 106, 15–25.

Poesen, J. & Lavee, H. (1994). Rock fragments in top soils: significance and processes. *CATENA*, Rock Fragments in Soil: Surface Dynamics, 23, 1–28.

Portenga, E.W. & Bierman, P.R. (2011). Understanding Earth's eroding surface with 10Be. *GSAT*, 21, 4–10.

Portes, R., Dahms, D., Brandová, D., Raab, G., Christl, M., Kühn, P., *et al.* (2018). Evolution of soil erosion rates in alpine soils of the Central Rocky Mountains using fallout Pu and δ13C. *Earth and Planetary Science Letters*, 496, 257–269.

Price, J.R. & Velbel, M.A. (2003). Chemical weathering indices applied to weathering profiles developed on heterogeneous felsic metamorphic parent rocks. *Chemical Geology*, Controls on Chemical Weathering, 202, 397–416.

Pulinowa, M.Z. (1989). *Rzeźba Gór Stołowych [The relief of the Stołowe Mountains]*. Uniwersytet Śląski.

Raab, G., Scarciglia, F., Norton, K., Dahms, D., Brandová, D., Portes, R. de C., *et al.* (2018). Denudation variability of the Sila Massif upland (Italy) from decades to millennia using 10Be and 239+240Pu. *Land Degradation & Development*, 29, 3736–3752.

Raab, T. & Völkel, J. (2003). Late Pleistocene glaciation of the Kleiner Arbersee area in the Bavarian Forest, south Germany. *Quaternary Science Reviews*, 22, 581–593.

Reczyńska, K. & Świerkosz, K. (2012). Remarks about the diversity of mountain Norway spruce forest in the Sudetes, with particular reference to the Szczeliniec Massif (Stołowe Mts, Poland). In: *Proceedings of the 3rd International Conference on Sandstone Landscapes*. Presented at the Sandstone Landscapes: Diversity, Ecology and Conservation, [object Object], Kudowa-Zdrój (Poland), p. 1143585 Bytes.

Rhodes, E.J. (2011). Optically stimulated luminescence dating of sediments over the past 200,000 years. *Annual Review of Earth and Planetary Sciences*, 39, 461–488.

Rotnicka, J. (2007). Cykle transgresywne i regresywne w drobnoziarnistych sukcesjach osadowych na przykładzie górnokredowych margli plenerskich (Góry Stołowe, Sudety)[Transgressive and regressive cycles in fine-grained rocks successions: an example from the Upper Cretaceous Plänermergel (Góry Stołowe Mts., Sudetes)]. *Sedimentologica*, 1, 18–30.

Šamonil, P., Antolík, L., Svoboda, M. & Adam, D. (2009). Dynamics of windthrow events in a natural fir-beech forest in the Carpathian mountains. *Forest Ecology and Management*, 257, 1148–1156.

Šamonil, P., Daněk, P., Adam, D. & Phillips, J.D. (2017). Breakage or uprooting: How tree death type affects hillslope processes in old-growth temperate forests. *Geomorphology*, 299, 76–84.

Šamonil, P., Daněk, P., Senecká, A., Adam, D. & Phillips, J.D. (2018). Biomechanical effects of trees in an old-growth temperate forest: Biomechanical effects of trees. *Earth Surface Processes and Landforms*, 43, 1063–1072.

Šamonil, P., Egli, M., Steinert, T., Norton, K., Abiven, S., Daněk, P., *et al.* (2019). Soil denudation rates in an old-growth mountain temperate forest driven by tree uprooting dynamics, Central Europe. *Land Degradation & Development*, 31, 222–239.

Šamonil, P., Vašíčková, I., Daněk, P., Janík, D. & Adam, D. (2014). Disturbances can control fine-scale pedodiversity in old-growth forests: is the soil evolution theory disturbed as well? *Biogeosciences*, 11, 5889–5905.

Sanderson, D.C. & Murphy, S. (2010). Using simple portable OSL measurements and laboratory characterisation to help understand complex and heterogeneous sediment sequences for luminescence dating. *Quaternary Geochronology*, 5, 299–305.

Sauer, D., Sponagel, H., Sommer, M., Giani, L., Jahn, R. & Stahr, K. (2007). Podzol: Soil of the Year 2007. A review on its genesis, occurrence, and functions. *Journal of Plant Nutrition and Soil Science*, 170, 581–597.

Saunders, I. & Young, A. (1983). Rates of surface processes on slopes, slope retreat and denudation. *Earth Surface Processes and Landforms*, 8, 473–501.

Schaetzl, R.J. & Anderson, S. (2005). *Soils: genesis and geomorphology*. Cambridge University Press, Cambridge ; New York.

Schaetzl, R.J., Johnson, D.L., Burns, S.F. & Small, T.W. (1989). Tree uprooting: review of terminology, process, and environmental implications. *Canadian Journal of Forest Research*, 19, 1–11.

Schlichting, E. & Schweikle, V. (1980). Interpedon translocations and soil classification. *Soil Science*, 130, 200–204.

Singer, M.J. & Blackard, J. (1982). Slope angle-interrill soil loss relationships for slopes up to 50%. *Soil Science Society of America Journal*, 46, 1270–1273.

Small, T.W., Schaetzl, R.J. & Brixie, J.M. (1990). Redistribution and Mixing of Soil Gravels by Tree Uprooting∗. *The Professional Geographer*, 42, 445–457.

Smithson, P., Addison, K. & Atkinson, K. (2013). *Fundamentals of the Physical Environment: Fourth Edition*. Routledge.

Sobik, M. & Błaś, M. (2010). Wyjątkowe zdarzenia meteorologiczne (Extreme meteorological events). *Wyjątkowe zdarzenia przyrodnicze na Dolnym Śląsku i ich skutki, Rozprawy naukowe Instytutu Geografii i Rozwoju Regionalnego*, 14, 35–80.

Sommer, M., Halm, D., Geisinger, C., Andruschkewitsch, I., Zarei, M. & Stahr, K. (2001). Lateral podzolization in a sandstone catchment. *Geoderma*, 103, 231–247.

Sommer, M., Halm, D., Weller, U., Zarei, M. & Stahr, K. (2000). Lateral Podzolization in a Granite Landscape. *Soil Science Society of America Journal*, 64, 1434–1442.

Stiles, C.A., Mora, C.I. & Driese, S.G. (2003). Pedogenic processes and domain boundaries in a Vertisol climosequence: evidence from titanium and zirconium distribution and morphology. *Geoderma*, 116, 279–299.

Strzyżowski, D. (2021). The role of tree uprooting in the transporting of sediment and mixing of soil in the Tatra Mountains. *J. Mt. Sci.*, 18, 38–50.

Strzyżowski, D., Fidelus, J. & Żelazny, M. (2016). Geomorphological changes within a hillslope caused by a windthrow event in the tatra mountains, southern poland. *Geografiska Annaler: Series A, Physical Geography*, 98, 347–360.

Strzyżowski, D., Fidelus-Orzechowska, J. & Żelazny, M. (2018). Sediment transport by uprooting in the forested part of the Tatra Mountains, southern Poland. *CATENA*, 160, 329–338.

Synowiec, G. (1999). Rock mass strength assessment for geomorphological purposes and its application to sandstone slopes in the Stołowe Mountains. *Czasopismo Geograficzne*, 70, 351–361.

Szopka, K., Karczewska, A., Jezierski, P. & Kabała, C. (2013). Spatial distribution of lead in the surface layers of mountain forest soils, an example from the Karkonosze National Park, Poland. *Geoderma*, 192, 259–268.

Szymanowski, M., Jancewicz, K., Różycka, M. & Migoń, P. (2019). Geomorphometry-based detection of enhanced erosional signal in polygenetic medium-altitude mountain relief and its tectonic interpretation, the Sudetes (Central Europe). *Geomorphology*, 341.

Tamm, O. (1922). Eine Methode zur Bestimmung des anorganischen Gelkomplexes im Boden. *Meddelanden från Statens Skogsförsöksanstalt*, 19, 385–404.

Taylor, S.R. & McLennan, S.M. (1985). The continental crust: its composition and evolution.

Topographic map. (2023). .

Traczyk, A. & Migoń, P. (2003). Cold-climate landform patterns in the Sudetes. Effects of lithology, relief and glacial history. *Acta Universitatis Carolinae, Geographica*, 35, 185–210.

Treml, V., Jankovská, V. & Petr, L. (2006). Holocene timberline fluctuations in the mid-mountains of Central Europe. *Fennia-International Journal of Geography*, 184, 107–119.

Valtera, M. & Schaetzl, R.J. (2017). Pit-mound microrelief in forest soils: Review of implications for water retention and hydrologic modelling. *Forest Ecology and Management*, 393, 40–51.

Van Vliet-Lanoë, B. (1998). Frost and soils: implications for paleosols, paleoclimates and stratigraphy. *CATENA*, 34, 157–183.

Vanacker, V., Bellin, N., Molina, A. & Kubik, P.W. (2014). Erosion regulation as a function of human disturbances to vegetation cover: a conceptual model. *Landscape Ecology*, 29, 293–309.

Verbovšek, T. (2011). A comparison of parameters below the limit of detection in geochemical analyses by substitution methods. *Materials and Geoenvironment*, 58, 393–404.

Wada, K. (1977). Allophane and Iimogolite. In 'Minerals in soil environments'.(Eds RC Dinauer, J Nagler, JH Nauseef) pp. 603–638. *Soil Science Society of America: Madison*.

Walczak, W. (1963). Geneza form skalnych na północno-wschodniej krawędzi Gór Stołowych [The origin of rock-forms on the NE ridge of the Stołowe Mountains]. *Acta Universitatis Wratislaviensis*, 9, 191–200.

Wallbrink, P.J. & Murray, A.S. (1993). Use of fallout radionuclides as indicators of erosion processes. *Hydrological Processes*, 7, 297–304.

Walling, D.E. & He, Q. (1999). Improved models for estimating Soil erosion rates from Cesium-137 measurements. *Journal of Environmental Quality*, 28, 611–622.

Walling, D.E. & Quine, T.A. (1990). Calibration of caesium-137 measurements to provide quantitative erosion rate data. *Land Degradation & Development*, 2, 161–175.

Waroszewski, J., Egli, M., Kabala, C., Kierczak, J. & Brandova, D. (2016). Mass fluxes and clay mineral formation in soils developed on slope deposits of the Kowarski Grzbiet (Karkonosze Mountains, Czech Republic/Poland). *Geoderma*, Soil mapping, classification, and modelling: history and future directions, 264, 363–378.

Waroszewski, J., Kabala, C. & Jezierski, P. (2015a). Relief-induced soil differentiation at the sandstone-mudstone contact in the Stołowe Mountains, SW Poland. *zfg_suppl*, 59, 209–224.

Waroszewski, J., Kabała, C. & Malkiewicz, M. (2012). Pollen spectra in the upper mineral horizons of Podzols in the Stołowe Mountains. In: *3rd International Conference on Sandstone Landscapes*. Presented at the Sandstone landscapes: diversity, ecology and conservation, Instytut Geografii i Rozwoju Regionalnego Uniwersytetu Wrocławskiego, Kudowa Zdrój (Poland).

Waroszewski, J., Kalinski, K., Malkiewicz, M., Mazurek, R., Kozlowski, G. & Kabala, C. (2013). Pleistocene–Holocene cover-beds on granite regolith as parent material for Podzols — An example from the Sudeten Mountains. *CATENA*, 104, 161–173.

Waroszewski, J., Malkiewicz, M., Mazurek, R., Labaz, B., Jezierski, P. & Kabala, C. (2015b). Lithological discontinuities in Podzols developed from sandstone cover beds in the Stołowe Mountains (Poland). *CATENA*, 126, 11–19.

Waroszewski, J., Szopka, K. & Kabala, C. (2009). Trace elements in soils of upper zone of spruce forest on Szrenica Mount and the Kowarski Grzbiet Range in the Karkonosze Mountains. *Journal of Elementology*, 14, 805–814.

Weber, J., Tyszka, R., Kocowicz, A., Szadorski, J., Debicka, M. & Jamroz, E. (2012). Mineralogical composition of the clay fraction of soils derived from granitoids of the Sudetes and Fore-Sudetic Block, southwest Poland. *European Journal of Soil Science*, 63, 762–772.

Wicik, B. (1986). Asynchronicznosé procesow wietrzenia i sedymentacji w zbiornikach jeziornych Tatr i karkonoszy w postglacjale [Asynchrony of weathering and sedimentation processes in lake reservoirs of the Tatra Mountains and the Karkonosze Mountains in the post-glacial period]. *Przegląd geograficzny*, 58, 809–823.

Wojewoda, J. (1997). Upper Cretaceous littoral-to-shelf succession in the Intrasudetic Basin and Nysa Trough, Sudety Mts. In: *Source Areas: Signals in Sediments [Obszary źródłowe: zapis w osadach]*. WIND, Wrocław., pp. 81–96.

Wojewoda, J. (2011). *Geoatrakcje Gór Stołowych: przewodnik geologiczny po Parku Narodowym Gór Stołowych [Geoattractions of the Stołowe Mountains: geological guide to the Stołowe Mountains National Park]*. Park Narodowy Gór Stołowych.

Wojewoda, J., Bialek, D., Bucha, M., Głuszyński, A., Gotowala, R., Krawczewski, J., *et al.* (2011). Geologia Parku Narodowego Gór Stołowych - wybrane zagadnienia [Geology of the Stołowe

Mountains National Park - selected issues]. *Geoekologiczne Warunki Środowiska Przyrodniczego PNGS*, 53–96.

Wray, R.A.L. & Sauro, F. (2017). An updated global review of solutional weathering processes and forms in quartz sandstones and quartzites. *Earth-Science Reviews*, 171, 520–557.

Zawieja, B. & Glina, B. (2017). Application of multivariate statistical methods in the assessment of mountain organic soil transformation in the central Sudetes. *Biometrical Letters*, 54, 43–59.

Zhang, X., Higgitt, D.L. & Walling, D.E. (1990). A preliminary assessment of the potential for using caesium-137 to estimate rates of soil erosion in the Loess Plateau of China. *Hydrological Sciences Journal*, 35, 243–252.

Zhang, X.B., Walling, D.E. & He, Q. (1999). Simplified mass balance models for assessing soil erosion rates on cultivated land using caesium-137 measurements. *Hydrological Sciences Journal*, 44, 33–45.

Zingg, A.W. (1940). Degree and length of land slope as it affects soil loss in run-off. *Agric. Engng.*, 21, 59–64.

ACKNOWLEDGEMENTS

This study was carried out as a master's thesis at the University of Zurich, and I would like to thank my alma mater for the wide range of courses and excursions I was given the opportunity to participate.

I would like to express my gratitude to Prof. Dr. Markus Egli for providing me with the opportunity to work on this research project, for the organization of the sampling and his support in the field work.

I am also grateful to Dr. Filip Duszyński for his assistance in understanding the morphology of the Stołowe Mountains. The preparation on site, his extensive help during the fieldwork and provisioning with the relevant literature have been essential.

For his expert instruction and steadfast support in the preparation and measurement of Pu isotope samples I would like to thank Dr. Dmitry Tikhomirov.

I am also thankful to Marysia Kotowska, Dr. Aleksandra Michniewicz, Dr. Kacper Jancewicz, and Dr. Jaroslaw Waroszewski for their invaluable help during our fieldwork. Their contributions have been vital in gathering and analyzing field data effectively. I'd also like to thank Dr. Kacper Jancewicz for the DEM he provided.

Special thanks to Yves Brügger, Trang Vu Bouquet and Barbara Siegfried for their support in the Geography Laboratories. Their assistance with sample preparations and measurements has been greatly appreciated.

GLOSSARY

a.s.l.	above sea level
AAS	atomic absorption spectrometry
CIA	Chemical Index of Alteration
CIW	Chemical Index of Weathering
DBH	diameter at breast height
DEM	digital elevation model
FAO	Food and Agriculture Organization of the United Nations
FRN	fallout radionuclides
IM	Inventory Method
IRSL	infrared stimulated luminescence
IUSS	International Union of Soil Sciences
LiDAR	light detection and ranging
LOD	limit of detection
LOI	loss on ignition
MODERN	Modelling Deposition and Erosion rates with Radionuclides
OSL	optical stimulated luminescence
P factor	particle size correction factor
PDM	Profile Distribution Method
rpm	rounds per minute
rps	rounds per second
RSD	relative standard deviation
sd	standard deviation
TWI	Topographic Wetness Index

WIP Weathering Index of Parker

WRB World Reference Base for Soil Resources

XRF X-ray fluorescence spectroscopy

FIGURES

Figure 1: Conceptual model of in situ disintegration according to (Duszyński & Migoń 2015) (modified after Duszyński et al. (2019)). 4

Figure 2: Location of the study area and the topographic cross-section (red line) in the Stołowe Góry National Park ("Topographic map" 2023). 11

Figure 3: Relief models and geomorphometric parametrization of land surface of the study areas based on 1 × 1 m DEM built from LiDAR data (modified after Kasprzak & Migoń (2015a)). 13

Figure 4: Extract of the detailed geological map of Poland 1:50'000 and cross-section line A–B (modified after (Cymerman 2019)) 14

Figure 5: Geological cross-section A–B (modified after (Cymerman 2019)) 15

Figure 6: Extract of the legend of the detailed geological map of Poland 1:50'000 (modified after (Cymerman 2019)). 15

Figure 7: Stratigraphy of the Stołowe Mountains tableland (left) and geological boundaries on cross-sections of Urwisko Batorowskie (right) with its position in respect to the stratigraphic column (modified after Wojewoda et al. (2011) and Migoń & Kasprzak (2016)). 16

Figure 8: Electrical resistivity tomography (ERT) at Urwisko Batarowskie (modified after Duszyński et al. (2016)) 17

Figure 9: Orthophoto ("Ortofotomapa" 2023) with sampling sites P1–P8 (red points) and cross-section (red line) at the southwestern slope of Urwisko Batarowskie. 24

Figure 10: Relief from Digital elevation model (DEM) ("Digital Terrain Model" 2023) with sampling sites P1–P8 (red points) and cross-section (red line) at the southwestern slope of Urwisko Batarowskie. 25

Figure 11: Longitudinal slope profile of the topography and relative position of the sampling sites P1–P8 at the southwestern slope of Urwisko Batarowskie (height exaggeration 2:1). 25

Figure 12: Bulk density as a function of depth in soil profiles P1–P8. 40

Figure 13: Skeletal fraction as a function of depth in soil profiles P1–P8. 41

Figure 14: Fine earth grain size distribution as a function of depth in soil profiles P1–P8. 42

Figure 15: Clay content as a function of depth in soil profiles P1–P8. 43

Figure 16: Silt content as a function of depth in soil profiles P1–P8. 44

Figure 17: Sand content as a function of depth in soil profiles P1–P8. 45

Figure 18: Soil texture diagram. 46

Figure 19: Moist soil profile horizon colors in different depths of soil profiles P1–P8 47

Figure 20: Dry soil profile horizon colors in different depths of soil profiles P1–P8. 47

Figure 21: pH as a function of depth in soil profiles P1–P8. 48

Figure 22: Soil organic matter as a function of depth in soil profiles P1–P8. 49

Figure 23: The content of different oxides a)–k) as a function of depth in soil profiles P1–P8. 52

Figure 24: The content of a) amorphous Al and b) amorphous Fe and c) the displacement ratio of amorphous Al+1/2Fe as a function of depth in soil profiles P1–P8. 54

Figure 25: The Chemical Index of Alteration (CIA) as a function of depth in soil profiles P1–P8. 55

Figure 26: The Chemical Index of Weathering (CIW) as a function of depth in soil profiles P1–P8. 56

Figure 27: The Weathering Index of Parker (WIP) as a function of depth in soil profiles P1–P8. 57

Figure 28: (Ca+K)/Ti-Index as a function of depth in soil profiles P1–P8. 58

Figure 29: (Na+K)/Ti-Index as a function of depth in soil profiles P1–P8. 59

Figure 30: Infrared Stimulated Luminescence (IRSL) as a function of depth in soil profiles P1–P8. 60

Figure 31: Optical Stimulated Luminescence (OSL) as a function of depth in soil profiles P1–P8. 61

Figure 32: The ratio of IRSL to OSL (IRSL/OSL) as a function of depth in soil profiles P1–P8. 62

Figure 33: Distribution of $^{239+240}$Pu inventory with depth on eight sampling sites P1–P8 (a – h) and the reference sites R1 and R2 (i – j). The error bars indicate standard deviation. 66

Figure 34: Boxplot of $^{239+240}$Pu inventories of sampling sites P1–P8 and the reference site R1–R2 in four depths a) 0 to 5 cm, b) 5 to 10 cm, c) 10 to 15 cm, d) 15 to 20 cm and the e) average cumulative inventories. The error bars indicate standard deviation. 67

Figure 35: With MODERN created depth profiles of sampling site P1. 70

Figure 36: With MODERN created depth profiles of sampling site P2. 70

Figure 37: With MODERN created depth profiles of sampling site P3. 71

Figure 38: With MODERN created depth profiles of sampling site P4. 71

Figure 39: With MODERN created depth profiles of sampling site P5. 72

Figure 40: With MODERN created depth profiles of sampling site P6. 72

Figure 41: With MODERN created depth profiles of sampling site P7. 73

Figure 42: With MODERN created depth profiles of sampling site P8. 73

Figure 43: Comparison and linear regression of soil redistribution rates between PDM, IM and MODERN a)–e). 74

Figure 44: Comparison and linear regression of soil loss between IM and MODERN. 75

Figure 45: Correlation coefficient matrices showing relationships between properties of the sites of soil profiles P1–P8. The Spearman rank coefficient was applied. 76

Figure 46: Correlation coefficient matrices showing relationships between properties of soil horizons in soil profiles P1–P8. The Spearman rank coefficient was applied. 77

Figure 47: Relief cross-section with relative position of soil profiles P1–P8 at the southwestern slope of Urwisko Batarowskie (relief height exaggerated 2:1, soil profiles are not in scale). 79

Figure 48: Amorphous Al+1/2Fe in soil profiles P1–P8 in relative topographical position with indicated potential lateral podzolization. 85

Figure 49: Ratio of Infrared Stimulated Luminescence (IRSL) to Optical Stimulated Luminescence (OSL) in soil profiles P1–P8 in relative topographical position with boundary of older mineral surface and later deposited cover material. 88

Figure 50: Relief cross-section with calculated average soil erosion and deposition rates since 1963 on sampling sites P1–P8 at the southwestern slope of Urwisko Batarowskie (relief height exaggerated 2:1). 89

Figure 51: Parameters of soil profile P1. 146

Figure 52: Parameters of soil profile P2. 147

Figure 53: Parameters of soil profile P3. 148

Figure 54: Parameters of soil profile P4. 149

Figure 55: Parameters of soil profile P5. 150

Figure 56: Parameters of soil profile P6. 151

Figure 57: Parameters of soil profile P7. 152

Figure 58: Parameters of soil profile P8. 153

Figure 59: IRSL and OSL as a function of depth in soil profile P1. 176

Figure 60: IRSL and OSL as a function of depth in soil profile P2. 176

Figure 61: IRSL and OSL as a function of depth in soil profile P3. 177

Figure 62: IRSL and OSL as a function of depth in soil profile P4. 177

Figure 63: IRSL and OSL as a function of depth in soil profile P5. 178

Figure 64: IRSL and OSL as a function of depth in soil profile P6. 178

Figure 65: IRSL and OSL as a function of depth in soil profile P7. 179

Figure 66: IRSL and OSL as a function of depth in soil profile P8. 179

Figure 67: Munsell moist soil color in soil profiles P1–P8 in relative topographical position. 180

Figure 68: Munsell dry soil color in soil profiles P1–P8 in relative topographical position. 180

Figure 69: Munsell chroma moist in soil profiles P1–P8 in relative topographical position. 181

Figure 70: Munsell chroma dry in soil profiles P1–P8 in relative topographical position. 181

Figure 71: Munsell value moist in soil profiles P1–P8 in relative topographical position. 182

Figure 72: Munsell value dry in soil profiles P1–P8 in relative topographical position. 182

Figure 73: Bulk density in soil profiles P1–P8 in relative topographical position. 183

Figure 74: Rock fragment fraction in soil profiles P1–P8 in relative topographical position. 183

Figure 75: Clay content in soil profiles P1–P8 in relative topographical position. 184

Figure 76: Silt content in soil profiles P1–P8 in relative topographical position. 184

Figure 77: Sand content in soil profiles P1–P8 in relative topographical position. 185

Figure 78: pH in soil profiles P1–P8 in relative topographical position. 185

Figure 79: Soil organic matter in soil profiles P1–P8 in relative topographical position. 186

Figure 80: Al2O3 in soil profiles P1–P8 in relative topographical position. 187

Figure 81: CaO in soil profiles P1–P8 in relative topographical position. 187

Figure 82: Fe2O3 in soil profiles P1–P8 in relative topographical position. 188

Figure 83: K2O in soil profiles P1–P8 in relative topographical position. 188

Figure 84: MgO in soil profiles P1–P8 in relative topographical position. 189

Figure 85: MnO in soil profiles P1–P8 in relative topographical position. 189

Figure 86: Na2O in soil profiles P1–P8 in relative topographical position. 190

Figure 87: P2O5 in soil profiles P1–P8 in relative topographical position. 190

Figure 88: SiO2 in soil profiles P1–P8 in relative topographical position. 191

Figure 89: SO3 in soil profiles P1–P8 in relative topographical position. 191

Figure 90: TiO2 in soil profiles P1–P8 in relative topographical position. 192

Figure 91: Amorphous Fe in soil profiles P1–P8 in relative topographical position. 193

Figure 92: Amorphous Al in soil profiles P1–P8 in relative topographical position. 193

Figure 93: Chemical Index of Alteration (CIA) in soil profiles P1–P8 in relative topographical position. 194

Figure 94: Chemical Index of Weathering (CIW) in soil profiles P1–P8 in relative topographical position. 194

Figure 95: Weathering Index of Parker (WIP) in soil profiles P1–P8 in relative topographical position. 195

Figure 96: [CaKTi] -Index in soil profiles P1–P8 in relative topographical position. 195

Figure 97: [NaKTi]-Index in soil profiles P1–P8 in relative topographical position. 196

Figure 98: Infrared Stimulated Luminescence (IRSL) in soil profiles P1–P8 in relative topographical position. 197

Figure 99: Optical Stimulated Luminescence (OSL) in soil profiles P1–P8 in relative topographical position. 197

Figure 100: Cr in soil profiles P1–P8 in relative topographical position. 198

Figure 101: Cu in soil profiles P1–P8 in relative topographical position. 198

Figure 102: Pb in soil profiles P1–P8 in relative topographical position. 199

Figure 103: Zn in soil profiles P1–P8 in relative topographical position. 199

Figure 104: Zr in soil profiles P1–P8 in relative topographical position. 200

TABLES

Table 1: Coordinates of the sites soil profile (P1–P8) and the reference sampling sites (R1 and R2). 24

Table 2: Mass of molecules 29

Table 3: Soil profiles with classification and horizon designation according to IUSS Working Group WRB (2022) (see Appendix Appendix 4 and Appendix 5). 39

Table 4: Average and cumulative $^{239+240}$Pu inventories per depth increment of sampling sites P1–P8 and reference sites R1–R2 64

Table 5: Soil redistribution rates from IM (Lal *et al.* 2013), PDM (Walling & He 1999) and MODERN (Arata *et al.* 2016) in t ha^{-1} yr^{-1}. Negative values indicate soil erosion (loss) and positive values accumulation (gain). 69

Table 6: Soil loss and gain from IM (Lal *et al.* 2013) and MODERN (Arata *et al.* 2016) in cm. Negative values indicate soil erosion (loss) and positive values accumulation (gain). 69

Table 7: Munsell soil color, pH, and soil organic matter in soil profiles P1–P8 156

Table 8: Bulk density in soil profiles P1–P8 157

Table 9: Skeletal fraction in soil profiles P1–P8 157

Table 10: Grain size distribution in soil profiles P1–P8 158

Table 11: Soil texture in soil profiles P1–P8 160

Table 12: Oxides in soil profiles P1–P8 161

Table 13: Amorphous forms of iron and aluminium in soil profiles P1–P8 162

Table 14: Chemical Index of Alteration (CIA), Chemical Index of Weathering (CIW), Weathering Index of Parker (WIP), [CaKTi]-index and [NaKTi]-index in soil profiles P1–P8. 163

Table 15: Infrared (IRSL) and Optical Stimulated Luminescence (OSL) in soil profiles P1–P8 163

Table 16: $^{239+240}$Pu activity in soil profiles P1–P8 165

Table 17: Sum of $^{239+240}$Pu inventories per soil profile 169

Table 18: Correlation and p-values of selected site variables with a p-value ≤ 0.05. 170

Table 19: Correlation and p-values of selected horizon variables with a p-value ≤ 0.05 170

EQUATIONS

Equation 1: Bulk density 26

Equation 2: Skeletal fraction 26

Equation 3: Settling velocity 27

Equation 4: Chemical Index of Alteration (CIA) 29

Equation 5: Chemical Index of Weathering (CIW) 30

Equation 6: Weathering Index of Parker (WIP) 30

Equation 7: Ratio of calcium and potassium to titanium 30

Equation 8: Ratio of sodium and potassium to titanium 31

Equation 9: Inventory change 33

Equation 10: Inventory of $^{239+240}$Pu activities 34

Equation 11: Isotope inventory according to the profile distribution model (PDM) (Walling & He 1999) 34

Equation 12: Erosion rate according to the profile distribution model (PDM) (Walling & He 1999) 34

Equation 13: Soil erosion rates according to the inventory method (IM) (Lal *et al.* 2013) 35

Equation 14: Inventory of sampling site (Arata *et al.* 2016) 36

Equation 15: Simulated depth profile (Arata *et al.* 2016) 36

Equation 16: Distribution function (Arata *et al.* 2016) 36

Equation 17: Soil loss rates (Arata *et al.* 2016) 37

Equation 18: Substitution method for parameters below the limit of detection. 63

PHOTOS

Photo 1: The sandstone top of Szczeliniec Wielki in the Stołowe Mountains. 12

Photo 2: Escarpment of Urwisko Batorowskie at the study site with sandstone boulders and single-aged planted stands of Norway spruce. 19

Photo 3: Plateau of Urwisko Batorowskie at the study site with peatland vegetation of Wielkie Torfowisko Batorows-kie. 22

Photo 4: Picture of the site of soil profile P1. 131

Photo 5: Picture of the site of soil profile P2. 131

Photo 6: Picture of the site of soil profile P3. 132

Photo 7: Picture of the site of soil profile P4. 132

Photo 8: Picture of the site of soil profile P5. 133

Photo 9: Picture of the site of soil profile P6. 133

Photo 10: Picture of the site of soil profile P7. 134

Photo 11: Picture of the site of soil profile P8. 134

Photo 12: Picture of the reference site R1. 135

Photo 13: Picture of the reference site R2. 135

Photo 14: Picture of soil profile P1. 136

Photo 15: Picture of soil profile P2. 137

Photo 16: Picture of soil profile P3. 138

Photo 17: Picture of soil profile P4. 139

Photo 18: Picture of soil profile P5. 140

Photo 19: Picture of soil profile P6. 141

Photo 20: Picture of soil profile P7. 142

Photo 21: Picture of soil profile P8. 143

Photo 22: Picture of the soil at reference site R1. 144

Photo 23: Picture of the soil at reference site R2. 145

APPENDIX

APPENDIX 1 PICTURES OF THE SAMPLING SITES 131

APPENDIX 2 SOIL PROFILE AND SITE PICTURES 136

APPENDIX 3 GRAPHS OF PROPERTIES IN SOIL PROFILES 146

APPENDIX 4 MAIN SOIL HORIZON SYMBOLS 154

APPENDIX 5 SOIL HORIZON SYMBOL SUFFIXES 155

APPENDIX 6 TABLE OF MUNSELL SOIL COLOR, PH AND SOIL ORGANIC MATTER 156

APPENDIX 7 TABLE OF BULK DENSITY MEASUREMENTS 156

APPENDIX 8 TABLE OF SKELETAL FRACTION MEASUREMENTS 157

APPENDIX 9 TABLE OF GRAIN SIZE DISTRIBUTION 158

APPENDIX 10 TABLE OF SOIL TEXTURE 160

APPENDIX 11 TABLE OF OXIDES 161

APPENDIX 12 TABLE OF AMORPHOUS FORMS OF IRON AND ALUMINIUM 162

APPENDIX 13 TABLE OF WEATHERING INDICES 162

APPENDIX 14 TABLE OF INFRARED AND OPTICAL STIMULATED LUMINESCENCE 163

APPENDIX 15 TABLE OF $^{239+240}$PU ACTIVITY 165

APPENDIX 16 TABLE OF $^{239+240}$PU INVENTORY SUMS 169

APPENDIX 17 TABLE OF CORRELATION AND P-VALUES OF SITE VARIABLES 170

APPENDIX 18 TABLE OF CORRELATION AND P-VALUES OF HORIZON VARIABLES 170

APPENDIX 19 MODERN R CODE USED IN THIS STUDY 172

APPENDIX 20 FIGURES OF INFRARED AND OPTICAL STIMULATED LUMINESCENCE AS A FUNCTION OF DEPTH PER SOIL PROFILE 176

APPENDIX 21 FIGURES OF SOIL PROPERTIES IN RELATIVE TOPOGRAPHICAL POSITION 180

APPENDIX 22 FIGURES OF OXIDES IN SOIL PROFILES IN RELATIVE TOPOGRAPHICAL POSITION 187

APPENDIX 23 FIGURES OF AMORPHOUS FE AND AL IN SOIL PROFILES IN RELATIVE TOPOGRAPHICAL POSITION 193

APPENDIX 24 FIGURES OF WEATHERING INDICES IN SOIL PROFILES IN RELATIVE TOPOGRAPHICAL POSITION 194

APPENDIX 25 FIGURES OF LUMINESCENCE IN SOIL PROFILES IN RELATIVE TOPOGRAPHICAL POSITION 197

APPENDIX 26 FIGURES OF SELECTED ELEMENTS IN SOIL PROFILES IN RELATIVE TOPOGRAPHICAL POSITION..... 198

Appendix 1 PICTURES OF THE SAMPLING SITES

Photo 4: Picture of the site of soil profile P1.

Photo 5: Picture of the site of soil profile P2.

Photo 6: Picture of the site of soil profile P3.

Photo 7: Picture of the site of soil profile P4.

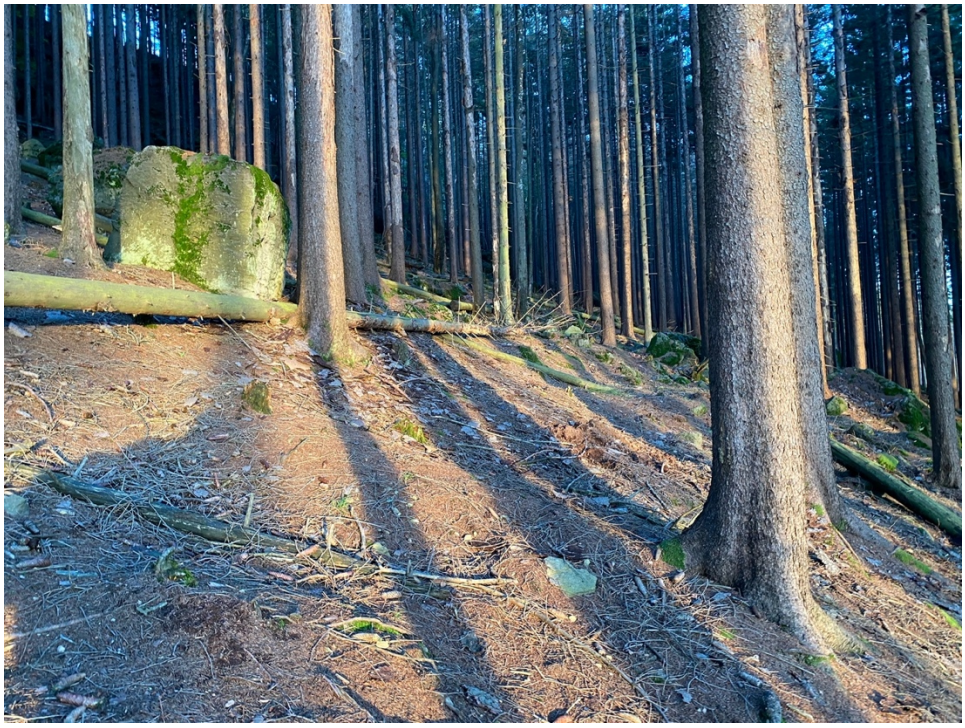

Photo 8: Picture of the site of soil profile P5.

Photo 9: Picture of the site of soil profile P6.

Photo 10: Picture of the site of soil profile P7.

Photo 11: Picture of the site of soil profile P8.

Photo 12: Picture of the reference site R1.

Photo 13: Picture of the reference site R2.

Appendix 2 SOIL PROFILE AND SITE PICTURES

Photo 14: Picture of soil profile P1.

Photo 15: Picture of soil profile P2.

Photo 16: Picture of soil profile P3.

Photo 17: Picture of soil profile P4.

Photo 18: Picture of soil profile P5.

Photo 19: Picture of soil profile P6.

Photo 20: Picture of soil profile P7.

Photo 21: Picture of soil profile P8.

Photo 22: Picture of the soil at reference site R1.

Photo 23: Picture of the soil at reference site R2.

Appendix 3 GRAPHS OF PROPERTIES IN SOIL PROFILES

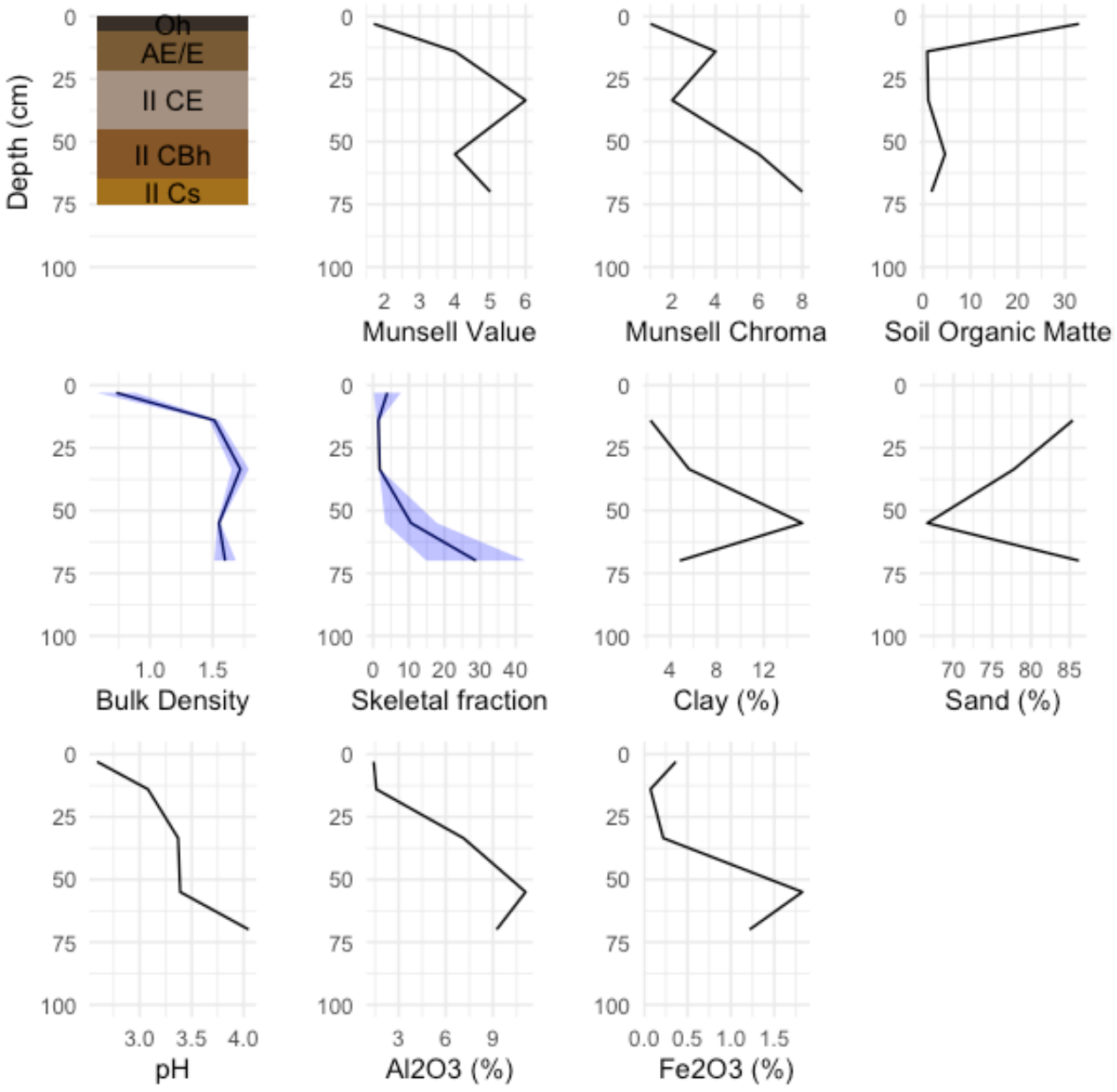

Figure 51: Parameters of soil profile P1.

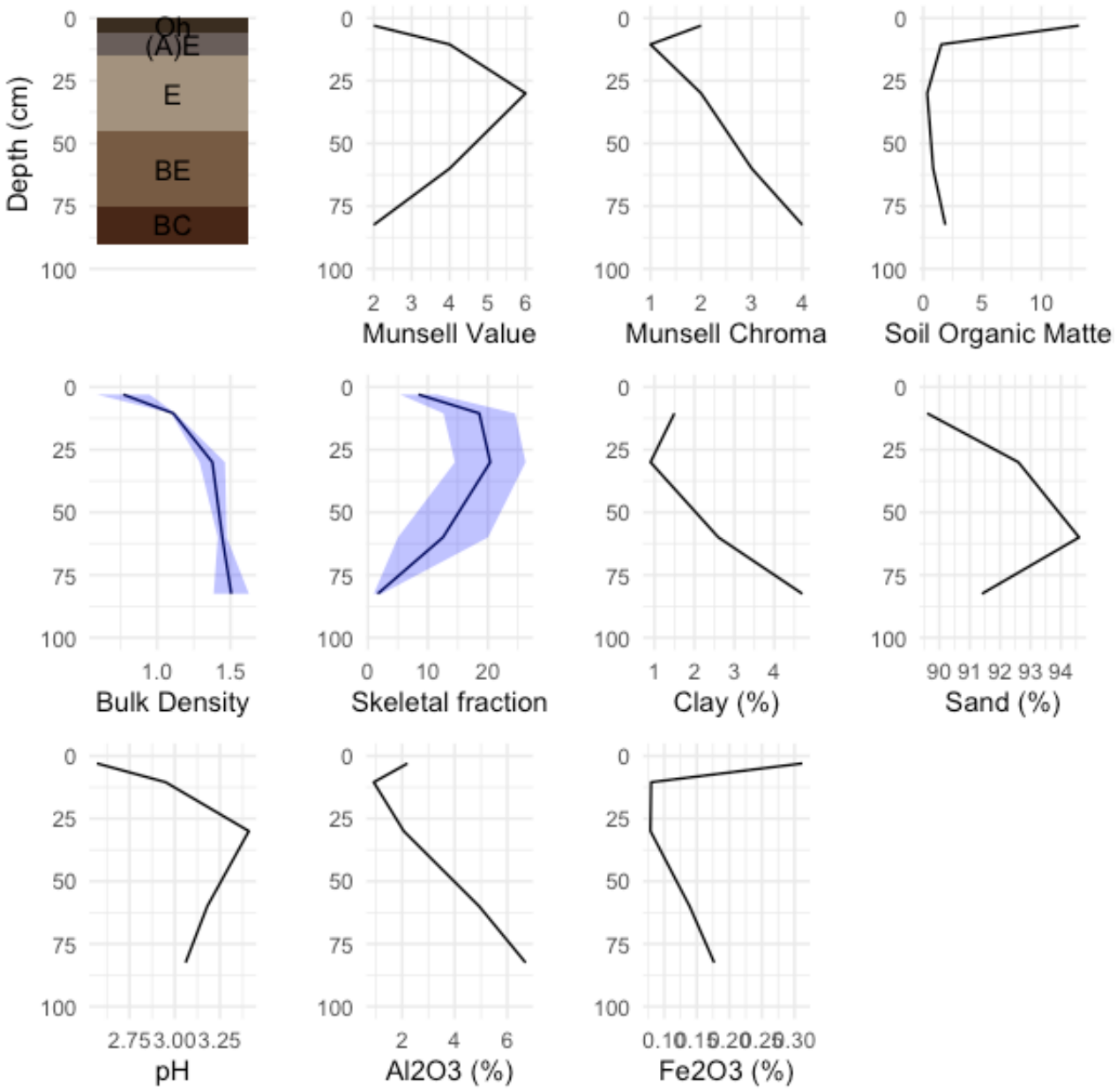

Figure 52: Parameters of soil profile P2.

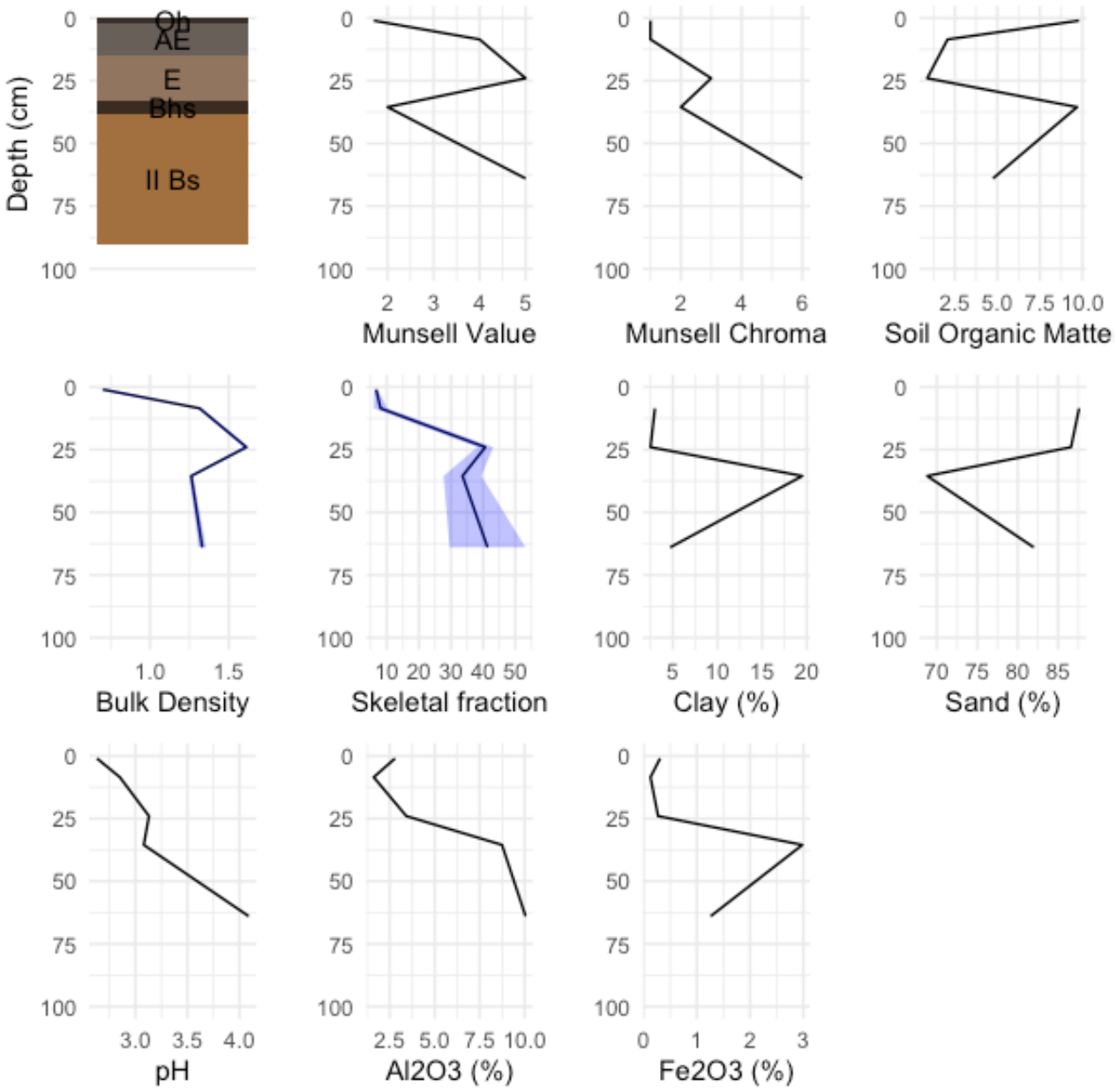

Figure 53: Parameters of soil profile P3.

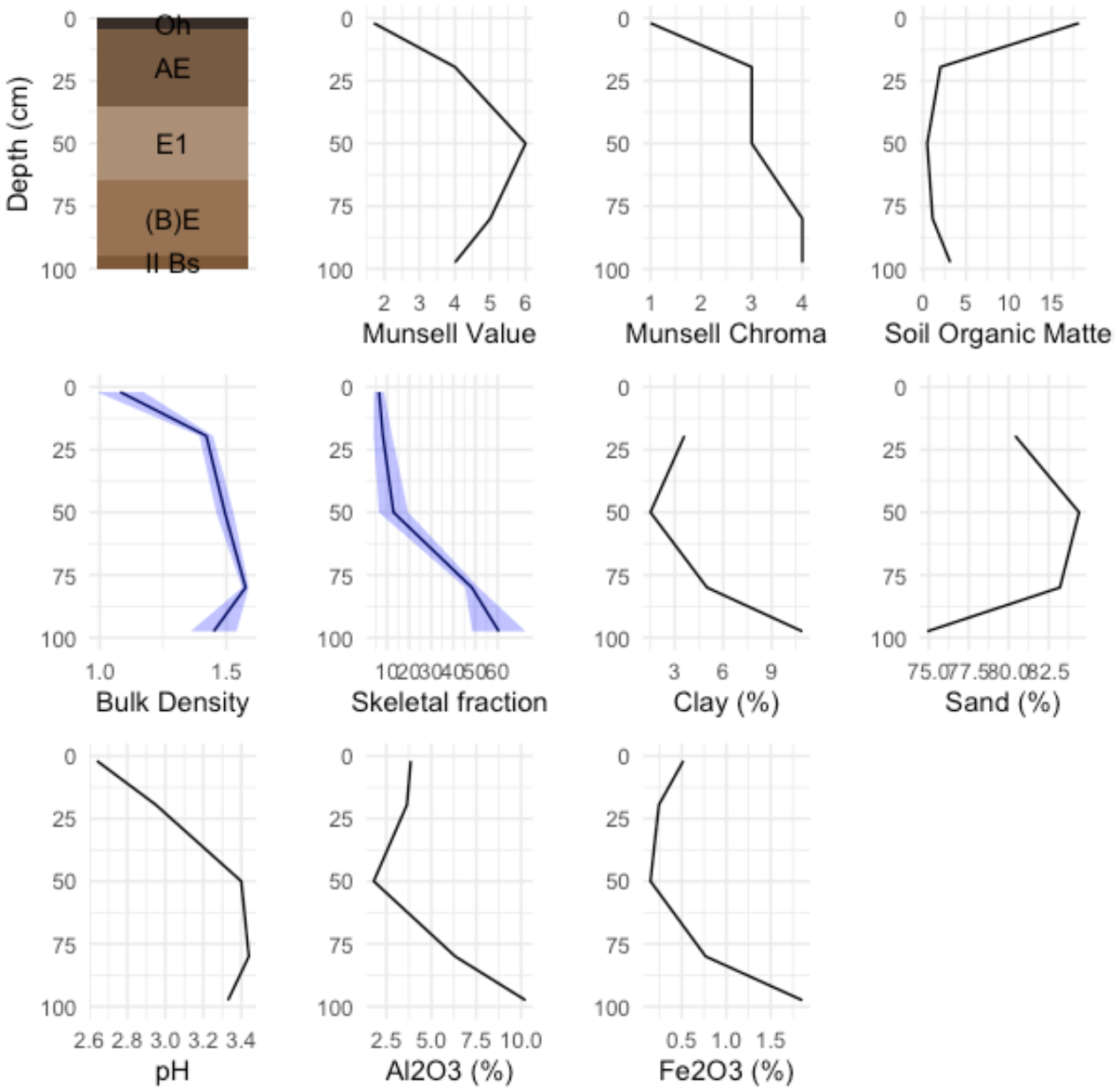

Figure 54: Parameters of soil profile P4.

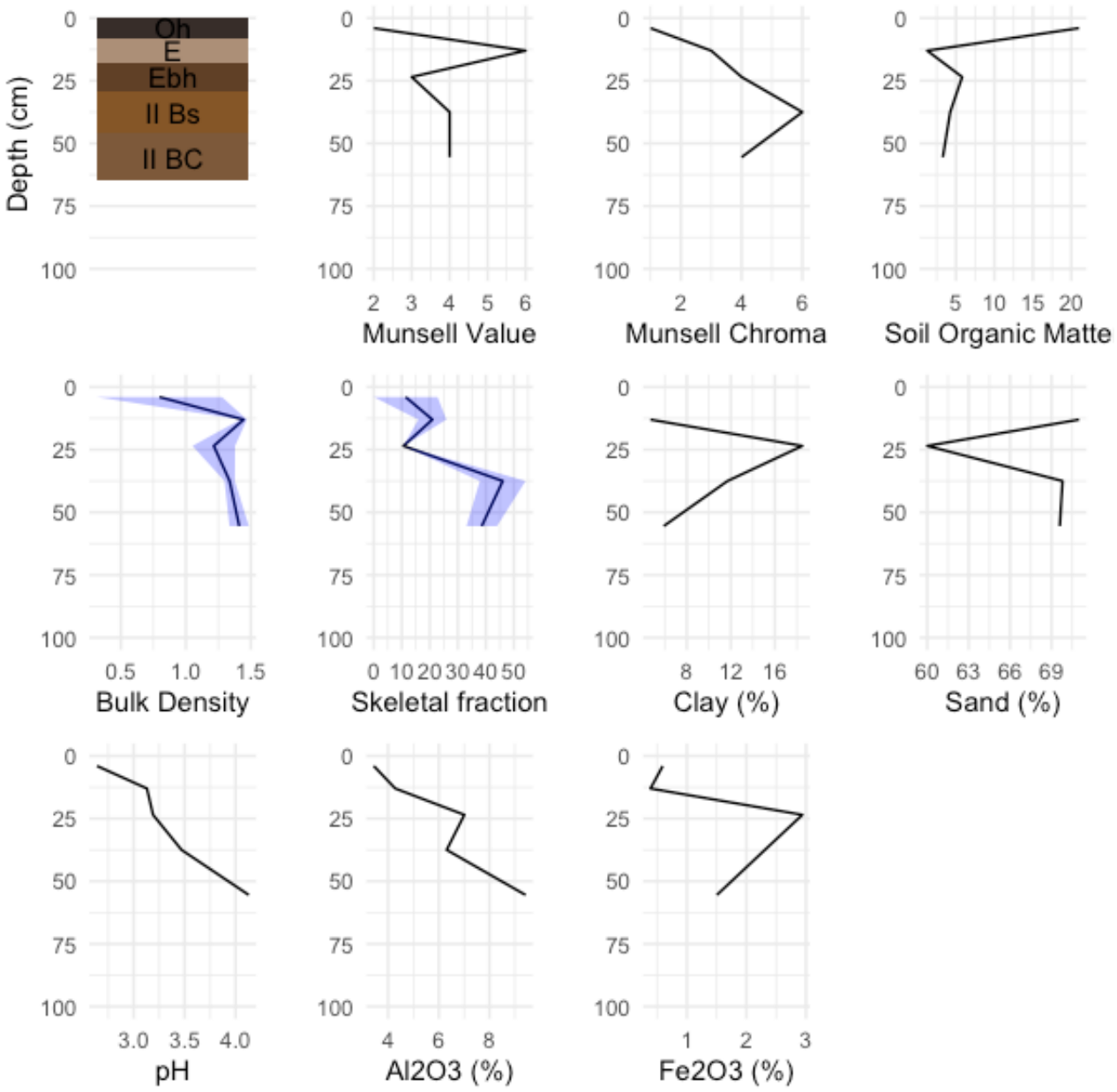

Figure 55: Parameters of soil profile P5.

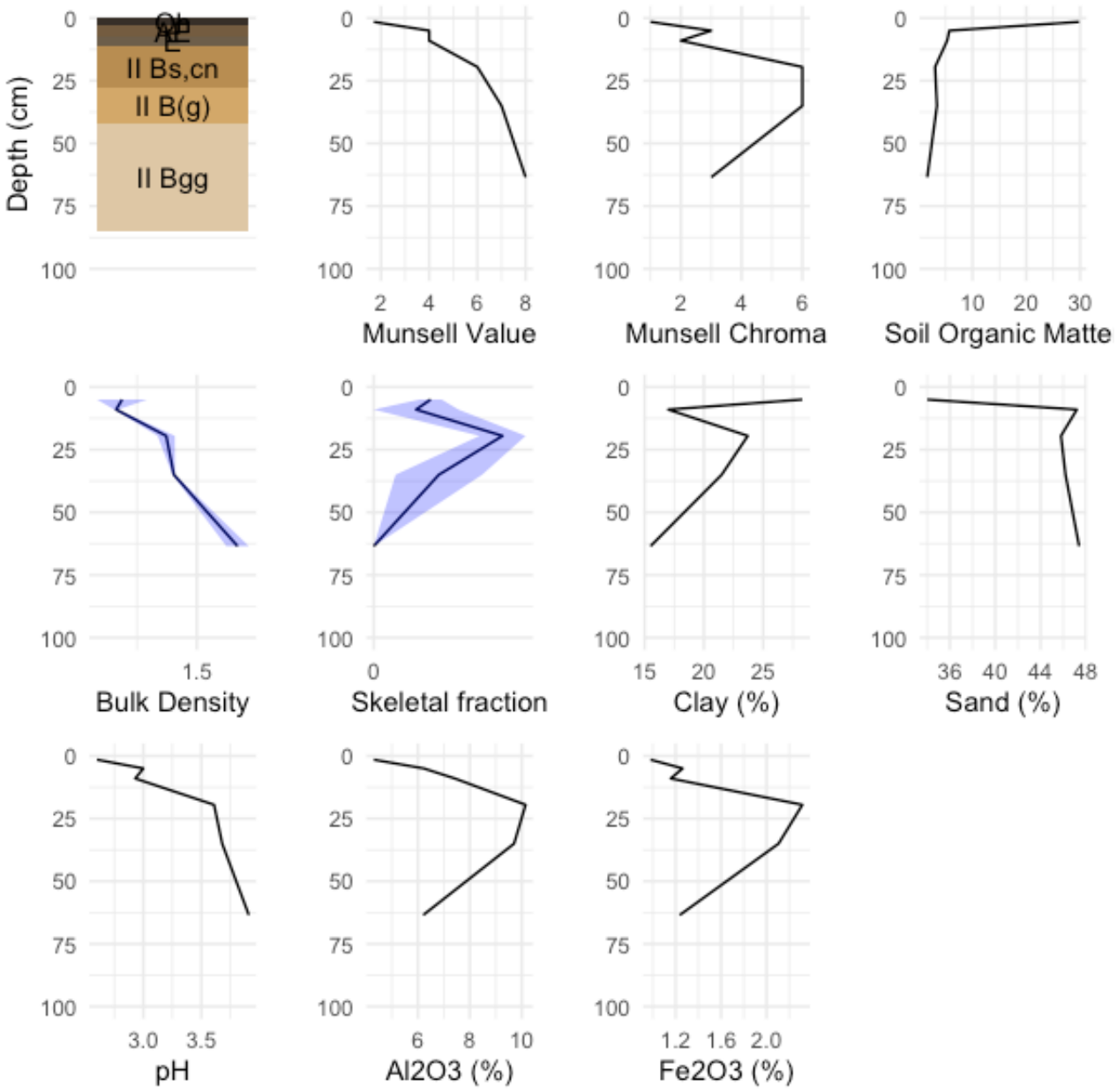

Figure 56: Parameters of soil profile P6.

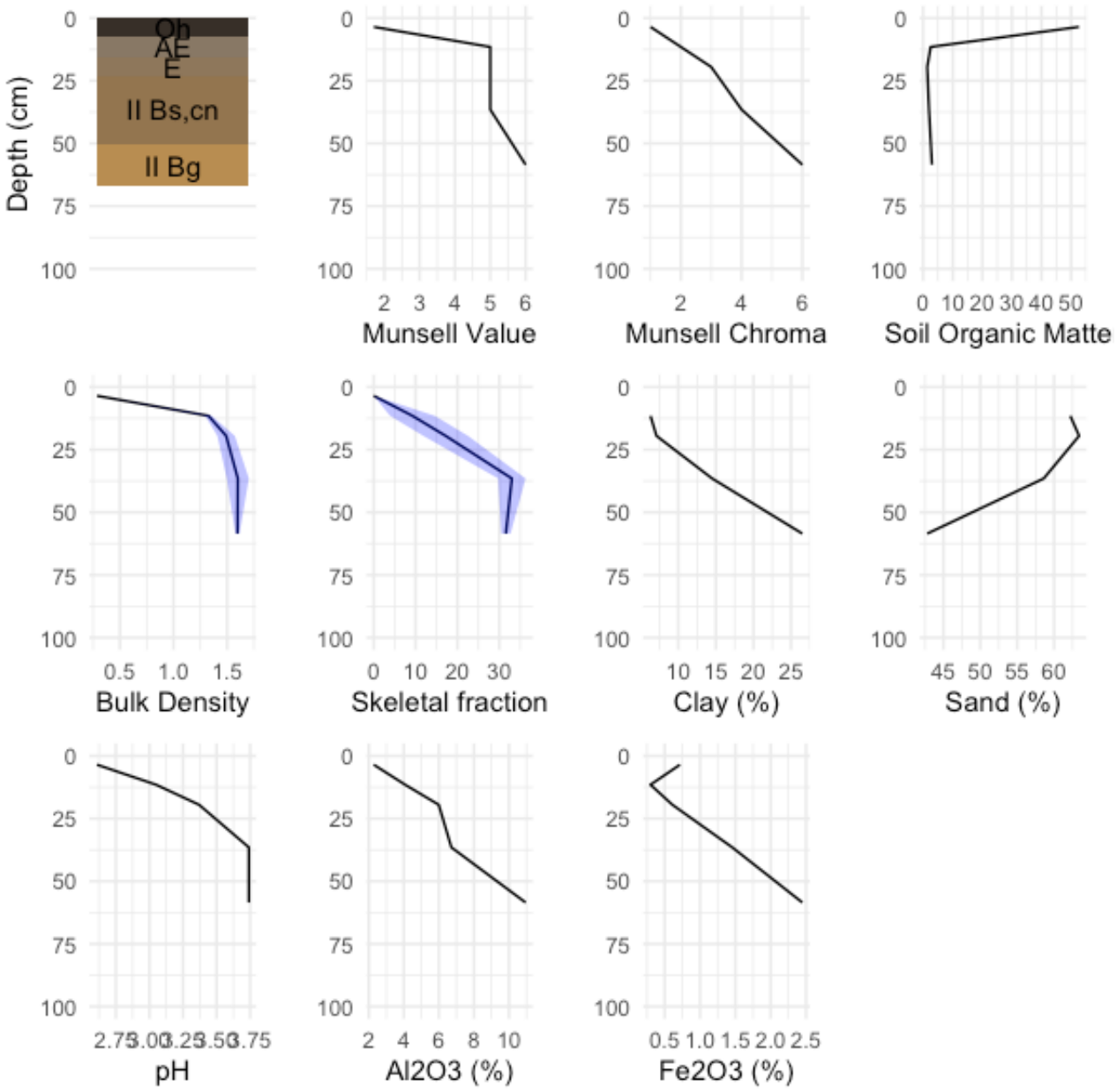

Figure 57: Parameters of soil profile P7.

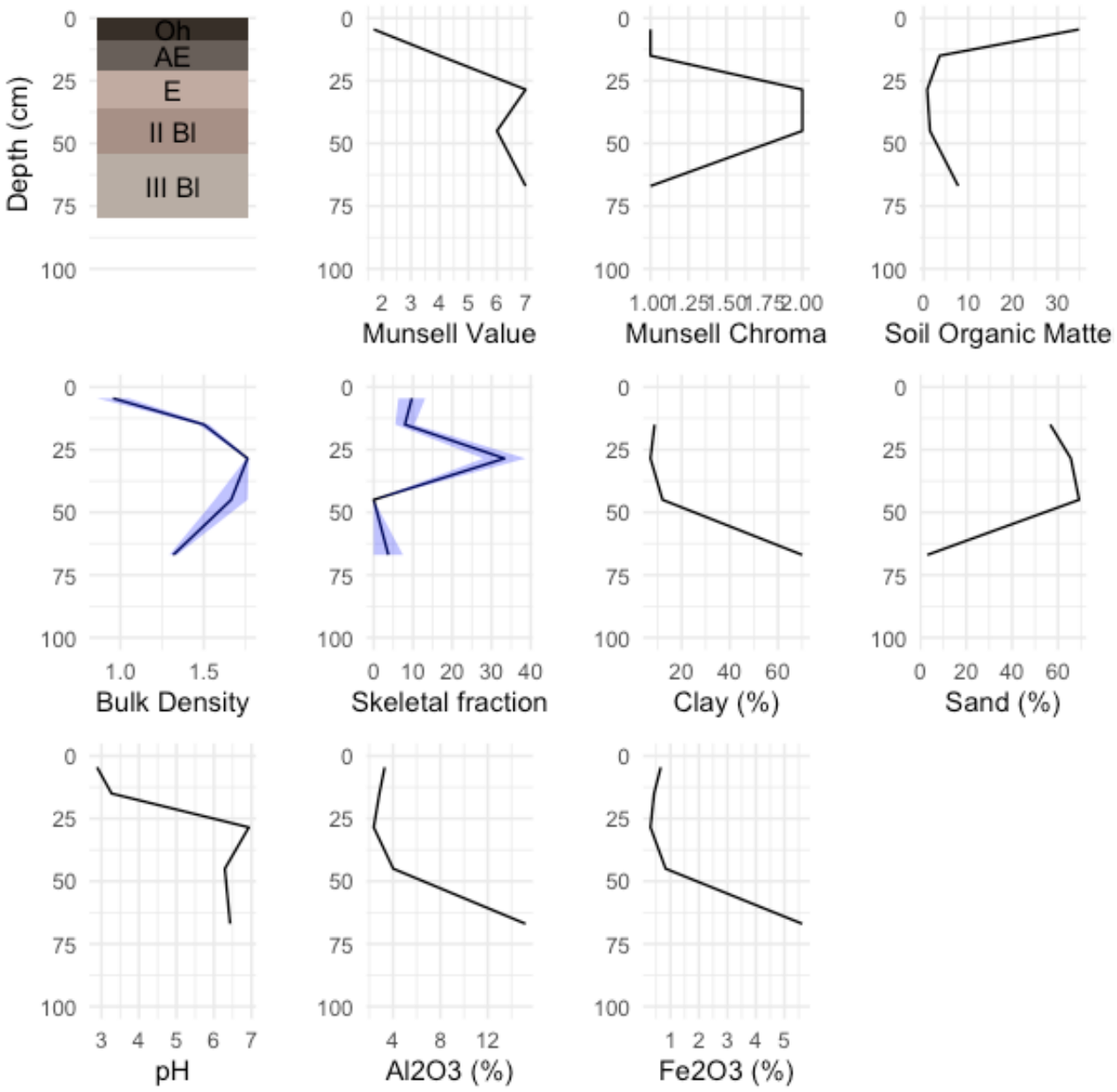

Figure 58: Parameters of soil profile P8.

Appendix 4 MAIN SOIL HORIZON SYMBOLS

O Organic horizon, which is non-peat and non-limnic, with water saturation ≤ 30 consecutive days in most years.

A Mineral horizon at the mineral soil surface or buried; contains organic matter that has at least partly been modified in-situ and rock structure in < 50 vol.-%.

E Mineral horizon with eluvial loss of Fe, Al, and/or Mn species, clay minerals or organic matter.

B Mineral horizon that has formed below an A or E horizon with rock structure in < 50 vol.-% and one or more of the following processes of soil formation: formation of soil aggregate structure, formation of clay minerals and/or oxides, accumulation of Fe, Al, Mn species, clay minerals, organic matter, silica, carbonates, gypsum by illuviation processes, removal of carbonates or gypsum.

C Mineral layer, which is unconsolidated, or consolidated and more fractured than consolidate rock and shows no soil formation, or soil formation that does not meet the criteria of the A, E, and B horizon.

Appendix 5 SOIL HORIZON SYMBOL SUFFIXES

i Organic material in an initial state of decomposition.

e Organic material in an intermediate state of decomposition.

a Organic material in an advanced state of decomposition.

h Significant amount of organic matter which is in A horizons at least partly modified in situ, in B horizons predominantly by illuviation.

s Accumulation of Fe oxides, Mn oxides and/or Al (related to the fine earth plus accumulations of Fe oxides, Mn oxides and/or Al of any size and any cementation class) by vertical illuviation processes from above.

v Plinthite.

c Concretions and/or nodules, following another suffix that indicates the accumulated substance.

g Accumulation of Fe and/or Mn oxides predominantly inside soil aggregates and loss of these oxides on aggregate surfaces, or loss of Fe and/or Mn by lateral subsurface flow and transport in reduced form.

l Accumulation of Fe and/or Mn in reduced form by upward moving capillary water with subsequent oxidation.

r Strong reduction.

Appendix 6 TABLE OF MUNSELL SOIL COLOR, PH AND SOIL ORGANIC MATTER

Table 7: Munsell soil color, pH, and soil organic matter in soil profiles P1–P8

Site	Horizon	Depth	Munsell color		pH	organic matter
		cm	moist	dry	(CaCl2)	%
P1	Oa	0 - 6	10YR 1.7/1	10YR 3/2	2.59	33.0
P1	AhE	6 - 22	10YR 4/4	10YR 7/1	3.08	0.9
P1	2E	22 - 45	7.5YR 6/2	10YR 8/1	3.37	1.1
P1	2Bhs	45 - 65	7.5YR 4/6	10YR 6/2	3.39	4.6
P1	2Cs	65 - 75	10YR 5/8	10YR 7/6	4.05	1.8
P2	Oa	0 - 6	10YR 2/2	10YR 4/1	2.57	13.2
P2	AhE	6 - 15	2.5Y 4/1	10YR 7/1	2.95	1.5
P2	E	15 - 45	10YR 6/2	10YR 7/2	3.41	0.3
P2	BE	45 - 75	7.5YR 4/3	10YR 6/2	3.18	0.8
P2	BhsC	75 - 90	5YR 2/4	10YR 5/3	3.06	1.9
P3	Oa	0 - 2	10YR 1.7/1	10YR 4/1	2.63	9.8
P3	AhE	2 - 15	7.5YR 4/1	10YR 5/1	2.85	2.1
P3	E	15 - 33	7.5YR 5/3	10YR 6/2	3.13	0.9
P3	Bh	33 - 38	7.5YR 2/2	10YR 3/3	3.08	9.7
P3	2BsC	38 - 90	7.5YR 5/6	10YR 6/6	4.09	4.7
P4	Oa	0 - 4	7.5YR 1.7/1	10YR 4/1	2.64	18.2
P4	AhE	4 - 35	7.5YR 4/3	10YR 6/2	2.95	2.0
P4	E	35 - 65	7.5YR 6/3	10YR 7/1	3.4	0.5
P4	BhC	65 - 95	7.5YR 5/4	10YR 6/3	3.44	1.1
P4	2BhsC	95 - 100	7.5YR 4/4	10YR 5/4	3.33	3.2
P5	Oa	0 - 8	7.5YR 2/1	10YR 4/1	2.64	21.0
P5	E	8 - 18	7.5YR 6/3	10YR 7/2	3.13	1.3
P5	Bh	18 - 29	7.5YR 3/4	10YR 5/4	3.19	5.8
P5	2Bs	29 - 46	7.5YR 4/6	10YR 6/4	3.47	4.2
P5	2CB	46 - 65	7.5YR 4/4	10YR 7/4	4.13	3.3
P6	Oa	0 - 3	10YR 1.7/1	10YR 2/2	2.6	29.8
P6	AhE	3 - 7	10YR 4/3	10YR 6/3	3	5.7
P6	E	7 - 11	10YR 4/2	10YR 6/2	2.93	5.3
P6	2Bsvc	11 - 28	10YR 6/6	10YR 7/4	3.61	3.0
P6	2Bg	28 - 42	10YR 7/6	10YR 8/4	3.68	3.4
P6	2BCg	42 - 85	10YR 8/3	10YR 8/3	3.91	1.6
P7	Oa	0 - 7	10YR 1.7/1	10YR 2/2	2.61	52.7
P7	AhE	7 - 16	10YR 5/2	10YR 6/2	3.05	2.6
P7	E	16 - 23	10YR 5/3	10YR 8/2	3.37	1.4
P7	2Bhsvc	23 - 50	10YR 5/4	10YR 8/3	3.74	2.0
P7	2Bg	50 - 67	10YR 6/6	10YR 8/4	3.74	3.0
P8	Oa	0 - 9	10YR 1.7/1	10YR 2/1	2.88	34.9
P8	AhE	9 - 21	7.5YR 4/1	10YR 7/1	3.27	3.6
P8	El	21 - 36	2.5Y 7/2	2.5YR 8/1	6.93	0.8
P8	2Bl	36 - 54	2.5Y 6/2	2.5YR 7/2	6.29	1.4
P8	3Cr	54 - 80	7.5Y 7/1	7.5Y 8/1	6.43	7.8

Appendix 7 TABLE OF BULK DENSITY MEASUREMENTS

Table 8: Bulk density in soil profiles P1–P8

Site	Horizon	Depth	Bulk density			
			Cylinder 1	Cylinder 2	mean	sd
		cm	g cm^{-3}	g cm^{-3}	g cm^{-3}	g cm^{-3}
P1	Oa	0 - 6	0.886	0.578	0.732	± 0.218
P1	AhE	6 - 22	1.473	1.552	1.513	± 0.056
P1	2E	22 - 45	1.65	1.787	1.719	± 0.097
P1	2Bhs	45 - 65	1.536	1.561	1.549	± 0.018
P1	2Cs	65 - 75	1.684	1.511	1.598	± 0.122
P2	Oa	0 - 6	0.59	0.948	0.769	± 0.253
P2	AhE	6 - 15	1.125	1.096	1.111	± 0.021
P2	E	15 - 45	1.29	1.463	1.377	± 0.122
P2	BE	45 - 75	1.414	1.476	1.445	± 0.044
P2	BhsC	75 - 90	1.386	1.626	1.506	± 0.17
P3	Oa	0 - 2	0.739	0.663	0.701	± 0.054
P3	AhE	2 - 15	1.328	1.301	1.315	± 0.019
P3	E	15 - 33	1.628	1.596	1.612	± 0.023
P3	Bh	33 - 38	1.25	1.274	1.262	± 0.017
P3	2BsC	38 - 90	1.308	1.356	1.332	± 0.034
P4	Oa	0 - 4	1.173	0.989	1.081	± 0.13
P4	AhE	4 - 35	1.447	1.394	1.421	± 0.037
P4	E	35 - 65	1.46	1.528	1.494	± 0.048
P4	BhC	65 - 95	1.562	1.589	1.576	± 0.019
P4	2BhsC	95 - 100	1.54	1.359	1.45	± 0.128
P5	Oa	0 - 8	1.278	0.316	0.797	± 0.68
P5	E	8 - 18	1.47	1.42	1.445	± 0.035
P5	Bh	18 - 29	1.051	1.379	1.215	± 0.232
P5	2Bs	29 - 46	1.377	1.297	1.337	± 0.057
P5	2CB	46 - 65	1.485	1.336	1.411	± 0.105
P6	AhE	3 - 7	1.083	1.293	1.188	± 0.148
P6	E	7 - 11	1.155	1.171	1.163	± 0.011
P6	2Bsvc	11 - 28	1.336	1.408	1.372	± 0.051
P6	2Bg	28 - 42	1.409	1.398	1.404	± 0.008
P6	2BCg	42 - 85	1.717	1.623	1.67	± 0.066
P7	Oa	0 - 7	0.286	0.286	0.286	± 0
P7	AhE	7 - 16	1.357	1.296	1.327	± 0.043
P7	E	16 - 23	1.572	1.409	1.491	± 0.115
P7	2Bhsvc	23 - 50	1.497	1.703	1.6	± 0.146
P7	2Bg	50 - 67	1.577	1.616	1.597	± 0.028
P8	Oa	0 - 9	1.051	0.86	0.956	± 0.135
P8	AhE	9 - 21	1.533	1.469	1.501	± 0.045
P8	El	21 - 36	1.754	1.77	1.762	± 0.011
P8	2Bl	36 - 54	1.762	1.565	1.664	± 0.139
P8	3Cr	54 - 80	1.294	1.34	1.317	± 0.033

Appendix 8 TABLE OF SKELETAL FRACTION MEASUREMENTS

Table 9: Skeletal fraction in soil profiles P1–P8

Site	Horizon	Depth	Skeletal fraction				
			Cylinder 1	Cylinder 2	mean	sd	Field estimation
		cm	%	%	%	%	%
P1	Oa	0 - 6	7.79	0.17	3.98	± 5.38	0
P1	AhE	6 - 22	1.83	1.10	1.46	± 0.52	3
P1	2E	22 - 45	1.70	1.96	1.83	± 0.18	7
P1	2Bhs	45 - 65	3.39	17.87	10.63	± 10.24	11
P1	2Cs	65 - 75	42.76	14.96	28.86	± 19.66	16
P2	Oa	0 - 6	11.53	5.38	8.45	± 4.35	0
P2	AhE	6 - 15	24.53	12.59	18.56	± 8.44	2
P2	E	15 - 45	26.28	14.49	20.38	± 8.34	7
P2	BE	45 - 75	20.01	5.01	12.51	± 10.61	12
P2	BhsC	75 - 90	2.31	0.98	1.65	± 0.94	30
P3	Oa	0 - 2	6.09	7.24	6.66	± 0.81	4
P3	AhE	2 - 15	10.17	5.92	8.04	± 3.00	6
P3	E	15 - 33	38.14	43.11	40.63	± 3.51	16
P3	Bh	33 - 38	39.44	27.63	33.53	± 8.35	30
P3	2BsC	38 - 90	29.51	53.17	41.34	± 16.73	40
P4	Oa	0 - 4	4.09	8.59	6.34	± 3.18	5
P4	AhE	4 - 35	12.30	3.95	8.12	± 5.91	12
P4	E	35 - 65	19.52	6.28	12.90	± 9.36	18
P4	BhC	65 - 95	51.47	45.37	48.42	± 4.31	30
P4	2BhsC	95 - 100	48.57	72.77	60.67	± 17.11	35
P5	Oa	0 - 8	22.77	0.00	11.38	± 16.10	0
P5	E	8 - 18	25.92	15.92	20.92	± 7.07	12
P5	Bh	18 - 29	10.56	10.66	10.61	± 0.07	18
P5	2Bs	29 - 46	54.18	37.86	46.02	± 11.54	15
P5	2CB	46 - 65	43.97	33.08	38.53	± 7.70	22
P6	Oa	0 - 3	-	-	-	-	2
P6	AhE	3 - 7	1.20	1.78	1.49	± 0.41	4
P6	E	7 - 11	0.00	2.22	1.11	± 1.57	4
P6	2Bsvc	11 - 28	2.77	3.98	3.37	± 0.85	6
P6	2Bg	28 - 42	2.84	0.57	1.71	± 1.60	6
P6	2BCg	42 - 85	0.00	0.00	0.00	± 0.00	7
P7	Oa	0 - 7	0.00	0.00	0.00	± 0.00	3
P7	AhE	7 - 16	3.91	14.58	9.24	± 7.55	4
P7	E	16 - 23	22.52	11.85	17.19	± 7.54	6
P7	2Bhsvc	23 - 50	36.27	29.71	32.99	± 4.64	17
P7	2Bg	50 - 67	30.44	32.67	31.56	± 1.58	12
P8	Oa	0 - 9	13.13	6.28	9.70	± 4.84	6
P8	AhE	9 - 21	5.48	10.42	7.95	± 3.49	21
P8	El	21 - 36	27.94	38.70	33.32	± 7.61	28
P8	2Bl	36 - 54	0.00	0.00	0.00	± 0.00	12
P8	3Cr	54 - 80	0.00	7.46	3.73	± 5.28	0

Appendix 9 TABLE OF GRAIN SIZE DISTRIBUTION

Table 10: Grain size distribution in soil profiles P1–P8

Site	Depth	Clay	Silt	Sand

		fine	coarse	fine	medium	coarse	very fine	fine	medium	coarse	very coarse
	cm	mass-%	mass-%	mass-%	mass-%	mass-%	mass-%	mass-%	mass-%	mass-%	mass-%
P1	6 - 22	1.8	0.5	2.8	5.8	3.7	9.0	46.4	20.0	5.0	5.0
P1	22 - 45	3.9	1.7	4.9	7.1	4.6	8.0	39.8	20.4	4.8	4.8
P1	45 - 65	3.6	11.7	6.9	7.6	3.6	4.2	27.2	17.2	5.4	12.6
P1	65 - 75	3.4	1.3	3.0	2.8	3.3	10.0	50.2	18.2	4.4	3.4
P2	6 - 15	1.4	0.1	1.7	4.1	3.1	3.7	45.5	26.1	5.1	9.2
P2	15 - 45	0.8	0.2	1.3	2.4	2.8	3.4	50.8	27.2	4.6	6.6
P2	45 - 75	2.0	0.6	1.0	0.6	1.1	2.2	53.6	31.0	6.0	1.8
P2	75 - 90	4.2	0.5	1.0	1.1	1.8	4.0	46.4	31.0	4.4	5.6
P3	2 - 15	1.4	1.6	2.7	4.0	2.8	5.6	36.6	19.0	15.2	11.2
P3	15 - 33	1.7	0.9	2.9	4.7	3.3	4.0	31.4	21.6	15.0	14.6
P3	33 - 38	19.0	0.6	3.9	5.6	2.2	3.1	24.4	17.3	11.2	12.8
P3	38 - 90	2.9	1.8	2.8	5.5	5.0	5.2	29.0	18.6	16.4	12.8
P4	4 - 35	2.4	1.3	4.3	8.1	3.5	6.4	35.4	19.8	12.8	6.0
P4	35 - 65	0.6	0.9	2.5	7.1	4.4	7.4	34.0	19.6	17.4	6.0
P4	65 - 95	2.5	2.5	3.0	3.5	5.3	19.2	24.4	13.2	18.0	8.4
P4	95 - 100	9.7	1.3	3.5	4.3	6.4	24.7	22.1	11.1	10.3	6.7
P5	8 - 18	2.9	1.8	4.9	9.7	9.7	21.4	23.0	10.6	11.4	4.6
P5	18 - 29	16.1	2.4	5.2	10.2	6.1	10.6	19.4	11.6	11.0	7.4
P5	29 - 46	9.4	2.3	4.6	7.7	6.1	10.8	20.0	14.4	12.6	12.0
P5	46 - 65	3.8	2.1	6.1	11.3	7.0	7.6	23.0	16.0	10.4	12.6
P6	3 - 7	25.7	2.6	9.5	12.1	16.1	26.2	4.8	1.4	1.2	0.4
P6	7 - 11	2.1	14.9	7.9	10.2	17.7	35.2	6.4	2.6	2.2	0.8
P6	11 - 28	20.4	3.3	5.8	7.0	17.7	34.6	6.0	2.4	1.8	1.0
P6	28 - 42	9.8	11.7	5.6	7.5	19.1	35.8	6.0	2.0	1.8	0.6
P6	42 - 85	11.9	3.6	7.1	9.9	20.1	36.6	5.8	2.0	2.0	1.0
P7	7 - 16	3.8	2.5	5.4	12.2	13.8	14.8	20.2	11.4	11.4	4.4
P7	16 - 23	5.1	2.0	5.5	11.6	12.5	15.0	18.6	11.4	18.4	0.0
P7	23 - 50	11.5	3.0	6.4	10.2	10.3	14.2	17.4	10.8	10.6	5.6
P7	50 - 67	23.3	3.2	5.7	7.8	17.3	15.2	10.8	7.6	4.8	4.4
P8	9 - 21	3.3	5.5	9.8	14.8	10.0	10.2	16.8	10.6	15.0	4.0
P8	21 - 36	2.7	4.3	6.3	11.6	9.4	11.0	20.0	12.2	11.8	10.6
P8	36 - 54	9.5	2.6	4.6	6.1	8.0	11.0	21.2	13.0	17.2	6.8
P8	54 - 80	61.1	9.0	11.1	7.2	8.5	1.0	0.6	0.6	0.6	0.2

Appendix 10 TABLE OF SOIL TEXTURE

Table 11: Soil texture in soil profiles P1–P8

Site	Horizon	Depth	Clay	Silt	Sand	Texture class
		cm	mass-%	mass-%	mass-%	
P1	AhE	6 - 22	2.3	12.3	85.4	Loamy Sand
P1	2E	22 - 45	5.6	16.6	77.8	Loamy Sand
P1	2Bhs	45 - 65	15.3	18.1	66.6	Sandy Loam
P1	2Cs	65 - 75	4.8	9.0	86.2	Loamy Sand
P2	AhE	6 - 15	1.5	8.9	89.6	Sand
P2	E	15 - 45	0.9	6.5	92.6	Sand
P2	BE	45 - 75	2.6	2.8	94.6	Sand
P2	BhsC	75 - 90	4.7	3.9	91.4	Sand
P3	AhE	2 - 15	3.0	9.4	87.6	Sand
P3	E	15 - 33	2.5	10.9	86.6	Sand
P3	Bh	33 - 38	19.5	11.7	68.8	Sandy Loam
P3	2BsC	38 - 90	4.7	13.3	82.0	Loamy Sand
P4	AhE	4 - 35	3.6	16.0	80.4	Loamy Sand
P4	E	35 - 65	1.5	14.1	84.4	Loamy Sand
P4	BhC	65 - 95	5.0	11.8	83.2	Loamy Sand
P4	2BhsC	95 - 100	10.9	14.2	74.9	Sandy Loam
P5	E	8 - 18	4.7	24.3	71.0	Sandy Loam
P5	Bh	18 - 29	18.5	21.5	60.0	Sandy Loam
P5	2Bs	29 - 46	11.7	18.5	69.8	Sandy Loam
P5	2CB	46 - 65	5.9	24.5	69.6	Sandy Loam
P6	AhE	3 - 7	28.3	37.7	34.0	Clay Loam
P6	E	7 - 11	17.0	35.8	47.2	Loam
P6	2Bsvc	11 - 28	23.7	30.5	45.8	Loam
P6	2Bg	28 - 42	21.5	32.3	46.2	Loam
P6	2BCg	42 - 85	15.5	37.1	47.4	Loam
P7	AhE	7 - 16	6.3	31.5	62.2	Sandy Loam
P7	E	16 - 23	7.1	29.5	63.4	Sandy Loam
P7	2Bhsvc	23 - 50	14.5	26.9	58.6	Sandy Loam
P7	2Bg	50 - 67	26.5	30.7	42.8	Loam
P8	AhE	9 - 21	8.8	34.6	56.6	Sandy Loam
P8	El	21 - 36	7.1	27.3	65.6	Sandy Loam
P8	2Bl	36 - 54	12.1	18.7	69.2	Sandy Loam
P8	3Cr	54 - 80	70.1	26.9	3.0	Clay

Appendix 11 TABLE OF OXIDES

Table 12: Oxides in soil profiles P1–P8

Site	Depth	Na_2O	MgO	Al_2O_3	SiO_2	P_2O_5	SO_3	K_2O	CaO	TiO_2	MnO	Fe_2O_3
	cm	%	%	%	%	%	%	%	%	%	%	%
P1	0 - 6	0.501	0.082	1.41	67.4	0.039	0.300	0.216	0.024	0.219	0.003	0.366
P1	6 - 22	0.155	0.014	1.58	96.8	0.001	0.041	0.132	0.006	0.275	0.002	0.072
P1	22 - 45	0.266	0.347	7.12	89.6	0.001	0.033	0.811	0.014	0.396	0.002	0.220
P1	45 - 65	0.758	0.787	11.07	78.1	0.137	0.091	1.438	0.053	0.578	0.005	1.823
P1	65 - 75	0.552	0.579	9.23	85.3	0.035	0.033	0.942	0.017	0.183	0.009	1.215
P2	0 - 6	0.793	0.194	2.21	80.8	0.116	0.568	0.298	0.042	0.271	0.003	0.312
P2	6 - 15	0.266	0.003	0.92	96.7	0.001	0.061	0.164	0.010	0.191	0.002	0.080
P2	15 - 45	0.263	0.033	2.06	96.7	0.001	0.018	0.379	0.006	0.137	0.001	0.079
P2	45 - 75	0.263	0.241	4.93	92.8	0.001	0.015	0.593	0.004	0.093	0.001	0.139
P2	75 - 90	0.203	0.400	6.70	89.7	0.001	0.055	0.680	0.006	0.125	0.001	0.177
P3	0 - 2	0.717	0.161	2.80	84.2	0.091	0.475	0.434	0.032	0.286	0.002	0.311
P3	2 - 15	0.229	0.019	1.61	95.3	0.001	0.064	0.267	0.012	0.236	0.002	0.130
P3	15 - 33	0.346	0.202	3.42	93.9	0.001	0.026	0.642	0.008	0.264	0.002	0.273
P3	33 - 38	0.756	0.677	8.74	74.2	0.447	0.171	1.112	0.044	0.376	0.006	2.981
P3	38 - 90	0.583	0.616	10.05	80.8	0.201	0.174	0.895	0.044	0.246	0.003	1.258
P4	0 - 4	1.027	0.314	3.86	72.4	0.157	0.633	0.759	0.087	0.396	0.005	0.516
P4	4 - 35	0.400	0.178	3.64	92.2	0.001	0.060	0.760	0.021	0.408	0.003	0.242
P4	35 - 65	0.378	0.074	1.80	96.3	0.001	0.016	0.519	0.008	0.313	0.002	0.147
P4	65 - 95	0.321	0.498	6.33	89.0	0.001	0.035	1.503	0.020	0.328	0.002	0.768
P4	95 - 100	0.564	0.902	10.24	80.3	0.052	0.099	1.919	0.028	0.463	0.004	1.856
P5	0 - 8	0.819	0.324	3.43	70.8	0.135	0.578	0.788	0.057	0.368	0.005	0.595
P5	8 - 18	0.420	0.242	4.28	91.4	0.001	0.042	1.322	0.022	0.533	0.003	0.388
P5	18 - 29	0.698	0.571	7.01	80.3	0.027	0.137	1.468	0.068	0.536	0.011	2.940
P5	29 - 46	0.837	0.457	6.31	83.8	0.004	0.095	1.538	0.077	0.482	0.015	2.310
P5	46 - 65	0.777	0.747	9.42	81.3	0.049	0.094	1.924	0.130	0.507	0.012	1.503
P6	0 - 3	0.625	0.397	4.30	63.1	0.084	0.339	1.162	0.055	0.421	0.007	0.979
P6	3 - 7	0.628	0.525	6.23	83.2	0.001	0.095	1.671	0.034	0.591	0.012	1.262
P6	7 - 11	0.671	0.649	7.42	82.3	0.001	0.099	1.689	0.038	0.603	0.010	1.158
P6	11 - 28	0.564	1.163	10.15	79.7	0.001	0.058	2.182	0.030	0.631	0.020	2.315
P6	28 - 42	0.768	1.038	9.70	80.1	0.001	0.062	2.118	0.028	0.597	0.027	2.106
P6	42 - 85	0.533	0.378	6.20	87.6	0.001	0.048	1.807	0.029	0.610	0.026	1.236
P7	0 - 7	0.770	0.264	2.28	40.0	0.131	0.614	0.512	0.095	0.262	0.006	0.716
P7	7 - 16	0.588	0.221	4.08	90.7	0.001	0.066	1.192	0.057	0.553	0.004	0.299
P7	16 - 23	0.632	0.389	5.99	88.5	0.001	0.046	1.707	0.075	0.628	0.009	0.609
P7	23 - 50	0.609	0.581	6.71	86.6	0.001	0.031	1.659	0.079	0.550	0.055	1.456
P7	50 - 67	0.682	1.318	10.95	78.8	0.001	0.040	2.221	0.038	0.619	0.017	2.448
P8	0 - 9	0.917	0.355	3.30	59.0	0.113	0.639	0.626	0.333	0.341	0.004	0.661
P8	9 - 21	0.257	0.173	2.85	91.6	0.001	0.045	0.784	0.058	0.474	0.004	0.425
P8	21 - 36	0.184	0.127	2.37	94.9	0.001	0.016	0.849	0.107	0.411	0.004	0.299
P8	36 - 54	0.497	0.377	4.02	91.2	0.001	0.013	1.068	0.181	0.404	0.004	0.830
P8	54 - 80	0.748	2.144	15.20	63.8	0.001	0.017	3.068	0.841	0.841	0.021	5.631

Appendix 12 TABLE OF AMORPHOUS FORMS OF IRON AND ALUMINIUM

Table 13: Amorphous forms of iron and aluminium in soil profiles P1–P8.

Site	Horizon	Depth	Oxalate Al				Oxalate Fe				Displace-ment ratio
			Rep 1	Rep 2	Average	sd	Rep 1	Rep 2	Average	sd	Alo+1/2Feo
		cm	mg/kg	mg/kg	mg/kg	mg/kg	mg/kg	mg/kg	mg/kg	mg/kg	%
P1	Oa	0 - 6	890.2	845.5	867.9 ±	2.6	937.4	985.9	961.6 ±	2.5	0.135
P1	AhE	6 - 22	69.2	81.5	75.3 ±	8.2	14.4	13.4	13.9 ±	3.7	0.008
P1	2E	22 - 45	256.9	243.0	250.0 ±	2.8	209.0	205.4	207.2 ±	0.9	0.035
P1	2Bhs	45 - 65	1730.0	2129.0	1929.5 ±	10.3	3426.0	3855.0	3640.5 ±	5.9	0.375
P1	2Cs	65 - 75	1681.0	1658.0	1669.5 ±	0.7	2527.0	2440.0	2483.5 ±	1.8	0.291
P2	Oa	0 - 6	347.6	342.6	345.1 ±	0.7	372.3	378.2	375.3 ±	0.8	0.053
P2	AhE	6 - 15	98.8	91.0	94.9 ±	4.1	12.7	17.4	15.0 ±	15.6	0.010
P2	E	15 - 45	12.2	19.9	16.1 ±	24.1	9.5	10.2	9.8 ±	4.0	0.002
P2	BE	45 - 75	182.1	155.4	168.8 ±	7.9	36.1	35.6	35.9 ±	0.7	0.019
P2	BhsC	75 - 90	431.5	365.2	398.4 ±	8.3	178.1	161.2	169.7 ±	5.0	0.048
P3	Oa	0 - 2	371.6	317.3	344.5 ±	7.9	490.8	432.4	461.6 ±	6.3	0.058
P3	AhE	2 - 15	207.9	240.9	224.4 ±	7.4	81.7	86.8	84.2 ±	3.0	0.027
P3	E	15 - 33	74.4	82.6	78.5 ±	5.2	60.0	66.1	63.0 ±	4.8	0.011
P3	Bh	33 - 38	2765.0	2573.0	2669.0 ±	3.6	8312.0	7899.0	8105.5 ±	2.5	0.672
P3	2BsC	38 - 90	4752.0	4243.0	4497.5 ±	5.7	3214.0	3043.0	3128.5 ±	2.7	0.606
P4	Oa	0 - 4	571.5	495.8	533.7 ±	7.1	1006.0	848.7	927.4 ±	8.5	0.100
P4	AhE	4 - 35	221.2	201.4	211.3 ±	4.7	48.4	39.4	43.9 ±	10.3	0.023
P4	E	35 - 65	133.5	133.7	133.6 ±	0.1	4.2	9.2	6.7 ±	37.2	0.014
P4	BhC	65 - 95	317.6	268.8	293.2 ±	8.3	800.2	678.5	739.4 ±	8.2	0.066
P4	2BhsC	95 - 100	1080.0	960.8	1020.4 ±	5.8	3933.0	3366.0	3649.5 ±	7.8	0.285
P5	Oa	0 - 8	708.3	637.6	673.0 ±	5.3	1027.0	924.5	975.8 ±	5.3	0.116
P5	E	8 - 18	118.1	130.0	124.1 ±	4.8	35.1	7.8	21.4 ±	63.8	0.013
P5	Bh	18 - 29	1363.0	1226.0	1294.5 ±	5.3	10190.0	9342.0	9766.0 ±	4.3	0.618
P5	2Bs	29 - 46	1324.0	1317.0	1320.5 ±	0.3	6916.0	7219.0	7067.5 ±	2.1	0.485
P5	2CB	46 - 65	2907.0	3130.0	3018.5 ±	3.7	2186.0	2142.0	2164.0 ±	1.0	0.410
P6	Oa	0 - 3	1456.0	1444.0	1450.0 ±	0.4	2190.0	1987.0	2088.5 ±	4.9	0.249
P6	AhE	3 - 7	926.5	923.6	925.1 ±	0.2	5042.0	4869.0	4955.5 ±	1.7	0.340
P6	E	7 - 11	867.1	899.1	883.1 ±	1.8	2944.0	2909.0	2926.5 ±	0.6	0.235
P6	2Bsvc	11 - 28	1495.0	1480.0	1487.5 ±	0.5	3580.7	3660.3	3620.5 ±	1.1	0.330
P6	2Bg	28 - 42	1584.0	1439.0	1511.5 ±	4.8	4113.0	3492.0	3802.5 ±	8.2	0.341
P6	2BCg	42 - 85	892.1	817.5	854.8 ±	4.4	3197.8	3358.9	3278.3 ±	2.5	0.249
P7	Oa	0 - 7	1530.0	1409.0	1469.5 ±	4.1	1829.0	1632.0	1730.5 ±	5.7	0.233
P7	AhE	7 - 16	197.5	211.1	204.3 ±	3.3	97.6	107.6	102.6 ±	4.9	0.026
P7	E	16 - 23	249.9	243.8	246.9 ±	1.2	487.2	486.0	486.6 ±	0.1	0.049
P7	2Bhsvc	23 - 50	1043.0	944.9	994.0 ±	4.9	2336.0	2084.0	2210.0 ±	5.7	0.210
P7	2Bg	50 - 67	1689.0	1453.0	1571.0 ±	7.5	1669.0	1424.0	1546.5 ±	7.9	0.234
P8	Oa	0 - 9	1408.0	1364.0	1386.0 ±	1.6	1744.8	1808.9	1776.8 ±	1.8	0.227
P8	AhE	9 - 21	686.6	682.3	684.5 ±	0.3	745.6	778.9	762.3 ±	2.2	0.107
P8	El	21 - 36	128.7	108.0	118.4 ±	8.7	142.1	118.2	130.2 ±	9.2	0.018
P8	2Bl	36 - 54	312.9	223.4	268.2 ±	16.7	201.2	183.0	192.1 ±	4.7	0.036
P8	3Cr	54 - 80	1110.0	937.6	1023.8 ±	8.4	1568.0	1219.0	1393.5 ±	12.5	0.172

Appendix 13 TABLE OF WEATHERING INDICES

Table 14: Chemical Index of Alteration (CIA), Chemical Index of Weathering (CIW), Weathering Index of Parker (WIP), [CaKTi]-index and [NaKTi]-index in soil profiles P1–P8.

Site	Horizon	Depth cm	CIA	CIW	WIP	CaKTi	NaKTi
P1	Oa	0 - 6	56.20	61.97	6.74	1.84	7.59
P1	AhE	6 - 22	79.47	85.60	2.60	0.84	2.26
P1	2E	22 - 45	84.16	93.91	10.33	3.52	5.20
P1	2Bhs	45 - 65	79.24	89.17	21.51	4.35	7.60
P1	2Cs	65 - 75	82.49	90.76	14.73	8.88	16.54
P2	Oa	0 - 6	56.44	61.51	10.48	2.09	9.42
P2	AhE	6 - 15	59.24	66.85	3.88	1.53	5.04
P2	E	15 - 45	70.74	82.32	5.75	4.76	9.67
P2	BE	45 - 75	82.00	91.79	8.14	10.88	18.12
P2	BhsC	75 - 90	86.12	95.12	8.76	9.26	13.36
P3	Oa	0 - 2	62.11	69.33	10.82	2.73	9.02
P3	AhE	2 - 15	70.16	80.24	4.45	1.99	4.41
P3	E	15 - 33	72.81	85.43	9.22	4.16	7.49
P3	Bh	33 - 38	77.56	86.83	18.39	5.18	10.20
P3	2BsC	38 - 90	83.34	90.62	14.79	6.43	12.28
P4	Oa	0 - 4	59.11	67.62	17.00	3.56	9.92
P4	AhE	4 - 35	70.57	83.95	10.69	3.23	5.69
P4	E	35 - 65	59.99	73.84	8.12	2.85	5.93
P4	BhC	65 - 95	74.28	91.81	17.15	7.85	10.28
P4	2BhsC	95 - 100	77.02	91.28	24.05	7.12	10.18
P5	Oa	0 - 8	59.84	70.29	15.28	3.85	9.37
P5	E	8 - 18	66.46	85.42	15.82	4.26	6.24
P5	Bh	18 - 29	71.01	84.64	20.65	4.83	8.01
P5	2Bs	29 - 46	66.49	80.63	22.23	5.64	9.88
P5	2CB	46 - 65	72.37	86.15	25.89	6.80	10.38
P6	Oa	0 - 3	64.30	79.20	16.87	4.87	8.52
P6	AhE	3 - 7	68.21	85.06	21.51	4.88	7.53
P6	E	7 - 11	71.20	86.34	22.42	4.84	7.62
P6	2Bsvc	11 - 28	75.21	91.17	27.01	5.93	8.16
P6	2Bg	28 - 42	72.90	88.08	28.00	6.08	9.33
P6	2BCg	42 - 85	68.26	86.96	21.37	5.09	7.28
P7	Oa	0 - 7	53.41	61.36	12.41	3.83	10.90
P7	AhE	7 - 16	63.32	79.20	16.30	3.80	6.40
P7	E	16 - 23	66.46	83.59	21.59	4.78	7.20
P7	2Bhsvc	23 - 50	69.54	85.43	21.50	5.32	7.97
P7	2Bg	50 - 67	75.27	90.18	28.88	6.17	8.92
P8	Oa	0 - 9	54.19	60.96	15.59	4.51	10.06
P8	AhE	9 - 21	67.43	84.37	9.65	2.98	4.20
P8	El	21 - 36	62.64	82.72	9.53	3.87	4.66
P8	2Bl	36 - 54	63.56	77.79	15.15	5.12	7.65
P8	3Cr	54 - 80	71.42	84.63	41.00	7.61	8.48

Appendix 14 TABLE OF INFRARED AND OPTICAL STIMULATED LUMINESCENCE

Table 15: Infrared (IRSL) and Optical Stimulated Luminescence (OSL) in soil profiles P1–P8

Site	Depth	IRSL		OSL		IRSL/OSL	
	cm	net counts	error	net counts	error		error
P1	5	1538	57.93099	27860	171.79639	0.05520	0.00211
P1	12	2277	64.57554	246696	499.45570	0.00923	0.00026
P1	30	80168	292.89247	298929	550.62056	0.26818	0.00110
P1	50	85425	306.29398	214096	469.20784	0.39900	0.00168
P1	60	32123	224.27884	64708	271.95404	0.49643	0.00405
P2	5	792	56.08030	5241	85.95348	0.15112	0.01098
P2	10	28580	172.01453	505445	712.08216	0.05654	0.00035
P2	50	85425	306.29398	214096	469.20784	0.39900	0.00168
P2	60	32123	224.27884	64708	271.95404	0.49643	0.00405
P2	85	1538	57.93099	27860	171.79639	0.05520	0.00211
P3	10	7615	157.17188	195596	451.08757	0.03893	0.00081
P3	30	120434	352.32513	742347	864.51431	0.16223	0.00051
P3	80	31252	203.19941	51362	250.85653	0.60847	0.00495
P4	4	4392	84.02976	27872	173.58283	0.15758	0.00317
P4	20	13669	131.32783	152101	394.26387	0.08987	0.00089
P4	50	105624	336.33614	1491198	1224.25283	0.07083	0.00023
P4	80	1057890	1033.66097	2496515	1588.08753	0.42375	0.00049
P4	100	175833	437.89839	358851	604.15561	0.48999	0.00147
P5	2	2587	80.95060	31465	188.95502	0.08222	0.00262
P5	10	111498	341.11875	673515	825.06060	0.16555	0.00055
P5	45	79265	286.38785	143023	382.23422	0.55421	0.00249
P6	5	289680	575.70652	643515	819.70970	0.45015	0.00106
P6	15	536699	736.85752	914154	963.25230	0.58710	0.00102
P6	35	549969	753.55557	1238819	1122.11541	0.44395	0.00073
P6	80	1295947	1143.42118	3256038	1812.96387	0.39801	0.00042
P7	10	59592	249.86596	252008	505.65205	0.23647	0.00110
P7	35	116260	349.74133	288666	543.18873	0.40275	0.00143
P7	60	144913	386.16965	436305	665.39988	0.33214	0.00102
P8	30	169760	416.18505	710093	846.66581	0.23907	0.00065
P8	50	316540	569.93859	917028	963.00935	0.34518	0.00072
P8	85	72092	272.71780	211315	464.23485	0.34116	0.00149

Appendix 15 TABLE OF $^{239+240}$PU ACTIVITY

Table 16: $^{239+240}$Pu activity in soil profiles P1–P8

Site	Sample	Depth cm	Sample ^{239}Pu+^{240}Pu activity Bq/kg	RSD (%)	^{240}Pu/ ^{239}Pu mass ratio	RSD (%)
P1	P1-11	0–5	1.7259	7.2	0.2327	6.7
P1	P1-21	0–5	2.3787	5.6	0.1789	5.1
P1	P1-31	0–5	3.8001	6.0	0.1871	5.4
P1	P1-41	0–5	4.6895	4.8	0.1929	4.0
P1	P1-12	5–10	0.7607	9.9	0.1998	9.6
P1	P1-22	5–10	0.1853	13.3	0.1868	13.1
P1	P1-32	5–10	0.1763	16.3	0.1770	16.1
P1	P1-42	5–10	1.1237	11.5	0.1925	11.2
P1	P1-13	10–15	0.0261	80.2	0.1667	79.1
P1	P1-23	10–15	0.0744	51.4	0.2247	51.2
P1	P1-33	10–15	0.0431	73.6	0.1748	73.1
P1	P1-43	10–15	0.0443	29.4	0.2234	29.0
P1	P1-14	15–20	0.0139	78.1	0.1706	75.6
P1	P1-24	15–20	0.0131	89.8	0.2583	86.2
P1	P1-34	15–20	0.0172	63.2	0.2678	61.1
P1	P1-44	15–20	0.0326	56.5	0.2010	55.8
P1	P1-46	25–30	0.0116	123.8	0.2369	118.9
P2	P2-11	0–5	0.3884	14.3	0.2059	13.9
P2	P2-21	0–5	0.8995	10.0	0.1963	9.7
P2	P2-31	0–5	0.3619	15.0	0.1975	14.4
P2	P2-41	0–5	0.0566	46.9	0.2449	46.3
P2	P2-12	5–10	1.7387	9.4	0.1860	9.1
P2	P2-22	5–10	0.1441	23.0	0.2070	22.9
P2	P2-32	5–10	0.0267	58.9	0.2141	57.8
P2	P2-42	5–10	0.2307	13.9	0.2003	13.7
P2	P2-13	10–15	0.0362	54.1	0.1673	53.5
P2	P2-23	10–15	0.0935	27.2	0.1896	27.0
P2	P2-33	10–15	0.0200	67.6	0.2620	65.7
P2	P2-43	10–15	0.2006	25.0	0.2081	24.9
P2	P2-14	15–20	0.0035	294.1	0.1315	263.8
P2	P2-24	15–20	0.0289	70.1	0.1359	69.3
P2	P2-34	15–20	0.0145	78.9	0.2697	75.7
P2	P2-44	15–20	0.0238	43.5	0.1605	42.6
P2	P2-36	25–30	0.0078	137.0	0.3419	126.7
P3	P3-11	0–5	0.6532	20.9	0.1809	20.8
P3	P3-21	0–5	0.0498	37.2	0.2137	36.8
P3	P3-31	0–5	1.9166	6.3	0.1860	5.7
P3	P3-41	0–5	2.0558	7.2	0.1885	6.7
P3	P3-12	5–10	0.0139	79.7	0.2036	76.9
P3	P3-22	5–10	0.0681	37.8	0.2173	37.6
P3	P3-32	5–10	0.1918	17.8	0.1825	17.7
P3	P3-42	5–10	0.1033	31.0	0.2376	30.8
Site	**Sample**	**Depth cm**	**Sample 239Pu+240Pu activity Bq/kg**	**RSD (%)**	**240Pu/ 239Pu mass ratio**	**RSD (%)**

P3	P3-13	10–15	0.0042	131.0	0.1129	118.0
P3	P3-23	10–15	0.1653	19.2	0.1827	19.0
P3	P3-33	10–15	0.0514	44.1	0.1985	43.8
P3	P3-43	10–15	0.1576	21.6	0.1981	21.4
P3	P3-14	15–20	0.0053	127.1	0.2991	112.8
P3	P3-24	15–20	0.0075	111.4	0.1595	104.9
P3	P3-34	15–20	0.1076	24.1	0.1905	23.9
P3	P3-44	15–20	0.0254	66.8	0.1658	65.6
P4	P4-11	0–5	0.0007	12.9	0.1737	12.7
P4	P4-21	0–5	1.8656	10.2	0.1919	10.0
P4	P4-31	0–5	2.0416	11.0	0.1934	10.8
P4	P4-41	0–5	1.4376	10.4	0.1880	10.1
P4	P4-12	5–10	0.1277	27.7	0.2066	27.6
P4	P4-22	5–10	0.5717	13.2	0.1922	12.9
P4	P4-32	5–10	1.2576	8.7	0.1884	8.4
P4	P4-42	5–10	0.1812	28.6	0.1736	28.3
P4	P4-13	10–15	0.0353	55.5	0.1862	54.9
P4	P4-23	10–15	0.0771	31.4	0.1722	31.2
P4	P4-33	10–15	0.0724	38.6	0.1962	38.4
P4	P4-43	10–15	0.0470	46.9	0.1905	46.5
P4	P4-14	15–20	0.0171	91.8	0.2235	89.3
P4	P4-24	15–20	0.0574	36.5	0.1654	36.2
P4	P4-34	15–20	0.0525	43.7	0.1910	43.4
P4	P4-44	15–20	0.0274	75.5	0.2001	74.4
P5	P5-11	0–5	0.0007	18.6	0.1647	18.5
P5	P5-21	0–5	0.6234	16.3	0.1827	16.1
P5	P5-31	0–5	0.3097	19.8	0.1850	19.7
P5	P5-41	0–5	2.0350	8.3	0.1840	7.9
P5	P5-12	5–10	0.5035	12.1	0.1902	11.9
P5	P5-22	5–10	0.1110	24.4	0.2186	24.2
P5	P5-32	5–10	2.5251	6.4	0.1951	5.8
P5	P5-42	5–10	0.0706	47.7	0.2015	47.5
P5	P5-13	10–15	0.0803	30.2	0.1662	30.0
P5	P5-23	10–15	0.0722	37.2	0.1835	37.1
P5	P5-33	10–15	0.1272	20.0	0.1975	19.4
P5	P5-43	10–15	0.0378	48.9	0.1886	48.3
P5	P5-14	15–20	0.0140	90.7	0.2074	87.6
P5	P5-24	15–20	0.0766	38.3	0.1815	38.1
P5	P5-34	15–20	0.0969	34.4	0.2004	34.2
P5	P5-44	15–20	0.0374	55.5	0.2482	54.7
P5	P5-36	25–30	0.1625	20.3	0.2008	20.2
P6	P6-11	0–5	3.6120	6.8	0.1842	6.4
P6	P6-21	0–5	5.7966	5.3	0.1895	4.6
P6	P6-31	0–5	1.6484	9.5	0.1894	9.1
P6	P6-41	0–5	1.7297	5.8	0.0018	5.3
P6	P6-12	5–10	1.2927	9.3	0.1865	9.0

Site	Sample	Depth	Sample 239Pu+240Pu activity		240Pu/ 239Pu	
		cm	Bq/kg	RSD (%)	mass ratio	RSD (%)
P6	P6-22	5–10	0.1596	25.9	0.2219	25.8

P6	P6-32	5–10	0.2907	22.0	0.2022	21.8
P6	P6-42	5–10	2.9489	5.3	0.0013	4.9
P6	P6-13	10–15	0.1118	48.3	0.1905	48.2
P6	P6-23	10–15	0.0702	39.1	0.2105	38.9
P6	P6-33	10–15	0.0852	61.7	0.2168	61.5
P6	P6-43	10–15	0.3395	18.7	0.0008	18.6
P6	P6-14	15–20	0.0563	40.5	0.2369	39.8
P6	P6-24	15–20	0.0446	41.4	0.1647	41.0
P6	P6-34	15–20	0.0290	83.9	0.2103	82.8
P6	P6-44	15–20	0.2506	26.9	0.0006	26.7
P6	P6-36	25–30	0.0165	58.5	0.0017	56.8
P7	P7-11	0–5	0.7775	13.2	0.1824	12.4
P7	P7-21	0–5	4.0038	5.1	0.1902	4.4
P7	P7-31	0–5	0.7807	12.6	0.1909	12.4
P7	P7-41	0–5	2.5723	6.1	0.1830	5.7
P7	P7-12	5–10	0.0733	23.2	0.2094	23.0
P7	P7-22	5–10	0.1098	35.3	0.2451	35.1
P7	P7-32	5–10	0.7623	21.8	0.1935	21.7
P7	P7-42	5–10	0.3976	14.5	0.2083	13.8
P7	P7-13	10–15	0.0707	26.5	0.2483	26.3
P7	P7-23	10–15	0.0870	19.9	0.2183	19.7
P7	P7-33	10–15	0.0482	66.2	0.1100	65.9
P7	P7-43	10–15	0.0899	27.1	0.1990	26.9
P7	P7-14	15–20	0.0408	32.7	0.1698	32.3
P7	P7-24	15–20	0.0857	42.8	0.2232	42.6
P7	P7-34	15–20	0.0584	36.7	0.2749	36.3
P7	P7-44	15–20	0.0927	23.1	0.2253	22.9
P7	P7-36	25–30	0.0382	51.1	0.1504	50.6
P8	P8-11	0–5	1.1538	7.7	0.1803	7.3
P8	P8-21	0–5	2.1402	9.0	0.1896	8.7
P8	P8-31	0–5	2.1377	8.0	0.1798	7.5
P8	P8-41	0–5	1.5140	11.3	0.1919	10.8
P8	P8-12	5–10	1.5993	7.2	0.1998	6.8
P8	P8-22	5–10	0.7042	10.0	0.2001	9.8
P8	P8-32	5–10	0.1711	23.6	0.1825	23.5
P8	P8-42	5–10	1.0464	12.9	0.1641	12.6
P8	P8-13	10–15	0.2475	17.3	0.1843	17.1
P8	P8-23	10–15	0.1457	26.6	0.2118	26.4
P8	P8-33	10–15	0.2478	30.2	0.1824	30.2
P8	P8-43	10–15	0.1465	42.5	0.1722	42.4
P8	P8-14	15–20	0.2670	18.4	0.1999	18.3
P8	P8-24	15–20	0.1270	27.1	0.2099	27.0
P8	P8-34	15–20	0.1241	50.4	0.2106	50.4
P8	P8-44	15–20	0.0111	135.9	0.2047	130.5
P8	P8-26	25–30	0.0304	93.5	0.1514	92.5

Site	Sample	Depth	Sample 239Pu+240Pu activity		240Pu/ 239Pu	
		cm	Bq/kg	RSD (%)	mass ratio	RSD (%)
R1	R1-11	0–5	0.5635	16.8	0.1906	16.6
R1	R1-21	0–5	0.5611	11.8	0.0012	11.6

R1	R1-31	0–5	0.7106	7.8	0.2034	7.5
R1	R1-41	0–5	0.4986	11.3	0.1948	11.0
R1	R1-12	5–10	0.0769	28.4	0.0017	28.2
R1	R1-22	5–10	0.4424	18.1	0.1939	18.0
R1	R1-32	5–10	0.5238	15.3	0.2017	15.0
R1	R1-42	5–10	0.5362	17.6	0.1931	17.5
R1	R1-13	10–15	0.0398	40.1	0.0015	39.7
R1	R1-23	10–15	0.0602	44.0	0.1838	43.2
R1	R1-33	10–15	0.1130	28.3	0.1670	28.2
R1	R1-43	10–15	0.3086	15.3	0.1810	15.1
R1	R1-14	15–20	0.0095	123.8	0.0006	118.7
R1	R1-24	15–20	0.0391	46.1	0.2102	45.5
R1	R1-34	15–20	0.0451	68.5	0.1354	68.1
R1	R1-44	15–20	0.0100	108.5	0.1110	104.2
R1	R1-26	25–30	0.0073	141.8	0.1809	133.5
R2	R2-11	0–5	0.4004	26.8	0.2050	26.7
R2	R2-21	0–5	0.3743	22.9	0.1900	22.8
R2	R2-12	5–10	0.4348	22.1	0.1893	22.0
R2	R2-22	5–10	0.3985	12.5	0.2008	12.4
R2	R2-13	10–15	0.0851	42.2	0.1881	42.0
R2	R2-23	10–15	0.0834	29.5	0.2086	29.3
R2	R2-14	15–20	0.1130	23.4	0.1832	23.3
R2	R2-24	15–20	0.0132	80.3	0.2592	76.9

Appendix 16 TABLE OF $^{239+240}$PU INVENTORY SUMS

Table 17: Sum of $^{239+240}$Pu inventories per soil profile

Site	Sample	$^{239+240}$Pu inventory				
		Depth 0–5 cm	Depth 5–10 cm	Depth 10–15 cm	Depth 15–20 cm	Sum
		Bq m^{-2}	Bq m^{-2}	Bq m^{-2}	Bq m^{-2}	Bq m^{-2}
P1	P1-1	19.24	16.20	1.68	1.01	38.13
P1	P1-2	25.81	7.14	4.41	1.00	38.36
P1	P1-3	37.43	8.83	3.06	1.37	50.69
P1	P1-4	52.05	31.52	3.15	2.27	88.99
P2	P2-1	4.33	40.51	2.55	0.25	47.65
P2	P2-2	10.16	7.93	5.52	2.34	25.95
P2	P2-3	14.35	1.65	1.36	0.98	18.34
P2	P2-4	0.57	11.81	12.24	1.65	26.27
P3	P3-1	25.51	0.81	0.29	0.38	26.98
P3	P3-2	2.26	2.68	10.91	0.55	16.40
P3	P3-3	20.41	9.56	2.56	5.61	38.15
P3	P3-4	73.91	5.35	8.79	1.78	89.82
P4	P4-1	0.00	7.71	2.29	1.31	11.31
P4	P4-2	67.26	36.56	5.32	1.06	110.20
P4	P4-3	23.17	51.69	5.85	4.17	84.89
P4	P4-4	19.62	9.73	3.21	1.75	34.31
P5	P5-1	0.00	22.28	5.35	0.86	28.50
P5	P5-2	29.71	6.63	4.57	5.40	46.30
P5	P5-3	2.66	54.04	7.50	6.88	71.08
P5	P5-4	31.95	5.14	2.47	2.36	41.92
P6	P6-1	65.02	58.24	7.12	4.15	134.52
P6	P6-2	75.94	9.29	4.47	3.20	92.89
P6	P6-3	25.47	16.69	5.54	1.99	49.69
P6	P6-4	11.07	90.68	20.00	11.67	133.41
P7	P7-1	21.03	4.65	4.36	3.43	33.47
P7	P7-2	57.25	7.04	6.23	4.51	75.03
P7	P7-3	11.24	11.02	3.09	4.17	29.52
P7	P7-4	31.51	18.01	6.77	6.30	62.59
P8	P8-1	36.75	109.63	13.76	12.66	172.80
P8	P8-2	66.24	34.75	9.59	5.78	116.36
P8	P8-3	61.46	10.85	14.23	8.54	95.07
P8	P8-4	23.77	37.15	10.54	0.88	72.33
R1	R1-1	22.96	4.42	2.39	0.57	30.34
R1	R1-2	20.37	22.12	3.64	2.36	48.49
R1	R1-3	27.25	23.78	7.13	3.01	61.18
R1	R1-4	17.85	25.12	16.42	0.61	59.99
R2	R2-1	15.37	26.81	6.93	9.38	58.49
R2	R2-2	24.76	28.07	6.01	1.10	59.95

Appendix 17 TABLE OF CORRELATION AND P-VALUES OF SITE VARIABLES

Table 18: Correlation and p-values of selected site variables with a p-value ≤ 0.05.

Pair		Correlation	p-value
Al_2O_3	amorphous Fe	0.942	4.71E-04
sand content	SiO_2	0.911	1.64E-03
slope inclination	amorphous Al	0.911	1.67E-03
clay content	Fe_2O_3	0.901	2.25E-03
clay content	erosion rate	0.894	2.78E-03
altitude	clay content	-0.868	5.16E-03
distance from cliffside	clay content	0.843	8.61E-03
silt content	erosion rate	0.839	9.22E-03
soil organic matter	Fe_2O_3	0.836	9.72E-03
sand content	Fe_2O_3	-0.830	1.08E-02
altitude	Fe_2O_3	-0.829	1.09E-02
Fe_2O_3	erosion rate	0.794	1.86E-02
distance from cliffside	Fe_2O_3	0.792	1.92E-02
pH	clay content	0.791	1.94E-02
rock fragment fraction	bulk density	0.788	2.01E-02
soil organic matter	sand content	-0.769	2.57E-02
soil organic matter	amorphous Fe	0.761	2.84E-02
silt content	Fe_2O_3	0.751	3.19E-02
soil organic matter	clay content	0.745	3.41E-02
Al_2O_3	soil organic matter	0.722	4.32E-02
distance from cliffside	pH	0.721	4.38E-02
Al_2O_3	Fe_2O_3	0.711	4.78E-02

Appendix 18 TABLE OF CORRELATION AND P-VALUES OF HORIZON VARIABLES

Table 19: Correlation and p-values of selected horizon variables with a p-value ≤ 0.05.

Pair		Correlation	p-value
Al_2O_3	SiO_2	-0.937	1.03E-15
SiO_2	Fe_2O_3	-0.931	3.72E-15
clay content	Fe_2O_3	0.883	1.03E-11
SiO_2	LOI	-0.823	4.08E-09
Al_2O_3	Fe_2O_3	0.813	9.18E-09
clay content	SiO2	-0.811	1.08E-08
Fe_2O_3	LOI	0.763	2.43E-07
LOI	amorphous Fe	0.748	5.76E-07
sand content	Fe2O3	-0.732	1.28E-06
Munsell chroma (dry)	amorphous Al	0.724	1.93E-06
sand content	SiO_2	0.703	5.14E-06
clay content	Al_2O_3	0.689	9.23E-06
SiO_2	amorphous Al	-0.658	3.17E-05
clay content	LOI	0.635	7.23E-05
SiO_2	amorphous Fe	-0.627	9.42E-05
LOI	amorphous Al	0.627	9.54E-05

Al_2O_3	LOI	0.615	1.38E-04
sand content	Al_2O_3	-0.576	4.52E-04
amorphous Fe	amorphous Al	0.567	5.76E-04
Munsell chroma (dry)	Al_2O_3	0.562	6.60E-04
horizon depth	estimated rock fraction	0.559	7.21E-04
bulk density	LOI	-0.556	7.74E-04
Munsell chroma (dry)	amorphous Fe	0.551	8.99E-04
Munsell value (moist)	pH	0.545	1.05E-03
horizon depth	Al_2O_3	0.532	1.42E-03
sand content	LOI	-0.529	1.55E-03
Munsell chroma (moist)	amorphous Al	0.526	1.66E-03
Fe_2O_3	amorphous Al	0.499	3.12E-03
Munsell chroma (moist)	Al_2O_3	0.495	3.40E-03
Munsell value (dry)	LOI	-0.480	4.70E-03
clay content	silt content	0.477	5.00E-03
Munsell value (dry)	bulk density	0.466	6.24E-03
Munsell chroma (dry)	SiO2	-0.464	6.56E-03
Al_2O_3	amorphous Fe	0.463	6.69E-03
Munsell value (moist)	bulk density	0.457	7.54E-03
horizon depth	Munsell chroma (dry)	0.445	9.52E-03
rock fragment fraction	amorphous Al	0.443	9.84E-03
Munsell value (dry)	pH	0.443	9.91E-03
Munsell value (dry)	silt content	0.439	1.05E-02
Munsell value (dry)	amorphous Fe	-0.432	1.21E-02
pH	clay content	0.422	1.44E-02
bulk density	amorphous Fe	-0.406	1.89E-02
Munsell value (moist)	silt content	0.404	1.97E-02
horizon depth	Munsell chroma (moist)	0.403	2.01E-02
pH	bulk density	0.395	2.28E-02
Munsell value (moist)	sand content	-0.370	3.41E-02
pH	sand content	-0.368	3.52E-02
Munsell value (moist)	LOI	-0.367	3.56E-02
horizon depth	bulk density	0.367	3.58E-02
Munsell chroma (moist)	amorphous Fe	0.366	3.62E-02
clay content	amorphous Fe	0.351	4.49E-02
horizon depth	SiO_2	-0.348	4.72E-02
silt	SiO_2	-0.345	4.93E-02
pH	Fe_2O_3	0.344	5.00E-02

Appendix 19 MODERN R CODE USED IN THIS STUDY

```
install.packages("modeRn", repos = NULL, type="source")
# load the library
library("modeRn")
# creates a reference profile composed of 4 layers of thickness 5 cm
RDP = createReferenceProfile(FRNinv = c(22.11, 18.86, 7.4, 1.64), thickness =
                                5, name = 'Reference site', falloutTime = 1963,
refTime = 2022, massDepth = 208.86)
plot(RDP)

print(RDP)

# creates sampling layers of thickness 20 cm
P1 = createSamplingProfile(FRNinv = 54.04, thickness = 20, name = 'Site 1',
                           falloutTime = 1963, refTime = 2022)
P2 = createSamplingProfile(FRNinv = 29.55, thickness = 20, name = 'Site 2'
                           , falloutTime = 1963, refTime = 2022)
P3 = createSamplingProfile(FRNinv = 42.84, thickness = 20, name = 'Site 3',
                           falloutTime = 1963, refTime = 2022)
P4 = createSamplingProfile(FRNinv = 60.18, thickness = 20, name = 'Site 4',
                           falloutTime = 1963, refTime = 2022)
P5 = createSamplingProfile(FRNinv = 46.95, thickness = 20, name = 'Site 5',
                           falloutTime = 1963, refTime = 2022)
P6 = createSamplingProfile(FRNinv = 102.63, thickness = 20, name = 'Site 6',
                           falloutTime = 1963, refTime = 2022)
P7 = createSamplingProfile(FRNinv = 50.15, thickness = 20, name = 'Site 7',
                           falloutTime = 1963, refTime = 2022)
P8 = createSamplingProfile(FRNinv = 114.14, thickness = 20, name = 'Site 8',
                           falloutTime = 1963, refTime = 2022)

# creates smoothed layers below the reference profile
RDP_smooth1 = addSmoothedLayers(RDP, P1)
plot(RDP_smooth1, main = 'Simulated depth profile')
print(P1)

RDP_smooth2 = addSmoothedLayers(RDP, P2)
plot(RDP_smooth2, main = 'Simulated depth profile')

print(P2)

RDP_smooth3 = addSmoothedLayers(RDP, P3)
plot(RDP_smooth3, main = 'Simulated depth profile')
print(P3)

RDP_smooth4 = addSmoothedLayers(RDP, P4)
plot(RDP_smooth4, main = 'Simulated depth profile')
print(P4)

RDP_smooth5 = addSmoothedLayers(RDP, P5)
plot(RDP_smooth5, main = 'Simulated depth profile')
print(P5)
```

```
RDP_smooth6 = addSmoothedLayers(RDP, P6)
plot(RDP_smooth6, main = 'Simulated depth profile')


RDP_smooth7 = addSmoothedLayers(RDP, P7)
plot(RDP_smooth7, main = 'Simulated depth profile')
print(P7)

RDP_smooth8 = addSmoothedLayers(RDP, P8)
plot(RDP_smooth8, main = 'Simulated depth profile')
print(P8)

# sampling profiles with eroded layers
MODERN_P1 = MODERN(RDP_smooth1, P1)

plot(MODERN_P1)

print(MODERN_P1)

ER1 <-yearlyEDRates(MODERN_P1, samplingTime = 2022, falloutTime = 1963, massDep
th = 186.08, sampleDepth = 20)

show(ER1)

MODERN_P2 = MODERN(RDP_smooth2, P2)

plot(MODERN_P2)

print(MODERN_P2)

yearlyEDRates(MODERN_P2, samplingTime = 2022, falloutTime = 1963, massDepth = 2
03.2, sampleDepth = 20)

MODERN_P3 = MODERN(RDP_smooth3, P3)

plot(MODERN_P3)

print(MODERN_P3)

yearlyEDRates(MODERN_P3, samplingTime = 2022, falloutTime = 1963, massDepth = 2
09.28, sampleDepth = 20)

plot(MODERN_P4)

print(MODERN_P4)

yearlyEDRates(MODERN_P4, samplingTime = 2022, falloutTime = 1963, massDepth = 2
02.65, sampleDepth = 20)

MODERN_P5 = MODERN(RDP_smooth5, P5)

plot(MODERN_P5)

print(MODERN_P5)

yearlyEDRates(MODERN_P5, samplingTime = 2022, falloutTime = 1963, massDepth = 1
99.45, sampleDepth = 20)
```

```
MODERN_P6 = MODERN(RDP_smooth6, P6)

plot(MODERN_P6)

print(MODERN_P6)

yearlyEDRates(MODERN_P6, samplingTime = 2022, falloutTime = 1963, massDepth = 1
89.11, sampleDepth = 20)

MODERN_P7 = MODERN(RDP_smooth7, P7)

plot(MODERN_P7)

print(MODERN_P7)

yearlyEDRates(MODERN_P7, samplingTime = 2022, falloutTime = 1963, massDepth = 2
01.04, sampleDepth = 20)

MODERN_P8 = MODERN(RDP_smooth8, P8)

plot(MODERN_P8)

print(MODERN_P8)

yearlyEDRates(MODERN_P8, samplingTime = 2022, falloutTime = 1963, massDepth = 2
03.89, sampleDepth = 20)

#mit Deposition
RDP_depP1 = addDepositionLayers(RDP_smooth1, 54.04, 1)
MODERN_P1 = MODERN(RDP_depP1, P1)

plot(MODERN_P1)

print(MODERN_P1)

yearlyEDRates(MODERN_P1, samplingTime = 2022, falloutTime = 1963, massDepth = 1
86.08, sampleDepth = 20)

RDP_depP2 = addDepositionLayers(RDP_smooth2, 29.55, 1)
MODERN_P2 = MODERN(RDP_depP2, P2)

plot(MODERN_P2)

print(MODERN_P2)

yearlyEDRates(MODERN_P2, samplingTime = 2022, falloutTime = 1963, massDepth = 2
03.2, sampleDepth = 20)

RDP_depP3 = addDepositionLayers(RDP_smooth3, 42.84, 1)
MODERN_P3 = MODERN(RDP_depP3, P3)

plot(MODERN_P3)

print(MODERN_P3)

yearlyEDRates(MODERN_P3, samplingTime = 2022, falloutTime = 1963, massDepth =
209.28, sampleDepth = 20)
```

```
RDP_depP4 = addDepositionLayers(RDP_smooth4, 60.18, 1)
MODERN_P4 = MODERN(RDP_depP4, P4)

plot(MODERN_P4)

print(MODERN_P4)

yearlyEDRates(MODERN_P4, samplingTime = 2022, falloutTime = 1963, massDepth = 2
02.65, sampleDepth = 20)

RDP_depP5 = addDepositionLayers(RDP_smooth5, 46.95, 1)
MODERN_P5 = MODERN(RDP_depP5, P5)

plot(MODERN_P5)

print(MODERN_P5)

yearlyEDRates(MODERN_P5, samplingTime = 2022, falloutTime = 1963, massDepth = 1
99.45, sampleDepth = 20)

RDP_depP6 = addDepositionLayers(RDP_smooth6, 102.63, 1)
MODERN_P6 = MODERN(RDP_depP6, P6)

plot(MODERN_P6)

print(MODERN_P6)

yearlyEDRates(MODERN_P6, samplingTime = 2022, falloutTime = 1963, massDepth = 1
89.11, sampleDepth = 20)

RDP_depP7 = addDepositionLayers(RDP_smooth7, 50.15, 1)
MODERN_P7 = MODERN(RDP_depP7, P7)

plot(MODERN_P7)

print(MODERN_P7)

yearlyEDRates(MODERN_P7, samplingTime = 2022, falloutTime = 1963, massDepth = 2
01.04, sampleDepth = 20)

RDP_depP8 = addDepositionLayers(RDP_smooth8, 114.14, 1)
MODERN_P8 = MODERN(RDP_depP8, P8)

plot(MODERN_P8)

print(MODERN_P8)

yearlyEDRates(MODERN_P8, samplingTime = 2022, falloutTime = 1963, massDepth = 2
03.89, sampleDepth = 20)
```

Appendix 20 FIGURES OF INFRARED AND OPTICAL STIMULATED LUMINESCENCE AS A FUNCTION OF DEPTH PER SOIL PROFILE

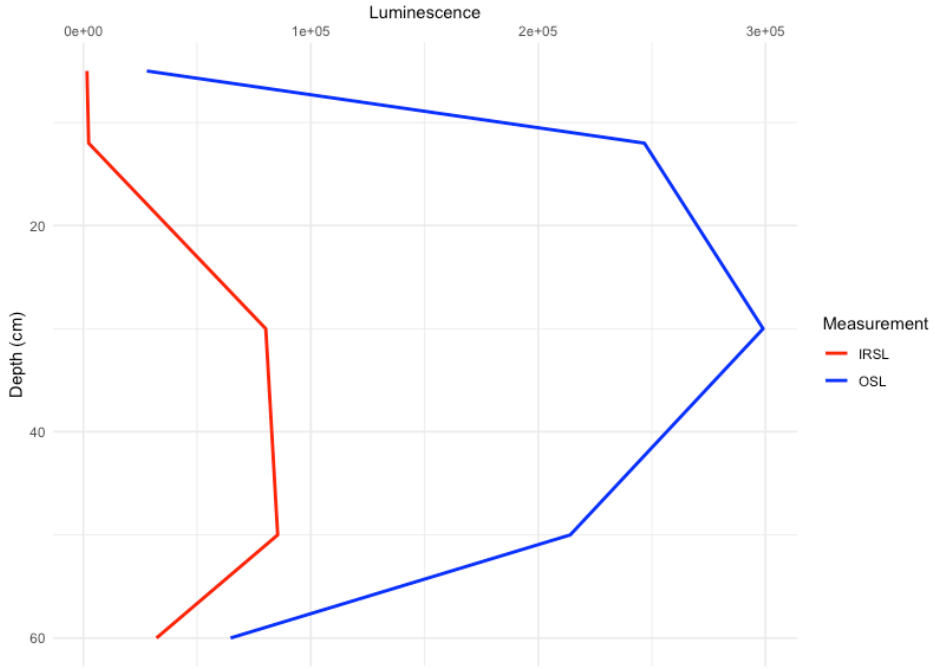

Figure 59: IRSL and OSL as a function of depth in soil profile P1.

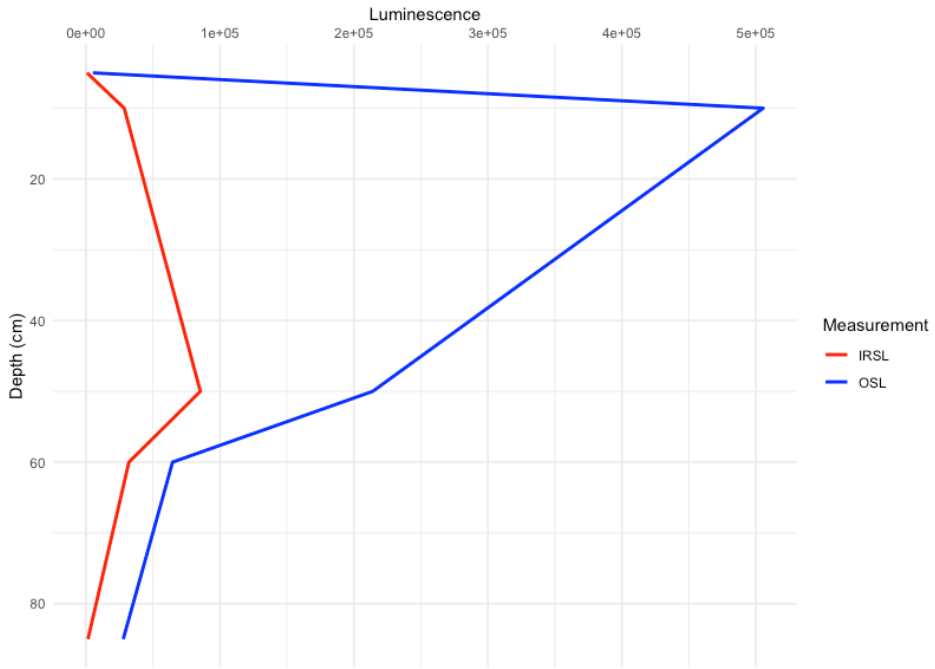

Figure 60: IRSL and OSL as a function of depth in soil profile P2.

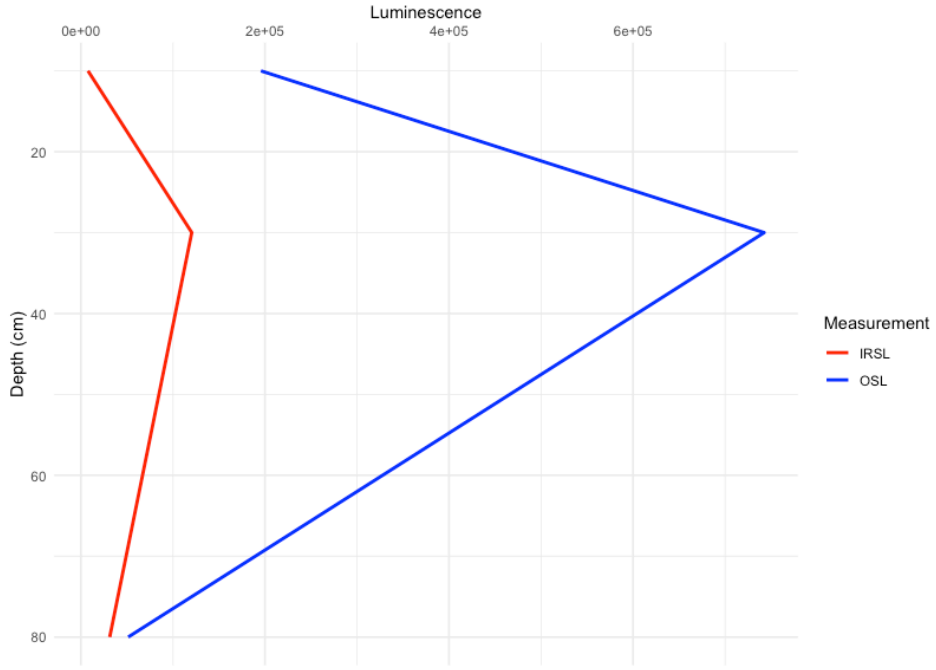

Figure 61: IRSL and OSL as a function of depth in soil profile P3.

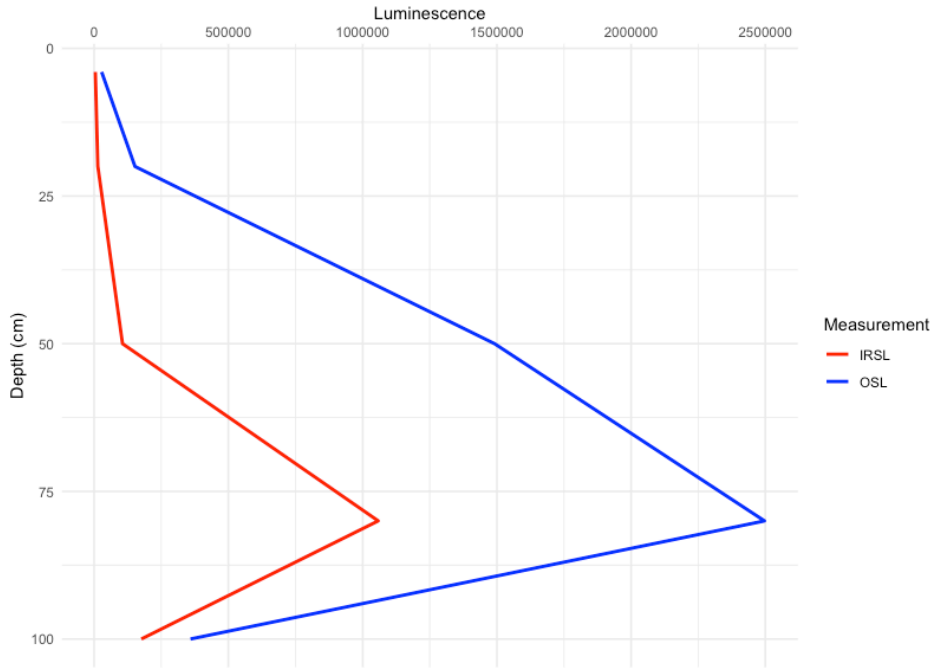

Figure 62: IRSL and OSL as a function of depth in soil profile P4.

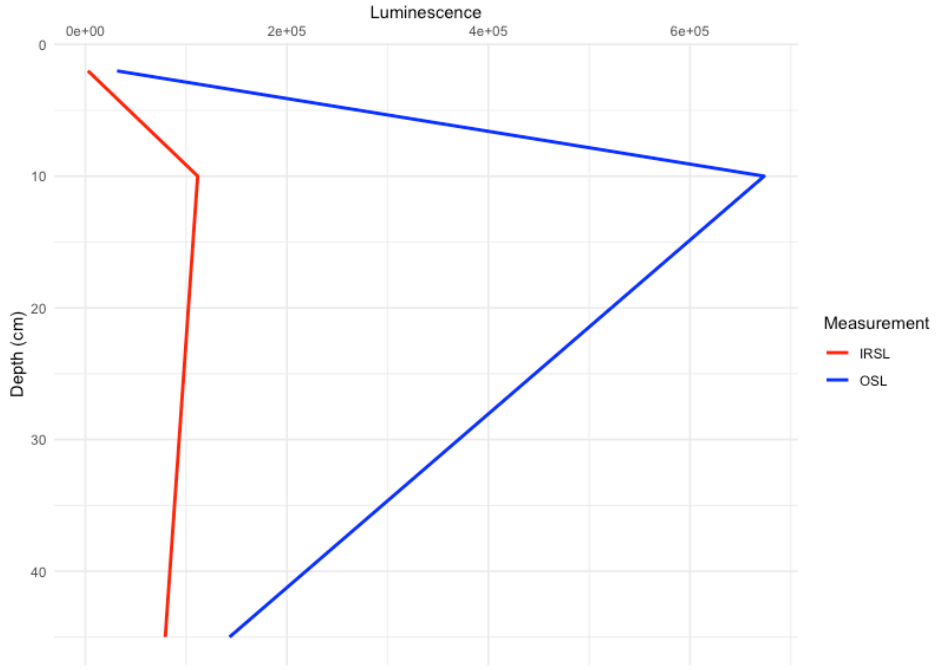

Figure 63: IRSL and OSL as a function of depth in soil profile P5.

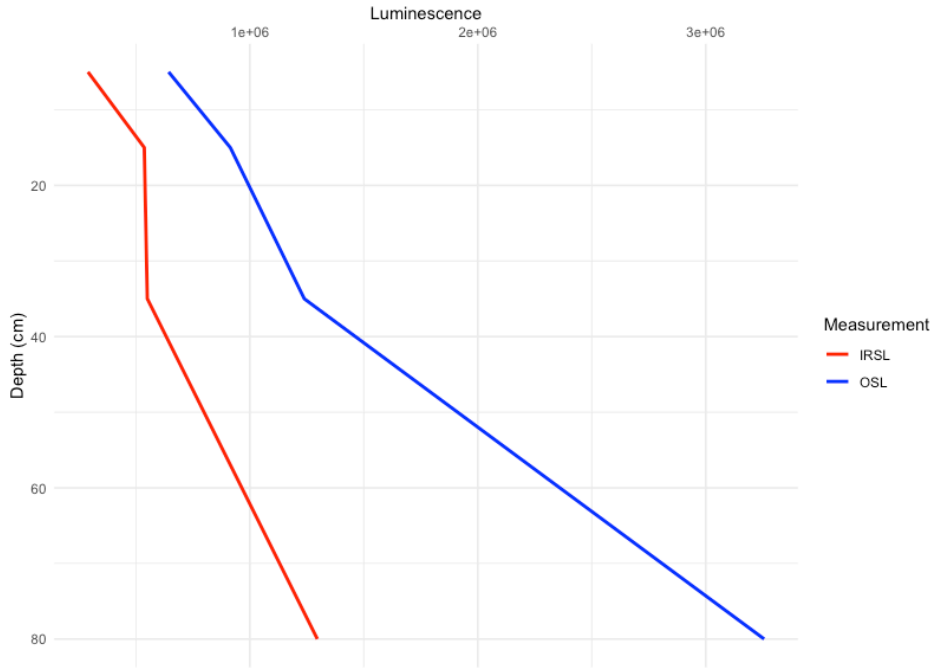

Figure 64: IRSL and OSL as a function of depth in soil profile P6.

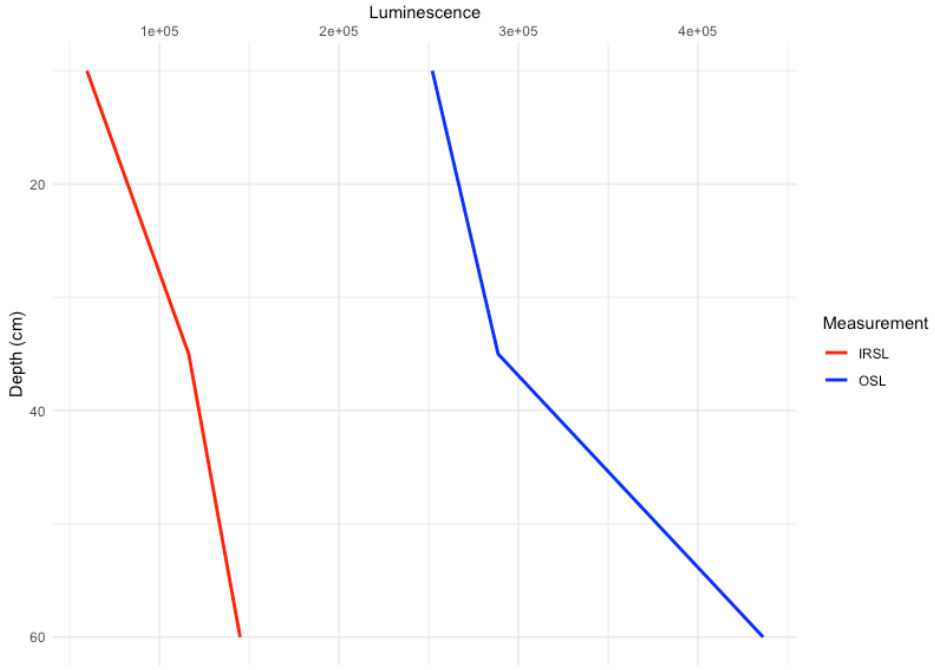

Figure 65: IRSL and OSL as a function of depth in soil profile P7.

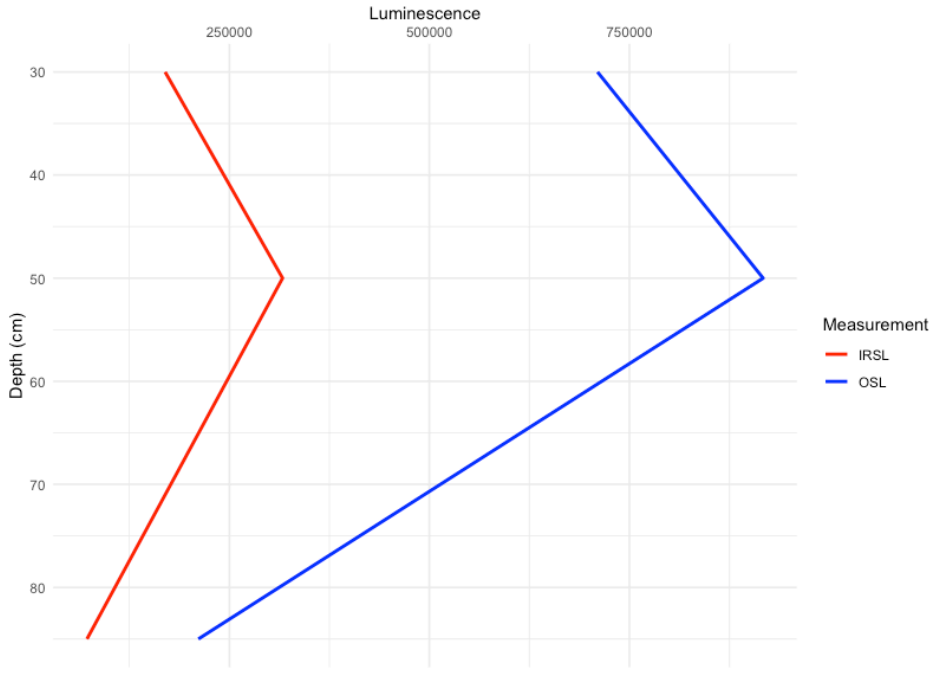

Figure 66: IRSL and OSL as a function of depth in soil profile P8.

Appendix 21 FIGURES OF SOIL PROPERTIES IN RELATIVE TOPOGRAPHICAL POSITION

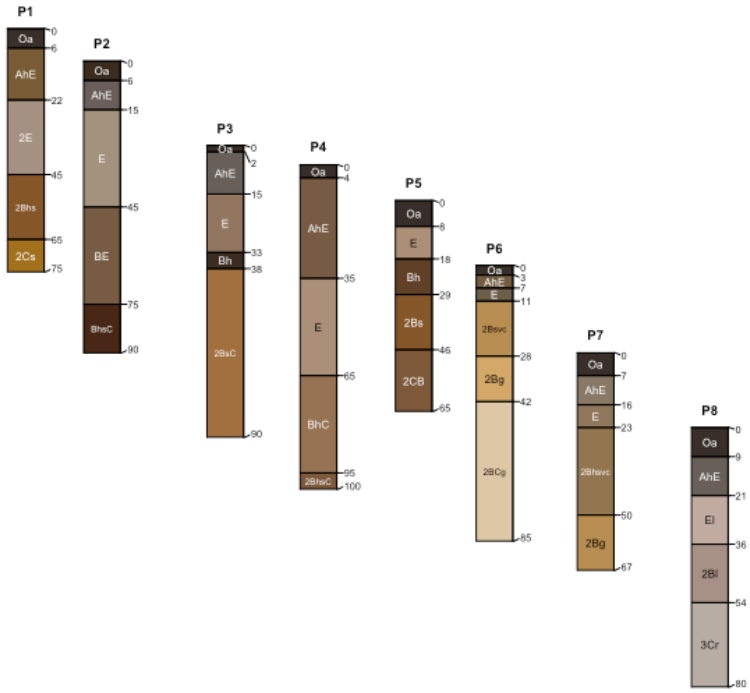

Figure 67: Munsell moist soil color in soil profiles P1–P8 in relative topographical position.

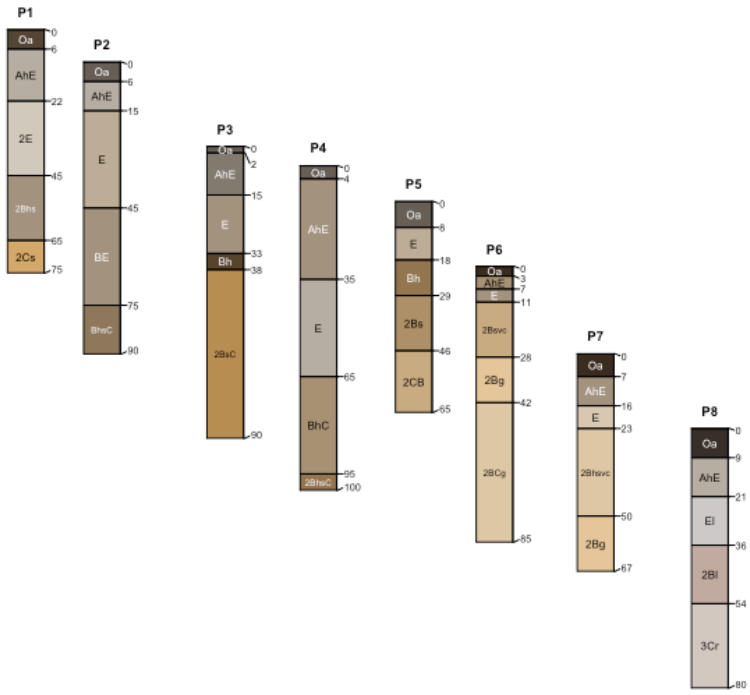

Figure 68: Munsell dry soil color in soil profiles P1–P8 in relative topographical position.

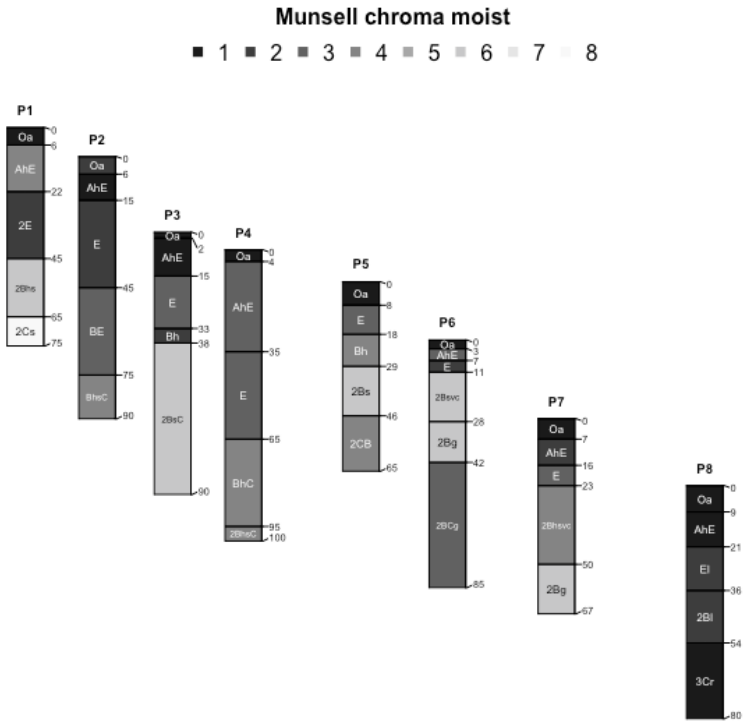

Figure 69: Munsell chroma moist in soil profiles P1–P8 in relative topographical position.

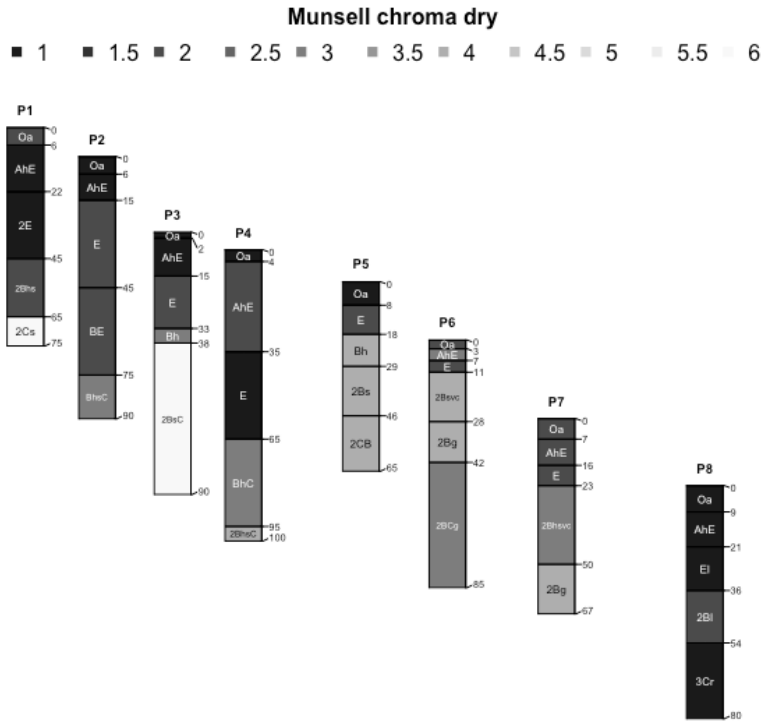

Figure 70: Munsell chroma dry in soil profiles P1–P8 in relative topographical position.

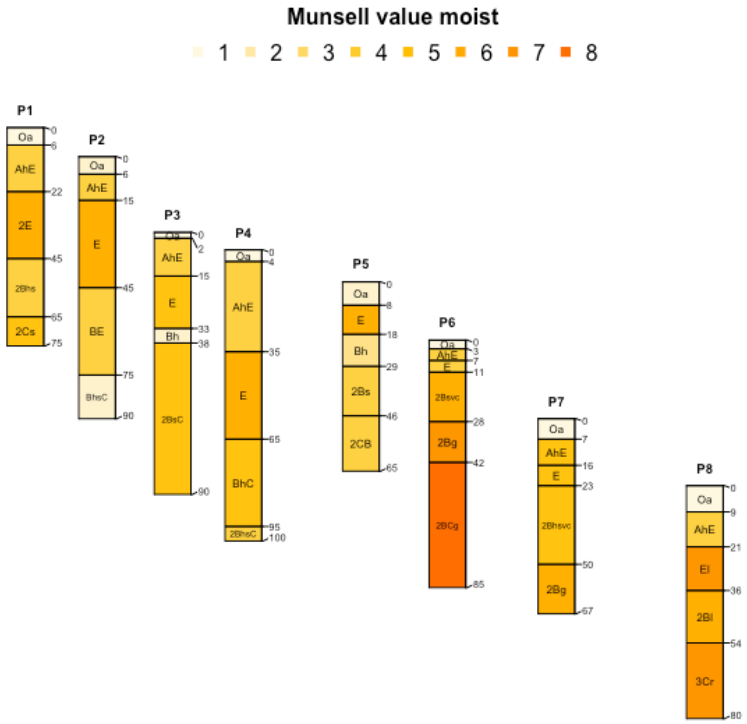

Figure 71: Munsell value moist in soil profiles P1–P8 in relative topographical position.

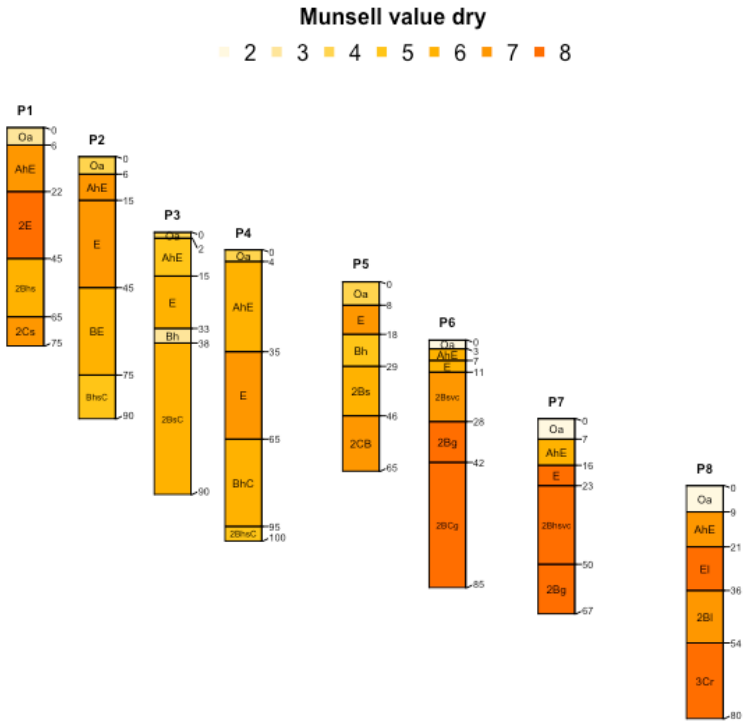

Figure 72: Munsell value dry in soil profiles P1–P8 in relative topographical position.

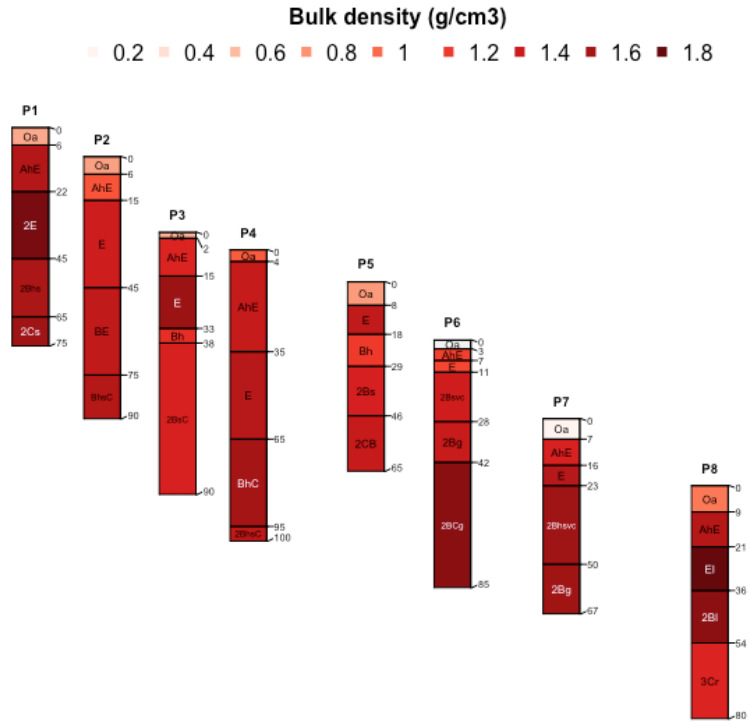

Figure 73: Bulk density in soil profiles P1–P8 in relative topographical position.

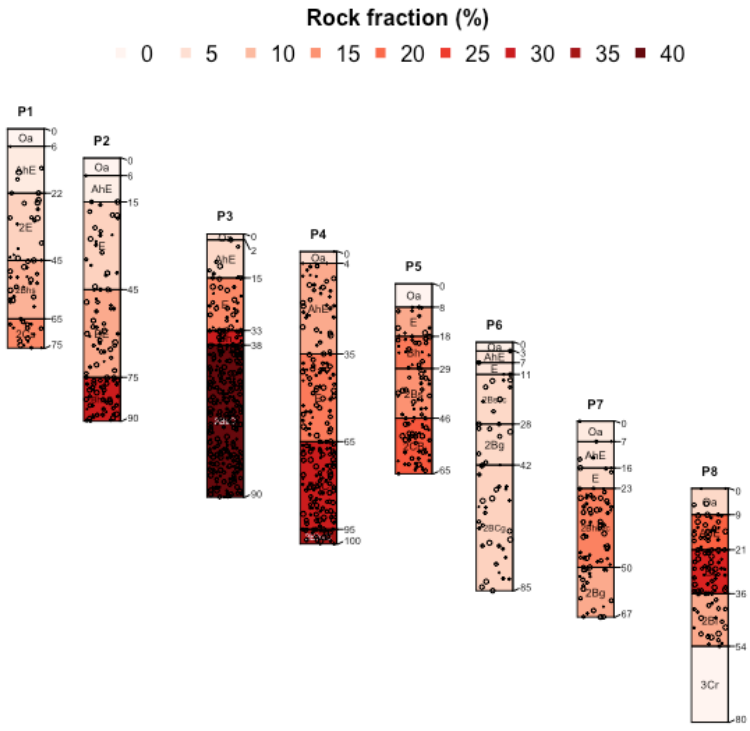

Figure 74: Rock fragment fraction in soil profiles P1–P8 in relative topographical position.

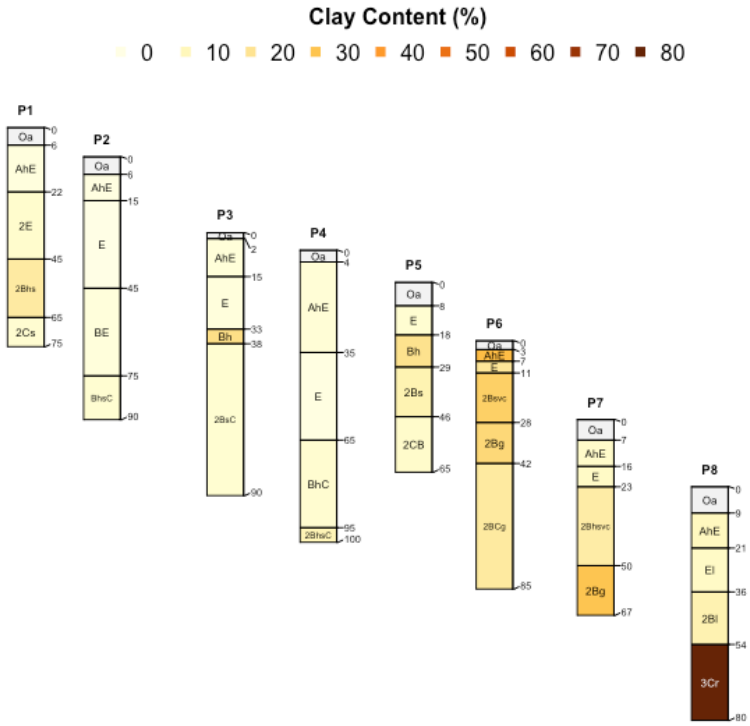

Figure 75: Clay content in soil profiles P1–P8 in relative topographical position.

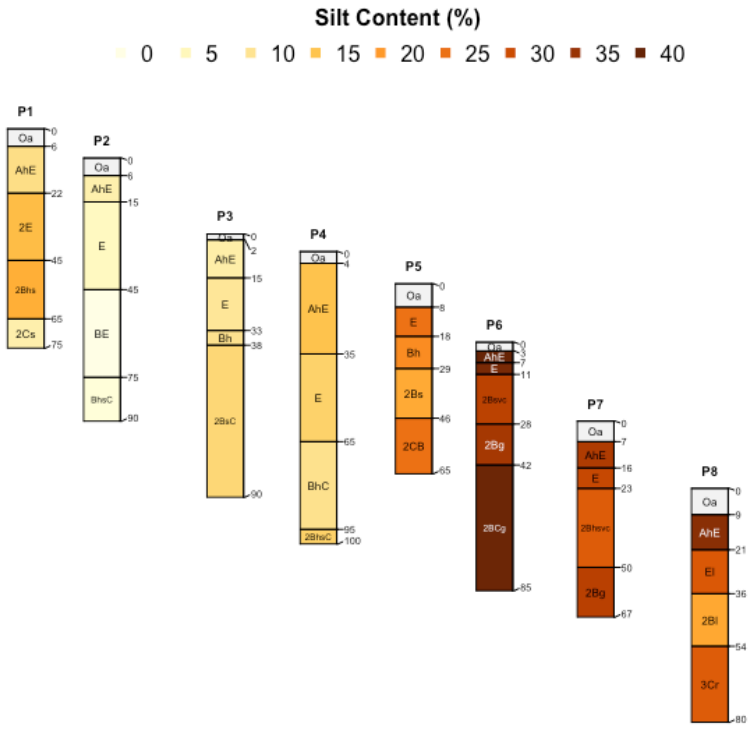

Figure 76: Silt content in soil profiles P1–P8 in relative topographical position.

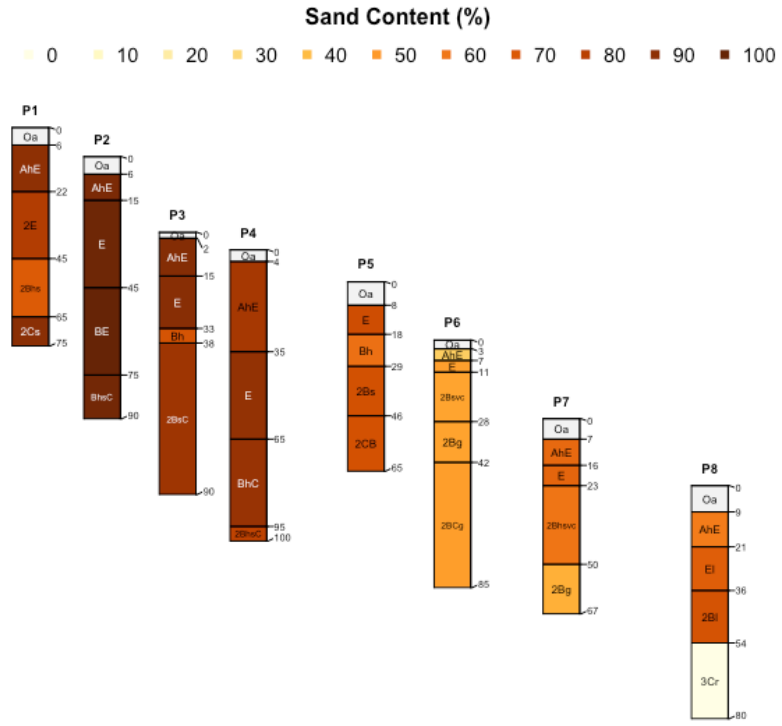

Figure 77: Sand content in soil profiles P1–P8 in relative topographical position.

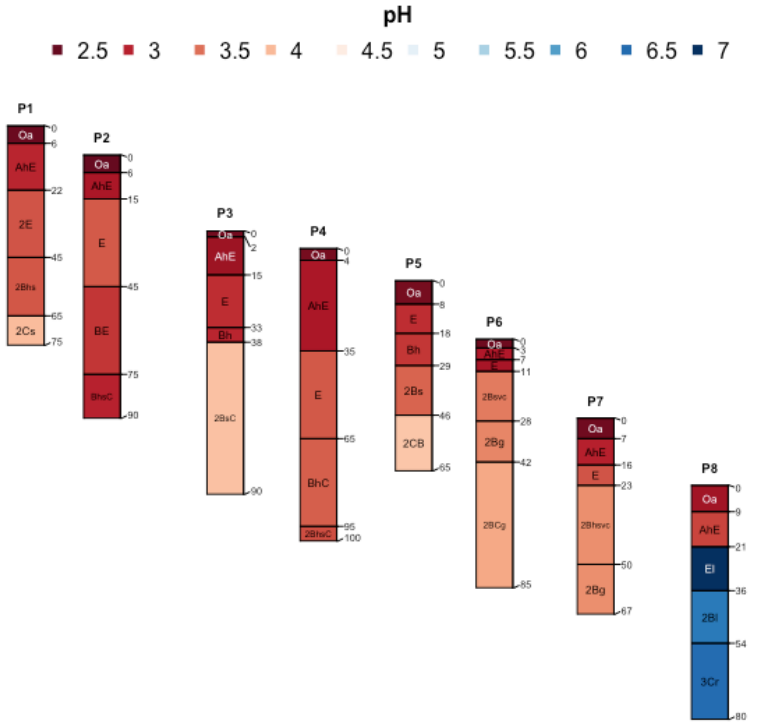

Figure 78: pH in soil profiles P1–P8 in relative topographical position.

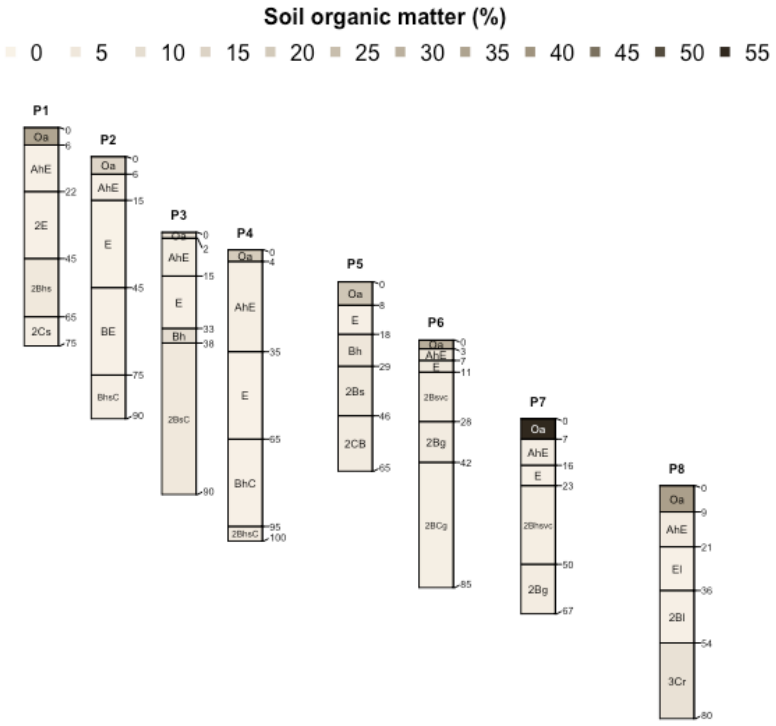

Figure 79: Soil organic matter in soil profiles P1–P8 in relative topographical position.

Appendix 22 FIGURES OF OXIDES IN SOIL PROFILES IN RELATIVE TOPOGRAPHICAL POSITION

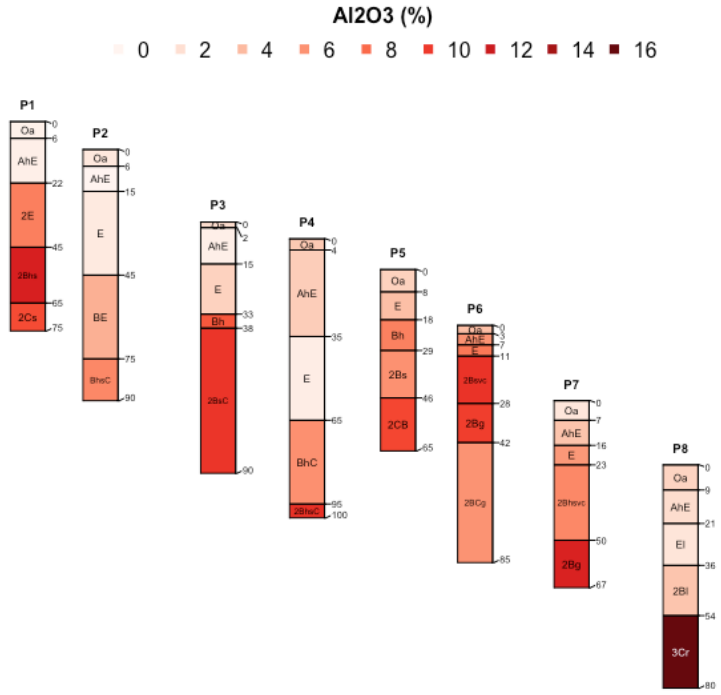

Figure 80: Al2O3 in soil profiles P1–P8 in relative topographical position.

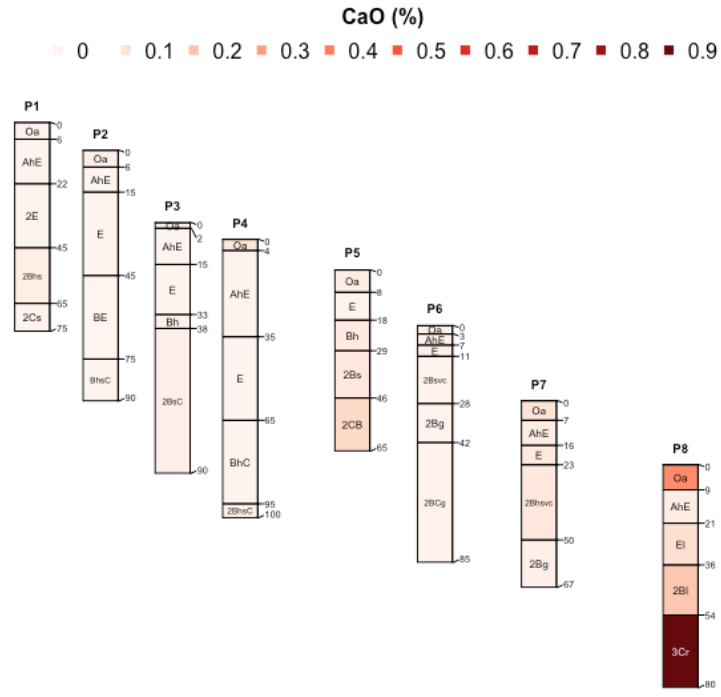

Figure 81: CaO in soil profiles P1–P8 in relative topographical position.

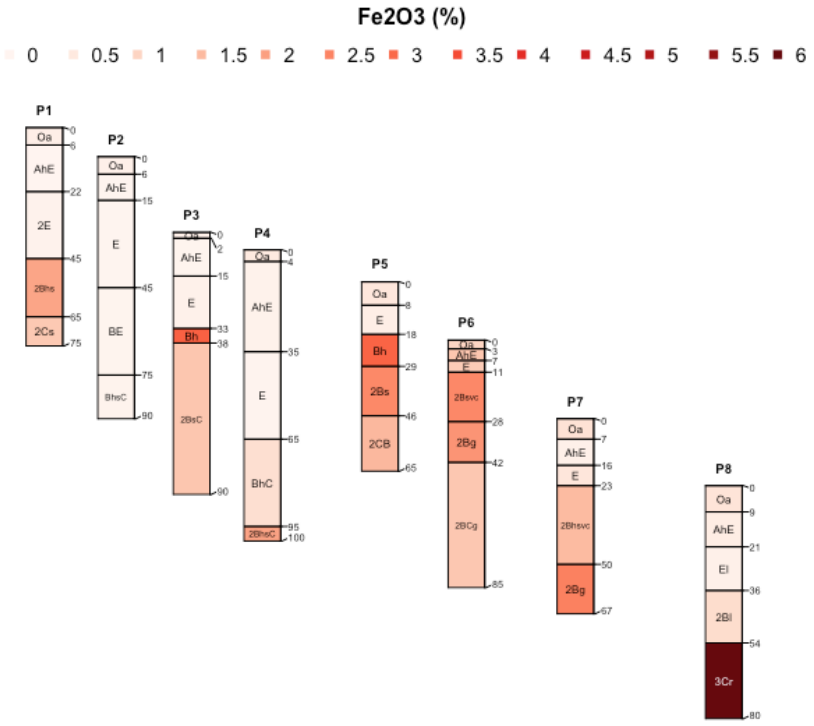

Figure 82: Fe2O3 in soil profiles P1–P8 in relative topographical position.

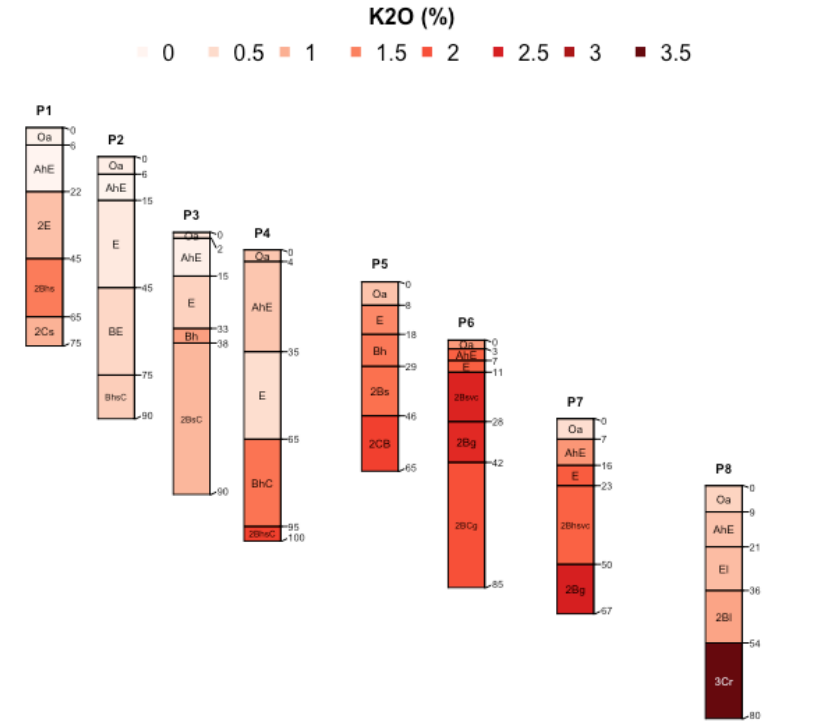

Figure 83: K2O in soil profiles P1–P8 in relative topographical position.

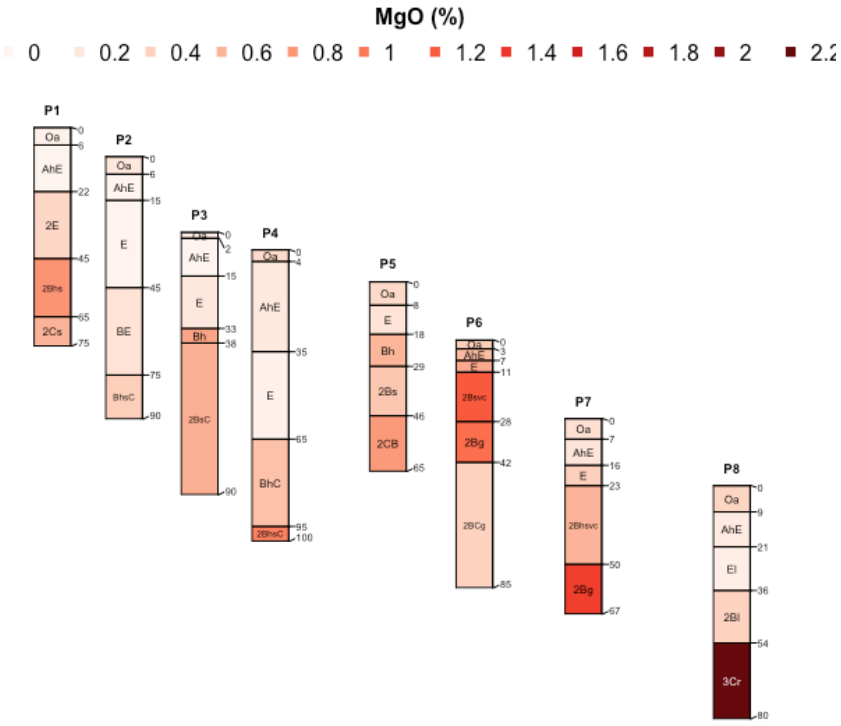

Figure 84: MgO in soil profiles P1–P8 in relative topographical position.

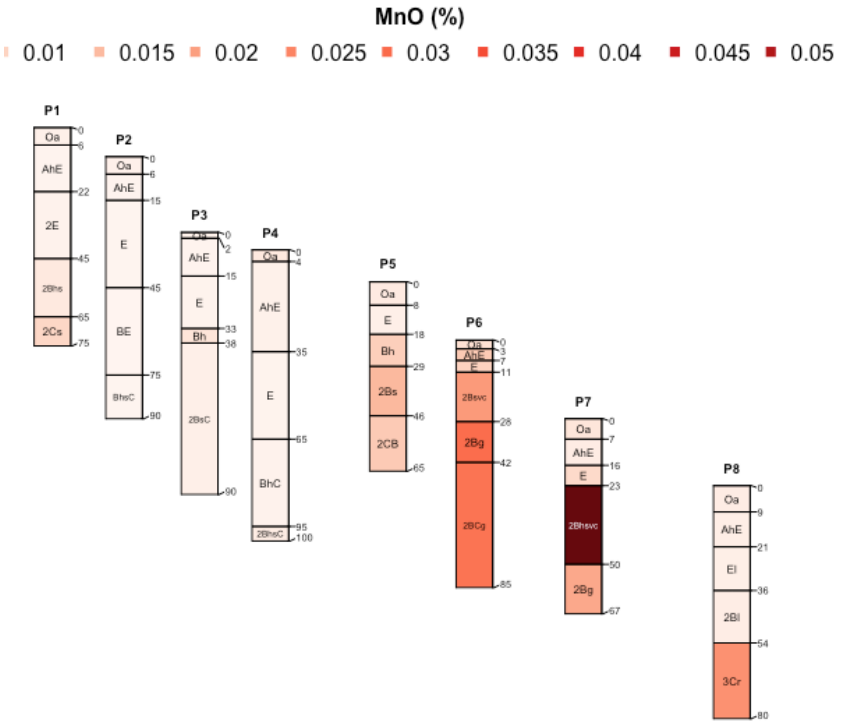

Figure 85: MnO in soil profiles P1–P8 in relative topographical position.

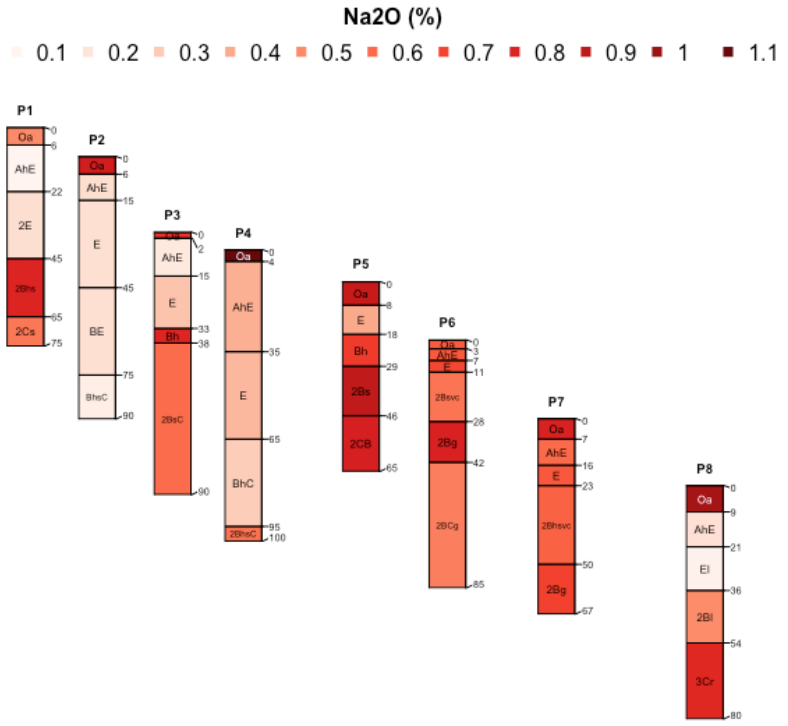

Figure 86: Na2O in soil profiles P1–P8 in relative topographical position.

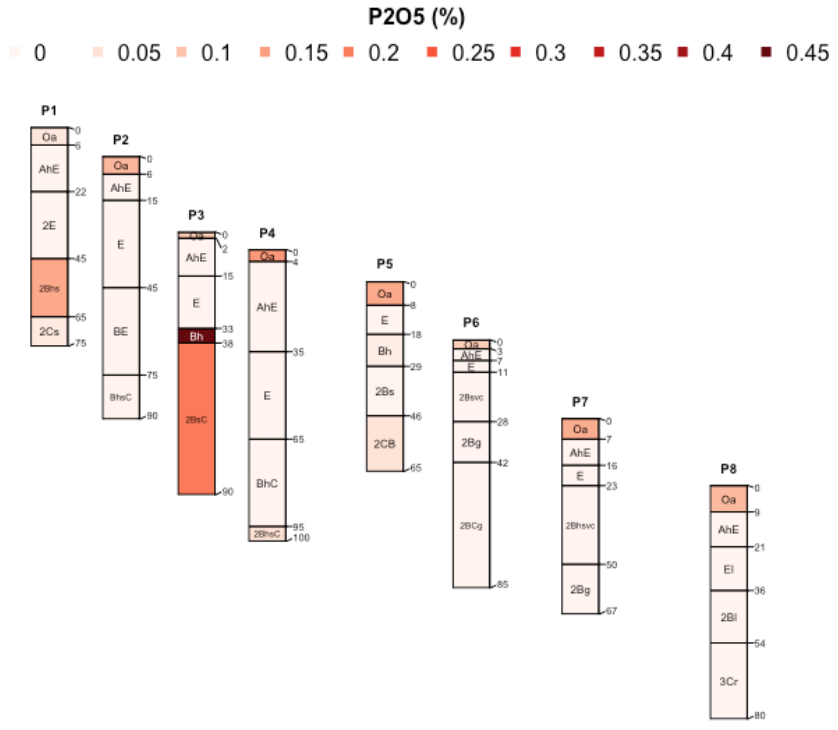

Figure 87: P2O5 in soil profiles P1–P8 in relative topographical position.

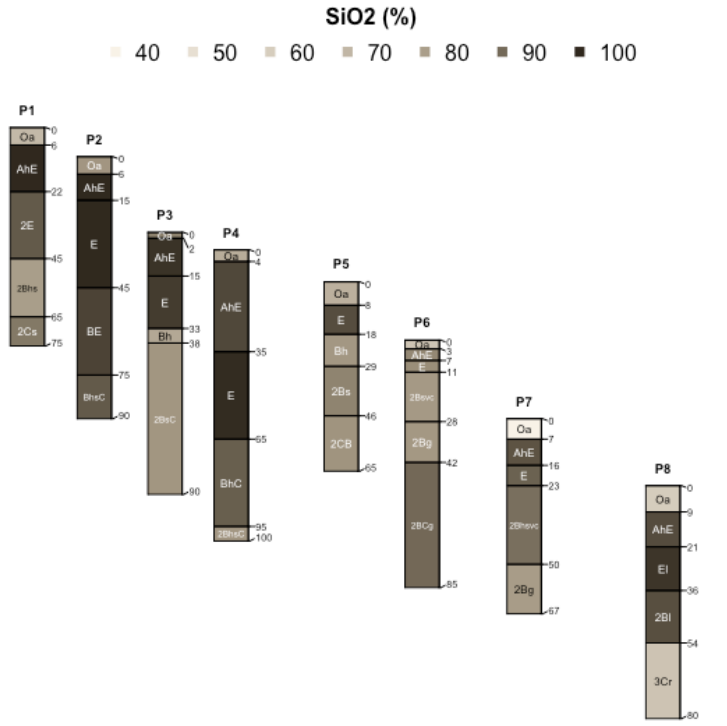

Figure 88: SiO2 in soil profiles P1–P8 in relative topographical position.

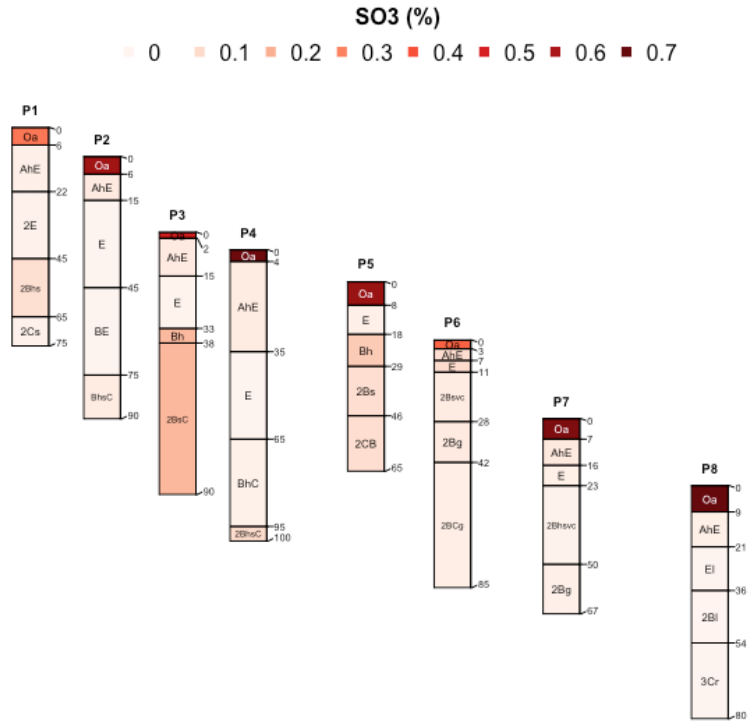

Figure 89: SO3 in soil profiles P1–P8 in relative topographical position.

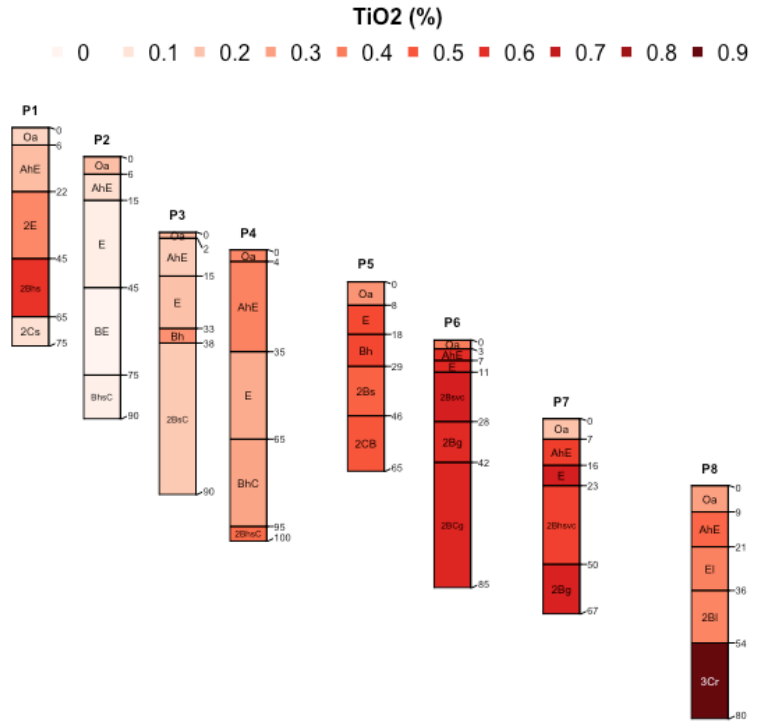

Figure 90: TiO2 in soil profiles P1–P8 in relative topographical position.

Appendix 23 FIGURES OF AMORPHOUS FE AND AL IN SOIL PROFILES IN RELATIVE TOPOGRAPHICAL POSITION

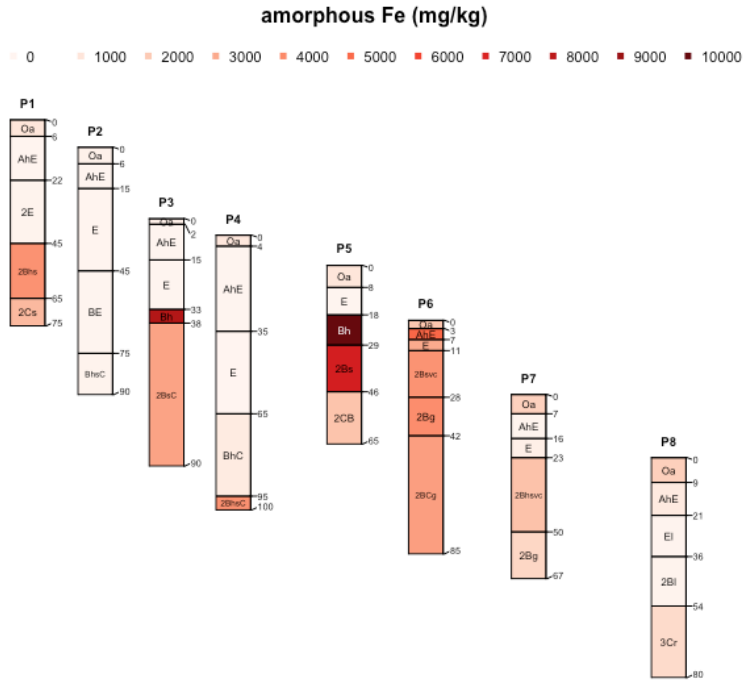

Figure 91: Amorphous Fe in soil profiles P1–P8 in relative topographical position.

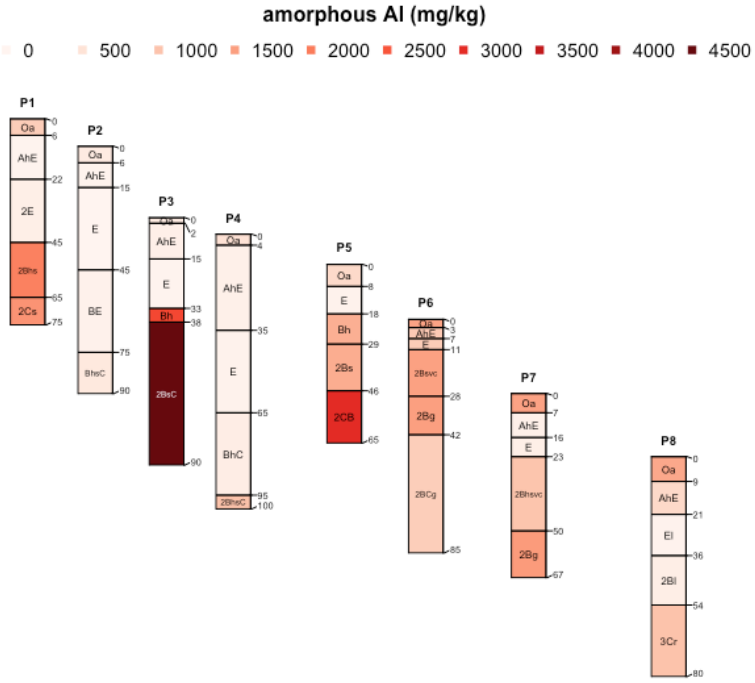

Figure 92: Amorphous Al in soil profiles P1–P8 in relative topographical position.

Appendix 24 FIGURES OF WEATHERING INDICES IN SOIL PROFILES IN RELATIVE TOPOGRAPHICAL POSITION

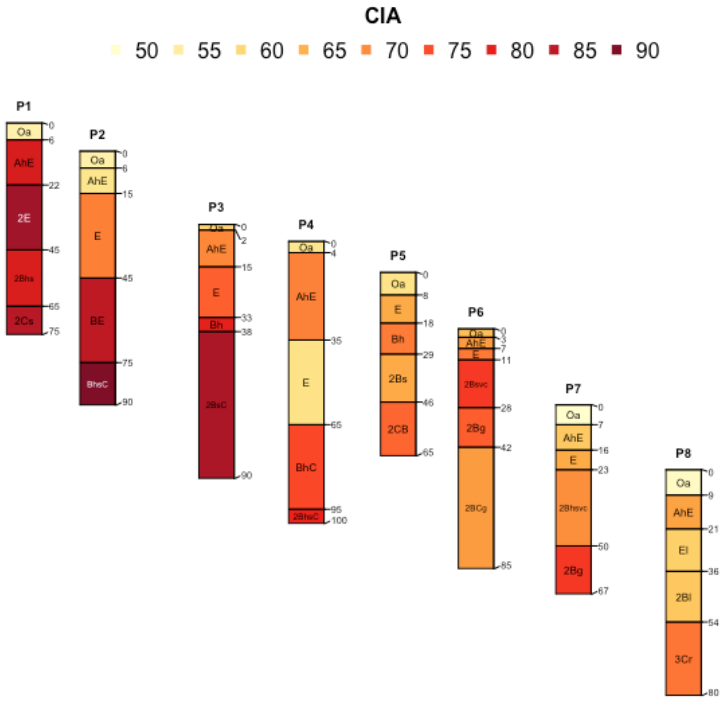

Figure 93: Chemical Index of Alteration (CIA) in soil profiles P1–P8 in relative topographical position.

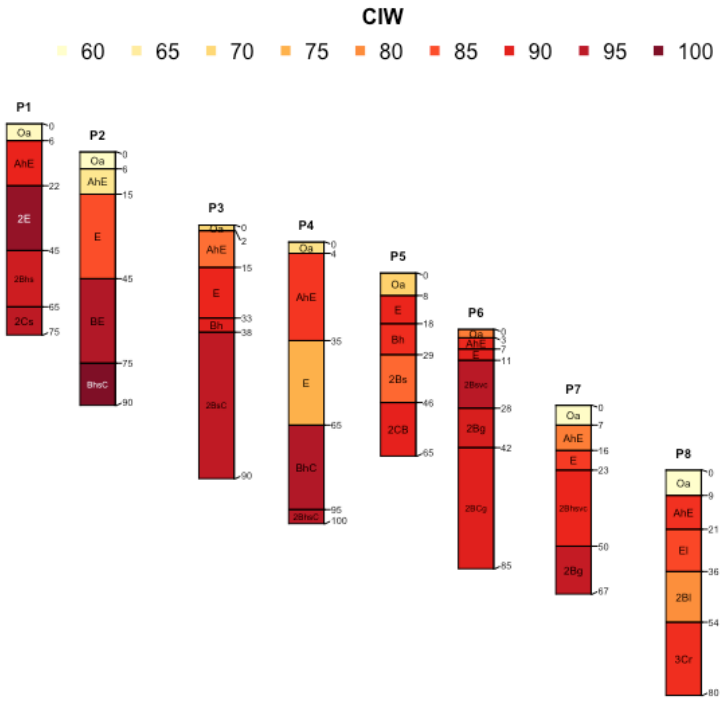

Figure 94: Chemical Index of Weathering (CIW) in soil profiles P1–P8 in relative topographical position.

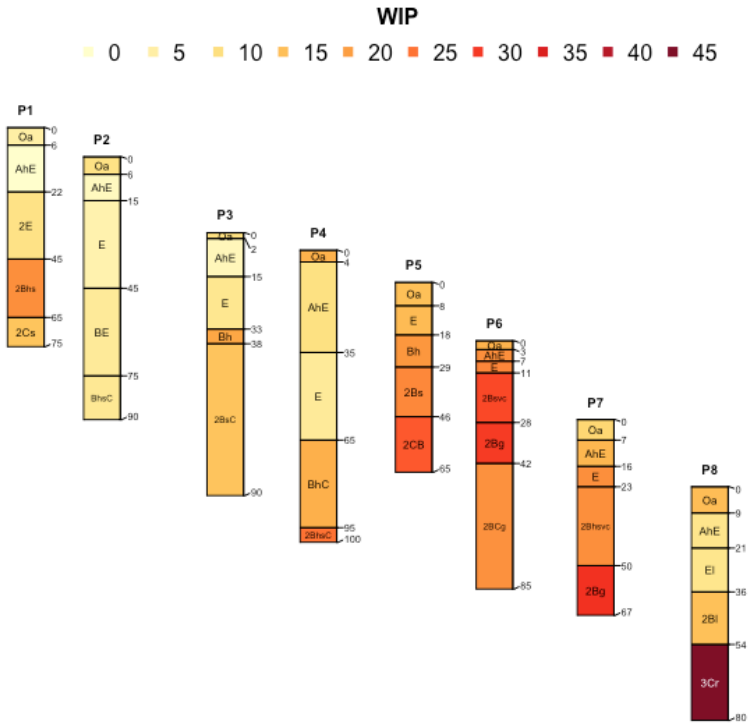

Figure 95: Weathering Index of Parker (WIP) in soil profiles P1–P8 in relative topographical position.

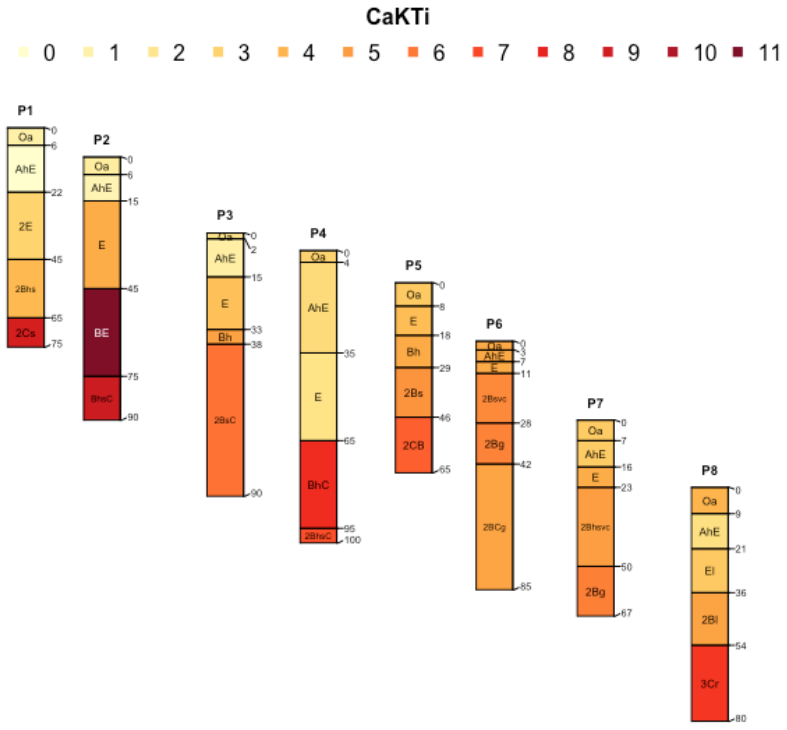

Figure 96: [CaKTi] -Index in soil profiles P1–P8 in relative topographical position.

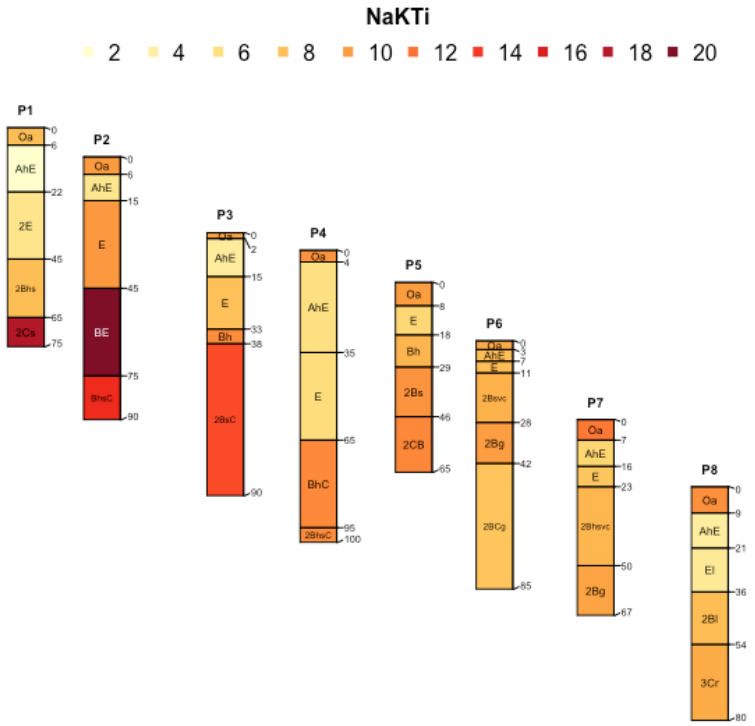

Figure 97: [NaKTi]-Index in soil profiles P1–P8 in relative topographical position.

Appendix 25 FIGURES OF LUMINESCENCE IN SOIL PROFILES IN RELATIVE TOPOGRAPHICAL POSITION

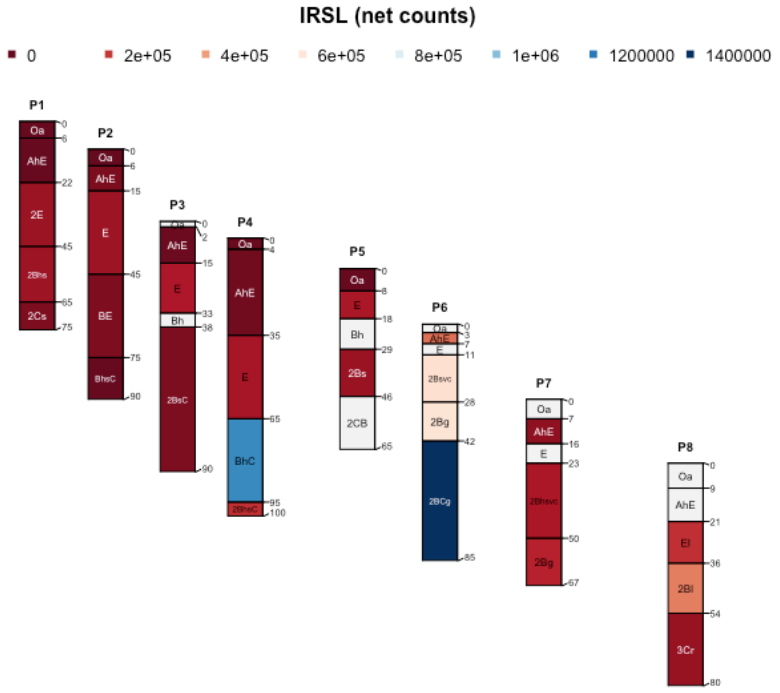

Figure 98: Infrared Stimulated Luminescence (IRSL) in soil profiles P1–P8 in relative topographical position.

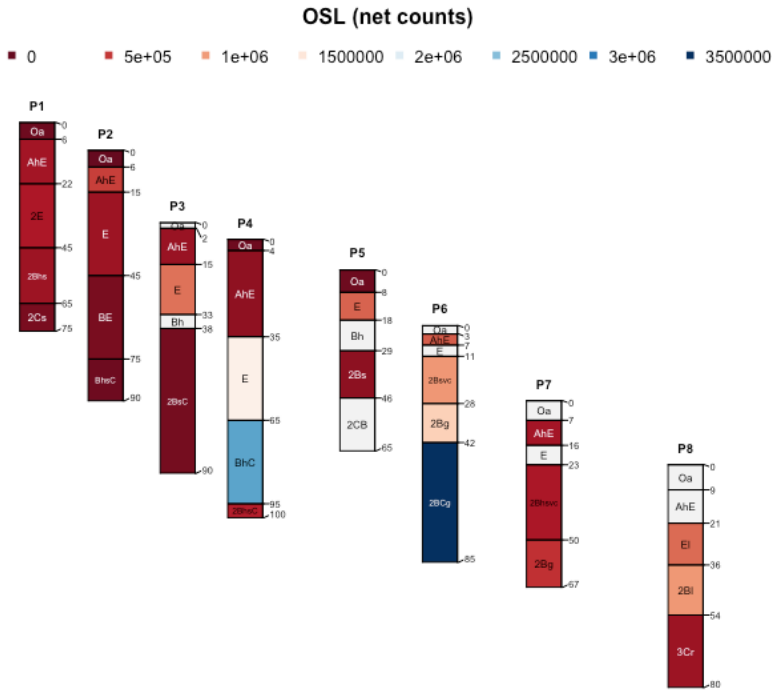

Figure 99: Optical Stimulated Luminescence (OSL) in soil profiles P1–P8 in relative topographical position.

Appendix 26 FIGURES OF SELECTED ELEMENTS IN SOIL PROFILES IN RELATIVE TOPOGRAPHICAL POSITION

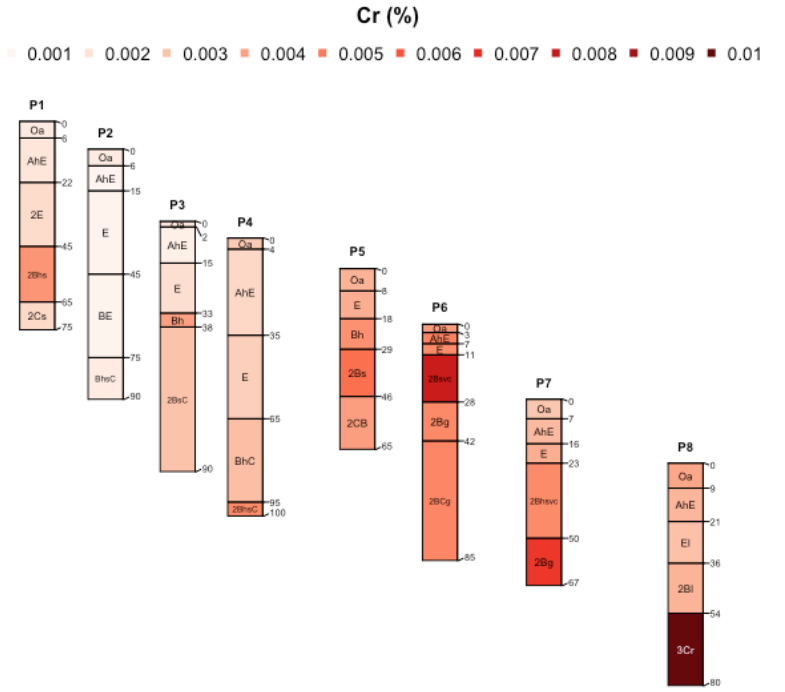

Figure 100: Cr in soil profiles P1–P8 in relative topographical position.

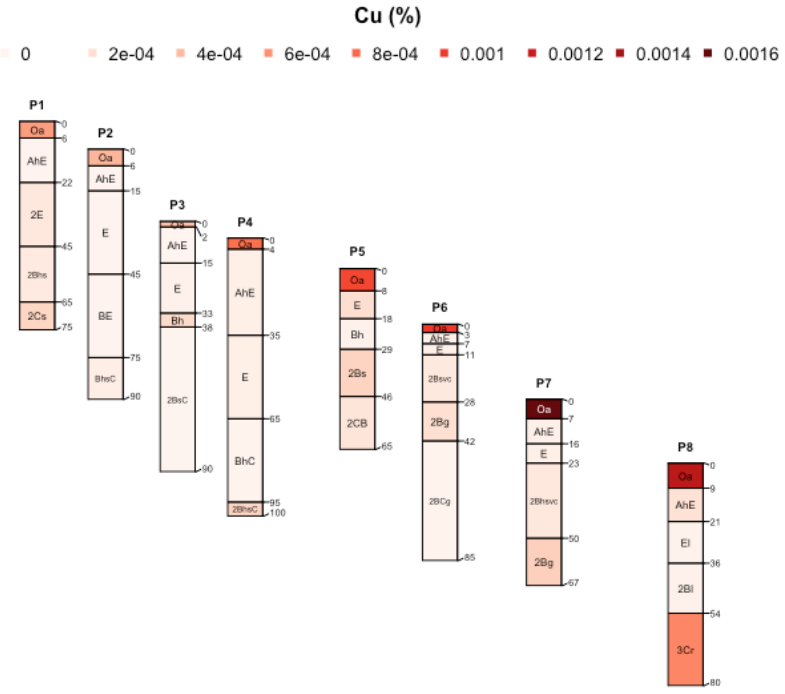

Figure 101: Cu in soil profiles P1–P8 in relative topographical position.

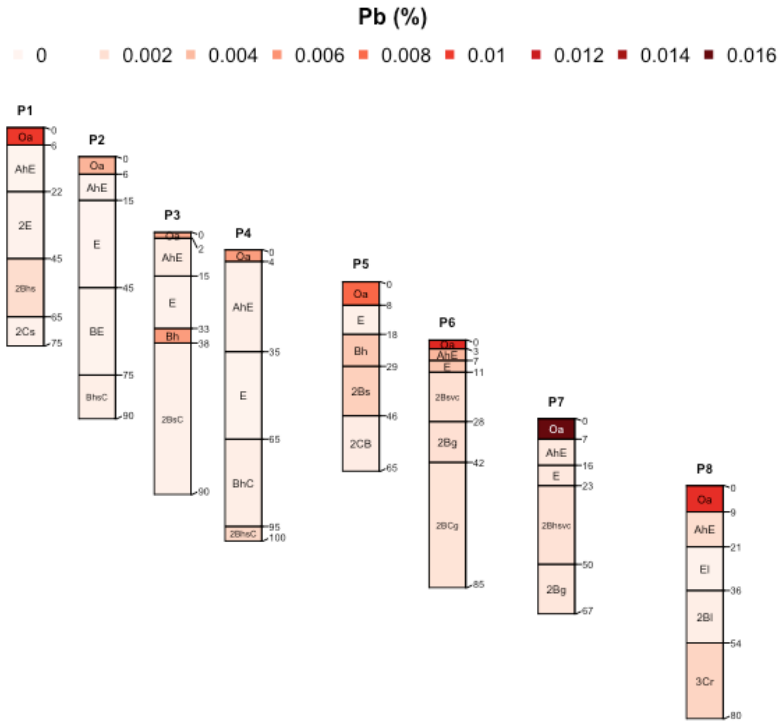

Figure 102: Pb in soil profiles P1–P8 in relative topographical position.

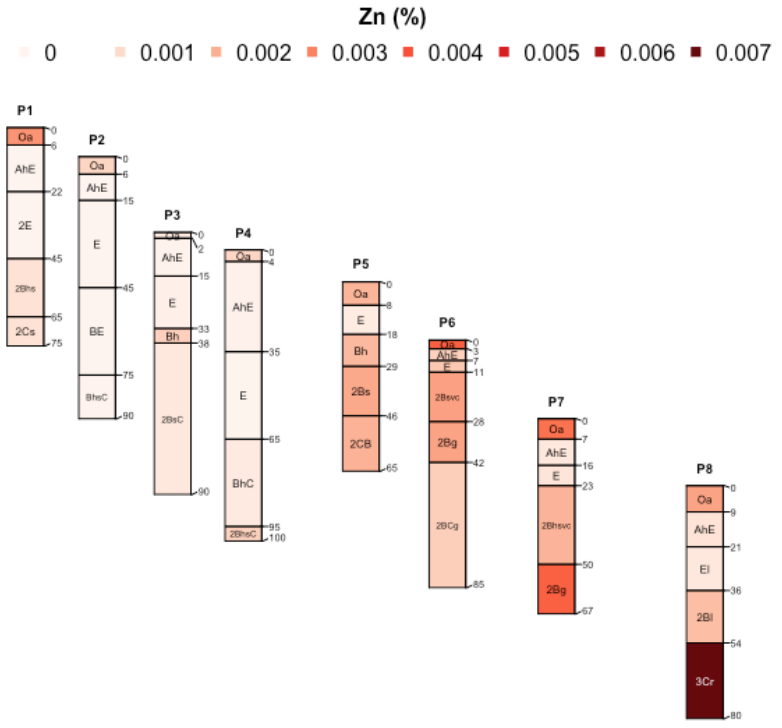

Figure 103: Zn in soil profiles P1–P8 in relative topographical position.

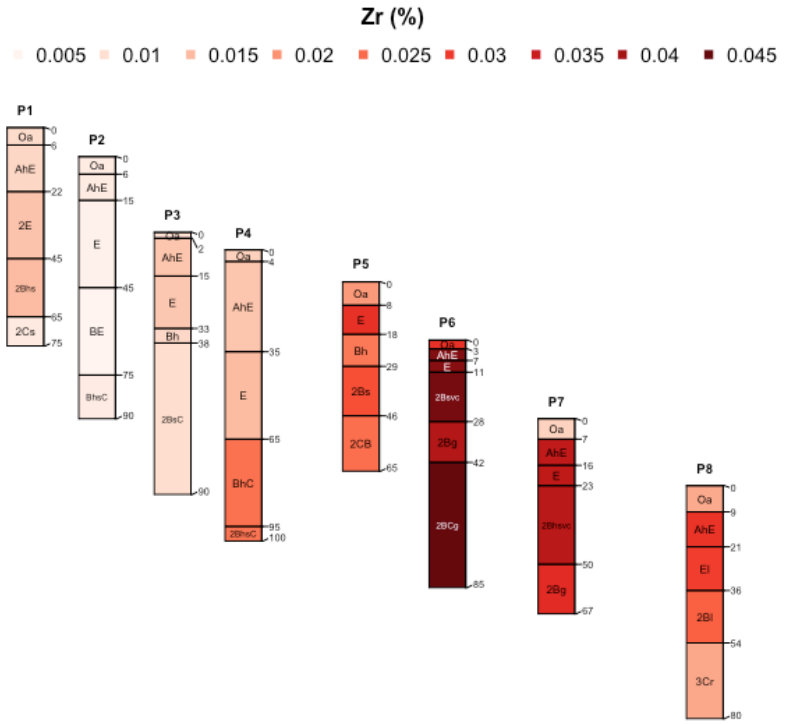

Figure 104: Zr in soil profiles P1–P8 in relative topographical position.

Personal declaration

I hereby declare that the submitted thesis is the result of my own, independent work. All external sources are explicitly acknowledged in the thesis

Simon Amrein Wädenswil, 30 April 2024